EMBEDDED ANTENNA TECHNOLOGY IN SMART POLYMERIC COMPOSITE STRUCTURES

A dissertation submitted in fulfilment of
the requirements for the degree of
Doctor of Philosophy

By

Edin Sulic
BEng (Manufacturing Engineering & Management) and
BAppSc (Computer Science)

School of Aerospace, Mechanical & Manufacturing Engineering
RMIT University

October 2012

Declaration

I certify that except where due references are made, the work reported in this thesis is that of the author alone; the work has not been submitted previously, in whole or in part, to qualify for any other academic award.

The content of the thesis is the result of work that was carried out between the official periods of candidature at RMIT University. Any editorial work, paid or unpaid, carried out by a third party is acknowledged.

Edin Sulic October 2012

Acknowledgements

First and foremost, I wish to thank my primary supervisor, Professor Sabu John of the Royal Melbourne Institute of Technology (RMIT), for his incalculable technical guidance, endless forbearance and unvarying encouragement. He has played a vital role in the success of this project.

I wish to thank my second supervisor, Dr Rahul Gupta of the RMIT, for his suggestions and for guidance during the research project.

I thank the industry partner in this project, Composite Materials Engineers (CME), for assisting me with material, equipment and technical support required during the research project.

I wish to thank Mr Andrew Chryss, Professional Officer at RMIT, for his assistance in the testing of sheet moulding compounds (SMC) rheology using ARIS 2000 at RMIT's Rheology and Materials Processing Centre (RMPC).

I also wish to thank Brendan Pell for his assistance in the progress of the project and for supporting the manufacture and required testing of the antennas pre- and post-embedding.

I wish to thank other project team members, in no particular order: Dr Wayne Rowe, Dr Kamran Ghorbani, Prof. Kefei Zhang of RMIT and Mr Brian Hughes of CME for their suggestions, support and assistance in this project.

I wish to thank my parents for supporting and encouraging me throughout the project.

Lastly, I would like to thank my wife Aida Salihovic, who has helped me complete this project with her invaluable support, motivation and tolerance all through.

Abstract

One of the fastest-growing uses of sheet moulding compound (SMC) material is in the area of manufacturing of vehicle body components for both structural and non-structural applications. This trend is accelerating, driven by original equipment manufacturers (OEM) and their need for lighter and more fuel-efficient vehicles. In addition, over the last 20 years, the number of entertainment and communication systems in vehicles has also been expanding.

The aim of this research is the development of a single wideband antenna that is capable of receiving all of the major services of interest. Taking this approach one step further and embedding such an antenna in a polymeric composite vehicle body panel would combine the benefits of reduced coefficient of drag, lower vehicle weight, reduced assembly complexity and shorter assembly time. These benefits would manifest themselves in the form of lower overall design and manufacturing vehicle cost for the OEMs and lower fuel consumption for customers. This thesis will deal with the development of such an antenna and the challenges faced in embedding it in a polymeric composite vehicle panel to such an extent that it becomes a seamless part of the vehicle body. This application required the development of a detailed understanding of the following three areas. Firstly, understanding of the interactions and effects of SMC material and automotive paint on antenna signal quality and performance through experiments and electromagnetic modelling (EM). Secondly, the development of the manufacturing process and material used to embed the antenna and its impact on the physical properties of the antenna through rheological testing, analytical modelling and experimentation. Lastly, the development of a wideband antenna capable of receiving pre-determined signals, through EM and field testing.

The effects of paint application and presence of SMC resulted in a frequency shift of less than 1%. The experiments correlated well with the analytical model developed for compression moulding which incorporates a novel inclusion of the Maxwell's model to predict the shear forces in the material flow within a confined space. A modular planar inverted conical antenna (PICA) was developed and optimised for the frequency range 700MHz – 9000MHz, which includes the commercial global positioning system (GPS) frequency. This development was then deployed as an embedded prototype in the deck lid of a test vehicle. Comparison against commercial GPS and mobile phone antennas was undertaken. This field test comparison showed that the developed PICA antenna performed better than the commercial antenna by up to 17%, especially in spaces devoid of multi-path signals.

Table of Contents

List of Figures

List of Tables

List of Symbols and Units

C_p	specific heat capacity
Ea	activation energy
g	gravity
G	complex viscosity
G’	storage modulus
G’’	loss modulus
K	thermal conductivity
λ	relaxation time of the material
m	adjustable variable (rate of change of shear rate)
η	Pa.s viscosity
η’	complex viscosity component
p	pressure
ρ	density
R	universal gas constant
$\|S_{11}\|$	input port voltage reflection coefficient
T	℃ temperature in Celsius
T	(K) reference temperature in Kelvin
t_i	seconds time material is in contact with bottom tool surface
t_j	seconds time material is in contact with top tool surface
v	velocity
$\dot{\gamma}$	s^{-1} shear rate

ω	angular frequency
dB	decibel
Ω	ohm
ε_r	dimensionless dielectric constant
m'	activation energy to flow (function of temperature)
m"	slope of shear viscosity on frequency
m	overall slope parameter taking into effect the temperature, frequency dependency
η	shear viscosity
η_0	zero-shear viscosity
$2\pi / \omega$	angular frequency
T_v	tool velocity
τ_{12}	Pa shear stress is in the elastic material
G	elasticity modulus of the material
$\dot{\gamma}_{12}$	net strain in the material

List of Abbreviations

2D	Two-dimensional
3D	Three-dimensional
ABS	Acrylonitrile butadiene styrene
ACC	Adaptive cruise control
AR	Aspect ratio
ARES 2000	Advanced Rheometric Expansion System 2000
BMC	Bulk moulding compound
CAD	Computer-aided design
CAE	Computer-aided engineering
CBD	Central business district
CFRP	Carbon fibre reinforced plastic
CME	Composite Materials Engineers
CPW	Coplanar waveguide
CSL	Coupled slotline
DAB	Digital audio broadcasting
DSC	Differential scanning calorimetry
DSRC	Dedicated short-range communication
EMI	Electromagnetic interference
FCC	Federal Communications Commission
GFRP	Glass fibre reinforced polymers
GNSS	Global navigation satellite system
GMT	Glass mat thermoplastic
GPS	Global positioning system
GRP	Glass reinforced plastic

HFE	High frequency equivalent
HSPA	High Speed Packet Access
HSV	Holden Special Vehicles
ISM	Industrial, scientific and medical
ITS	Intelligent transportation system
LAOS	Large amplitude oscillatory shear
LFE	Low-frequency equivalent
LNA	Low noise amplifier
LTE	Long Term Evolution
OEM	Original equipment manufacturers
O-PICA	Optimised PICA
PC	Polycarbonate
PCB	Printed circuit board
PET	Polyethylene terephthalate
PICA	Planar inverted cone antenna
PP	Polypropylene
PVB	Polyvinyl butyral
PVC	Polyvinyl chloride
RF	Radio frequency
RFID	Radio frequency identification
RHCP	Right-hand circular polarisation
RMIT	Royal Melbourne Institute of Technology
RMPC	Rheology and Materials Processing Centre
SAOS	Small amplitude oscillatory shear
SDARS	Satellite Digital Audio Radio Service
SEM	Scanning electron microscope

SMC	Sheet moulding compound
SNR	Signal-to-noise ratio
SUV	Sport utility vehicle
TGA	Thermo gravimetric analysis
TPMS	Tyre pressure monitoring systems
TTS	Time–temperature superposition
UMTS	Universal Mobile Telecommunications System
UV	Ultraviolet
UWB	Ultra-wideband
V2I	Vehicle-to-infrastructure
V2R	Vehicle-to-roadside
V2V	Vehicle-to-vehicle
VII	Vehicle-Infrastructure Integration
VNA	Vector network analyser
VOC	Volatile organic compounds
VSWR	Voltage standing wave ratio
WAVE	Wireless access in vehicular environment
XRD	X-ray diffraction

CHAPTER 1: Introduction

1.1 Background

Nowadays, a large number of structural and non-structural composite parts are used in the automotive industry. The composite materials exhibit an excellent strength-to-weight ratio compared to steel and aluminium, which are the materials used traditionally for the construction of automotive parts. This results in overall vehicle weight reduction and subsequent reduction in fuel consumption. In addition, composite materials allow the use of more complex part designs that are not possible to achieve with stamped steel and aluminium. This clearly indicates the superiority of composite components.

To enhance the superiority of the composites further, it is feasible to integrate additional functionality in such components, one of them being a communication device such as an antenna. Other communication devices, such as radio frequency identification (RFID) tags for vehicle identification and tracking, can also be embedded, using the same approach as the embedding of an antenna. However, this research will focus on the antenna as a communication device that is embedded into a composite component.

Creating a multifunctional vehicle component such as a roof, bonnet or a trunk offers significant advantages to original equipment manufacturers (OEMs) as it significantly reduces whole-life vehicle costs, ensuring the long-term viability and sustainability of the automotive sector. In addition, these types of new technologies will offer significant advantages to automotive suppliers in the competitive global supply market.

1.2 Objectives and Rationale

The aim of the research was to develop a smart multifunctional vehicle component. To achieve this aim, the research team had to overcome and address a number of challenges:

1. Is the selected sheet moulding compound (SMC) material suitable for the intended application?

    a. Is the dielectric constant of SMC such that it would not significantly influence antenna performance?
2. What are the effects of metallic and non-metallic paint on signal quality?
3. What effect will embedding have on the antenna as it will need to go through compression-moulding process that will exert relatively high pressures and temperatures on the antenna structure?
4. Can the compression-moulding process parameters be optimised to minimise any deleterious effects if discovered in item 3 above?
5. Can a single wideband antenna be designed to work from a few hundred MHz to several GHz and produce usable signal quality?
6. How will the developed embedded antenna perform against commercially available counterparts at typical global positioning system (GPS) frequencies?

A major part of this project relating to items 3 and 4 above was to develop a detailed understanding of material flow characteristics and their effects on the antenna being embedded in the material used, namely, SMC, during the first two stages of the compression-moulding cycle. These two stages consisted of loading the SMC charge and the antenna, in a sandwich-like arrangement, into the tool and closing the tool so that the material completely filled the tool cavity.

In conjunction, the development of a wideband antenna that would have acceptable performance and signal quality from a few hundred MHz to several GHz would represent a second major challenge.

The key objective of this research was to investigate if the initial research aim was feasible to achieve, thereby confirming proof of the concept that a seamless painted composite vehicle component can provide two functions, namely, the function of a structural or class A component (a class A component is defined as a visible vehicle panel) and that of an antenna. This second function will negate the need for other antennas in the vehicle, acting as a single replacement for the five to 10 different antennas currently used in vehicles to receive signals for several currently used devices, ranging from

car radio, satellite navigation, digital TV and central locking to future (five to 10 years) devices, such as collision avoidance radar, vehicle-to-vehicle (V2V) and vehicle-to-roadside/vehicle-to-infrastructure (V2R/V2I) communication at 5.9 GHz frequency. This frequency of 5.9 GHz has been reserved globally for the new types of services, V2V and V2R.

The advantages of this multifunctional component for OEMs and end users are numerous: reduced cost and complexity of vehicle manufacture, reduction in vehicle weight and therefore fuel usage, shorter vehicle assembly times, reduction in vehicle component and sub-system testing and increased freedom for vehicle designers, as the use of composite panels will allow for more complex design shapes that are not possible with traditionally used materials such as stamped steel and aluminium.

1.3 Methodology

Initially, a comprehensive literature review was conducted on the various types of vehicle antennas currently used and the latest developments in the field of automotive antennas. This was followed by a review of composite materials and their use in vehicle design and manufacturing. Establishing the dielectric constant of SMC was essential for assessing the viability of the antenna embedding as a feasible concept for the end application. The effects of automotive paints, both oil and water based, on the transmission and reception of signals in free space and on the overall antenna performance.

After this detailed study, the best grade of SMC composite material was chosen as the most appropriate material to be used for the end application. This approach was supported by two very important facts. The first is that Composite Materials Engineers (CME), the industry partner in the project, already used SMC material for its automotive applications, and so they had the required technology and expertise to support research involving this material. The second is that the use of SMC material in the automotive sector is on the increase, especially by European vehicle manufacturers such as BMW, Mercedes and the VW group.

To develop a material model that could be used to predict antenna deformation during the embedding, a detailed rheological study of the SMC had to be undertaken, as the author could not find any literature dealing with the deformation of components being embedded into SMC material. The study was performed using the latest generation optical rheometer and accompanying software: the Advanced Rheometric Expansion System 2000 (ARES 2000), with a force rebalance transducer of 20 mN*m, parallel plates of Ø 25 and Ø 50 mm, temperature range from 25 to 160 °C, heating rate from 4 to 40 °C/min and excitation frequency from 1 to 16 rad/second. During the study, the viscoelastic behaviour of the material was observed, and parameters such as G' (storage modulus) and G'' (loss modulus) were recorded.

Data from the rheological characterisation of SMC was used to develop a material model based on the classical Maxwell model in which springs are used to represent the elastic properties of the SMC and dash pods are used to represent the viscous properties of SMC during the curing cycle. As the material under study was a thermosetting polymer, its viscoelastic behaviour depended on time, temperature and viscosity. Therefore, the calculation of the net deformation in the antenna using a rheological model required the use of a scheme that incorporated the combined and related effects of temperature, time and viscosity. The model results were evaluated against experimental results.

Finally, an antenna design had to be developed that was suitable for the application, where good antenna performance and signal quality are required in the frequency range of from a few hundred MHz to several GHz. This was to be validated by simulation and experiments. In addition, the shape and the dimensions of the antenna had to be such that they would lend themselves to being embedded in a composite panel that is no more than 3 mm thick and that could be processed at high temperatures and pressures (150 °C and 0.785 MPa).

Lastly, detailed antenna simulation, measurement and performance benchmarking testing was performed at two frequencies of interest, one being the mobile phone frequency of 900 MHz, and the other being a GPS frequency of 1.575 GHz. These two services were chosen due to their popularity and the fact that the hardware required to perform the tests is readily available. In addition, they would provide good insight into the antenna performance a) when directional signal quality is used, as in a mobile phone, and b) in terms of the effect of multipath signal quality as in GPS. Tests were performed on actual vehicles currently in production and in real world environments such as densely populated urban areas with all their associated obstacles and interferences.

1.4 Thesis Outline

Chapter 1: Introduction

A brief background of composite and antennas in the automotive industry, the objective and rationale of the research, the research methodology, the outline of the thesis and a list of publications.

Chapter 2: Literature Review: Automotive Antennas and Related Services

A comprehensive review of the literature on various types of automotive antennas and the service for which they cater, including the latest developments in the next generation of automotive antennas.

Chapter 3: Literature Review: Composite Materials and Their Use in Automobiles with Specific Focus on Sheet Moulding Compound

A comprehensive literature review of composite materials used in the automotive sector and research carried out in the area of SMC material flow during compression moulding and rheological models developed for SMC.

Chapter 4: Dielectric Constant Testing

Determination of the dielectric constant for the type of SMC used in this research application, using free-space measurement and rectangular waveguide techniques.

Chapter 5: Effect of Metallic and Non-Metallic Automotive Paint on Transmission and Reception of Signals in Free Space

Chapter 6: Rheological Characterisation of Sheet Moulding Compound

A study performed using the latest optical type rheometers with a force rebalance transducer.

Chapter 7: Deformation Modelling

A model developed using the classical Maxwell approach in which springs represent the elastic behaviour of SMC and dash pods represent the viscous behaviour of SMC during the curing stage.

Chapter 8: Wideband Antenna Selection and Development

Simulation modelling of antenna performance for the different designs investigated and comparisons to experimental data obtained from gain and radiation patterns.

Chapter 9: Antenna Simulation, Measurement and Performance Benchmarking

Benchmarking of the developed antenna, embedded in the SMC panel assembled to a Jeep Wrangler, at GPS frequency against a commercially available GPS antenna in real world applications.

Chapter 10: Conclusion

A summary of the outcomes of the work conducted in this study, followed by some suggestions for further work.

1.5 List of Publications

Journal Papers

1. Pell, B, **Sulic, E**, Rowe, W, Ghorbani, K & John, S 2011, 'Experimental study of the effect of modern automotive paints on vehicular antennas', *IEEE Transactions on Antennas and Propagation*, vol. 59, no: 2, pp. 434–442, DOI 10.1109/TAP.2010.2096182.
2. Pell, B, **Sulic, E**, Rowe, W, Ghorbani, K & John, S 2011, 'Wideband multi-service automotive antenna conformed to a curved surface', *SAE International Journal of Passenger Cars—Electronic and Electrical Systems*, vol. 4, no. 1, 189–197, DOI 10.4271/2011-01-0047.
3. **Sulic, E**, Pell, B, John, S, Rowe, W, Ghorbani, K, Gupta, R, Zhang, K & Hughes, B 2010, 'Deformation modelling of an embedded communication device in a polymeric composite material', *Journal of Advanced Research in Mechanical Engineering (JARME)*, vol. 1, no. 3, pp. 127–135.

Book Chapter

4. Pell, B, **Sulic, E**, Rowe, W, Ghorbani, K, John, S, Gupta, R, Zhang, K & Hughes, B 2011, 'Advancements in automotive antennas', in *New trends and developments in automotive engineering*, INTECH

Conference Papers

5. **Sulic, E**, Pell, B, John, S, Gupta, R, Ghorbani, K, Wayne, R & Zhang, K 2007, 'Parametric evaluation of communication devices in smart composite structures', in *Proceedings of the 5th Australasian Congress on Applied Mechanics, Brisbane, December 10–12, 2007*, vol.2, pp.477–482.
6. Pell B, **Sulic E**, Rowe, W, Ghorbani, K, John, S, Gupta, R, Zhang, K & Hughes, B 2008, 'Experimental study of the effect of paint on embedded automotive antennas', in *IEEE Vehicular Technology Conference*, *May, 2008*, pp. 3057–3061.
7. **Sulic, E**, Pell, B, John, S, Rowe, W, Ghorbani, K, Gupta, R, Zhang, K, Hughes, B 2008, 'Performance of embedded multi-frequency

communication devices in smart composite structures', in *Proceedings of ASME Conference on Smart Materials, Adaptive Structures and Intelligent Systems (SMASIS08)*, Ellicott City, Maryland, USA, October 2008.

8. Pell, B, **Sulic, E**, John, S, Rowe, W, Ghorbani, K, Gupta, R & Zhang, K December 2008, The design and realization of uniplanar CPW fed PICA slot antennas, paper presented at Asia-Pacific Microwave Conference (APMC2008), Hong Kong, China.
9. **Sulic, E**, Pell, B, John, S, Rowe, W, Ghorbani, K, Gupta, R & Zhang, K July 2009, Deformation evaluation of embedded antennas in vehicular components', paper presented at International conference on Integrity, Reliability and Failure, Porto, Portugal.
10. **Sulic, E**, Pell, B, John, S, Rowe, W, Ghorbani, K, Gupta, R, Zhang, K & Hughes, B 2009, 'Deformation modelling: embedding a communication device in a polymeric composite material', in *Proceedings of ASME Conference on Smart Materials, Adaptive Structures and Intelligent Systems (SMASIS09)*, Oxnard, California, USA, Sep 2009.
11. **Sulic, E**, Pell, B, John, S, Rowe, W, Ghorbani, K, Gupta, R, Zhang, K & Hughes, B 2010, 'Multifunctional vehicle components: key in sustainability and long term viability of auto industry', in *International Conference on Sustainable Automotive Technologies*, Gut Ising, Germany, Jan. 2010, pp. 72–79.
12. Pell, B, **Sulic, E**, Rowe, W, Ghorbani, K, John, S, Gupta, R, Zhang, K & Hughes, B 2010, 'Sustainable antennas: a wideband antenna for vehicular applications', in *International Conference on Sustainable Automotive Technologies,* Gut Ising, Germany, Jan 2010, pp. 48–53.
13. **Sulic, E**, Pell, B, John, S, Rowe, W, Ghorbani, K, John, S, Gupta, R, Zhang, K & Hughes, B 2010, 'Signal quality evaluation of embedded antennas in composite panels', in *Proceedings of ASME Conference on Smart Materials, Adaptive Structures and Intelligent Systems (SMASIS10)*, Philadelphia, Pennsylvania, USA, Sep. 2010.
14. **Sulic, E**, Pell, B, John, S, Rowe, W, Ghorbani, K, Gupta, R, Zhang, K & Hughes, B July 2010, Deformation evaluation of embedded antennas in vehicular components, paper presented at World Engineering Congress, London, UK, July 2010.

Symposium Presentation

15. **Sulic, E,** Pell, B, Rowe, W, Ghorbani, K, John, S, Zhang, K & Gupta, R February 2009, Wideband antennas for vehicles with painted coverings, symposium presented at Eleventh Australian Symposium on Antennas, Sydney, Australia.

CHAPTER 2: Literature Review: Automotive Antennas and Related Services

2.1 Introduction

Today's production vehicles are fitted with a multitude of antennas to facilitate communication and enable a moving vehicle to connect with the outside world. Recent years have seen the introduction of new electronic devices to the automotive environment. These devices are usually designed to aid the driver, increase safety or enhance the driving experience, and many of them rely on wireless communication to perform their task. Antennas are a necessary part of any wireless communication system, enabling transmission and reception of signals in free space. At the same time, automobile manufacturers have been seeking to create cost-effective, fuel-efficient vehicles with attractive styling. This leads to a focus on sleek, lightweight vehicles with reduced aerodynamic drag and improved styling-an emphasis that would naturally conflict with the fitment of traditional antennas. These market preferences, along with the technological factors, have combined in the past few years to drive significant innovation in the world of vehicular antennas.

In this chapter, the review focuses on the basics of antennas used in automobiles and examines the frequencies and services that are commonly used in the automotive environment, with a view to providing a background to the subject area. This is followed by a body of knowledge section that includes a brief discussion of the antennas traditionally used on vehicles and a detailed analysis of the recent developments and trends in automotive antenna research.

2.2 Background to the Subject Area: Antenna Fundamentals

Antennas are necessary components of any wireless communication device or system. An antenna is a device designed to send or receive radio waves. The antenna takes a guided wave, usually bound to a transmission line of

some type, such as a coaxial line, waveguide or microstrip transmission line, and allows that same energy to propagate through free space. Antennas are passive devices, meaning that they do not require an external power source. They are also linear, meaning that their function is preserved regardless of the applied power level, and reciprocal, which implies that they behave in an equivalent manner in either transmit or receive modes. Electrically conductive materials are commonly used to create antennas. Most antennas are made from metals, although they can be constructed from dielectric materials.

2.2.1 Key Properties of Antennas

Specialised terminology is used to describe antenna performance. This language allows engineers to express antenna behaviour, specify requirements and compare various design options. Some of the most commonly used terms are included below. Text that appears in quotation marks is from the *IEEE Standard Definitions of Terms for Antennas* (IEEE Std145-1993).

2.2.1.1 Bandwidth

The *bandwidth* of an antenna refers to 'the range of frequencies within which the performance of the antenna, with respect to some characteristic, conforms to a specified standard'. The most common usage of bandwidth is in the sense of *impedance bandwidth*, which refers to those frequencies over which an antenna may operate. This is often defined with the aid of the voltage standing wave ratio (VSWR) or return loss values from measurements. Other bandwidths that may be referred to are *gain bandwidth*, which defines the range of frequencies over which the gain is above a certain value, and *axial ratio bandwidth*, which may be used in the case of a circularly polarised antenna.

2.2.1.2 Radiation Pattern

The *radiation pattern* represents the energy radiated from the antenna in each direction, often pictorially. The IEEE definition states that it is 'the spatial distribution of a quantity that characterises the electromagnetic field

generated by an antenna'. Most often, this is the radiation intensity or power radiated in a given direction.

2.2.1.3 Gain

In many wireless systems, an antenna is designed to enhance radiation in one direction while minimising radiation in other directions. This is achieved by increasing the *directivity* of the antenna, which leads to *gain* in a particular direction. The *gain* is thus 'the ratio of the radiation intensity, in a given direction, to the radiation intensity that would be obtained if the power accepted by the antenna were radiated isotropically (that is, equally in all directions)'. In the case of a receiving antenna, an increase in gain produces increased sensitivity to signals coming from one direction with the corollary of a degree of rejection to signals coming from other directions. Antenna gain is often related to the gain of an isotropic radiator, resulting in units *dBi*. An alternative is to relate the gain of any given antenna to the gain of a dipole, thus producing the units *dBd*. (0 dBd = 2.15 dBi). Antenna gain may be viewed with the aid of a *radiation pattern*.

2.2.1.4 Polarisation

Polarisation of the wave radiated from an antenna describes the behaviour of the electric and magnetic field vectors as they propagate through free space. Polarisation is typically approximately *linear*. When linear, the polarisation may be further described as either *vertical* or *horizontal*, based on the orientation of the electric field with respect to earth. In the automotive environment, the polarisation of signals depends on the service in question. Many satellite services (such as GPS) use *circularly polarised* signals. For best performance, the polarisation of the receive antenna should match the polarisation of the transmitted signal.

2.2.2 Impedance Matching Conventions

In low-frequency electronic circuits, ordinary wires are used to connect components together to form a circuit. When the frequency in the circuit is high, or the circuit dimensions approach that of a wavelength, a transmission line (a special configuration of wires or flat conductors) must be used to

connect these components and avoid reflections. This transmission line has defined impedance, and allows the high-frequency energy to propagate down the line. Impedance discontinuities in this transmission line will cause a reflection and stop effective transmission down the line. For this reason, the input impedance of an antenna is critical for achieving proper matching to the transmitting device to which it is attached. Most transmission lines have an impedance of 50 Ω, while the impedance of an antenna changes with the frequency. At some frequencies, a given antenna will not be matched to the transmission line, and will not accept or radiate power, while at those frequencies at which the antenna is designed to operate, the impedance of the antenna will allow the electromagnetic energy to pass into the structure and radiate into the surrounding space. These frequencies would be deemed to be inside the antenna's *impedance bandwidth*. Two measures of stating the impedance matching are commonly used, both of which are based on the reflection coefficient, which is a measure of how much energy is reflected back into the source from the antenna's terminals. The first measure shows the reflection coefficient on a logarithmic scale as |S11|. Common definitions require that |S11| be below the –10 dB line to declare an acceptable impedance match. The second measure is similar, but on a linear scale, and is referred to as VSWR. In this terminology, an antenna is deemed to be well matched to the line where VSWR is less than 2:1. This corresponds to a value of –9.54 dB in the logarithmic scheme, meaning the measures are approximately equivalent. Figures 2.1 and 2.2 show plots of |S11| and VSWR respectively for a dipole antenna that is resonant near 900 MHz. Although the shapes of the curves are different due to the use of either log or linear scaling, both plots reveal that the antenna presents a good impedance match to frequencies in the range of from approximately 850 to 970 MHz. Although a 10 dB return loss is typically required in the majority of antenna applications, there are some exceptions. While some high-performance systems may specify more precise matching, a notable exception is the cellular phone industry, which permits more relaxed specifications. Most modern cellular phone antennas meet an |S11| requirement of –6 dB (Waterhouse 2008), which is equivalent to a VSWR of 3:1. Recent years of handset design have led to a trade-off that sacrifices antenna performance for an attractive, small

handset. The signal strengths used in cellular networks, combined with advances in receiver technology and modulation schemes, compensate for handset antennas having low radiation efficiency and poor electrical performance, resulting in adequate performance of the overall system.

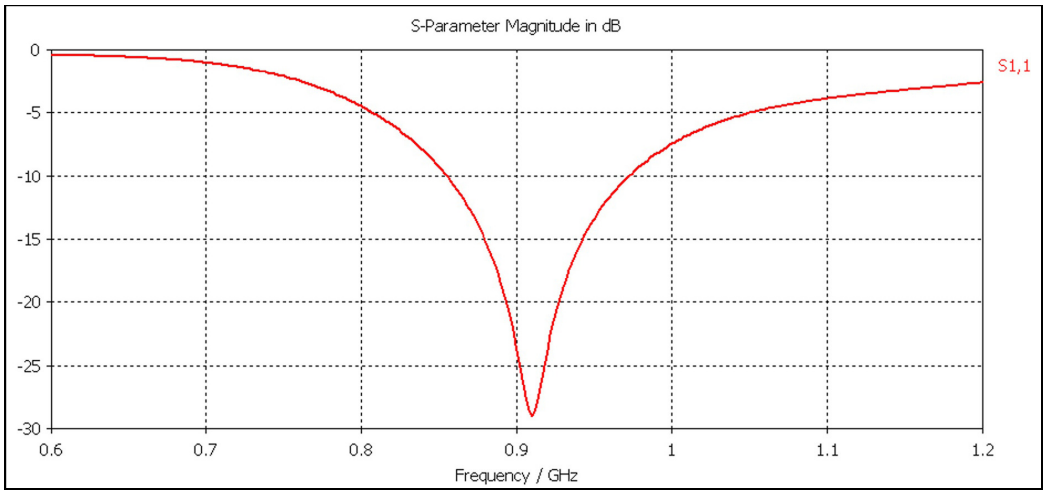

Figure 2.1: |S11| of a dipole antenna

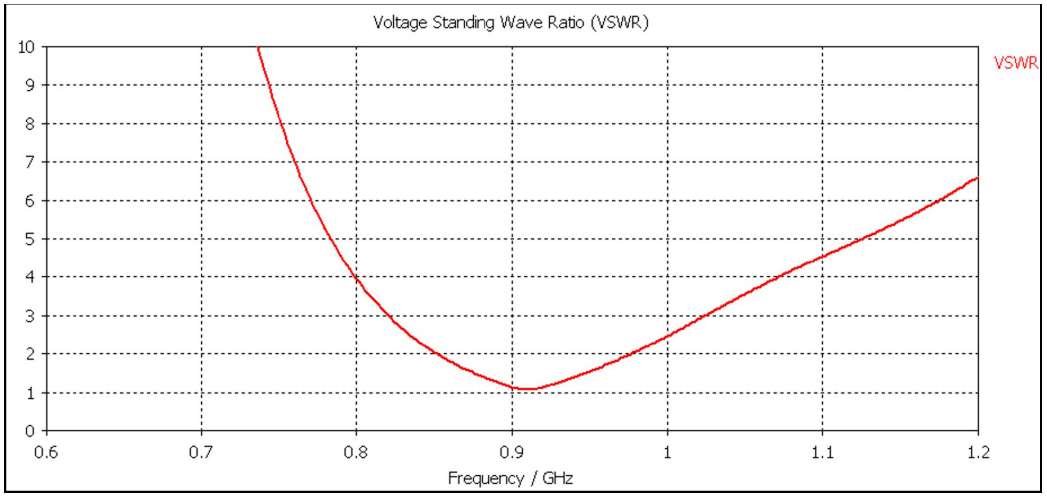

Figure 2.2: VSWR of same dipole antenna

2.2.3 Radiation Pattern Essentials

Gain and radiation pattern were introduced in Section 2.2.1. This section describes some common radiation patterns and identifies radiation pattern features. Three-dimensional (3D) radiation patterns are shown in Figure 2.3,

while a two-dimensional (2D) radiation pattern on a polar plot is shown in Figure 2.4.

2.2.3.1 Isotropic

According to IEEE Standard 145-1993, an *isotropic* radiator is 'a hypothetical, lossless antenna having equal radiation intensity in all directions' (see Figure 2.3(a)). Such an antenna does not exist, nor can one be created. Nevertheless, an isotropic radiator is a useful concept as a truly omnidirectional source and as a reference for gain comparison purposes. When gains are specified in *dBi*, the gain of the antenna under test is being described relative to this theoretical standard.

2.2.3.2 Omnidirectional

When an antenna is described as *omnidirectional* this is understood to mean that the antenna radiates an 'essentially non-directional pattern in a given plane of the antenna and a directional pattern in any orthogonal plane'. A pattern of this type is shown in Figure 2.3(b). In this figure, it may be observed that the magnitude of the radiation is non-directional in the azimuth (around the sides) but not in elevation (sweeping from high to low). A pattern of this type is produced by dipole antennas and monopoles on an infinite ground plane. It represents an ideal standard for many services in the automotive environment where coverage is required on all angles around the vehicle but not required in the upward direction towards the sky.

2.2.3.3 Directional

A *directional* radiation pattern is shown in Figure 2.3(c). This type of pattern can boost the signal strength due to its higher gain if aimed in the required direction. This comes at the expense of reduced effectiveness in other directions, which may be desirable in certain applications. Highly directional antennas are desirable for point-to-point links and have application in automotive radar systems where a narrow beam may be scanned to detect nearby targets.

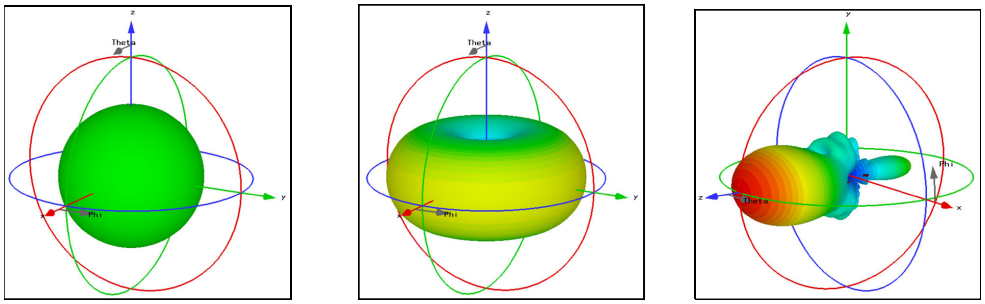

(a) (b) (c)

Figure 2.3: 3D radiation patterns: (a) isotropic, (b) omnidirectional and (c) directional

2.2.3.4 A Two-Dimensional Representation Highlighting Common Features

Radiation patterns are often plotted in 2D form. Figure 2.4 shows a 2D cut through the y-z plane of the 3D radiation pattern shown in Figure 2.3(c). A careful examination of both figures will reveal the equivalence of the radiation information presented. Distinct parts of a radiation pattern are referred to as lobes. These lobes and other characteristic features of radiation patterns are highlighted in Figure 2.4.

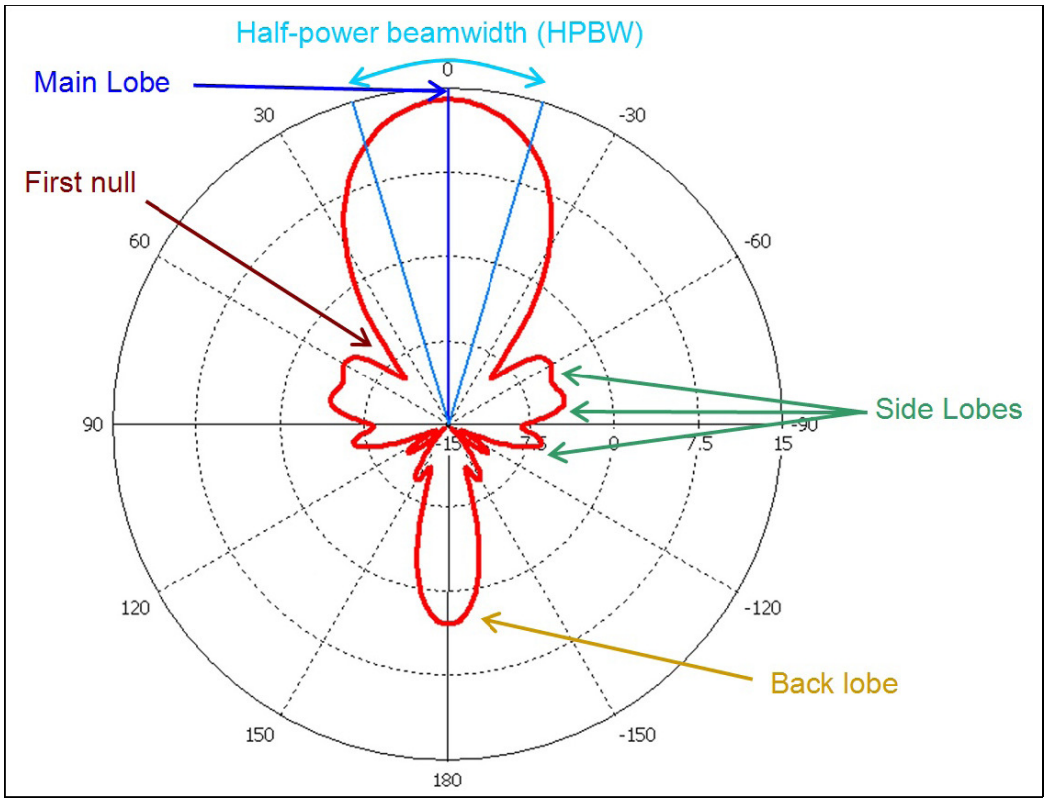

Figure 2.4: A sample 2D radiation pattern

2.2.4 Near-Field and Far-Field Regions

The space surrounding an antenna may be divided into three approximate regions, based on the behaviour of the electromagnetic fields in each of these regions. The first two regions are the *reactive near-field* and *radiating near-field* regions. The properties and configuration of surrounding material in these regions may alter antenna performance, and the field at any angle is dependent on the distance to the antenna. However, in the third region, known as the *far-field* region, it can be assumed that the antenna is a point source. The far-field region is normally regarded as beginning when the distance to the antenna is equal to $2D2/\lambda$, where D is the maximum overall dimension of the antenna and continues on to infinity. Once in the far-field region, the radiation pattern and gain may be measured.

2.2.5 System Considerations

Antennas are necessary components of all wireless systems, but are not of themselves sufficient for signal reception. Antennas do not operate in isolation. Here we briefly examine other important factors related to vehicular antenna systems.

2.2.5.1 Diversity Reception

Some automotive services use *diversity* to enhance the quality of the received signal. In non-line-of-site propagation environments such as the urban environment, reflections and shadows cast by buildings and other structures can cause fading in the signal strength in particular spatial locations or in given directions. In a diversity scheme, two or more antennas are mounted in different locations or with different orientations on the vehicle. This provides two independent propagation paths for the signal. On an elementary level, the diversity receiver switches between antennas to choose the one with the stronger signal. This provides a higher quality signal with fewer dropouts (Balanis 2005). Diversity is most commonly employed for FM radio reception purposes. Given that cars fitted with multiple antennas are regarded as being less visually appealing, vehicle manufacturers tend to combine an external mast antenna with a glass-mounted antenna to give two distinct antennas for diversity purposes. This approach often achieves spatial and polarisation diversity, along with diversity in radiation direction.

2.2.5.2 Noise, Sensitivity and the Receiver

Any communications system receives the desired signal plus an unwanted signal that we may call *noise*. Noise comes from a variety of sources, ranging from the random movement of electrons inside any conductor (at a temperature above absolute zero) to electromagnetic interference (EMI) coupled with the signal from nearby devices (Balanis 2005). In the automotive environment, the vehicle's ignition system can be a source of significant EMI, meaning that antennas mounted near the front of the vehicle may receive more noise than an equivalent antenna mounted towards the rear. Receiving systems have a specified *sensitivity*, which relates to the minimum signal strength at the input required to achieve an acceptable signal-to-noise ratio

(SNR). The sensitivity of commercial automotive receiving systems will have a large influence on the overall quality of the received service, particularly in areas of low signal strength. In car radio systems, the *receiver* may be called a *tuner* since it tunes its internal oscillators to demodulate the required station. The input impedance of the tuner, along with other fundamental properties, is important in ensuring proper system operation.

2.2.6 Automotive Frequencies and Wireless Services

In previous decades, the use of antennas in vehicles was primarily limited to those employed for AM and FM radio (Stutzman & Thiele 1997). In contrast, today's vehicles are often fitted with many antennas for additional purposes, such as remote keyless entry and satellite navigation. In the future, it is likely that vehicles will require still more antennas for such things as mobile Internet and mobile video, collision avoidance radar, and V2V or V2I communication. A list of present and soon-to-be-realised services is provided in Table 2.1. Each of these wireless services necessitates the incorporation of a suitable antenna into the vehicular platform to receive signals at the appropriate frequency.

Table 2.1: Summary of signals used on modern and next generation vehicles

Service	Typical Frequency	Tx*	Rx#	Direction of Radiation
AM Radio	Approximately 1 MHz		Yes	Horizontal
FM Radio	88 MHz to 108 MHz		Yes	Horizontal
In-vehicle TV	50 MHz to 400 MHz		Yes	Horizontal
Digital Audio Broadcasting (DAB)	100 MHz to 400 MHz		Yes	Horizontal
Remote Keyless Entry (RKE)	315 MHz/413 MHz/ 434 MHz		Yes	Horizontal
Tyre Pressure Monitoring System (TPMS)	315 MHz/413 MHz/ 434 MHz	Yes	Yes	Intra-vehicular
Cellular Phone (provision of Internet via HSPA)	850 MHz 900 MHz 1800 MHz 1900 MHz 2100 MHz	Yes	Yes	Horizontal
Satellite Navigation (GPS)	1.575 GHz		Yes	Satellite
Satellite Digital Audio Radio Service (SDARS)	2.3 GHz		Yes	Satellite
IEEE 802.11 b/g/n (Wi-Fi)	2.4 GHz	Yes	Yes	Horizontal
Bluetooth	2.4 GHz	Yes	Yes	Intra-vehicular
WiMAX	2.3 GHz/2.5 GHz/3.5 GHz	Yes	Yes	Horizontal
Electronic Toll Collection (ETC)	5.8 GHz (or 900 MHz)	Yes	Yes	Overhead
V2V+ and VII+	5.9 GHz	Yes	Yes	Horizontal
Collision Avoidance Radar	24 GHz and 77 GHz	Yes	Yes	Forward

* Transmit # Receive + These terms are acronyms for Vehicle-to-Vehicle communication and Vehicle-Infrastructure-Integration using IEEE 802.11p

The lowest frequencies used in vehicles are often for *AM* and *FM radio*. The history of radios in cars is vague but dates back to the 1920s. During this period, the installation of such devices was deemed unsafe and illegal in at least one US state (Rowan & Altgelt 1985). Significant policy change obviously occurred over the years, given that AM and FM radio are installed in nearly all modern-day passenger vehicles and are used to provide entertainment for the driver and passengers. The third entry in the list of services in Table 2.1 describes *in-vehicle television*, for which the necessary hardware is available, including diversity receivers to minimise dropouts. In-vehicle television is rarely installed by the factory in present-day vehicles, although DVD and multimedia entertainment systems are experiencing increased uptake in high-end luxury vehicles. *Digital audio broadcasting* (DAB) is a more modern format for broadcasting entertainment radio. DAB uses digital rather than analogue modulation schemes, providing higher spectral efficiency and better quality audio in certain circumstances.

Many present-day vehicles are able to be locked and unlocked by pressing a button on a radio transmitter integrated into the car's key or key ring. These services are known as *remote keyless entry*, and typically operate in one of the low power bands shown in the table. These bands are often shared with *tyre pressure monitoring systems* (TPMS), which are finding increased acceptance in the passenger vehicle market and are available as third-party accessories. A typical TPMS has an air pressure sensor and wireless transmitter fitted to each wheel, with a receiver unit mounted in or on the dash. The system can alert the driver to low tyre pressure before a flat tyre becomes a safety hazard. Many frequency bands are used globally for *cellular telephone* (aka mobile telephone) (Stutzman & Thiele 1997). Blocks of new spectrum are occasionally released by the authorities and purchased by telecommunications companies to cater for increased demand. The most commonly used frequencies are provided in the table. Inclusion of these frequency bands in a vehicle allows for voice calls, as well as a full suite of services based on high-speed access to the Internet provided by High Speed Packet Access (HSPA). This has the potential to bring about a realisation of useful location-based services, XML-based traffic updates and Internet connectivity almost anywhere in urban and rural environments. Guidance and navigation facilities are becoming more cost effective and experiencing large uptake in the modern market. These navigation systems usually rely on the constellation of approximately 30 *GPS* satellites to determine the location of the vehicle before plotting it on a map. The GPS L1 band is received in a narrow 20 MHz channel centred at 1.575 GHz. The *Satellite Digital Audio Radio Service* (SDARS) is also described in the table. This service delivers hundreds of additional radio stations and is implemented by using circularly polarised signals from satellites arranged in an orbit that dwells over the North American continent. In urban environments, where buildings can cause multipath and shadowing of the satellites, terrestrial-based transmitters are also used. The 2.4 GHz industrial, scientific and medical (ISM) band has seen enormous growth in the past decade due to the ubiquitous application and implementation of *wi-fi* and *Bluetooth,* which occupy part of this band. Bluetooth is incorporated into many present-day vehicles to allow hands-free

calling and operation of an equipped mobile through the vehicle's multimedia system. Future vehicles may be fitted with wi-fi to enable passengers to access the Internet while on a journey. An emerging technology that will need to compete with Long Term Evolution (LTE) and HSPA technologies is *WiMAX*. In a manner similar to the 3G and 4G cellular wireless standards, WiMAX could be used to provide a high-speed wireless Internet connection to a moving vehicle many kilometres from a base station. Many *electronic toll collection* systems are implemented at 5.8 GHz, often achieved by windscreen-mounted removable wireless tags operating in an active-RFID system. *V2V communication systems* are currently being developed and trialled to enable safer and more efficient road transport. A portion of the spectrum at 5.9 GHz has been reserved in many countries for this purpose, with vehicles and roadside objects forming networks and sharing safety information as part of an intelligent transportation system (ITS). An example of such a system is one that would alert the driver to sudden braking in the traffic ahead, and of upcoming lane closures or unexpected obstructions. Emergency vehicles could broadcast warnings to drivers up to 1 km away, signalling their presence and intentions. Many phrases have been coined to describe this technology, including dedicated short-range communications (DSRC), V2V, and Vehicle-Infrastructure Integration (VII). The relevant IEEE standard on which the wireless connection is based is IEEE 802.11p. The US Department of Transport is developing these technologies in the IntellidriveSM program. *Collision avoidance radar* is a technology that integrates with the adaptive cruise control (ACC) system of a vehicle to prevent accidents, or in a case where a collision is unavoidable, to reduce the severity of the impact. In normal use, the system uses RADAR (or optionally, LIDAR) to scan the road ahead and then reduce the throttle and apply brakes to maintain a safe buffer distance from the car in front automatically. Some systems will also detect pedestrians or other objects. In the event that the system detects an imminent collision, it may apply emergency braking and other precautionary measures to increase vehicle safety. Collision avoidance radar uses very high frequencies for numerous reasons, including spectrum availability, the small size of antenna elements enabling integration of necessary phased-array radar antennas, and the fact that a higher frequency

helps to increase the radar cross section and therefore the detection range of targets of interest, such as pedestrians and other vehicles.

2.3 Body of Knowledge: Traditional AM/FM Antennas

2.3.1 Mast Antennas

The low frequency and relatively high signal strengths encountered in AM and FM car radio systems have allowed the use of uncomplicated antenna systems in the past. The most common antenna traditionally used for these bands is the mast antenna (Balanis 2005). A conductive rod is used to form a monopole antenna, approximately one-quarter wavelength (λ/4) in length, which equates to approximately 75 cm in the middle of the FM band. Locating such an antenna in the centre of the roof gives the best radiation performance, with the antenna elevated above obstructions and surrounded by a conducting ground plane of approximately equal extent in all directions. Despite this, the front or rear fender is usually preferred for aesthetic reasons. Retractable and non-retractable versions are commercially available. Antennas for receiving FM radio in vehicles should receive signals equally well from all directions around the horizon, due to the movement and rotation of the vehicle with respect to the transmitting source. This quarter wavelength monopole antenna would provide an ideal radiation pattern in the azimuth if it were mounted above an infinite ground plane. However, typical fender mounting provides a very non-ideal ground plane, leading to radiation patterns that are less omnidirectional (i.e., the radiation becomes directional). Hence, designing such antennas for vehicles has traditionally been an iterative process involving several stages of prototyping and measurement on completed vehicle bodies. Retractable mast antennas (see Figure 2.5) allow the antenna to be retracted, hidden and protected when not in use. Such antennas consist of a long rod divided into numerous segments. The segments are appropriately dimensioned to slide inside one another when retracted, leading to a tapering profile when extended. Most modern retractable antennas are raised and lowered by an electric motor leading to increased cost. Such power retractable antennas are often mounted on the passenger side of the vehicle, while manually operated retractable antennas

tend to be installed on the driver side so the driver can raise or lower the mast without having to walk to the other side of the vehicle.

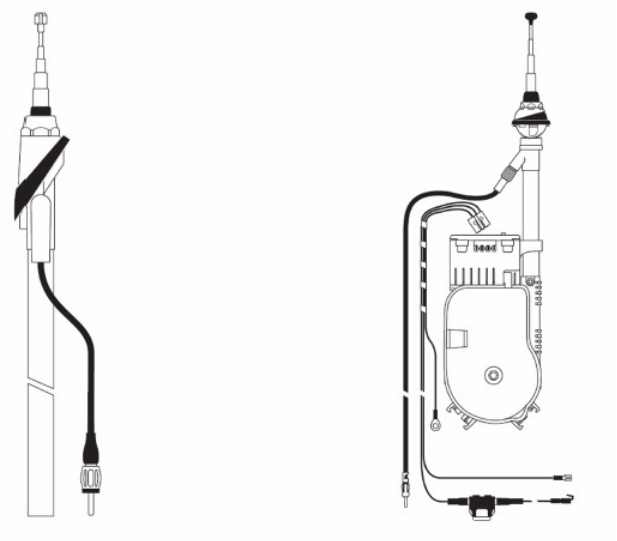

(a) (b)

Figure 2.5: Technical drawings of typical mast antennas: (a) manually retractable mast antenna and (b) power retractable mast antenna

2.3.2 Glass-Mounted AM/FM Antennas

A second kind of AM and FM antenna is the glass-mounted antenna. AM and FM antennas using this technique have become very common in the last decade, as preamplifiers have helped to compensate for poor radiation performance. On modern vehicles, these antennas are similar in appearance to the demister elements commonly embedded in the rear windscreen. Many glass-mounted antennas installed in present-day vehicles are based on wire geometry, although the antenna may or may not be an actual wire. It can be formed by using wire of a very thin diameter or a silk-screened film, which is laminated between layers of glass in the vehicle windows (Jensen 1971). Glass-mounted antennas provide no additional aerodynamic drag and create no wind noise, which is a significant advantage over mast type designs. They also require no holes to be created in the vehicle body, which may lead to cheaper tooling for the metalwork. Despite this, on-glass antennas tend to be more directional than mast antennas, which can lead to nulls in the reception

at certain angles around the vehicle. On-glass antennas were first located in the rear windscreen, and this remains a common position on sedans made today. Many sport utility vehicles (SUV) or station wagons use the rear quarter window in preference to the rear window. A variety of different shapes are used for the antennas, often forming grid or meandering geometries, with a shape that works well on one vehicle not necessarily performing well on other vehicles (Gottwald 1998). No universal glass-mounted antenna has yet been discovered. This is due to the effect of the vehicle body on the antenna's impedance and radiation, which is significant for on-glass antennas. Antennas oriented vertically may provide better reception of vertically polarised signals.

Figure 2.6 shows a typical active rear window antenna. Early designs adopted the defogger elements themselves and connected through a DC blocking capacitor to the radio tuner. Newer designs often separate these two functions, and have a defogger element that occupies most of the glass, with a smaller area set aside for antenna lines.

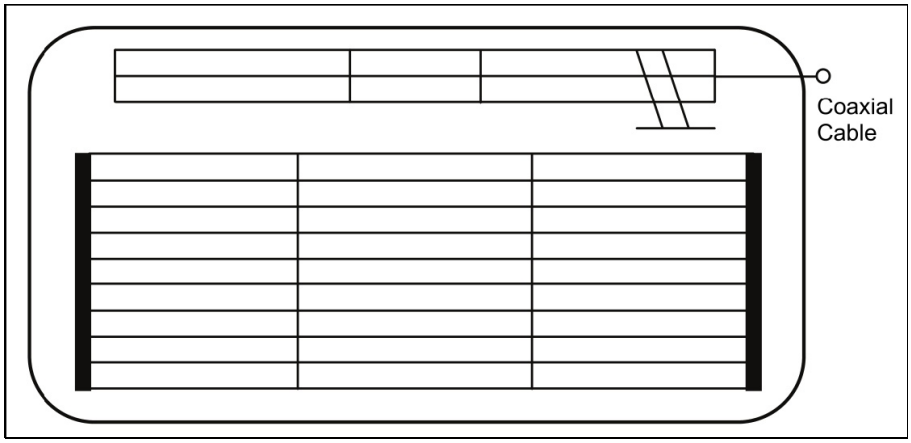

Figure 2.6: Schematic of a typical rear windscreen glass antenna

2.4 New Developments and Research Outcomes

Examination of production vehicles produced over the past ten to 15 years reveals a shift away from the traditional quarter wavelength mast antenna towards more aesthetically pleasing antennas. This section provides a review

of new findings and innovative solutions to vehicular antenna problems, along with the advantages and disadvantages of each type.

2.4.1 Bee Sting Antennas

The bee sting antenna is a wire antenna similar to the mast antenna that has been used for many decades, but it consists of a shortened element installed in a raked back attitude (see Figure 2.7). An amplifier is used to boost the signal level to compensate for the poor performance obtained by the shorter antenna length (Cerretelli & Biffi Gentili 2007). Some antennas also include a separate feed for a cellular phone or DAB system.

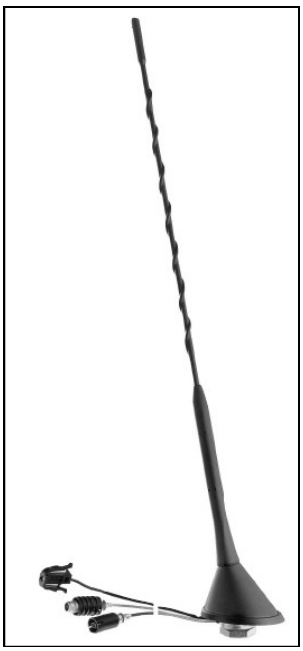

Figure 2.7: Bee sting antenna © IEEE with permission (Cerretelli & Biffi Gentili, 2007)

2.4.2 Blade or Shark-Fin Antennas

Many varieties of shark-fin antennas exist, having been popularised primarily by the European marques near the turn of the 21st century. Shark-fin antennas are commonly a collection of several antennas. Most designs consist of multiple narrowband antennas all located together under a single radome or housing. This housing is typically shaped like a blade or dorsal fin,

and is usually located on the roof towards the rear of the vehicle. Two examples of shark-fin designs are shown in Figure 2.8.

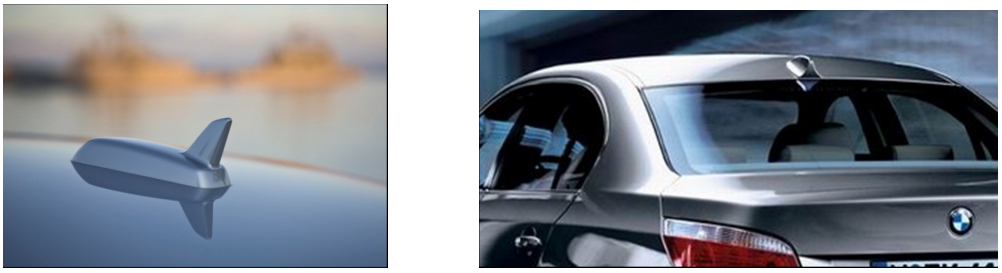

(a) (b)

Figure 2.8: Shark-fin Antennas: (a) Audi A8 and (b) BMW 5 series

Figure 2.9 shows an early shark-fin antenna design in detail. This design was fitted to the BMW 3-Series (E46) and provides for cellular phone frequencies (Hopf, Reiter & Lindenmeier 2007). The antenna consists of a cast steel base and a fin-shaped cover made from an acrylonitrile butadiene styrene (ABS) and polycarbonate (PC) polymer. Radiating elements are on both sides of an FR-4 circuit board, which stands erect in the middle of the device. Rubber gaskets are used to seal the inner components from the environment. The design achieves an impedance match (see Figure 2.10) at the required frequencies by incorporating inline filters that allow the radiators to be a quarter wavelength long at high and low frequencies simultaneously. A surface mount resistor is used in conjunction with a printed inductor on the reverse side of the board to form a filter. This filter has the effect of connecting the upper radiating elements at lower frequencies by creating an electrical short circuit. At higher frequencies, the filter creates an open circuit, leaving only the short elements connected to the feed line.

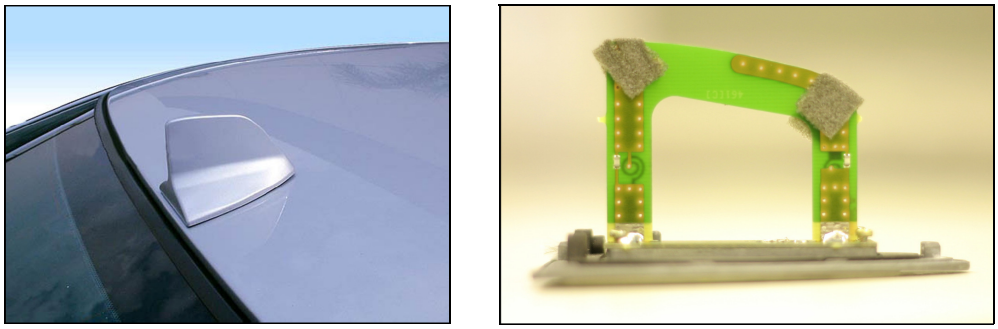

(a) (b)

Figure 2.9: BMW 3-Series E46 shark-fin antenna (a) on vehicle roof and (b) with radome removed showing filters

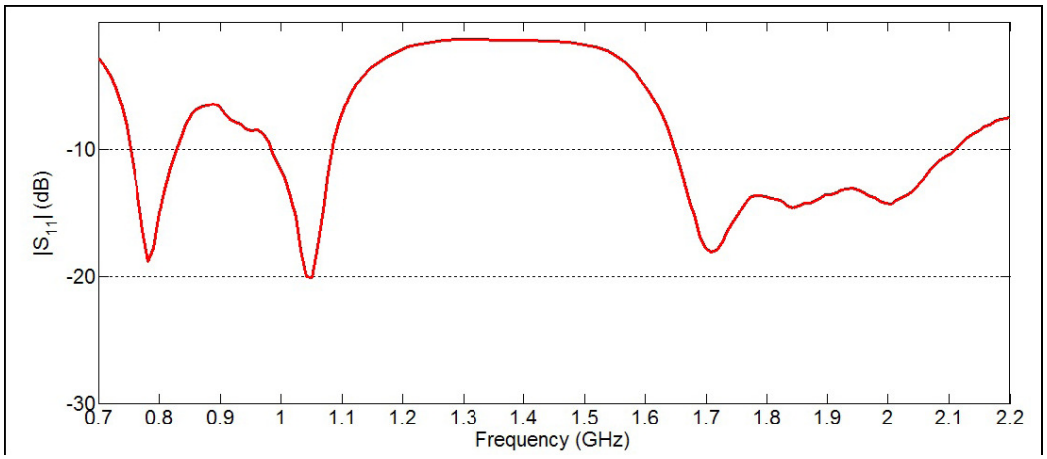

Figure 2.10: Measured reflection coefficient of BMW E46 Shark-fin Antenna

Figure 2.11 shows a shark-fin style antenna that was published in the literature for use in US automobiles (Hopf, Reiter & Lindenmeier 2007). With the cover removed, it is clear that this antenna demonstrates the case where multiple individual antennas are located together under a single radome. The left-most antenna in the figure is a GPS antenna, constructed using a probe-fed patch design on a high dielectric constant substrate. This provides a hemispherical radiation pattern covering the sky, which is appropriate for receiving satellite signals. Circular polarisation may be induced in patch antennas such as these by truncating diagonally opposite corners of the patch, or by feeding the antenna off centre. The white antenna to the right of centre in the figure is a crossed frame antenna for SDARS reception. The two posts present in the design provide for cellular telephone reception. The

elements are based on quarter wavelength monopoles with top-loading elements to increase the effective electrical length at the low end of the band. The presence of these posts is typical of shark-fin antennas; however, these particular posts contain filters that have been optimised to have minimal effect on the nearby SDARS antenna.

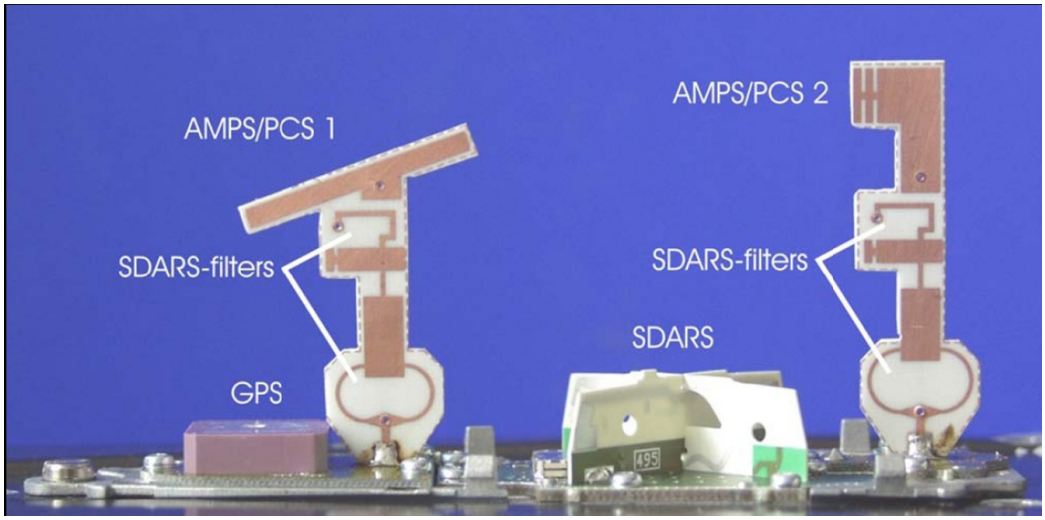

Figure 2.11: Internals of a modern shark-fin antenna © IEEE with permission (Hopf, Reiter & Lindenmeier 2007)

2.4.3 TV Antennas on Glass

Research has continued into traditional AM and FM antennas mounted on glass even today (Bogdanov et al. 2010), particularly in the area of effective simulation techniques. At the same time, antenna configurations for other services have also been investigated. An early paper describes the system shown in Figure 2.12 of a diversity reception system for analogue TV. The antennas are printed on the rear quarter glass and have four branches. The antennas are arranged symmetrically on the left and right sides of the vehicle. The design includes some meandering elements that give a long electrical length in a small space. Other branches of the design include slanted and short horizontal elements. The authors claim the system provides improved performance over a rod antenna, and is capable of operating in the range of from 90 MHz to 770 MHz (Toriyama et al. 1987).

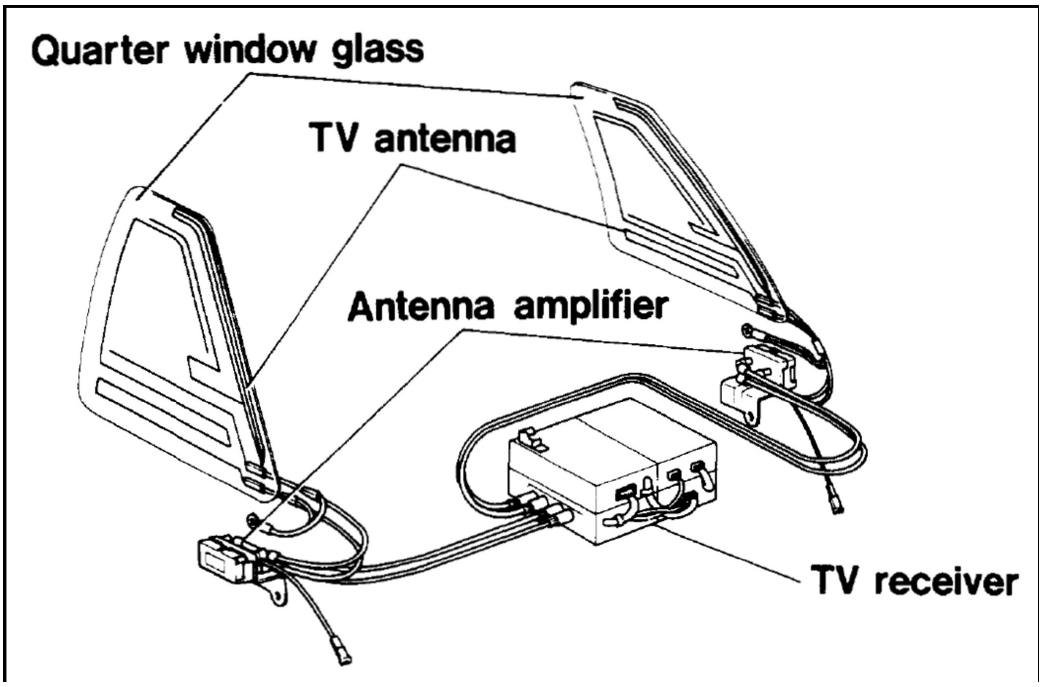

Figure 2.12: Analogue TV antenna system in rear quarter glass © IEEE with permission (Toriyama et al. 1987)

A glass-mounted antenna designed for the newer digital terrestrial TV reception is shown in Figure 2.13. The H-shaped elements allow both long and short current paths to be formed, providing a wideband impedance match (Iizuka et al. 2005). The long path occurs when current flows diagonally from top left to bottom right (see Figure 2.13(a)), while the shorter path runs diagonally from bottom left to top right. The impedance matching of this design results in a VSWR of less than 3:1 from 470 MHz to 710 MHz when connected to a 110 Ω line. The antenna is formed on a low-cost FR-4 substrate, and is integrated with an radio frequency (RF) circuit, which provides a balun, some filtering, and a low noise amplifier (LNA) to boost the signal before it is sent down the transmission line to the tuner. Four of these antennas were installed in the test vehicle shown in Figure 2.13(b), and located in the upper portion of both the front and rear windscreen on both driver and passenger sides. The gain and radiation pattern of the system was measured at 530 MHz, and it was found that the radiation pattern was nearly omnidirectional at this frequency when all four antennas were excited.

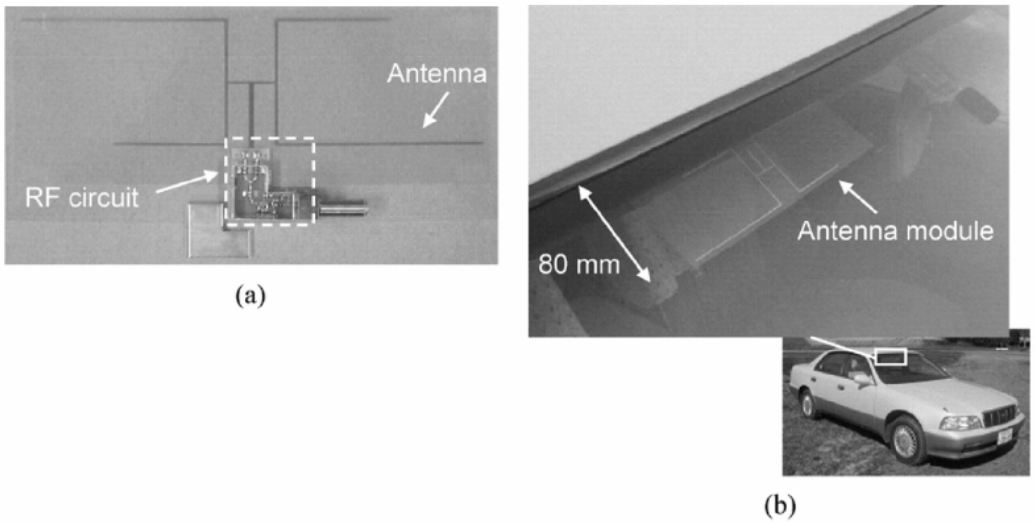

Figure 2.13: Digital TV antenna attached to vehicle glass © IEEE with permission (Iizuka et al. 2005)

2.4.4 Circular Microstrip Patch Antenna on Glass

Microstrip patch antennas have many advantages in communication systems, including being thin, cheap to produce and easy to integrate into devices. The application of this kind of antenna to automotive glass has been investigated by several researchers. One paper suggested two methods of patch antenna integration (Economou & Langley 1998). The first is a patch antenna formed on a traditional microwave substrate such as Rogers RT Duroid®, which is then attached to the inside of a vehicle windscreen (see Figure 2.14(a)). The second describes a more integrated concept, which uses a layer of glass itself as the antenna substrate, and excites the patch with a proximity coupled feed line (see Figure 2.14(b)). Patch antennas using the first method of integration were designed to resonate near 2 and 6 GHz respectively, and were adhered to a vehicle windscreen for testing. A useful increase in impedance bandwidth, from less than 2% to about 7%, was observed due to the addition of a thick dielectric superstrate. Presence of the glass also generates surface waves that create undesirable ripples in the far-field radiation pattern. The second method using glass as the antenna substrate poses fabrication complexities, and would lead to high windscreen replacement cost in the event of cracking or breakage, so it was only investigated by simulation. Simulation results showed that this geometry

would also result in lower radiation efficiency due to increased surface wave losses. The electrical properties of the layers in the windscreen were εr1 = 6.75, tan δ = 0.03 for the glass and εr2 = 2.9, tan δ = 0.05 for the middle plastic layer. The thickness of automotive glass may vary by up to 15% in the standard manufacturing process. This causes no problems or distortions for driver vision, but could present a problem for patch antennas attached to glass. The centre frequency of the antenna may be shifted by up to 3% and could be coupled with an additional but slight change in the impedance bandwidth.

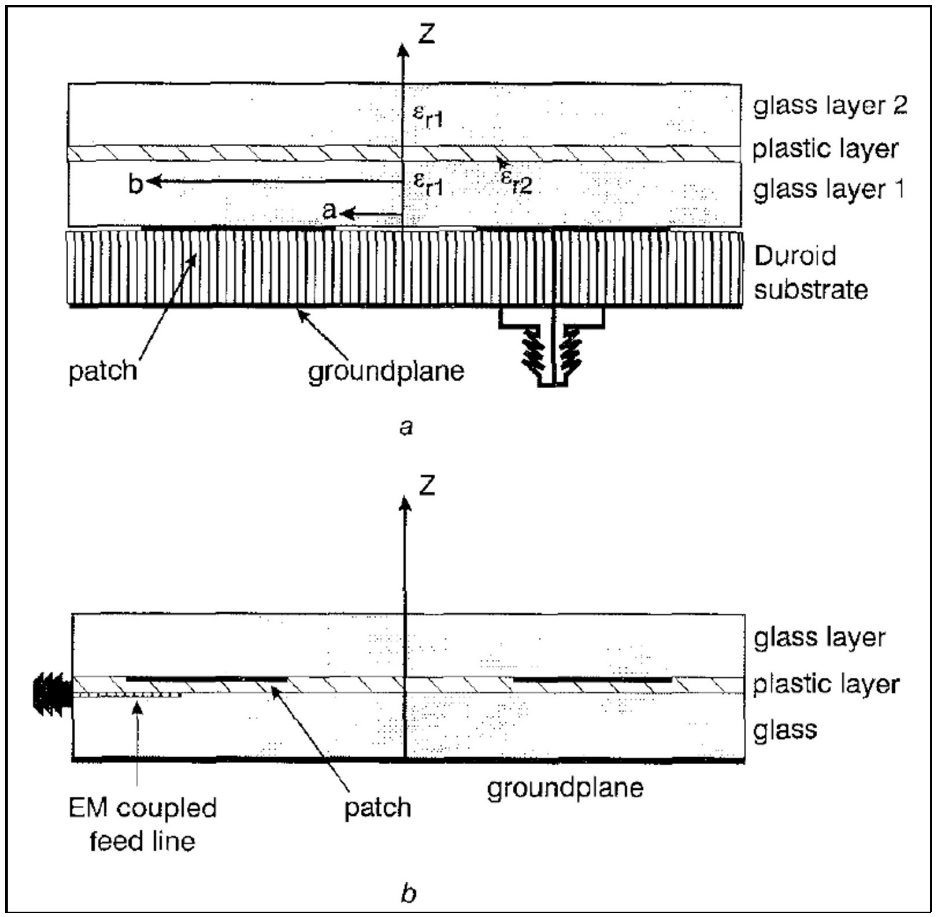

Figure 2.14: Patch antennas on glass © IEEE with permission (Economou & Langley, 1998)

2.4.5 Rear Spoiler with Built-In Antenna

In the late 1990s, a team of Japanese engineers working with Toyota and Aisin Seiki developed a rear spoiler to be mounted high on the rear of a compact SUV. This spoiler was the first to be fitted with an invisible antenna (see Figure 2.15). The paper describes a blow moulded part made from a polymeric material (Koike et al. 1999). The spoiler is located high on the vehicle, minimising shadowing from passing traffic. The antenna is similar to a dipole that would normally require a balanced feed. To connect a dipole antenna to a coaxial line, a balun is usually required. The geometry of the spoiler and processing temperature during manufacture would make integration of such a balun difficult. To overcome this, an innovative antenna design is used. The shorter element in Figure 2.15(a) is approximately λ/4 long, while the longer element is approximately λ/2. Parametric investigations found that a tab at the end of the longer radiating element improved antenna performance by coupling to the vehicle's metallic roof. Although the directivity is less than perfect (see Figure 2.15(b)), it is adequate for the intended application.

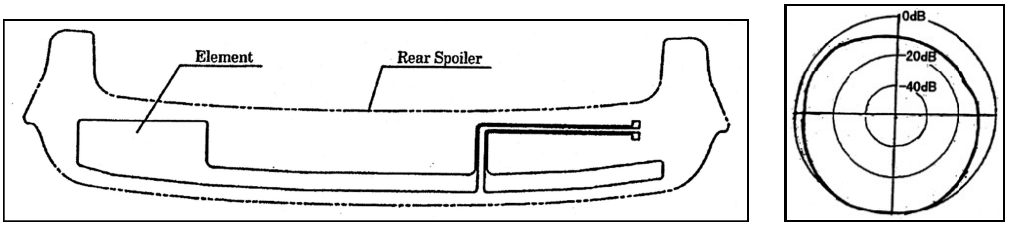

(a) (b)

Figure 2.15: Integrated antenna in spoiler © SAE International with permission (Koike et al. 1999)

2.4.6 Volvo XC90 Aperture Antenna

Swedish manufacturer Volvo fitted a unique antenna to their XC90 SUV, launched in 2003. The system provides an alternative to glass-mounted wire antennas, which may be adversely affected by heated windscreen elements and window tinting films containing conductive metallic layers (Low et al. 2006). The XC90 is fitted with a traditional metallic skinned 'turret top' roof,

but an aperture is created at the rear of the vehicle. This opening is covered with a polymeric panel, and forms an ideal location for some hidden antennas (Low et al. 2006). Figure 2.16(a) shows the XC90 from above and Figure 2.16(b) shows some simulation results of the vehicle's metallic structure for different antenna configurations. The aperture in the vehicle body is clearly shown. The portion of roof that contains the antennas is the black unpainted section at the rear of the vehicle in Figure 2.16(a), which at first glance may look like a sunroof. Seven antenna components (see Figure 2.16) are formed by printing wire shapes onto a large polyester film using conductive ink. The antennas act as monopole probes, exciting the aperture in which they are placed. For some services, multiple antennas are used in different locations to achieve radiation and polarisation differences between elements, thus allowing diversity reception. The film bearing the printed antennas is attached to a plastic carrier that contains the necessary amplifiers, and the whole unit is located in the aperture and covered with a black polymeric composite material. Examination of Figure 2.16 reveals that these antennas are for low-frequency services, with Table 2.1 revealing that each service is centred well below 1 GHz. This low frequency implies a long wavelength, which requires physically long antenna elements. Note that the services targeted in this design are different from those commonly used in the smaller shark-fin style antennas.

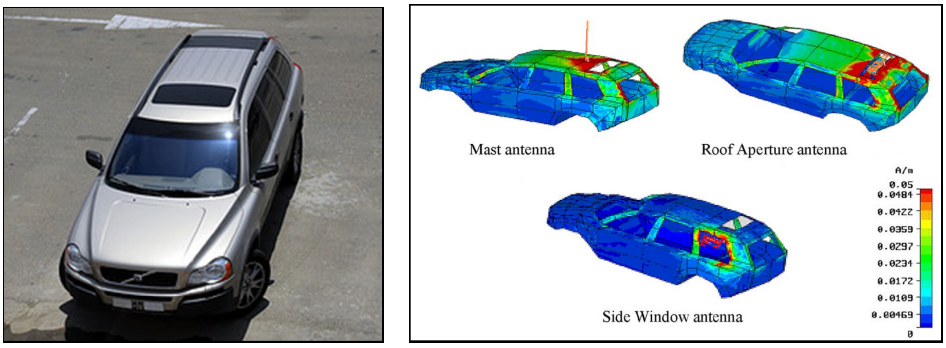

(a) (b)

Figure 2.16: Volvo XC90: (a) completed vehicle and (b) simulations of surface currents for various antennas© IEEE with permission (Low et al. 2006)

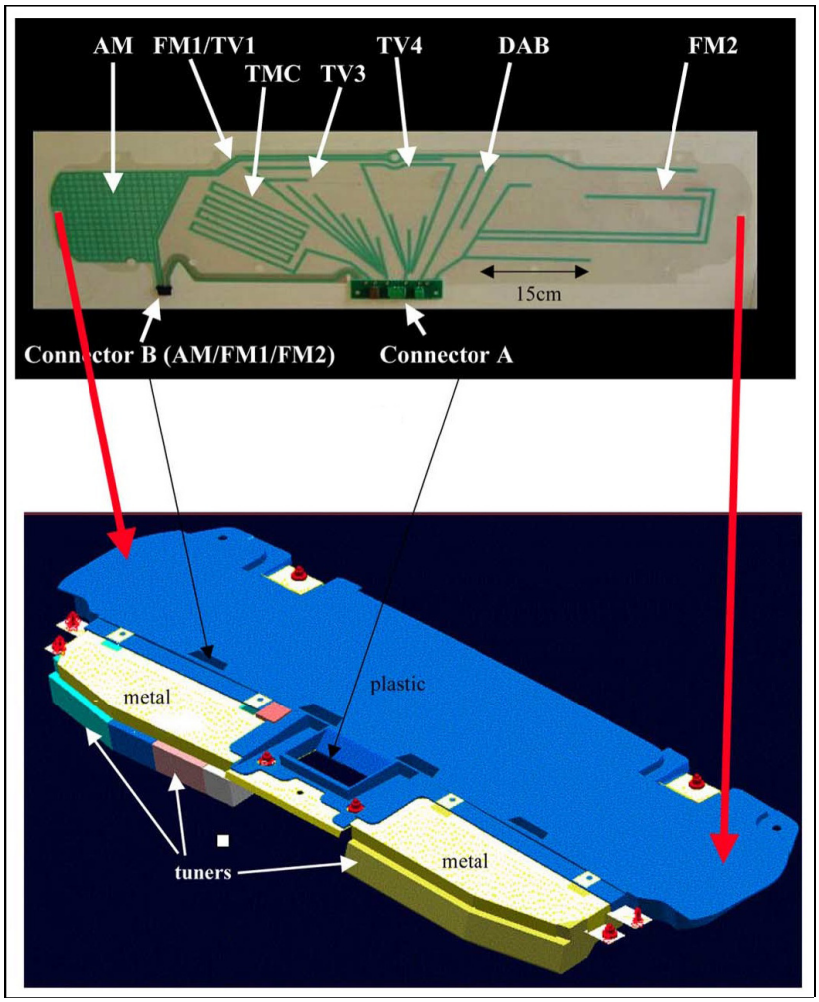

Figure 2.17: XC90 antenna configuration ©IEEE with permission (Low et al. 2006)

Performance of the roof aperture antenna for the FM band was compared in both simulation and measurement against a roof-mounted monopole with a length of 80 cm and a side window antenna as used in an estate car (see Figure 2.17 (Low et al. 2006). Unsurprisingly, the authors report that the roof-mounted monopole provided exceptional performance for vertically polarised signals, but performed poorly for horizontally polarised signals. On average, the roof-mounted aperture antenna performed approximately 2 dB better than the side window antenna, but was unable to trump the roof-mounted monopole for vertical polarisation gain.

2.4.7 Body-Integrated Spiral Antenna

Researchers in Germany investigated the possibility of mounting a cavity-backed spiral antenna in the trunk lid of a car (Gschwendtner & Wiesbeck 2003). The four-arm spiral antenna produced is approximately 40 cm in diameter and is backed by a metallic cavity (see Figure 2.18(a)). The spiral supports two modes of radiation depending on how the signal is fed into the structure. The first mode is a coplanar waveguide (CPW) mode, which creates a null at zenith (i.e., directly above the antenna), with omnidirectional radiation around the sides of the device. This mode generates a radiation pattern that is suitable for terrestrial services. The second mode, known as the coupled slotline (CSL) mode, feeds only two of the four arms, creating a circularly polarised radiator, with a maximum at zenith (directly overhead). This mode of radiation is ideal for satellite services. A metallic cavity with a height of 4 cm was placed below the spiral to prevent back radiation into the vehicle body. Measured S-parameters of the antenna with the cavity present are shown in Figure 2.18(b). The curve is below –10 dB from 670 MHz to beyond 5 GHz for the terrestrial mode (|S11|), with the exception of some peaks as high as –8 dB in the frequencies below 1.4 GHz. These peaks are due to the presence of the metallic cavity. The satellite mode (|S22|) meets the –10 dB requirement of from 1.3 GHz to 2.2 GHz, providing broadband circularly polarised satellite reception. The |S12| curve illustrates the coupling between the two ports.

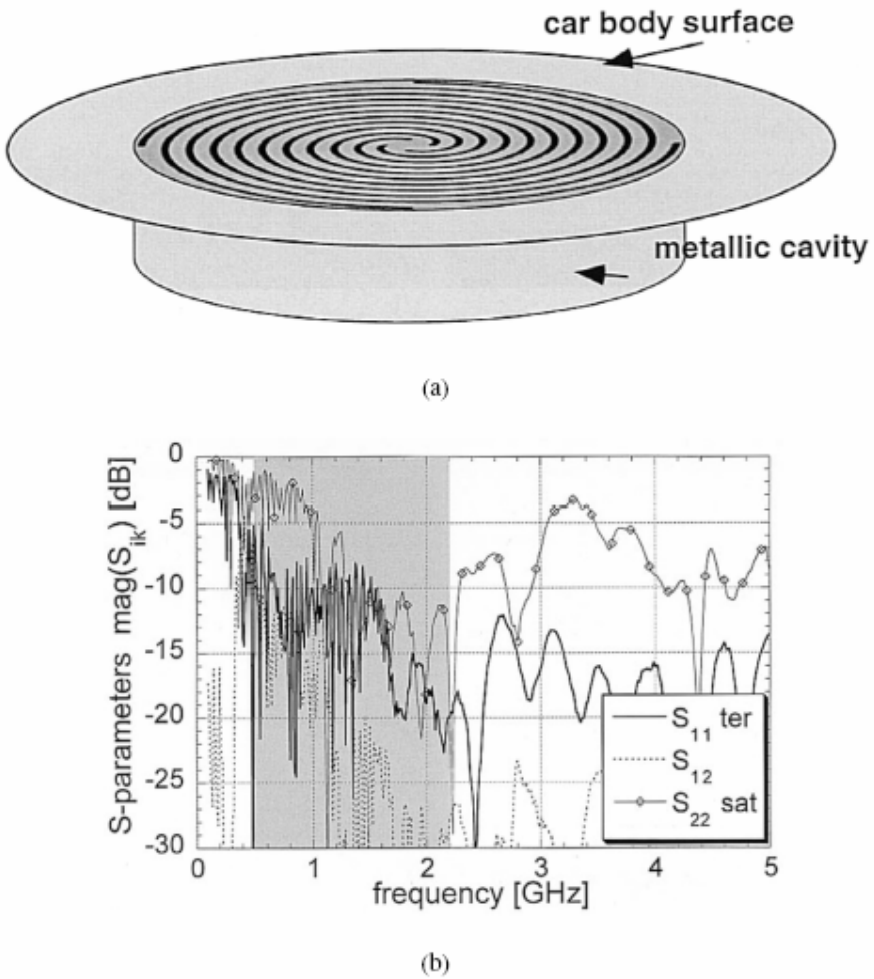

Figure 2.18: Four-arm spiral antenna: (a) antenna design showing metallic cavity and (b) measured S-parameters of antenna with cavity © IEEE with permission (Gschwendtner & Wiesbeck 2003)

Figure 2.19 shows the finished antenna installed in the intended location on a vehicle. The top surface is mounted flush with the exterior trunk lid panel. No measurements of the antenna installed in the vehicle were provided. The antenna provides for more services due to its wideband impedance match and results in an elegant solution, given that the structure does not protrude from the vehicle body, thus eliminating additional drag.

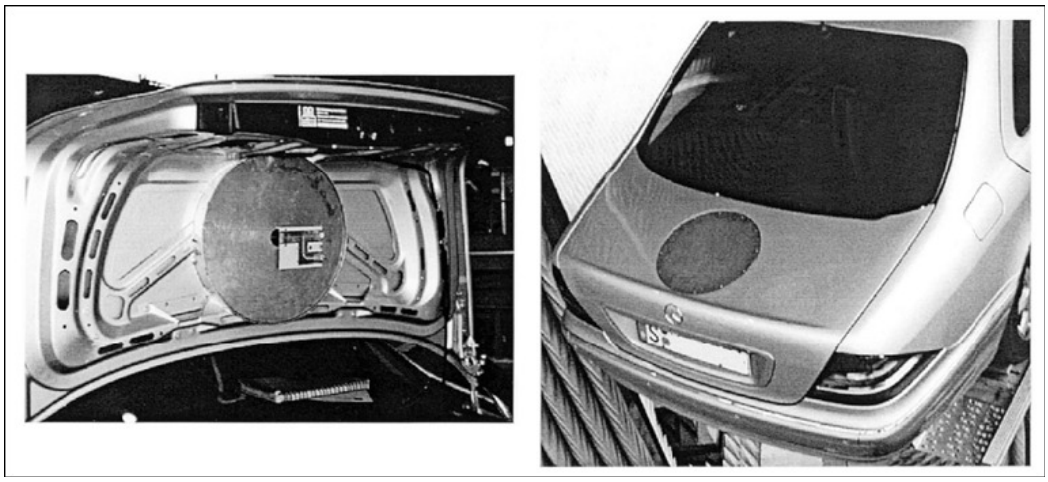

Figure 2.19: Spiral antenna integrated into the trunk lid of a Mercedes sedan
© IEEE with permission (Gschwendtner & Wiesbeck 2003)

2.4.8 Antennas Integrated into Plastic Trunk Lid

Heinz Lindenmeier and his team at the University of the Bundeswehr Munich have made an outstanding contribution to vehicular antennas over many decades, particularly with regard to amplifiers and diversity systems. Lindenmeier et al. (2006) presented an antenna concept for application in cars with plastic trunk lids, as is common in some cabriolets and convertibles. In such vehicles, a traditional fixed glass rear window is not normally available, so integration into the plastic trunk lid is an ideal substitute. To create an antenna, a copper ring is created around the perimeter of the plastic trunk lid near the metallic supporting structure (see Figure 2.20). Two switches are inserted into this ring, and act to control the impedance of the network. Both ends of the ring are connected to an amplifier unit, which is used to obtain both FM diversity and TV reception. A separate AM radio feed is connected to a wire antenna geometry, which is located inside the previously mentioned ring. A ground plane is also included in the middle of the ring. The intention is that a cellular phone antenna, or GPS patch antenna, may be installed in this location under the polymeric trunk lid. This would provide an ideal spot to locate antennas for higher frequency services and would not disrupt the operation of the lower frequency services.

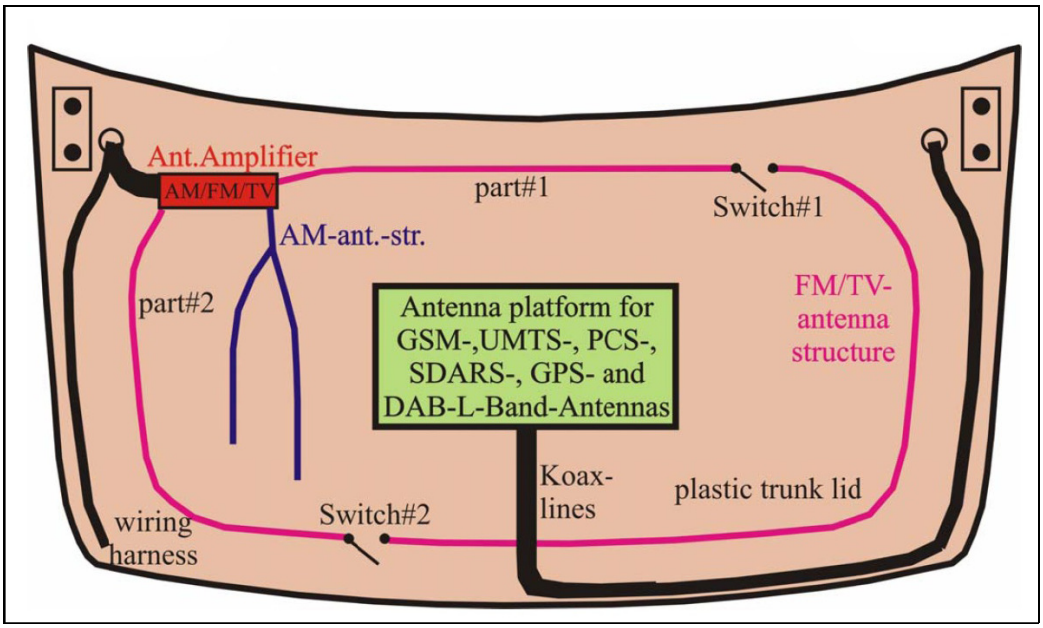

Figure 2.20: Active antennas integrated into plastic trunk lid © SAE International with permission (Lindenmeier et al. 2006)

2.4.9 Doorhandle Antenna for Smart Key

Engineers from Aisin Seiki recently published their findings of an investigation conducted into low-frequency magnetic fields for smart key systems (Okada, Tanaka & Yamane. 2007). In these systems, an alternative to remote keyless entry is provided. Rather than pressing a button to unlock the vehicle from a range of 10 m to 20 m, the system unlocks the vehicle when the key is detected to be within a range of several meters.

The frequency of operation for this application is not specified by the authors, but is likely to be in the order of 100 kHz. At frequencies as low as this, the radiating device is not an antenna in the traditional sense. A coil of wire is formed by wrapping wires around a ferrite bar. Passing low-frequency alternating current through such a device generates a strong magnetic field in the surrounding space. Although these fields are limited primarily to the reactive near-field region, this region extends for a number of meters because the low frequency creates a very long wavelength.

Contrary to radio frequencies, these low magnetic fields are able to penetrate the steel doors of the vehicle and the chrome-plated doorhandles, allowing the device to be installed behind the metal skin of the vehicle, or inside a plated doorhandle.

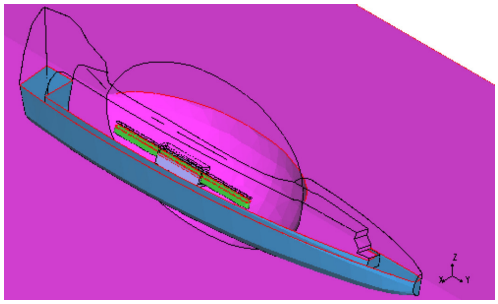

Figure: 2.21 Doorhandle configuration © SAE (Okada, Tanaka & Yamane 2007)

2.4.10 Other Automotive Antenna Configurations

2.4.10.1 Satellite Antennas

Several designs exist for reception of Ku-band satellite signals on either moving or stationary vehicles. High gains of 30 dBi or higher are required, leading to the use of reflector antennas (Eom et al. 2007) or array antennas (Mousavi et al. 2008). Reflector antennas are often mechanically steered and housed in a radome, which results in a high-profile device approaching half a meter in depth (see Figure 2.22(a)). Array antennas use a collection of many patch antennas and typically result in roof-mounted components with a lower profile, thinner than even 10 cm (see Figure 2.22(b)). These systems may be steered mechanically with motors, or electronically by changing the phase between elements.

(a) (b)

Figure 2.22: Satellite antennas: (a) reflector system © IEEE with permission (Eom et al. 2007) and (b) phased-array system © IEEE with permission (Mousavi et al. 2008)

2.4.10.2 Collision Avoidance Radar

Antennas designed to work as part of a collision avoidance radar system are very small because of the high frequencies of operation (typically 24 GHz or 77 GHz), which leads to a correspondingly short wavelength, and small antenna size. A frequency of 77 GHz is preferred for *long range radar* detection, up to 150 m in front of the vehicle, while 24 GHz systems are used for *short-range radar* where the distance is less than 30 m. Many requirements need to be satisfied in designing such antennas (Hoare & Hill 2000). Figure 2.23 shows some recently presented antennas for these purposes. Figure 23(a) and (c) show antennas for 77 GHz radar systems published in the literature, while Figure 2.23(b) shows a commercial system used by Mercedes.

(a)a fabricated 2x1 77 GHz Patch array

(b)the Mercedes Long Range Radar System

(c)a 77 GHz Yagi-Uda antenna used to feed a reflector

Figure 2.23: Automotive radar antenna configurations: (a) a fabricated 2x1 77 GHz patch array © IEEE with permission (Lee et al. 2005), (b) the Mercedes long range radar system ©IEEE with permission (Wenger 2005) and (c) a 77 GHz Yagi-Uda antenna used to feed a reflector © IEEE with permission (Beer, Adamiuk & Zwick 2009)

2.5 Conclusion

Automotive antennas have seen significant advancements in recent years. No longer is a large, protruding, fender-mounted mast antenna the norm for production vehicles. As shown in the antenna configurations mentioned here, a good impedance match can be obtained for a wide frequency range. In addition, depending on the frequency range being targeted, it is possible to achieve acceptable gains and directivities. These developments augur well for the deployment of a new range and type of integrated vehicular antennas. Future developments will likely focus on two key areas: further integration of the antenna components with the vehicle structure, and new antenna configurations for radar and V2V communication services. With the developments in antenna design mentioned in this review, further integration of antennas within vehicular components will be expected, particularly with the current inexorable drive from within the automotive industry to shift more automotive components from metallic to polymeric materials.

2.6 References

- Balanis, A.C, 2005, 'Antenna theory: Analysis and Design', Third Edition, John Wileys and Sons Inc., ISBN 0-471-66782-7
- Beer, S, Adamiuk, G & Zwick, T 2009, 'Novel antenna concept for compact millimeter-wave automotive radar sensors', *Antennas and Wireless Propagation Letters, IEEE*, vol. 8, pp. 771–774.
- Bogdanov, F, Karkashadze, D, Jobava, R, Gheonjian, A, Yavolovskaya, E, Bondarenko, N & Ullrich, C 2010, 'Validation of hybrid MoM scheme with included equivalent glass antenna model for handling automotive EMC problems', *IEEE Transactions on Electromagnetic Compatibility*, vol. 52, no. 1, pp. 164–172.
- Cerretelli, M & Biffi Gentili, G 2007, 'Progress in compact multifunction automotive antennas', in *International Conference on Electromagnetics in Advanced Applications*, pp. 93–96.
- Economou, L & Langley, J 1998, 'Circular microstrip patch antennas on glass for vehicle applications', *IEEE Proceedings Microwaves, Antennas and Propagation*, vol. 145, no. 5, pp. 416–420.
- Eom, SY, Son, SH, Jung, YB, Jeon, SI, Ganin, S, Shubov, A, Tobolev, A & Shishlov, A 2007, 'Design and test of a mobile antenna system with tri-band operation for broadband satellite communications and reception', *IEEE Transactions on Antennas and Propagation*, vol. 55, no. 11, pp. 3123–3133.
- Gottwald, G 1998, 'Numerical analysis of integrated glass antenna systems', *SAE Technical Paper Series*, Paper ID 982386, Society of Automotive Engineers.
- Gschwendtner, E & Wiesbeck, W 2003, 'Ultra-broadband car antennas for communications and navigation applications', *IEEE Transactions on Antennas and Propagation*, vol. 51, no. 8, pp. 2020–2027.
- Hoare, E & Hill, R 2000, 'System requirements for automotive radar antennas', in *IEE Colloquium on Antennas for Automotives*, pp. 1/1–111.
- Hopf, J, Reiter, L & Lindenmeier, S 2007, 'Compact multi-antenna system for cars with electrically invisible phone antennas for SDARS frequencies', in *2nd International ITG Conference on Antennas, INICA '07,* pp.171–175.

- IEEE, *IEEE standard definitions of terms for antennas*, IEEE Std 145-1993.
- Iizuka, H, Watanabe, T, Sato, K & Nishikawa, K 2005, 'Modified H-shaped antenna for automotive digital terrestrial reception', *IEEE Transactions on Antennas and Propagation*, vol. 53, no. 8, pp. 2542–2548.
- Jensen, WK 1971, *Concealed windshield broadband antenna*, US patent 3,576,576.
- Koike, T, Hase, N, Koide, E, Murakami, Y, Izawa, S, Ohira, T, Nagasaka, O, Tanaka, Y & Suzuki, T 1999, 'Development of a rear spoiler with built-in antenna', *SAE Technical Paper Series*, Paper ID 1999-01-0807, Society of Automotive Engineers.
- Lee, HS, Kim, J, Hong, S & Yoon, J 2005, 'Micromachined CPW-fed suspended patch antenna for 77 GHz automotive radar applications', in *The New Trends and Developments in Automotive System Engineering 538 European Conference on Wireless Technology, 2005,* pp. 249–252, DOI 10.1109/ECWT.2005.1617704.
- Lindenmeier, H, Reiter, L, Ramadan, A, Hopf, J & Lindenmeier, S 2006, 'A new design principle of active receiving antennas applied with a high impedance amplifier-diversity-module in a compact multi-band-antenna-system on a plastic trunk lid', *SAE Technical Paper Series*, Paper ID 2006-01-0480, Society of Automotive Engineers.
- Low, L, Langley, R, Breden, R & Callaghan, P 2006, 'Hidden automotive antenna performance and simulation', *IEEE Transactions on Antennas and Propagation*, vol. 54, no. 12, pp. 3707–3712.
- Mousavi, P, Fakharzadeh, M, Jamali, S, Narimani, K, Hossu, M, Bolandhemmat, H, Rafi, G & Safavi-Naeini, S 2008, 'A low-cost ultra low profile phased array system for mobile satellite reception using zero-knowledge beamforming algorithm', *IEEE Transactions on Antennas and Propagation*, vol. 56, no. 12, pp. 3667–3679.
- Okada, Y, Tanaka, H & Yamane, K 2007, 'Electromagnetic field analysis for smart key antenna', *SAE Technical Paper Series*, Paper ID 2007-01-0943, Society of Automotive Engineers.

- Pell, BD, Sulic, E, Rowe, WST & Ghorbani, K 2009, 'Custom-directional wideband PICA for multi-service vehicular applications', in *APMC 2009. Asia Pacific Microwave Conference, 2009,* pp. 1863–1866.
- Pell, BD, Sulic, E, Rowe, WST, Ghorbani, K & John, S n.d. Experimental study of the effect of modern automotive paints on vehicular antennas, *IEEE Transactions on Antennas and Propagation*, in press.
- Rowan, CW & Altgelt, CA 1985, 'When car radios were illegal: a history of early American and European car radios', *SAE Technical Paper Series*, Paper ID 850019, Society of Automotive Engineers.
- Stutzman, W, and Thiele, G 1997, 'Antenna Theory and Design', Second Edition, John Wileys and Sons Inc., ISBN 0-471-02590-9
- Sulic, E, Pell, B, John, S, Gupta, R, Rowe, W, Ghorbani, K, Zhang, K & Lewis, M 2007, 'Parametric evaluation of communication devices in smart composite structures', in *Proceedings of the 5th Australasian Congress on Applied Mechanics (ACAM)*, Engineers Australia, Brisbane, Australia, pp. 477–482.
- Sulic, E, Pell, B, John, S, Gupta, R, Rowe, W, Ghorbani, K & Zhang, K 2010, 'Deformation evaluation of embedded antennas in vehicular components', in *Proceedings of the World Congress of Engineering*, London, UK, pp. 2389–2394.
- Toriyama, H, Ohe, J, Kondo, H & Yotsuya, H 1987, 'Development of printed-on glass TV antenna system for car', in *37th IEEE Vehicular Technology Conference, 1987*, pp. 334–342.
- Waterhouse, R 2008, *Printed antennas for wireless communications,* Wiley, Chichester, UK.
- Wenger, J 2005, 'Automotive radar—status and perspectives', in *IEEE Compound Semiconductor Integrated Circuit Symposium, 2005. CSIC '05*, p. 4, DOI 10.1109/CSICS.2005.1531741.

CHAPTER 3: Literature Review: Composite Materials and Their Use in Automobiles with Specific Focus on Rheology of Sheet Moulding Compounds

3.1 Background

Composite (Hull 1996; Schwartz 1996) is an entity comprising a number of distinct components. Typically, they have two main constituent materials: reinforcement and matrix. According to Hull (1996) and Schwartz (1996), reinforcements are typically stiffer than matrix. The main role of the matrix is to act as a binding material for reinforcements and to transfer load to the reinforcements. Typical materials used as a matrix today are metals, ceramics and plastics. Resins, thermosetting and thermoplastic are the two kinds of matrix widely used for making composites. Thermoplastic resins, such as polyvinyl chloride (PVC), ABS, polypropylene (PP), polyamide, acrylic and PC, are formed under heat (Hull 1996; Schwartz 1996). In contrast, thermosetting resins, such as melamine, polyurethane, polyester, epoxy and silicone, undergo a chemical cross-linking reaction (Hull 1996; Schwartz 1996). Reinforcements that are commonly used today are classified as: a) continuous reinforcements (fibres run through the resin with no discontinuities); b) discontinuous aligned reinforcements (fibres are chopped and aligned within the resin); and c) discontinuous reinforcements (fibres are chopped and randomly distributed within the resin) as is shown in Figure 3.1, and particulate reinforcements (fibres are shaped in the form of plates or spheres). Glass fibres, carbon and aramid are some of the different types of fibre reinforcement materials commonly used in the industry today (Hull 1996; Schwartz 1996).

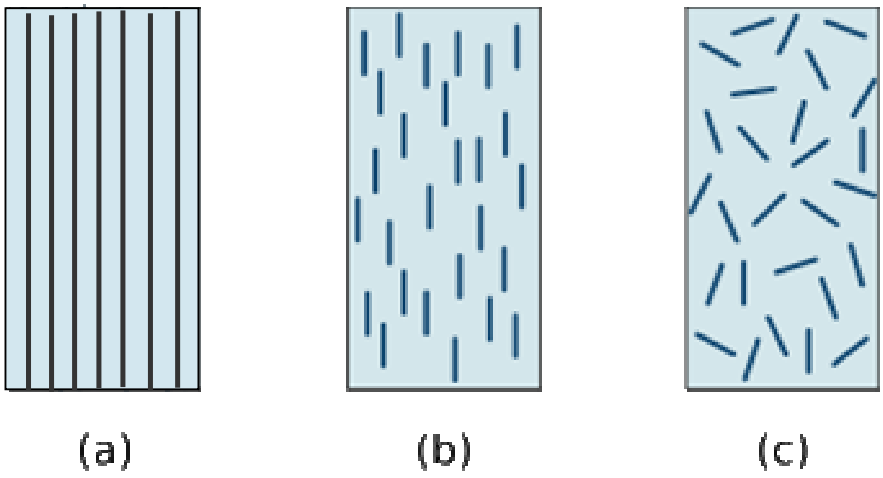

Figure 3.1: Types of fibre-reinforced composites. a) Continuous fibre-reinforced, b) discontinuous aligned fibre-reinforced and c) discontinuous random-oriented fibre-reinforced.

Glass fibre reinforced polymers (GFRP) are a category of composites that consist of short and/or long glass fibres as a reinforcing component, with thermoset materials, including polyester and vinyl ester, as the resin component (Keller & Tirelli 2004). The main physical properties of these GFRPs are good strength, derived from the glass fibres, and resistance to corrosion, derived from the plastic. These types of composites also include a number of other additives/fillers that enhance the physical and functional properties of the end product. They can include, among others, wear resistance, ultraviolet (UV) stability, gloss, electrical insulation and fire resistance. Mechanical properties of such composites mainly depend on fibre diameter and length. Hence, these two characteristics are specifically selected based on the end application and manufacturing method. Typical forms of the glass fibres used in the industry are yarn, continuous strand mat, chopped strand mat, roving, woven roving, woven cloth and stitched mat (Hull 1996; Schwartz 1996).

3.2 Application of Composites

Over the past few years, the use of composite structures has been increasing in a number of industries, such as the aeronautical, automotive, construction and marine industries (Barker et al 2004).

In the 1930s, Henry Ford used soya oil to produce a phenolic resin reinforced with sawdust composite material that was utilised in car bodies in very limited numbers, due to the limited availability and high cost of the initial parts. In the 1940s, a flax-reinforced fuselage was manufactured and used on Spitfire fighters (FLIGTH-1942). The earliest composite materials, developed in the 1930s and 1940s, did not make their way through to the wider automotive industry at that time, due to limitations in the then automotive engineering techniques. These were the first small forays into composite materials before the use of glass fibre reinforced polyester resins became commercially available in the early 1950s. This put the manufacture of complex, compound curved, streamlined automotive bodies into the reach of low-volume, low-capital companies.

Today, fibreglass is used extensively for building almost everything, including surfboards, building panels, boat hulls and, of course, car chassis. The advantage of composite materials over normal, single-layered metals is that they are many times stronger and lighter than the latter. As a result, not only does the use of such a composite material decrease the overall weight of the object, but it is also, compared to single-layered materials, much more break resistant. An example of a modern car manufactured using a number of different composites for the interior and exterior components is shown in Figure 3.2. A steel safety shell holds together a variety of different parts and panels, mostly made of plastics, including PP, polyvinyl butyral (PVB), PC and polyethylene terephthalate (PET). As on most cars, the ‘rubber’ tyres are actually composites made from rubber and numerous other materials, such as silica.

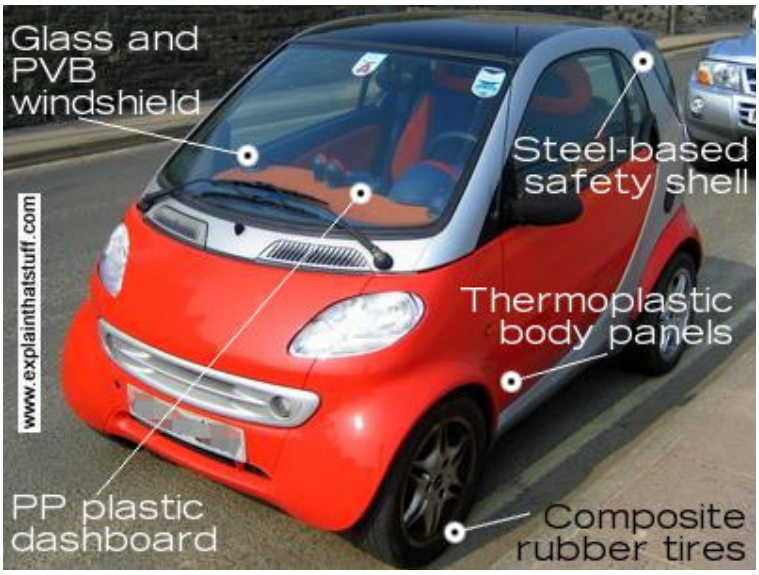

Figure 3.2: Mercedes Smart vehicles are lightweight, part composite vehicles

Automobile manufacturers use compression-moulding methods for the production of chassis and other components. Two of the main composite materials used are an SMC and a bulk moulding compound (BMC).

The recent innovations in the sphere of advanced composites in the automotive manufacturing industry have led to the use of carbon fibre reinforced plastic (CFRP), with various thermoset composites, including aramid fibre and carbon fibre in a matrix of epoxy resin. The Formula 1 racing cars in the early 1990s had chassis built with plastic-reinforced carbon fibres. In this process, a resin sheet is laid, already containing the carbon fibre reinforcement in the form of a woven mat. This is kept in a mould, which is then placed in a pressure-tight, high-grade oven, or autoclave, with a very high temperature and pressure. This baking process ultimately produces the hard set resin composite. Composite materials are used for high-performance racing cars, as the materials that build these should be lightweight as well as strong enough to withstand harsh operating conditions, including high temperature and incredible stress and strain.

3.3 Sheet Moulding Compound

The use of SMC is a very important production process for the production of glass reinforced plastic (GRP) parts. SMC is a flat, sheet-like compound, produced on a continuous moving belt process. As glass fibre reinforcement, in most cases, cut glass rovings are used. Calcium carbonate (chalk) is the most commonly used filler. Magnesium oxide in the formulation can react with the free acid groups of the resin. After a few days, this results in an enormous increase in the viscosity of the SMC formulation. A leather-like sheet is formed, which is almost non-sticky and easy to handle. At this stage, the resin is still not polymerised.

In the production of SMC, the resin is premixed to a paste with all the components of the formulation. The resin paste is transferred to a doctor box, where it is deposited onto a moving carrier film passing directly beneath. The doctor box controls the amount of resin paste applied. Simultaneously, glass fibre rovings are fed into a rotary cutter above the resin-covered carrier film. Fibres are chopped to length (generally, 25 mm or 50 mm) and randomly deposited onto the resin paste. The amount of glass is controlled by the cutter and by the speed of the carrier film. Downstream from the chopping operation, a second carrier film is coated with resin paste and is laid, resin side down, on top of the chopped fibres. This stage of the process creates a resin paste and glass fibre ‘sandwich’, which is then sent through a series of compaction rollers, where the glass fibres are consolidated with the resin paste and air is squeezed out of the sheet, as can be observed in the schematic diagram in Figure 3.3 and the image in Figure 3.4 of the SMC process. At the end, the SMC is rolled and stored for a few days to give the thickening reaction sufficient time. The ready and thickened SMC is stored and sold in the form of rolls. Depending on the requirements for the finished product, a wide variety of formulations is available nowadays.

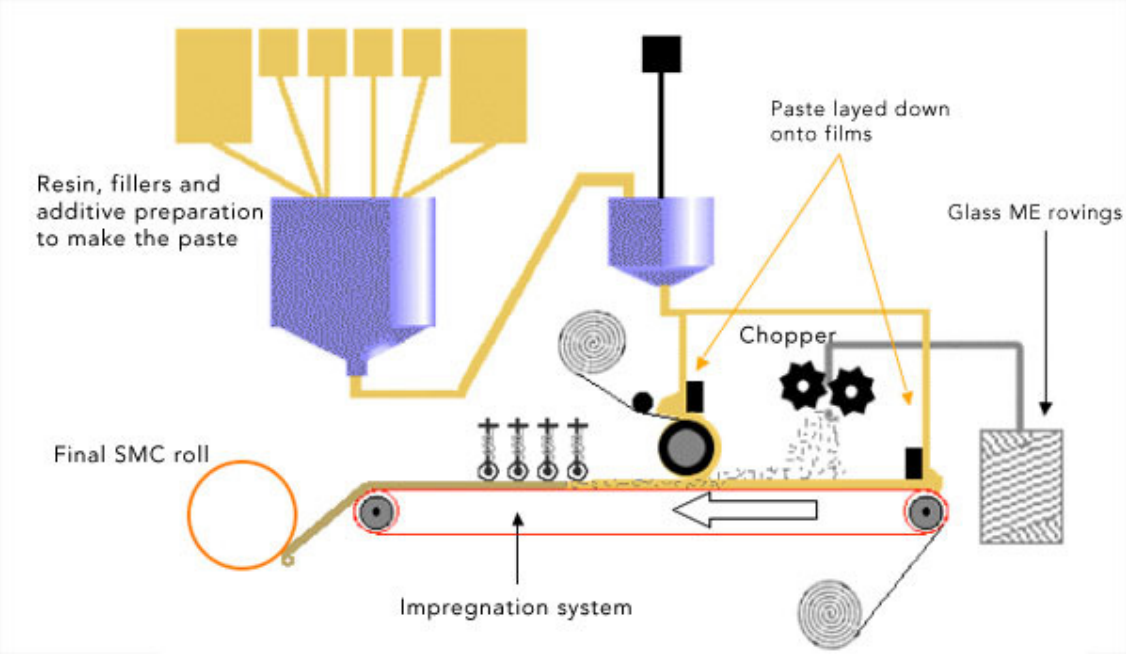

Figure 3.3: Schematic of a generic SMC manufacturing process

Figure 3.4: Image of SMC manufacturing line

Sheet dimensions are usually 4 mm thick and 1,500 mm wide, but the size can vary, ultimately depending on end application. The length and weight of the SMC sheet is determined by moulder preference for handling and is usually stored on a 350 kg (standard) and up to 1500 kg rolls, as shown in

Figure 3.5, or bi-folded (like computer paper) into large bins. Modern SMC production is a highly automated and computer-regulated process.

Before the SMC can be used for moulding, it must mature. This maturation time is necessary to allow the relatively low-viscosity resin to thicken chemically. The SMC will be kept in a maturation room at a controlled temperature (normally for 48 hours at 30 ℃) and typically requires two to five days to reach the desired moulding viscosity. Usually, SMC has a shelf life ranging from several weeks to several months from the date of manufacture. The period can be extended or reduced depending on the SMC formulation and storage conditions. A storage temperature of no higher than 20 ℃ is recommended.

Figure 3.5: SMC storage arrangement

3.3.1 SMC Characteristics

Products manufactured using SMC possess high weather—or corrosion—resistance, excellent surface finish or high mechanical properties. In the production of car body parts, SMC systems that cure without shrinkage have been developed. The result is a high-quality surface of the parts, a so-called ‘Class A’ surface. This quality is equivalent to ‘mirror-like’.

The leather-like consistency of the SMC makes a fully automated manufacturing process possible. Robot-controlled installations cut the SMC into predetermined pieces. The protective polyamide film is removed from the pieces, which are then placed into the steel mould. The mould is closed and, at a pressure of 100 bar and a temperature of 150 °C or similar, the SMC flows into the mould cavities, where it cures. The cycle time for an SMC press operation, depending on type, size and complexity of the product, ranges from 30 seconds to 3 minutes. The modern SMC production installations represent the latest technology, in which most of the process parameters, such as weight per unit area and composition, are controlled automatically.

Typical application of SMC in automotive products are:

- body panels for cars, trucks and agricultural vehicles
- under the hood components for trucks and passenger cars
- lighting systems, headlamp reflectors and LED lighting
- structural parts, front ends and bumpers
- interior dashboard parts.

Thermal resistance: All thermoset polymers are known for their excellent thermal resistance. Using specific resin systems, thermal resistance up to 300 °C can be achieved. From a technical viewpoint, these materials are superior to engineering thermoplastics and especially the more economical alternative solution in comparison to high-performance thermoplastics. The combination of cross-linked polymer and high inorganic filler content, which maintains the excellent moulding characteristics, makes SMC materials the first choice for applications where elevated service temperatures are required or high temperatures can occur temporarily. For demanding engineering applications, it is also crucial that the coefficient of thermal expansion is close to metals and ensure excellent performances in all temperatures.

Fire retardancy: High fire retardancy, nowadays, is most important for many applications and markets. To achieve high flame retardancy, a number of additives can be used for different polymers. SMCs do not contain any

halogens or other hazardous flame retardants. However, they still can be formulated to have excellent properties, even at very low wall thickness.

Precision: SMCs are first-choice solutions for the substitution of high-performance metal parts, where high precision is achieved through post machining. The tightest tolerances can be produced directly without post-operations, which will ensure not only cost savings but also increased profitability. As a main advantage over competing non-thermosetting polymers, the possible compensation of shrinkage makes even the most challenging jobs feasible.

Weight reduction: At present, when the focus in vehicle manufacture is placed increasingly on fuel consumption CO2 reduction, fossil fuels are becoming more scarce and the environmental stress must be reduced, high-performance composites can contribute with components that have less weight and therefore lower energy consumption. The mechanical properties of SMC make the substitution of a wide range of metal parts not only feasible but also quite easy.

Electrical performance: From the beginning of plastic manufacturing, thermoset materials have had excellent electrical performances, and this has been one of their greatest advantages. In addition to the excellent electrical properties of thermosets, SMC has a number of advantages in other important parameters, such as electrical strength, water absorption and surface resistivity. Somewhat counter-intuitively to its excellent isolation properties, SMC material is also available with reduced surface resistivity and elevated conductivity, resulting in good coverage of the full range of electrical requirements, both isolating and conductive.

Class A surfaces: SMC has excellent surface finish for online and offline painting as well as metallising (addition of metallic coatings to the surface of part). Excellent surface finish results from the use of unique technology to compensate for the material shrinkage and migration of volatile organic compounds (VOC) during material processing.

Low emissions: Interior parts, in general and not only in the automotive industry, require low emission materials. Any objectionable and unpleasant smell, hazardous or uncomfortable emissions are restricted. In addition, the use of SMC in the lighting system's headlamp reflectors must be free of any emissions to avoid the formation of fog film on the system components that would, over time, reduce the lamp's performance.

3.4 Body of Knowledge: Rheological Properties of SMC and Material Flow

SMC material is usually processed into finished components using compression moulding. Sheets of the predetermined size, at typically 25 ℃, are loaded into a steel mould that has been preheated to about 150 ℃, as shown in Figure 3.6 (stage 1). SMC is then squeezed by the top (moving) half of the mould and bottom (fixed) half of the mould at a typical closing rate of 5–10 mm per second, as shown in Figure 3.6 (stage 2). This is followed by the curing stage of the process, which typically takes 60–120 seconds. Finally, the tool is opened and the part ejected using an ejection pin.

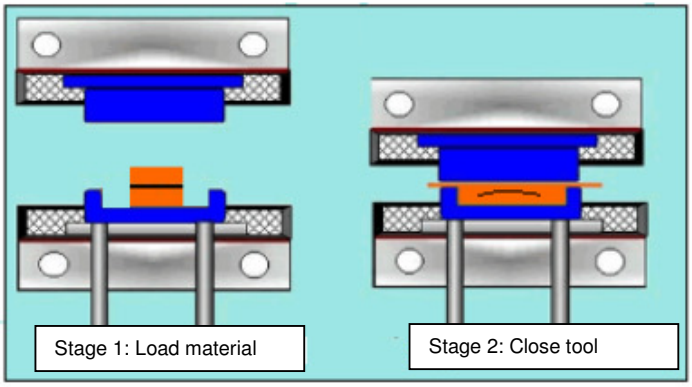

Figure 3.6: The compression-moulding process

A number of journal papers, conference proceedings and book chapters have dealt with SMC flow during the compression-moulding process (Barone & Caulk 1985; Castro & Griffith 1989; Marker & Ford 1977; Odenberger, Andersson & Lundström 2004; Olsson et al. 2008; Silva-Nieto, Fisher & Birley

1980; Xu et al. 1993). This work has mainly focused on analysing the mechanisms of SMC flow during the tool closing phase of the process. Therefore, it is therefore somewhat counterintuitive to find that, within the body of work, references to the rheological properties and behaviours of these compounds during the compression stage are quite scarce and incomplete (Bird, Armstrong & Hassager 1987; Costigan et al. 1985; Kim et al. 1992; Kim, Jeong & Im 1997; Lee, Marker & Griffith 1981; Lin, Weng & Ho 1997; Lin & Weng 1999; Michaeli, Mahlke & Osswald 1990; Silva-Nieto, Fisher & Birley 1981). A better understanding of the rheology of these compounds would contribute to the improvement of the rheological models developed and implemented in simulation software (Barone & Caulk 1986; Castro & Tomlinson 1990; Lee, Folgar & Tucker 1984).

3.4.1 Rheology of SMC

This gap in the research can be largely explained by reviewing the published material in detail. Silva-Nieto (1981) performed their research using the rheometers that were commonly available at the time, which were not well suited to characterising these materials. These rheometers were the first commercially available versions of the new generation of electrically driven, controlled-stress rheometers. They were still based on air bearings that had been developed in the early 1970s and greatly reduced friction during testing. In addition, they were using so-called drag-cup electrical motors that allowed controlled stresses to be more easily applied independently of rotation speed. These new features opened new ways of measuring smaller and smaller rotations and rotation rates. They produced excellent results when used to investigate thermoplastic and rubber-like compounds.

However, when it came to thermoset compounds, to obtain meaningful results, the dimensions of the tested samples had to be chosen in proportion to the size of the fibres that were used in the compound. This implies the use of a powerful machine to carry out tests on large samples. Silva-Nieto (1981), in their work with the SMC, studied its behaviour by squeezing cylindrical samples of 40 mm in diameter between parallel and non-lubricated plates. This study focused only on one glass fibre weight fraction of 25% by volume

and the tests were carried out at room temperature. In their test, they used constant plate-closure speeds ranging from 0.016 mm per second to 0.8 mm per second. It was found that the applied force was an increasing function of the plate-closure speed. However, no quantitative results could be drawn from their work for several reasons:

- The dimensions of the fibres were not mentioned, so it is impossible to check if the samples' diameter was sufficiently large compared with the fibres' length.
- Their experiments involved a heterogeneous stress state, which combined compression-shear stress states with spatial gradient, and were analysed assuming an incompressible and isotropic material behaviour (Scott 1931). The isotropy assumption is not consistent with the anisotropic microstructure of SMC, since fibres are randomly distributed in a loosely woven fibre matrix, parallel to the plane of the sheets.
- Their studied closure speed range was significantly less than that commonly used in the compression-moulding process, in which the typical tool closing speed ranges from 5 mm per second to 10 mm per second.

Among the early studies reviewed, the analyses performed by Lee, Marker and Griffith (1981) had the most rigorous approach. Testing was performed on samples made of either unsaturated polyester resin paste or SMC material, with a glass fibre weight fraction ranging from 10% to 30% and fibre length ranging from 12.5 to 25 mm. An extensive test regime was used, with a large number of shear tests performed with unsaturated polyester resin paste. The steady-state non-Newtonian viscosity was found to follow a Carreau-type function for the applied shear rate and an Arrhenius-type function for the temperature. The SMC material behaviour was mainly investigated by performing simple compression-creep tests, where applied force is held at a constant level on cylindrical samples with a diameter of 200 mm, squeezed between silicone lubricated plates.

The results show that the compressive viscosity of SMC material was strain-rate dependent. Further, a strong correlation between fibre content and the

compressive viscosity of SMC was recorded. This relationship correlated well with a Batchelor-type approach (Batchelor 1970). However, despite the good qualitative tendencies underlined by this work, no real quantitative data were drawn and no rheological model was proposed to describe the behaviour of SMC material during the compression-moulding process.

More recent research performed by Lin, Weng and Ho (1997) and Lin and Weng (1999) focused on simple compression and plane-strain compression tests. The SMC material tested had a 25% fibre volume fraction of glass fibre with a length of 25.4 mm. Simple compression tests were performed on cylindrical samples with a diameter of 150 mm. Samples were made of several stacked sheets measuring up to 8 mm in thickness. Testing for plane-strain compression was performed by deforming rectangular prisms measuring 120 mm x 44 mm x 8 mm through a rectangular mould measuring 120 mm long and 44 mm wide.

In both tests (simple compression and plane-strain compression), the axial strain rates were kept constant during loading but were then varied between 0.2 and 1 s^{-1} during testing. The results obtained from these two sets of experiments were then used to determine some of the parameters that were used in a rheological model initially proposed by Kim et al. (1992). This model was proposed as a good representation for the anisotropic, incompressible and non-Newtonian viscous behaviour of SMC material (Kim et al. 1992).

The model assumes that a viscoplastic potential is a function of an equivalent stress, where the equivalent stress is similar to the quadratic Hill yield stress when reduced to the case of planar isotropy (Hill 1950), and it involves three anisotropic parameters. The experimental results obtained showed that the equivalent stress was identical to a nonlinear function of the imposed strain rate. This, in turn, allows one to determine two of the three anisotropic parameters where the last required parameter can be estimated with a Batchelor-type approach. However, there are a number of limitations in this work undertaken by Lin, Weng and Ho (1997) and Lin and Weng (1999):

- Only one fibre volume fraction was studied (25%).

- A very small strain-rate range was analysed (0.2 to 1 s^{-1}).
- The identification procedure they used may yield to erroneous modelling.

In a later study undertaken by Dumont et al. (2003), a more detailed investigation was performed into strain rates ranging from 0.001 to 10 s^{-1}, glass fibre volume fractions from 0% to 23% and temperatures from 25 °C to 75 °C. In the experiments, a novel rheometer was used (see Figure 3.7). Two shapes of SMC samples were used: discs and rectangular prisms. The size of discs samples varied from 50 to 200 mm diameter and the size of the rectangular prisms from 20 to 120 mm. This rheometer allows the performance of shear tests, compression tests and plane-strain compression tests, as can be observed in Figure 3.7.

The surfaces of this modular apparatus in contact with the sample, manufactured from aluminium, were polished and coated with a thin layer of silicone grease-like lubricant for simple compression tests to reduce any errors due to friction. To measure the transverse force, a force transducer was fastened behind one side of the channel mounted in a slide, as shown in Figure 3.7(b).

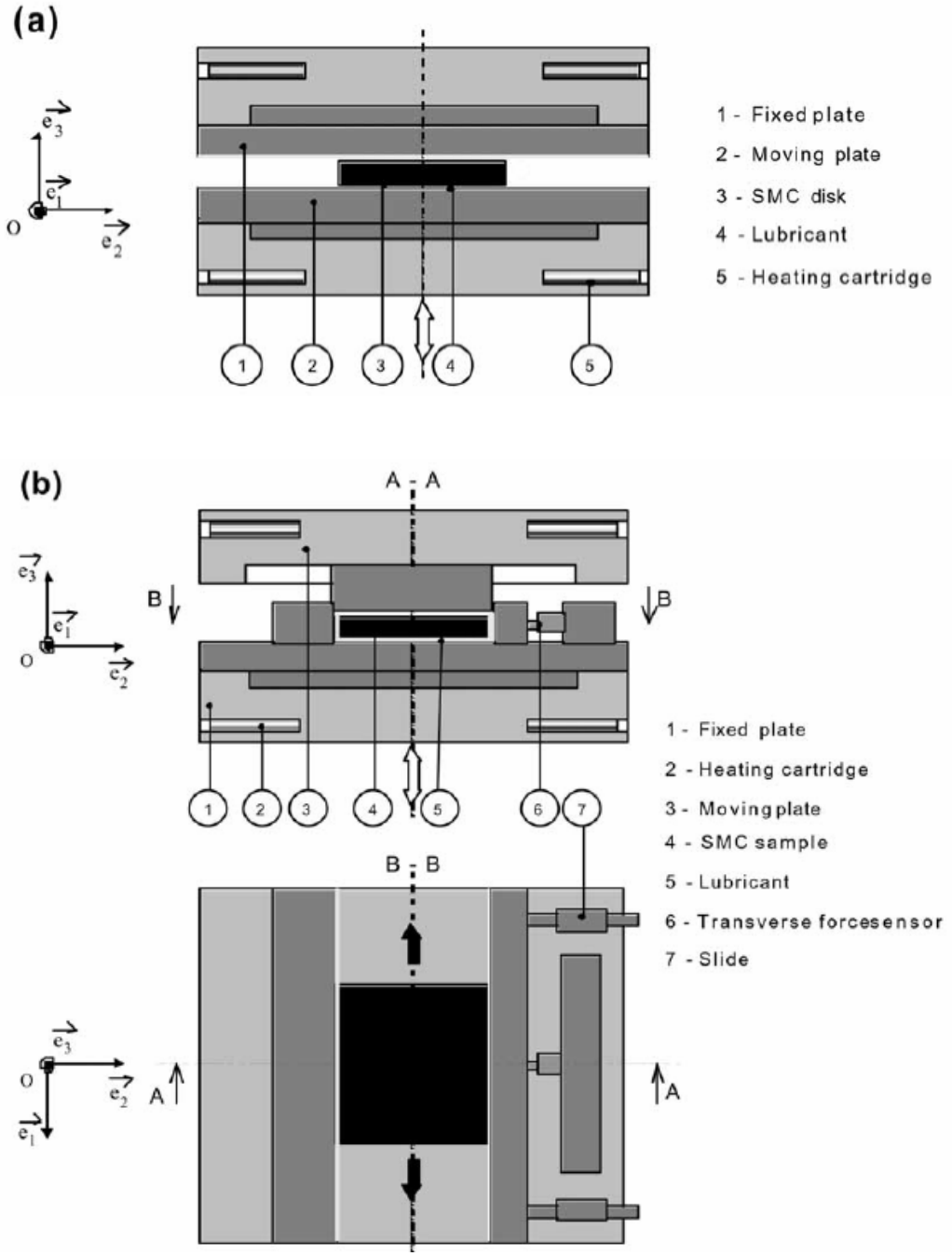

Figure 3.7: SMC rheometer using (a) simple compression configuration and (b) plane-strain compression configuration © *International Journal of Plasticity* with permission (Dumont et al. 2003)

- The results obtained in this study clearly underline the key role played by both the strain rate and the glass fibre content.

- Strong shear-thinning behaviour was observed as evidenced by stress levels that proved to be power law functions of the strain rate.
- They were also proved to be increasing functions of the glass fibre content.
- Increasing the fibre content shows a direct correlation with increase of the anisotropy of SMC.

Dumont et al. (2003) proposed a rather simple nonlinear viscous and transversely isotropic model that was used to fit stress levels recorded during the experiments. Strong agreement between the experimental data and the proposed model in the study was observed. This model accounts for the main characteristics of SMC rheology. The model can be easily integrated in commercial simulation codes in use for compression moulding to enhance their accuracy further.

3.5 Conclusion

Based on the literature review carried out in this chapter, it is evident that SMC material has significant potential to increase its use in high-end, complex applications such as automotive, marine and electronic applications. It already occupies a unique position as a high-performance, highly profitable composite material with enormous potential for further growth. The physical properties of cured SMC are well known and understood. The ability of SMC to tailor set performances, by changes to the formulation and process parameters, to specific application demands will expand the usage of these materials significantly in the future.

The body of knowledge regarding SMC flow during the compression-moulding process is extensive and well documented in the research carried out over the last 30 years. This knowledge has been used over the years to develop modelling software: CADPRESS, by the Madison group, based on the mould-filling model proposed by Barone and Caulk (1986) and confirmed through experimental studies performed by Osswald (1987) and Osswald and Tucker (1989), is capable of predicting the charge placement on the tool, optimal

amount of material, material flow path, fibre orientation, prediction of moulding forces and equipment requirements, surface finish, curing profile and shrinkage and warpage.

3.6 Research Gaps Identified – Basis of this research endeavour

Despite this detailed understanding of material flow during compression moulding, the author was unable to find any relevant information regarding the deformation of products/material when being embedded in SMC, and found even less information regarding rheology and inner workings of such an embedding process. As such, it was one of the main goals of this research to develop some understanding of this process and the effects it exerts on the product/material being embedded, with a view to contributing significantly to the existing body of knowledge regarding SMC. This could be used to enhance the computer-aided engineering (CAE) space for SMC and other similar composite materials further.

3.6 References

- Barone, MR & Caulk, DA 1985, 'Kinematics of flow of sheet molding compounds', *Polymer Composites*, vol. 6, no. 2, pp. 105–109.
- Barone, MR & Caulk, DA 1986, 'A model for the flow of a chopped reinforced polymer compound in compression moulding', *Journal of Applied Mechanics*, vol. 53, no. 2, pp. 361–371.
- Batchelor, GK 1970, 'The stress system in a suspension of force-free particles', *Journal of Fluid Mechanics*, vol. 41, no. 3, pp. 545–570.
- Betten, J 1988, 'Applications of tensor functions to the formulation of yield criteria for anisotropic materials', *International Journal of Plasticity*, vol. 4, no. 1, pp. 29–46.
- Bird, R, Armstrong, R & Hassager, O 1987, *Dynamics of polymeric liquids,* John Wiley & Sons, New York.
- Boehler, J-P 1987, 'Applications of tensor functions in solid mechanics', vol. 292, *Courses and lectures—International Centre for Mechanical Sciences*, Springer-Verlag, Wien, NY.
- Castro, JM & Griffith, RM 1989, 'Sheet molding compound compression-molding flow', *Polymer Engineering and Science*, vol. 29, no. 10, pp. 632–637.
- Castro, JM & Tomlinson, G 1990, 'Predicting molding forces in SMC compression molding', *Polymer Engineering and Science*, vol. 30, no. 24, pp. 1568–1573.
- Costigan, PJ et al. 1985, 'The rheology of SMC during compression molding, and resultant material properties', in *40th Annual Conference, Reinforced Plastics/Composites Institute, The Society of the Plastics Industry, Inc. Jan. 28–Feb. 1, 1985.*
- Davis, B, Theriault, A & Osswald, T 1997, 'Optimization of the compression (injection/compression) molding process using numerical simulation', *ASME Conference*.
- Dumont, P et al. 2003, 'Anisotropic viscous behaviour of sheet moulding compounds (SMC) during compression moulding', *International Journal of Plasticity*, vol. 19, no. 5, pp. 625–646.

- Folgar, F & Tucker, CL 1984, 'Orientation behavior of fibers in concentrated suspensions', *Journal of Reinforced Plastic Composites*, vol. 3, no. 2, pp. 98–119.
- Hill, R 1950, *Mathematical theory of plasticity*, Oxford University Press, Oxford, UK.
- Hull, D 1996, *Introduction to Composite Materials*, Cambridge University Press, New York.
- Khan, A & Haoyue, Z 2001, 'Finite deformation of a polymer: experiments and modeling'*, International Journal of Plasticity*, vol. 17, no. 9, pp. 1167–1188.
- Kim, J, Shiau, YC, Lee, LJ & Im, YT 1992, 'Compression molding simulation of chopped fiber reinforced polymeric composites in plate-rib type geometry'*, Polymer Composites*, vol. 13, no. 2, pp. 97–107.
- Kim, K-T, Jeong, J-H & Im, Y-T, 1997, 'Effect of molding parameters on compression molded sheet molding compounds parts', *Journal of Materials Processing Technology*, vol. 67, no. 1–3, pp. 105–111.
- Lee Corre, S, Orgéas, L, Favier, D, Tourabi, A, Maazouz, A & Venet, C, n.d. Shear and compression behavior of sheet molding compounds, *Composite Science and Technology*, in press.
- Lee, CC, Folgar, F & Tucker, C 1984, 'Simulation of compression molding for fiber-reinforced thermosetting polymers', *Polymer Composites*, 106, pp. 114–125.
- Lee, LJ, Marker, LF & Griffith, RM 1981, 'The rheology and mold flow of polyester sheet molding compound', *Polymer Composites*, vol. 2, no. 4, pp. 209–218.
- Lin, CM, Weng, CI & Ho, CT 1997, 'Anisotropy in sheet molding compounds during compression molding'*, Polymer Composites*, vol. 18, no. 5, pp. 613–622.
- Lin, CM & Weng, CI 1999, 'Simulation of compression molding for sheet molding compound considering the anisotropic effect'*, Polymer Composites*, vol. 20, no. 1, pp. 98–113.
- Marker, LF & Ford, B 1977, 'Flow and curing behavior of SMC during molding'*, Modern Plastics*, vol. 54, pp. 64–70.

- Martin, CL, Favier, D & Suery, M 1997, 'Viscoplastic behaviour of porous metallic materials saturated with liquid. Part I: constitutive equations', *International Journal of Plasticity*, vol. 13, no. 3, pp. 215–235.
- Martin, CL, Favier, D & Suery, M 1999, 'Fracture behaviour in tension of viscoplastic porous metallic materials saturated with liquid', *International Journal of Plasticity*, vol. 15, no. 10, pp. 981–1008.
- Meyssonnier, J, Duval, P, Gagliardini, O & Philip, A 2001, 'Constitutive modelling and flow simulation of anisotropic polar ice', in Straughan, B, Greve, R, Ehrentraut, H & Wang, Y (eds.), *Continuum mechanics and applications in geophysics and the environment*. Springer, Berlin, pp. 250–275.
- Michaeli, W, Mahlke & M, Osswald, TA 1990, 'Analyse und messung des fliessens von SMC mit einem pressrheometer', *Kunstoffe*, vol. 80, pp. 70–74.
- Nguyen, TG, Favier, D & Suery, M, 1994, 'Theoretical and experimental study of the isothermal mechanical behavior of alloys in the semi-solid state', *International Journal of Plasticity*, vol. 10, no. 6, pp. 663–693.
- Odenberger, PT, Andersson, HM & Lundström, TS 2004, 'Experimental flow-front visualisation in compression moulding of SMC', *Composites Part A: Applied Science and Manufacturing*, vol. *35*, no. 10, pp. 1125–1134.
- Olsson, NEJ et al. 2008, 'Process study on compression moulding of SMC using factorial design', in *Proceedings of the 19th International Symposium on Transport Phenomena (ISTP-19): Reykjavik, Iceland, August 17–21, 2008*.
- Osswald, TA 1980, 'Numerical methods for compression mold filling simulation', PhD Thesis, University of Illinois at Urbana-Champaign.
- Osswald, T, Sun, M & Tseng, S 1004, 'Experimental verification on simulating shrinkage and warpage of thin compression moulded SMC parts', *Polymers & Polymer Composites*, vol. 2, no. 3, p. 187.
- Osswald, TA, Sun, EM & Tseng, S 1996, 'Orientation and warpage prediction in polymer processing', in Stevenson, J (ed.), *Innovation in polymer processing: molding*, .

- Osswald, TA & Tucker, TL 1989, 'Compression mold filling simulation for non-planar parts using the finite element/control volume approach', *International Polymer Processing*, vol. 5, no. 2, p. 79.
- Scott, JR 1931, 'Theory and application of the parallel-plate plastimeter', *Trans. Inst. Rubber Ind*, vol. 7, pp. 169–186.
- Silva-Nieto, RJ, Fisher, BC & Birley, AW 1980, 'Predicting mold flow for unsaturated polyester resin sheet molding compounds', *Polymer Composites*, vol. 1, no. 1, pp. 14–23.
- Silva-Nieto, RJ, Fisher, BC & Birley, AW 1981, 'Rheological characterization of unsaturated polyester resin sheet molding compounds', *Polymer Engineering and Science*, vol. 21, no. 8, pp. 499–506.
- Schwartz, M.M. 1996, 'Composite Materials: Processing, Fabrication and Applications', Prentice Hall PTR, New Jersey.
- Ward, IM 1979, *Mechanical properties of solid polymers*, John Wiley & Sons, New York.
- Xu, J, Kim, J, Ho, T & Lee, JL 1993, 'Compression molding of sheet molding compounds in plate-rib type geometry', *Polymer Composites*, vol. 14, no. 1, pp. 51–58.

CHAPTER 4: Determining Dielectric Constant of Sheet Moulding Compound

4.1 Introduction

Before designing an antenna, it is crucial to know the electrical properties of the materials that surround it. The dielectric constant, κ, (also known as permittivity) describes the degree of interaction between an electric field and an electrical charge or electric dipoles in a dielectric medium. Permittivity of a material, according to the *IEEE Standard Definitions of Terms for Radio Wave Propagations*, is 'a macroscopic material property of the medium that relates the electric flux density, $\vec{D}$, to the electric field, $\vec{E}$, in the medium'. Typically, it is represented in equation form by the phasor equation:

$$\vec{D} = \bar{\varepsilon} \cdot \vec{E}$$

where the complex permittivity, $\bar{\varepsilon}$, is a tensor. Complex permittivity, $\bar{\varepsilon}$, is generally frequency dependent, so in the case of an isotropic medium, the tensor reduces to a complex scalar:

$$\varepsilon = \varepsilon' - j\varepsilon''$$

where ε' is the real part of the permittivity and ε'' accounts for losses.

Permittivity is a quantity that describes the degree of interaction between an electric field and electrical charges or dipoles in a dielectric medium, and is a function of frequency, temperature, humidity and other parameters. The permittivity of surrounding materials is an important consideration when designing electromagnetic devices such as antennas. When an electromagnetic wave travels through a dielectric medium, its frequency remains constant, but both the speed of propagation and wavelength will decrease as governed by the permittivity. This change in wavelength requires a change in the dimensions of the antenna because its dimensions are tuned in accordance with the wavelength of interest. Therefore, it was important to determine the dielectric constant of the composite materials we intended to use in conjunction with our antenna, as it was imperative to know by how much the desired wavelength would be shortened.

Changes to the real part of the permittivity, ε', primarily influence the physical size of an antenna designed to be resonant at a particular frequency. A higher permittivity leads to a shorter electrical length. However, if an antenna designed for a particular frequency in free space is surrounded by, or embedded in, a dielectric material with a higher permittivity, the frequency of operation of that antenna will be shifted towards lower frequencies. The imaginary part of the permittivity, ε'', predominantly effects the loss in the medium. If an antenna were embedded in a highly lossy medium, the radiated signal would be strongly attenuated. The dimensionless quantity loss tangent is often used to describe the relative magnitude of the imaginary part of a medium. The loss tangent $\tan\delta$ is defined by:

$$\tan\delta = -\frac{\varepsilon''}{\varepsilon'}$$

Given the potential effect on the antenna performance in terms of both frequency shifting and lossy attenuation, it was important to have an approximation of the values of both ε' and ε'' before commencing the design of an antenna intended to operate while embedded in or attached to the SMC or GMT dielectric material.

4.2 Determination of Permittivity

Numerous techniques are available to measure the permittivity of a material. Each of these techniques presents a range of advantages and disadvantages, along with a unique set of sources of error. Measurements of the real part of the permittivity, ε', tend to be more readily and accurately obtained than measurements of the imaginary part of the permittivity, ε''. At frequencies in the kilohertz (kHz) and megahertz (MHz) range, permittivity can be measured using standard capacitive techniques. The sample under test was placed between two conductive parallel plates and the capacitance of the system was measured and recorded. The sample was then removed from the structure, and the new value of the capacitance of the plates in air was measured. The difference in capacitance between the structure with the sample present and the structure with the sample removed can be used to

determine the permittivity of the material. At frequencies in the gigahertz (GHz) range, this technique is hampered by radiating fields from the structure.

At microwave frequencies, the variety of techniques available all fall into one of three broad categories: guided waves, resonators or free-space waves. The first category, guided waves, contains techniques that have been in use since the 1970s (Lynch 1974). Waveguide techniques that use either rectangular waveguides or circular 'airline' coaxial waveguides are well known. Open-ended coaxial probe set-ups that rely on fringing fields penetrating the material are also in this category. The second category involves resonator techniques, where a material under test would be placed in an enclosed metallic resonator. These techniques have the disadvantage of requiring fabrication of a custom resonator, and are usually very narrow band. The third category of free-space measurements emerged in the mid to late 1980s, the most notable being the method developed by Afsar et al. 1986; Ghodgaonkar and Varadan (1989). These techniques involved the use of horn antennas with lenses to focus the electromagnetic waves down to a small spot on a large planar sheet of material under test. The measurement of both transmission and reflection provides enough information to calculate both ε_r and μ_r; however, for most materials, it can be assumed that the permeability is the same as the permeability of free space, which enables the use of the $|S_{21}|$ alone, the transmission data, to calculate the permittivity.

4.3 Free-Space Measurement

In this measurement system, a vector network analyser (VNA) and a pair of horn antennas are used to measure transmission through a sample, as shown in Figure 4.1. The measurement set-up for this work closely resembled the configuration proposed by Amiet and Jewsbury (2000). Horn antennas covering the range of from 1 to 18 GHz were employed. No lenses were used to focus the radiation onto the panel. Flat samples of the cured SMC material were obtained from compression-moulded parts, and cut into large 500 mm x 500 mm squares to minimise the effect of any diffracted wave around the sample. Time gating was also employed on the network analyser to ensure

that only the signal of interest was used for the measurements, and reflections from conductive components in the measurement set-up or surrounding objects such as the walls of the room were ignored. Given that the materials under test were known to be non-magnetic, the relative permeability μ_r could be set to 1, and the transmission through the sample alone could be used to determine the permittivity.

This free-space technique has the advantage of being non-destructive, relatively quick to carry out, and able to measure a wide range of frequencies in a single test-the frequency range is only restricted by the specifications of the horns and the VNA.

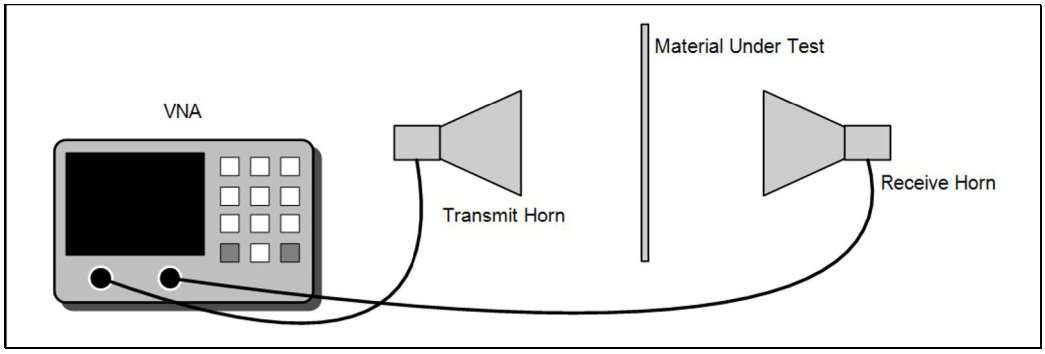

Figure 4.1: Schematic of free-space test set-up

4.3.1 Free-Space Test Results

Figure 4.2 shows the results from the SMC material variants and for galss mat thermoplastic (GMT). It can be observed that the permittivity of the SMC material was approximately 4.6, while the GMT was closer to 2.5. The evaluated permittivity for each material showed some variability over the frequency band. Some of this change may have been due to an actual change in permittivity, but some may have been due to errors in the measurement, such as movement of the sample while under test, or diffraction around sample edges.

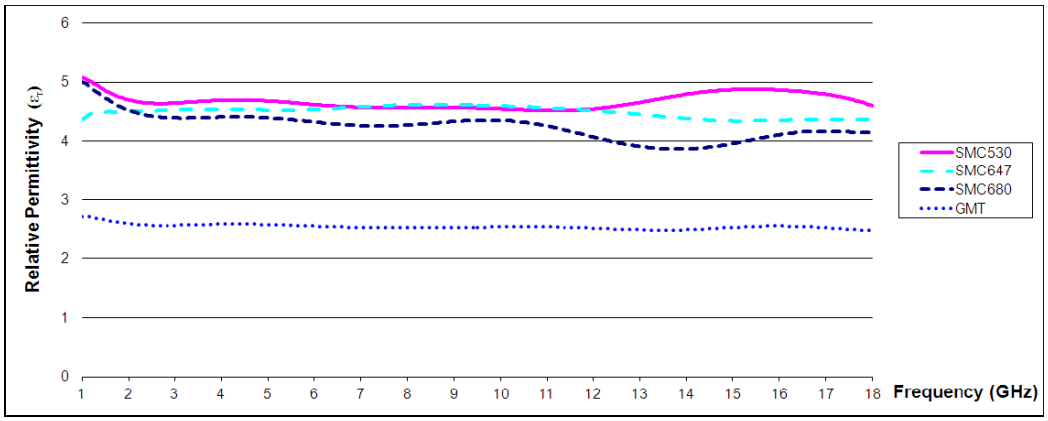

Figure 4.2: Real part of the relative permittivity of the samples under test

Figure 4.3 shows the imaginary component of the permittivity obtained during the measurements. These results appear to be typical of those obtained with this technique, including the changes in sign as the obtained value crosses the axis. It is difficult to conclude the loss tangent of the material from these results. Additional testing with alternative techniques were needed to verify the real part of the permittivity, ε_r', and to clarify the imaginary part, ε_r''.

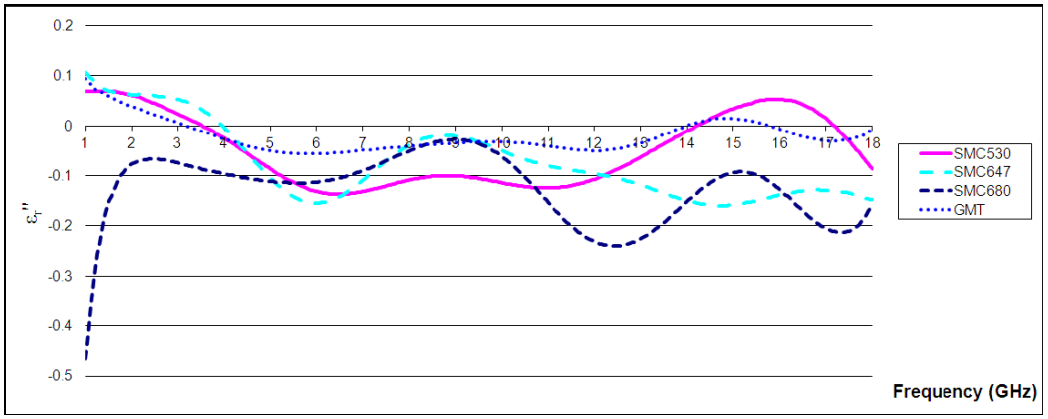

Figure 4.3: Imaginary part of the relative permittivity of the samples under test

4.4 Rectangular Waveguide

Waveguide measurements typically use a section of standard rectangular waveguide. The technique works best when the sample is less than half a wavelength thick. A sample of the material to be tested was cut and machined to fit precisely within the waveguide. Hence, in contrast to the free-space technique, this method is destructive, requiring that a flat sample of known

thickness be machined to match the inner dimensions of the waveguide. Any air gaps around the edge of the sample will lead to erroneous results, and hence a precisely fitting sample is important. While this technique may be used at any frequency band for which a waveguide may be obtained, implementing it at a higher frequency becomes difficult, due to the tighter tolerances required with increasingly small waveguide sections. Given the small sizes of some waveguides, inhomogeneous materials may give inaccurate results when the size of inclusions in the material becomes comparable to the size of the sample under test. Using many samples from different locations in the material would give an indication of the true permittivity by allowing an averaging of the measurements. Another drawback of this technique is the narrowband nature of the measurement. Measurements must be made within the normal frequency range of the selected waveguide, which usually corresponds to a percentage bandwidth of only about 40%. Although the literature shows (Agilent 1998; 2000a; 2000b; 2002; 2003; Baker-Jarvis et al. 1993; Nicolson 1970; Weir 1974) that WR-90 is commonly used for the technique, WR-430 waveguide was chosen for these measurements. WR-430 provides a more appropriate frequency range for our automotive interests, and has the benefit of having physically larger dimensions. WR-430 waveguide is typically operated from 1.7 GHz to 2.6 GHz, which falls in the middle of the band of interest for automotive frequencies, and would provide a snapshot of the relative permittivity of SMC and GMT in this region. Figure 4.4 shows typical test setup.

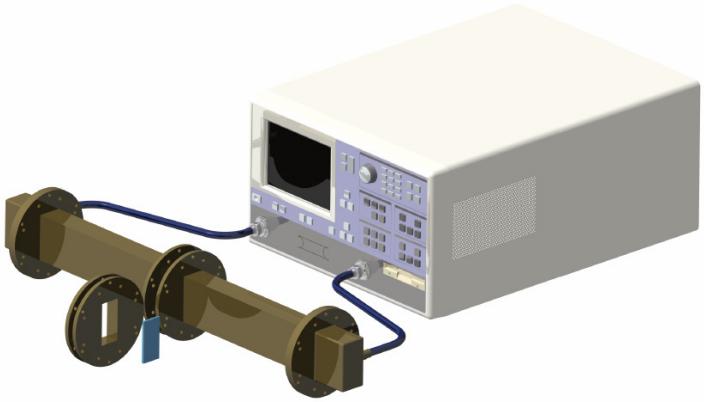

Figure 4.4: WR-430 used for rectangular waveguide testing

4.4.1 Rectangular Waveguide Test Results

While the results obtained for the real part of the permittivity using the waveguide technique largely agreed with those results obtained for the free-space method, the permittivity of the samples indicated values of 4.7, 4.6 and 4.5 for SMC530, SMC647 and SMC680 respectively. The results indicated a relative permittivity of approximately 3 for the GMT sample.

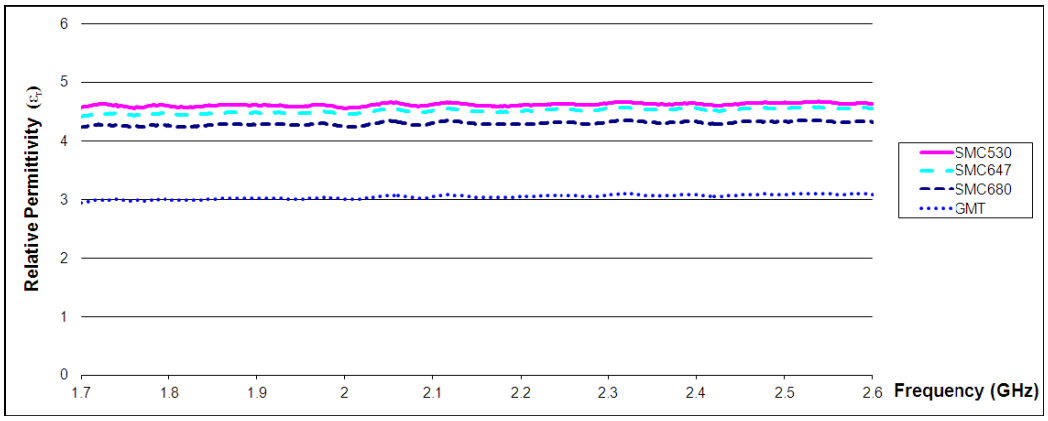

Figure 4.5: Real part of the relative permittivity of the samples under test

While the results for the real part of the permittivity harmonised with those obtained by the free-space method, just as with those obtained with the free-space technique, it was difficult to be confident in the results for the imaginary part of the permittivity. The results were very 'noisy', and appeared with both positive and negative signs.

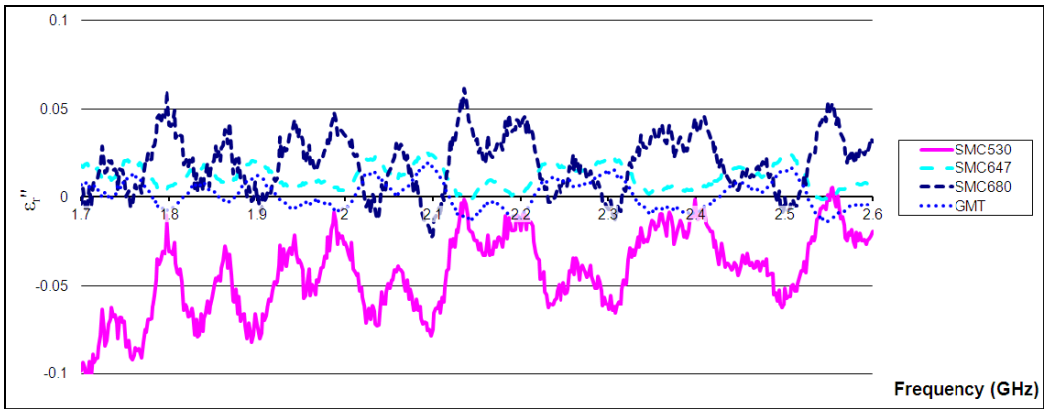

Figure 4.6: Imaginary part of the relative permittivity of the samples under test

4.5 Conclusion

Dielectric constant may vary with frequency, temperature and other parameters. In this application, the intent was to use a low-cost FR-4 (commonly used for manufacturing of computer boards. It consists of a composite material composed of woven fiberglass cloth with an epoxy resin binder that is flame resistant.) material for the antenna substrate. The dielectric constant of this material was already available in the manufacturer's datasheet. The dielectric constant of the host material, the composite glass-reinforced polymer known as SMC, given the results obtained from the free-space method and the waveguide method, we could have confidence that the dielectric constant of the SMC variants was approximately 4.6 and would vary slightly depending on which particular SMC variant was used in a given application. The magnitude of variation in the dielectric constant with different SMC variants was small, and the results obtained would allow commencement of the antenna design activities.

The real part of the permittivity for GMT appeared to be somewhere in the range of from 2.5 to 3.

Table 4.1: Summary of dielectric results for various SMC materials

Material	Dielectric Constant @ 1.575 GHz
SMC530	4.72
SMC680	4.61
SMC647	4.49
GMT	2.64

These obtained values, as summarised in Table 4.1, were to be used in antenna design simulations. It is important to note that any errors or differences in these values of permittivity would become apparent upon fabrication and measurement of antennas throughout the remainder of the process under study. Hence, while it was important to ensure these values were as accurate as possible at this point, opportunities for further verification

abounded, given that differences between measured and simulated antenna performance would become apparent.

These values were in the range of what would be expected for a glass-reinforced polymer, and appeared to be suitable for use in encapsulation of microstrip antennas. Future work may include validation of this result, by creating a microstrip line of known width, with the SMC material as a substrate. This would permit verification of the free-space measurement values by measuring the impedance of the microstrip line and comparing them against the predicted impedance from microstrip impedance formulae.

4.6 References

- Afsar, M, Birch, JB, Clarke, RN & Chantry, EW 1986, 'Measurement of the properties of materials', *Proceedings of the IEEE*, vol. 74*,* no. 1, pp. 183–199.
- Agilent application note 380-1, 1998, *Dielectric constant measurement of solid materials using the 16451B dielectric test fixture*, Agilent literature number 5950-2390.
- Agilent 2000a, *Application note 1287-1, Understanding the fundamental principles of vector network analysis,* Agilent literature number 5965-7707E.
- Agilent 2000b, *Application note 1287-2, Exploring the architectures of network analyzers,* Agilent literature number 5965-7708E.
- Agilent 2002, *Application note 1287-3, Applying error correction to network analyzer measurements,* Agilent literature number 5965-7709E.
- Agilent 2003, *Application note 1369-1, Solutions for measuring permittivity and permeability with LCR meters and impedance analyzers*, Agilent literature number 5980-2862EN.
- Altschuler, HM 1963, 'Dielectric constant', in *Handbook of microwave measurements*, Wiley.
- American Society for Testing and Materials , *Standard test methods for complex permittivity (dielectric constant) of solid electrical insulating materials at microwave frequencies and temperatures to 1650°C,* ASTM Standard D2520.
- Amiet, A & Jewsbury, P 2000, 'Free space microwave permittivity and permeability measurements', in *Asia-Pacific Microwave Conference 2000*, pp. 445–448.
- Baker-Jarvis, J, Janezic, MD, Grosvenor, JS & Geyer, RG 1993, *Transmission/reflection and short-circuit methods for measuring permittivity and permeability*, NIST technical note 1355-R.
- Blackham, DV & Pollard, D 1997, 'An improved technique for permittivity measurements using a coaxial probe', *IEEE Transactions on Instrumentation and Measurements*, vol. 46, no. 5, pp. 1093–1099.

- Bussey, HE 1967, 'Measurement of RF properties of materials: a survey', *Proceedings of the IEEE*, vol. 55, No. 6, pp. 1046–1053.
- Ghodgaonkar, D & Varadan, V 1989, 'A free-space method for measurement of dielectric constants and loss tangents at microwave frequencies', *IEEE Transactions on Instrumentation and Measurement*, vol. 38, no. 3, pp. 789–793.
- Lynch, AC 1974, 'Precise measurements on dielectric and magnetic materials', *IEEE Transactions on Instrumentation and Measurement*, vol. 23, no. 4, pp. 425–443.
- Nicolson, AM & Ross, G 1970, 'Measurement of the intrinsic properties of materials by time-domain techniques'*, IEEE Transactions on Instrumentation and Measurement*, vol. 19, no. 4, pp. 377–382.
- Von Hippel, A 1961, *Dielectric materials and applications,* MIT Press, Cambridge, MA.
- Weir, WB 1974, 'Automatic measurement of complex dielectric constant and permeability at microwave frequencies'*, Proceedings of the IEEE*, vol. 62, no. 1, pp. 33–36.

CHAPTER 5: Experimental Study of the Effect of Modern Automotive Paints on Vehicular Antennas

5.1 Introduction

Modern vehicles are fitted with a growing number of electronic devices designed to aid the driver and enhance the driving experience. Many of these devices rely on wireless communication to connect the moving vehicle with the outside world. Antennas are a necessary part of any wireless communication system, enabling transmission and reception of signals in free space. In past decades, the use of antennas in vehicles was primarily limited to services such as AM and FM radio. Today's vehicles are often fitted with antennas for additional purposes, including cellular communications for voice calls, GPS for satellite-based positioning and navigation, remote keyless entry applications and newer satellite radio services (i.e., SDARS). In the future, it is likely that vehicles will also require antennas for such things as mobile Internet and mobile video, collision avoidance radar, and V2V or V2I communication. Each of these wireless services necessitates the incorporation of additional antennas into the vehicular platform.

For many years, the standard AM/FM radio antenna was a monopole antenna, about 75 cm in length, which protruded vertically from the vehicle body. However, recent trends in vehicle design have seen a shift away from the traditional 'mast' antenna towards more aesthetically pleasing antennas, including smaller 'bee sting' type antennas (Cerretelli & Gentili 2007), antennas incorporated in window or windshield glass (Jensen 1971), 'shark-fin' designs (Lindenmeier, Hopf & Reiter 2007) popularised primarily by the European marques, and conformal planar designs (Hopf 2007). To continue to hide the antennas as much as possible and provide aesthetic freedom to vehicle designers, it would be desirable to paint the antennas so they blend in with the vehicle exterior, yet without disturbing their radiation performance. Some existing 'shark-fin' and conformal automotive antennas fitted to modern vehicles appear to have been painted, yet a detailed literature search revealed little about the effect of this paint on the antenna's performance.

An investigation of the effect of polyurethane-based metallic and non-metallic paints on a narrowband antenna at GPS frequencies was presented by Law et al. (2006). The work focused on a very limited selection of paints for one specific application. This chapter presents a detailed study on numerous additional paint types investigated over wider, multi-service frequency ranges.

References in the literature involving paint and antennas are sparse. The most complete are three investigations that involve paint applied to the surface of reflector antennas (Chu & Semplak 1976; Gschwendtner & Wiesbeck 2003; Hombach & Kuhn, 1989; Otoshi et al. 2001). These papers pertain to testing at frequencies in excess of 10 GHz, and report observed effects in cross-polar performance, noise, temperature and gain loss. Other existing references to paint effects on antennas in the literature are side comments that excessive layers of paint have the potential to affect automotive radar antennas significantly in the mm-wave region (Hoare & Hill 2000), or that metallic paint has little effect on microwave frequency applications (Lyons & Taskin 2000; Sabatier 1995). Therefore, a thorough investigation of the effect of automotive paint on planar antennas is required.

5.2 Overview of the Paints Investigated

Paints with different chemical compositions are used for different purposes around the world. This investigation focuses on paints that are used in automotive applications. Lacquers and enamels were traditionally used in the automotive industry, but these chemistries had the disadvantages of being fragile, easily damaged and creating excess amounts of pollution. Over the past 50 years, developments in the realm of automotive paints have included waterborne paints, base coat/clear coat systems and polyurethane topcoats (Pfanstiehl 1998). Water-based paints, in particular, are considered the future of automotive coatings because of the fewer VOCs released by this paint type and the subsequent environmental benefits (Robinson & Livesey 2006). In this chapter, we investigate these newer paint technologies, which are used on vehicles today, and into the future. The paints used are from two families. The first is a two-pack polyurethane topcoat manufactured by BC Coatings in

Australia, and marketed under the name VC800 Structure 105, while the second is a water-based paint that uses the base coat/clear coat system, made by PPG Industries, a dominant supplier in the world of automotive coatings. We also investigate the effect of an electrostatic primer. Electrostatic paints are used on some production lines and in other painting facilities to obtain a higher yield during the painting process. An applied DC voltage creates an electrostatic attraction between the object to be painted and the paint particles leaving the painting gun. Once airborne, the paint particles are drawn towards the target object, reducing overspray and more efficiently utilising the available paint. To enable electrostatic painting of inherently nonconductive polymeric panels, a partially conductive 'electrostatic' primer must first be applied. The electrostatic primer investigated here was supplied by PPG Industries. Table 5.1 provides a list of the samples investigated, and assigns an identification letter to each paint for simplicity. The painted samples and antennas used in the investigation are shown in Figure 5.1. The paint samples are presented in order from left to right, beginning in the upper left-hand corner of the image with sample A (which is blank to represent 'no superstrate').

Table 5.1: Sample descriptions

Sample ID	Paint Chemistry	Colour Name	Applied Thickness	Colour is Metallic	Primer	Clearcoat
A	no superstrate	-	-	-	-	-
B	no paint	-	-	-	-	-
C	Two-pack PU	VC800 "Wasabi"	50 µm	No	No	No
D	Two-pack PU	VC800 "Silver Satin"	170 µm	Yes	No	No
E	Water based	primer only	80 µm	-	(Yes)	No
F	Water based	"Lightning Strike (silver)	25 µm	Yes	No	No
G	Water based	"Lightning Strike (silver)	60 µm	Yes	No	Yes
H	Water based	"Ignition" (red)	80 µm	Yes	y	No
I	Water based	"Ignition" (red)	115 µm	Yes	y	Yes
J	Water based	"Caribbean" (blue)	90 µm	Yes	No	Yes
K	Water based	"Ink" (black)	25 µm	No	No	No
L	Water based	clearcoat only	30 µm	-	No	(Yes)
M	Electrostatic Primer	hyperprime only	15 µm	-	(Electrostatic)	No
N	Electrostatic Primer + topcoat	hyperprime + silver	50 µm	Yes	(Electrostatic)	No
O	copper Layer	no paint - copper layer only	36 µm	-	-	-

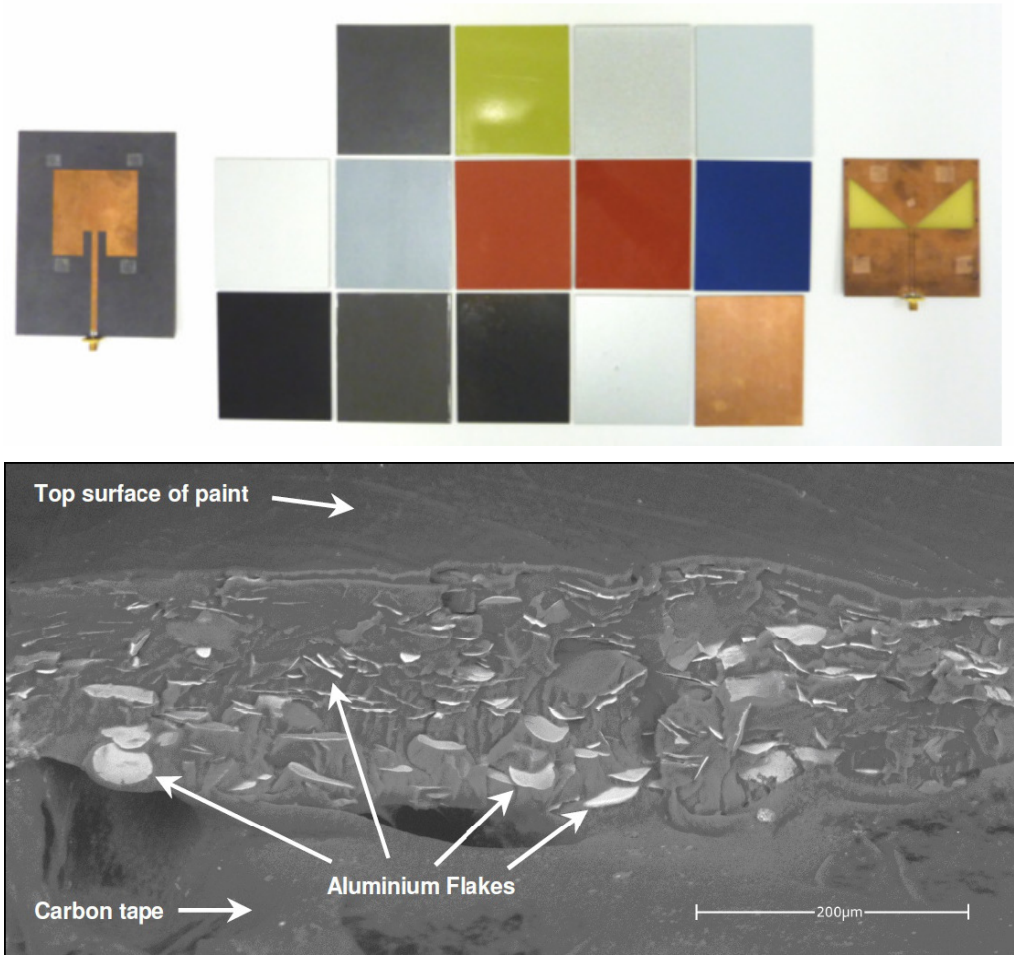

Figure 5.1: Paint samples to be tested and image of metallic flakes in the paint obtained using SEM

5.3 Aluminium Flake Size in the Paint

Prior to examining the effect of these automotive paints on an antenna, a small section of metallic paint from sample D was closely studied to inspect the metallic inclusions that create the metallic effect.

According to Lambourne and Strivens (1999), the size of the aluminium flake in metallic paints typically ranges from 15 to 30 µm in width. To determine the approximate size of the aluminium flakes in test sample D, a scanning electron microscope (SEM) was used to obtain a highly magnified image of the paint. An SEM creates a high-resolution image by scanning a beam of electrons across a sample inside a vacuum chamber, while a sensor

measures the magnitude of electrons returning from the sample. A sample of paint was placed inside the microscope, and it was found that the electrons would not travel through the paint binder, so observation of the flakes from the top surface was impossible. To overcome this observation difficulty, a small section of paint was lifted away from an offcut of the painted sample and placed in the microscope. This process of lifting the small section away from the main body of paint created a fractured edge along a small section of the paint. This fractured edge provides a useful surface for investigation in the SEM because it created flakes that protrude from the edge of the paint binder. By placing this small paint sample in the microscope, and rotating the stage, an image of the edge of the paint was obtained, which shows the protruding metallic flakes. A backscattered electron sensor was connected to the pole piece inside the microscope, aiding the determination of the materials of different chemical composition by creating visible variances in contrast. Figure 5.1 shows the edge of the paint sliver, with the protruding metallic flakes clearly visible. The lower portion of the image shows the conductive carbon tape used to adhere the paint to the sample holder in the microscope, while the upper portion of the image shows the top surface of the paint, which is smooth in appearance. The horizontal band running through the middle of the image is the area of interest and shows the fractured edge of the paint. Aluminium flakes can be observed to be protruding from the fractured edge and appear to be a lighter shade due to the backscattered electron sensor. The size of the flakes observed varies between 40 and 55μm in maximum dimension, while the thickness of the paint layer is approximately 170μm for this sample.

Close inspection of Figure 5.1 reveals the high-density packing of metallic inclusions in the paint under investigation. One may expect that, given the density of aluminium flakes in the sample, a significant alteration in antenna performance would be observed. Each metallic inclusion is a small flake of conductive aluminium, and it is intuitive to conclude that placing such a conductor in the near field of an antenna is likely to produce undesirable side effects.

5.4 Testing Approach

To examine the effect of the various paints on an antenna, the antenna architectures shown in Figure 5.2 were employed. The antenna of Figure 5.2(a) is a rectangular microstrip patch antenna, while Figure 5.2(b) is a bow-tie slot antenna.

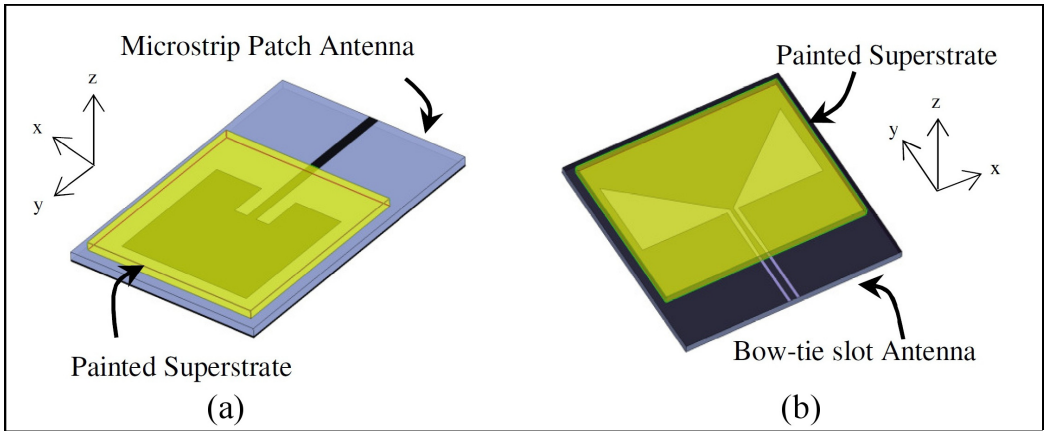

Figure 5.2: Paint test configuration: (a) narrowband antenna and (b) wideband antenna

Patch antennas typically have a narrow impedance bandwidth. They provide unidirectional radiation across a relatively narrow range of frequencies. In contrast, the bow-tie slot antenna has a wide impedance bandwidth and creates bidirectional radiation. These two kinds of antennas are each used in conjunction with removable coverings, which serve a dual purpose. The coverings (or 'superstrates') primarily act as a carrier for the paint, but they also model the scenario of automotive applications, where a radiating element may be concealed under a painted dielectric material. Both antennas are planar, and are appropriately dimensioned to allow either the radiating patch or slot to be covered by the paint sample during testing.

The L1-band GPS frequency of 1.575 GHz was chosen as the target frequency for the narrowband investigation because of the ubiquitous satellite navigation facilities in modern vehicles. The required bandwidth of 20 MHz at 1.575 GHz leads to a narrow percentage bandwidth of 1.3%. To test the effect of paint on such a system, a simple linearly polarised edge-fed square

microstrip patch antenna was designed and fabricated using Ansoft HFSS. Rogers RT/duroid® 5880 material with 0.062' thickness was chosen for the substrate. Identical material in the same thickness was chosen for the superstrates, with the antenna being designed so that its resonance would be close to the GPS L1-band frequency when covered by an unpainted reference sheet of RT/duroid® 5880. The antenna was fabricated, using standard photolithography process, and tested on a VNA and was found to have a centre frequency of 1.583 GHz in the presence of the reference RT/duroid® 5880 superstrate (see Figure 5.2(a)). The slight variation from the centre frequency in the design is attributable to magnification inaccuracies in the photographic stage of fabrication. For the wideband investigation, an asymmetrical bow-tie slot antenna similar to that of Huang and Lin (2006) was designed and fabricated on FR-4 material (see Figure 5.2(b)). It operates from 1.4 to 9.7 GHz, providing a bandwidth of 150% or approximately 7:1. A number of superstrates of equal size were cut from a sheet of Rogers RT/duroid® 5880 material and painted in a specialised facility, each with one of the paints listed in Table 5.1. Two additional samples were set aside for use as control samples. One was left unpainted, while the other retained its original copper cladding to demonstrate the effect of a solid conductive sheet in the near field of an antenna, and enable a comparison of the aluminium flecks of the metallic paints with a continuous conductor. Double-sided adhesive tape was used to hold the superstrates in place during testing. The tape is approximately 0.2 mm thick, and was located in areas of low surface current. The tape was present on the antennas during the measurement of sample A (when no superstrate was present), so any effects of the tape, however slight, were captured in the measurement data. Superstrates of 0.062' (1.575 mm) thickness result in paint samples that are reasonably rigid, and remain flat and straight when placed on the antenna. Extreme care was taken to ensure consistent x-y placement of the superstrates. The input impedance of both the narrowband and wideband antennas was recorded as each sample was placed on each antenna in turn. Changes in gain and radiation pattern caused by the addition of the painted superstrates were evaluated in an anechoic chamber.

It is worth noting that the effect of superstrates on various kinds of planar antennas has been extensively studied in the past, but never with superstrates bearing paint. Superstrate investigations have been conducted both theoretically (Alexopoulos & Jackson 1984; Jackson & Alexopoulos 1985; Yang & Alexopoulos 1987) and practically (Huang & Hsu 1991; Lee, Zaman & Lee 1989), and have considered patch antennas (Shavit 1994), cavity-backed slot antennas (Weihua et al. 2008), and linearly tapered slot antennas (Simons & Lee 1993), among others. They report that careful selection of the permittivity and thickness of the superstrate can enhance the gain (Jackson & Alexopoulos 1985; Weihua et al. 2008), affect the radiation efficiency and input impedance (Shavit 1994), and increase the electrical length of a tapered slot antenna (Simons & Lee 1993). This study used superstrates to enable comparison of the various paints under test, and to provide an approximation of a vehicular antenna mounted behind a painted non-metallic panel. However, the effect of the dielectric slab itself (which is the superstrate) can be assessed by comparison of sample A with sample B. The applied thickness of the paint is very thin relative to the wavelength of operation of the antennas in the frequency range considered here. This poses a challenge for the simulation of such scenarios. Computation time would be significantly increased due to the requirement to increase the mesh density in the plane of the paint to model the thin material accurately. This coupled with the difficulty of accurately determining the electrical properties of a thin layer of paint is the reason this research was conducted entirely by experimental means.

5.5 Results

5.5.1 Narrowband Antenna Results

i) Reflection Coefficient

The measured reflection coefficient of the narrowband antenna of Figure 5.2(a) is shown in Figure 5.3. The black curve shows the performance of the antenna without any superstrate present (representing sample A), and reveals that the antenna was resonant at approximately 1.613 GHz, yet had a narrow impedance bandwidth (defined as greater than 10 dB return loss) of 0.8%. A narrow impedance bandwidth is common for patch antennas. Placing sample B, the unpainted superstrate, on the antenna brought about a shift in resonant frequency due to the addition of the bulk dielectric material above the patch. The minimum of the reflection coefficient was shifted to 1.583 GHz, a shift of 2%, and the bandwidth remained unchanged at 0.8%. Painted samples C through to N were compositions of various paints, with and without primers and topcoats, yet all behaved in a similar way, with centre frequencies ranging from 1.581 to 1.588 GHz, a fairly narrow spread of 0.44%. Interestingly, samples M and N (which featured an electrostatic primer) created a slightly wider bandwidth, of about 0.95%. The effect of samples M and N is examined further in the discussion section of this chapter. The substitution of the copper-clad sample of RT/duroid® 5880, sample O, produced extremely degraded antenna performance, as expected. The majority of the input signal was reflected back into the source by the presence of the conductive metallic sheet over the patch antenna. In addition to the effect of the various paints, some of the observed variation in impedance response between these samples may have been due in part to permittivity tolerances in the RT/duroid® superstrate itself (from which the samples were constructed), and any air gaps that may have arisen between the substrate and superstrate.

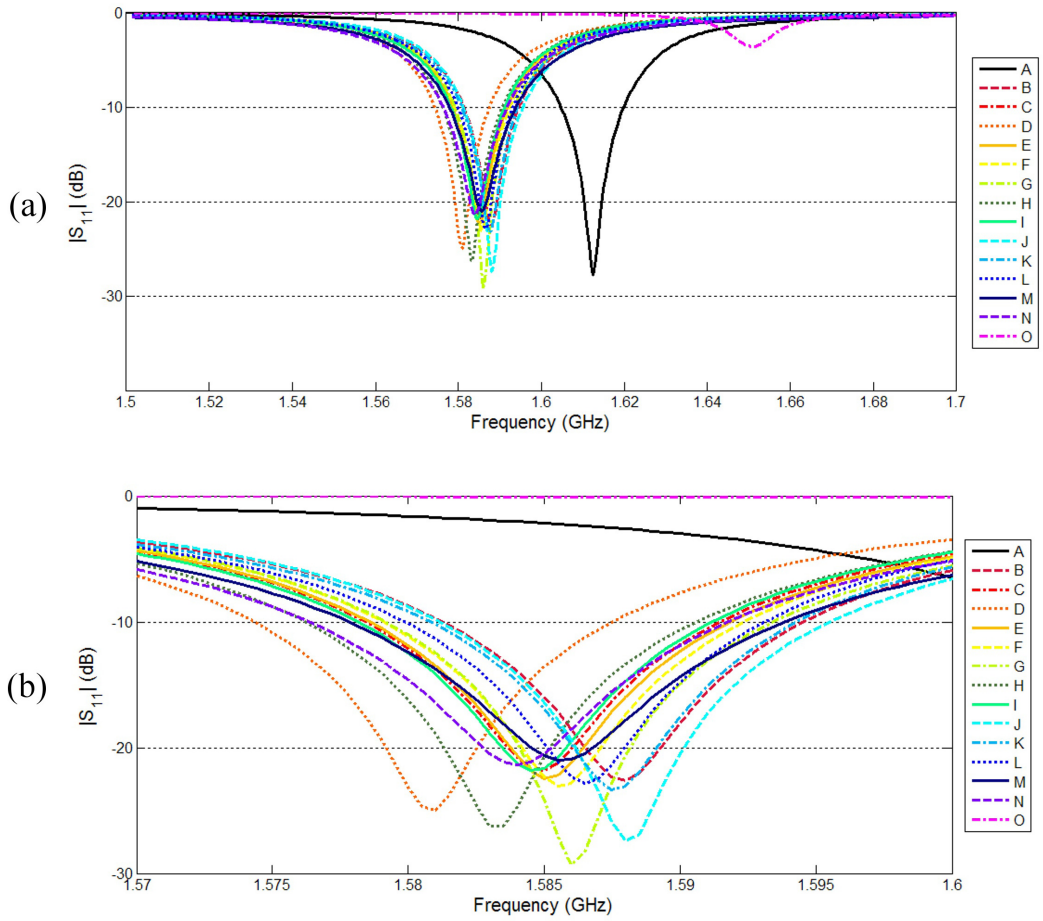

Figure 5.3: Measured reflection coefficient of the narrowband antenna with various superstrates on (a) a wide scale and (b) zoomed to a narrow scale

ii) Radiation Patterns

Figure 5.4 shows the co-polarised and cross-polarised radiation patterns of the patch antenna with various superstrates measured at the relevant centre frequency. The gain was measured by the standard gain substitution method and the plots were normalised to sample A, the maximum of the antenna without a superstrate. The antenna had hemispherical coverage, meaning that a roof-mounted GPS antenna would receive signals from the sky. In general, a large degree of similarity was found between the radiation patterns of the narrowband antenna with the various painted superstrates. The radiation pattern was essentially unchanged. Some variation in shape was evident in the back lobes of the antenna and in the cross-polarised patterns, yet these parts of the radiation contributed little to the received signal, as they were approximately 20 dB down on the main lobe at broadside, making any

differences of low importance. Unsurprisingly, the antenna's radiation performance was significantly degraded by the presence of the copper-clad superstrate (sample O), which catastrophically altered the radiation pattern, and reduced the gain of the antenna by almost 20 dB.

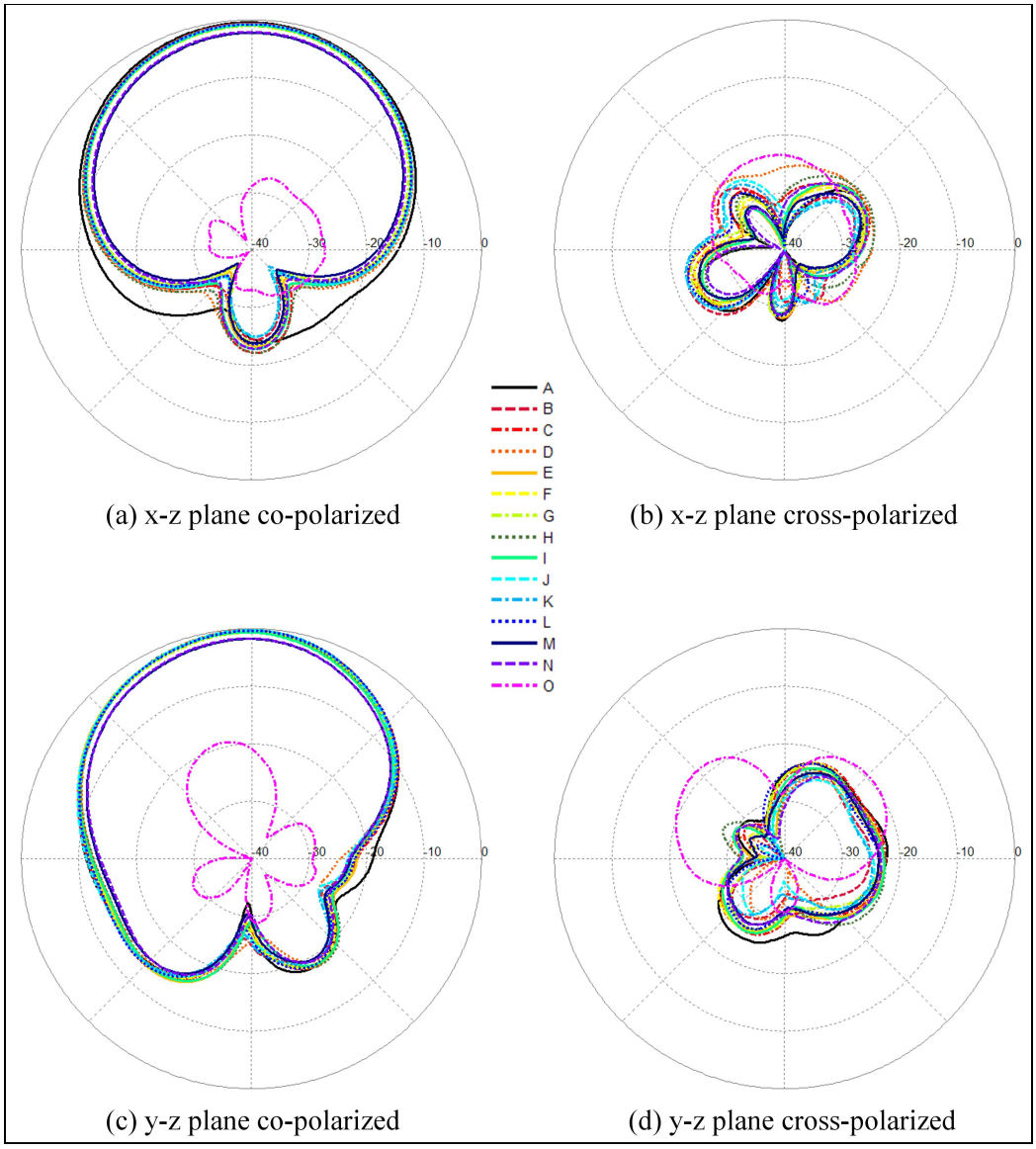

Figure 5.4: Measured radiation patterns of antenna A with superstrates. The measurement is performed at the centre frequency for each sample.

A valuable comparison of the performance of each of the superstrates was provided by examining the maximum gains produced by the narrowband antenna, as displayed in Figure 5.5. The gain is presented here in graphical form with error bars showing the repeatability of the gain measurements,

which was determined to be approximately ± 0.2 dB. The gain of the narrowband antenna without any paint sample present was found to be 8 dBi. The maximum gain produced with the unpainted dielectric superstrate present (sample B) was measured to be 7.9 dBi. Application of various paint types was found to produce a reduction in gain of up to 0.5 dB (samples C to L). Interestingly, samples M and N, bearing a partially conductive electrostatic primer, caused a reduction in antenna gain of approximately 1.5 dB. This was most notable in the main lobe of the co-polarised patterns (see Figure 5.4(a) and (c)). The shape of the radiation pattern was maintained, but at a reduced value of magnitude. The persistence of the pattern suggested minimal change in directivity had taken place. It is possible that the observed gain reduction was caused by a reduced efficiency due to the additional losses associated with the electrostatic primer. Once again, extreme disruption to the antenna's performance was caused by the copper-clad superstrate, as reflected by a large negative value for the gain.

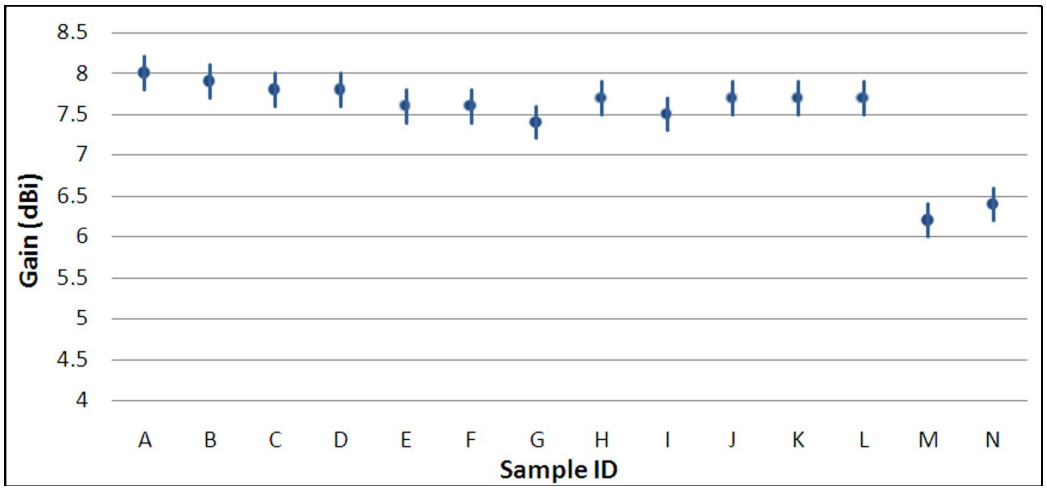

Figure 5.5: Maximum gain of the narrowband antenna with painted superstrates, showing error bars to indicate measurement tolerance. Note that sample O is not presented here as it is out of range (–17.5 dBi). Samples M and N provide a significant gain reduction.

The results indicate that all painted samples produced a reduced value of gain to some degree as no measurements of painted samples exceeded the gain of sample A or sample B, where no paint was present.

5.5.2 Wideband Antenna Results

i) Reflection Coefficient

To determine the input impedance variation created by each paint on a wideband antenna, the bow-tie antenna of Figure 5.2(b) was connected to the V and the reflection coefficient (see Figure 5.6) was measured in the presence of each superstrate. The addition of dielectric material created a band-shifting effect. This shift was dependent upon the permittivity and thickness of the dielectric, and hence was slightly different for each paint sample. The shift appeared to be larger at the upper end of the band, yet the percentage shift was approximately constant. Hence, although the wideband antenna's frequency response was shifted by the paint, the antenna was likely to remain operational at frequencies of interest. The copper-clad sample O was once again found to have extreme consequences on the antenna's impedance matching. Narrow sections of bandwidth existed where $|S_{11}|$ was below –10dB; however, the wideband response was lost.

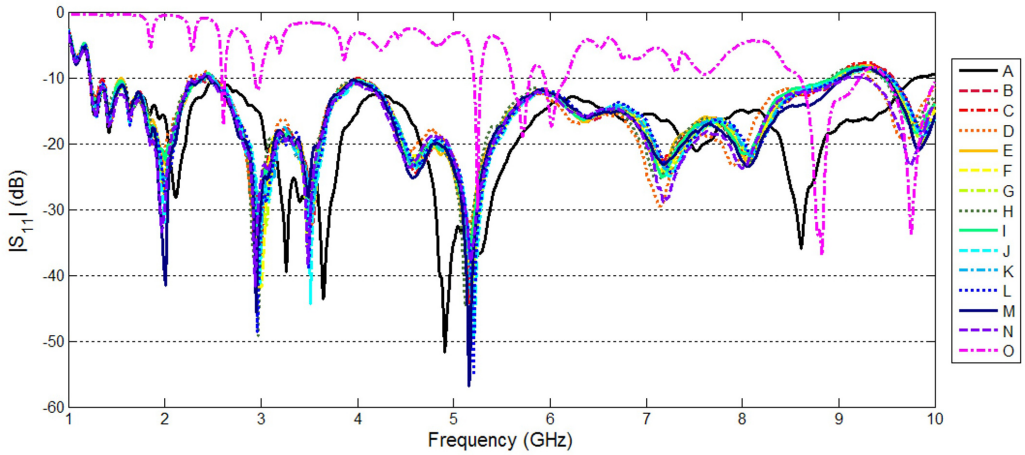

Figure 5.6: Measured reflection coefficient of the wideband antenna with each superstrate

ii) Radiation Patterns

The radiation pattern for the wideband antenna was investigated at numerous points across its bandwidth. Important communication bands in the automotive environment were chosen where possible. The first was the band

reserved for the L1 band of GPS signals broadcast by the orbiting satellites, at 1.575 GHz. The ISM band at 2.4 GHz was next and it has found worldwide application for IEEE 802.15.1 (Bluetooth) and IEEE 802.11b/g/n (wi-fi). The 5.9 GHz band has been reserved in many parts of the world for ITS applications. This includes V2V and V2I communication, primarily for the purpose of transmitting and receiving safety messages. This technology is often referred to as wireless access in vehicular environment (WAVE) or DSRC, with the relevant IEEE standard being 802.11p. The wideband antenna was also characterised near the upper end of its bandwidth, at 9.5 GHz to examine the effect of these paints in the X band.

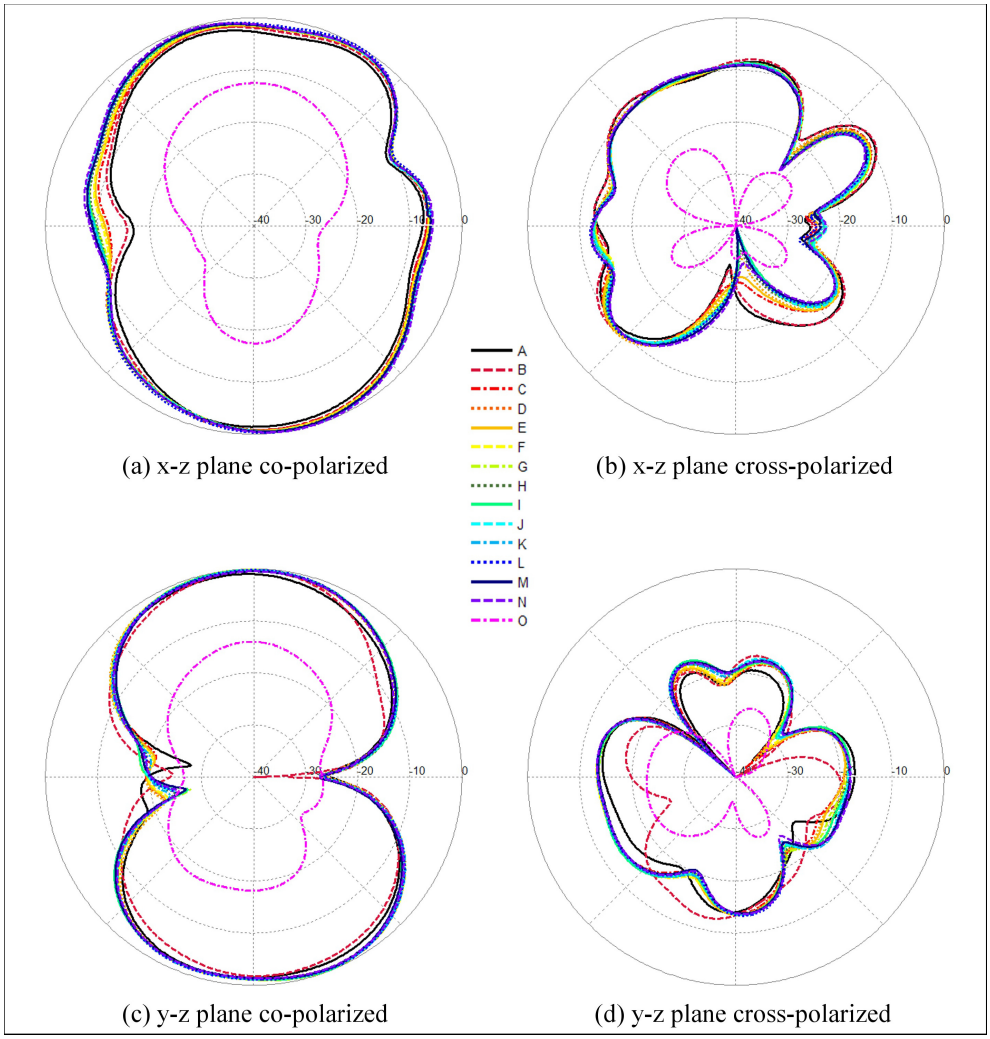

Figure 5.7: Measured radiation patterns of the wideband antenna with each superstrate—1.575 GHz

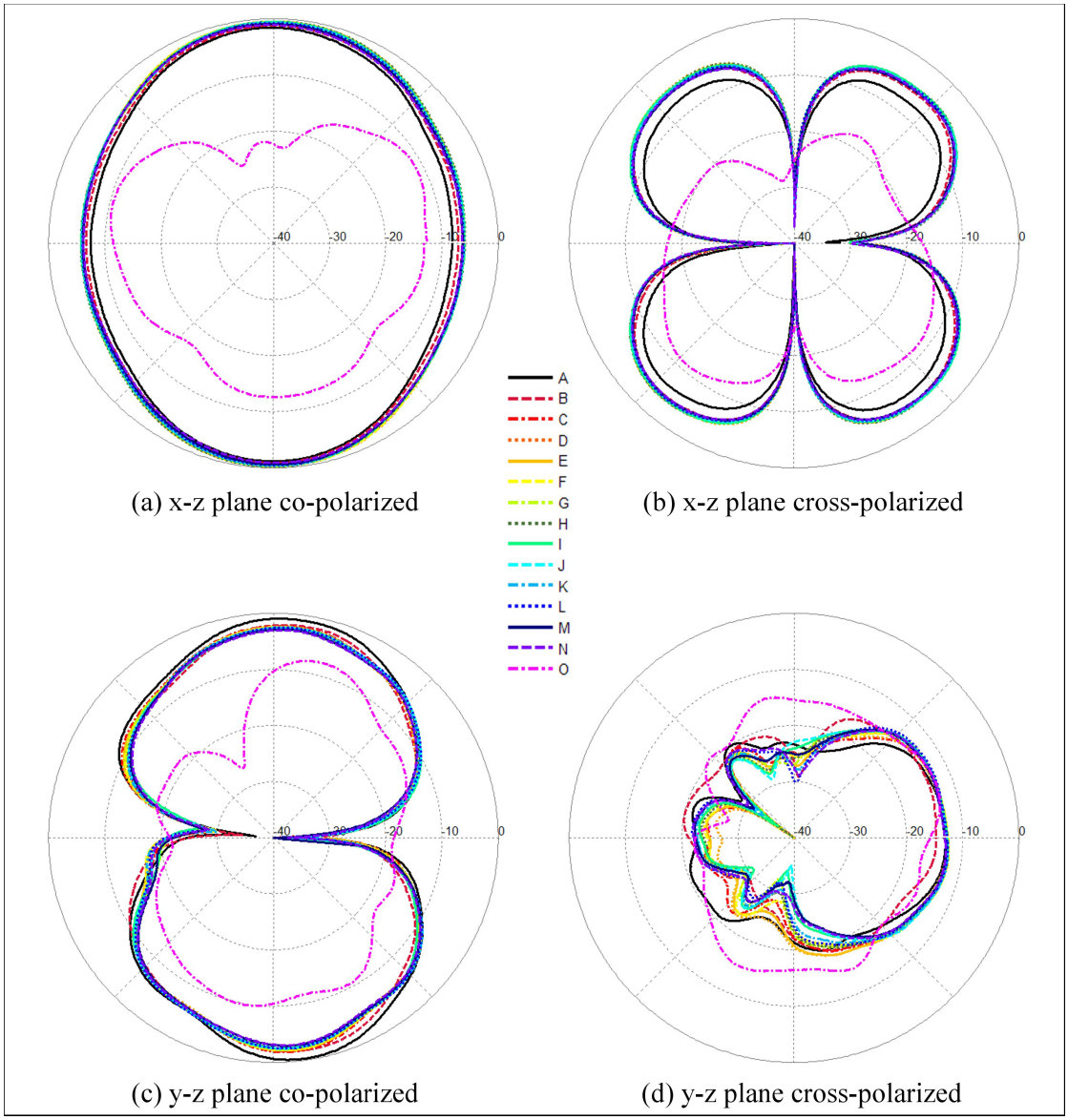

Figure 5.8: Measured radiation patterns of the wideband antenna with each superstrate—2.4 GHz

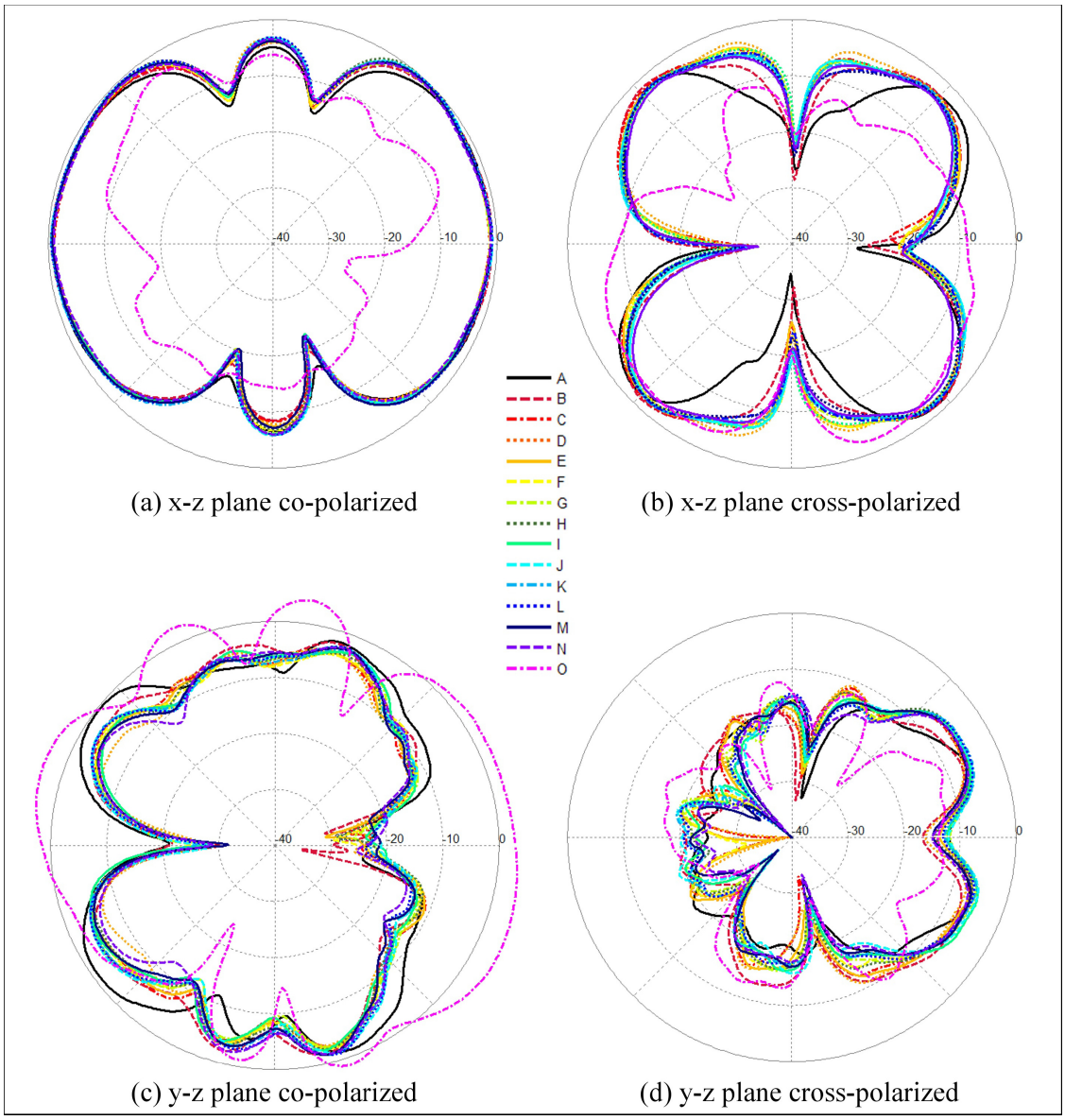

Figure 5.9: Measured radiation patterns of the wideband antenna with each superstrate—5.9 GHz

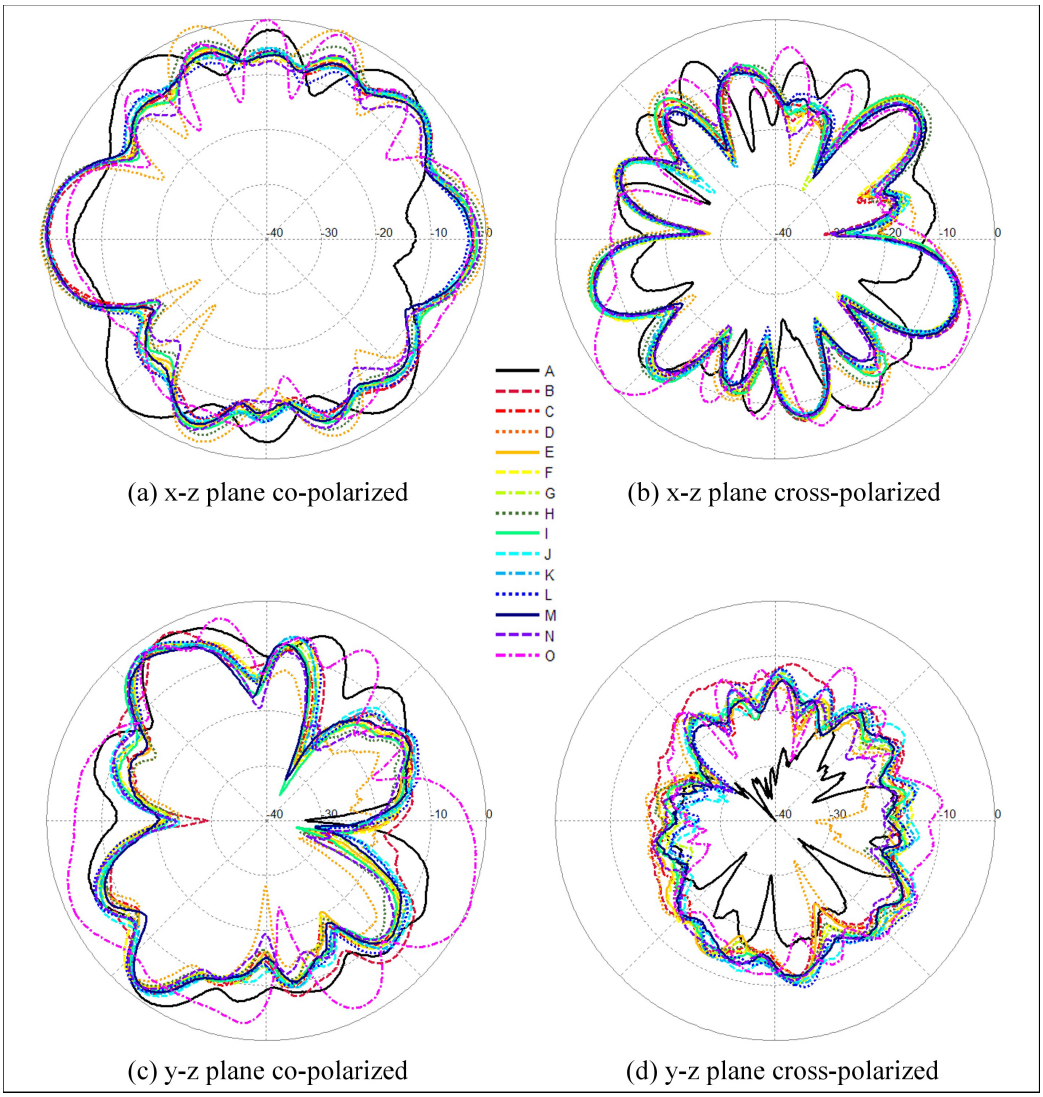

Figure 5.10: Measured radiation patterns of the wideband antenna with each superstrate—9.5 GHz

The radiation pattern for the wideband antenna at 1.575 GHz is shown in Figure 5.7. The antenna radiated a broad beam width pattern in the x-z plane. Each of the superstrates were found to produce approximately equivalent performance as the unpainted superstrate (sample B), with the exception of sample O, which, as previously noted, had a disruptive effect on antenna function.

The wideband antenna's radiation patterns at 2.4 GHz are shown in Figure 5.8. Once again, the copper-clad superstrate of sample O was found to

interfere with proper antenna operation, while the other superstrates were closer in performance. Interestingly, sample A, which denotes the antenna without any superstrate, was found to have slightly lower gain in the x-z plane, higher gain in the y-z plane and lower cross-polarisation levels.

Radiation patterns for the wideband antenna at 5.9 GHz are shown in Figure 5.9. At these frequencies, the effect of painted superstrates on such an antenna were negligible, with each sample producing approximately equivalent gain and radiation characteristics. Figure 5.9 reveals that sample O obtained an impedance match at this frequency, yet the radiation patterns were substantially different to the remainder of the samples. Of particular interest is Figure 5.9(c), where the y-z plane co-polarised pattern level was enhanced in the end-fire directions, even above the level of sample A (to which the figure was normalised). Simulated field results revealed that, at this frequency, a parallel-plate waveguide mode was formed between the copper of the antenna and the copper of the superstrate. This created a narrowband impedance match and led to radiation at the edge of the plates.

The radiation performance of the paint samples of the wideband antenna at 9.5 GHz is illustrated in Figure 5.10. Inspection of the plots reveals ripples in the radiation associated with operating an electrically large structure at these higher frequencies. Once again, samples A and O were found to provide varied performance from the painted superstrates. The departure of sample O from the norm was reduced compared to 1.575, 2.4 and 5.9 GHz.

5.6 Discussion

The addition of paint created an observable shift in the resonant frequency of both the narrowband and wideband antennas. Both polyurethane and water-based paints are dielectric materials; hence, their addition to the structure altered the effective relative permittivity and therefore the electrical size of the antenna itself. This created a shift in frequency, yet due to the thin layer of paint commonly applied, the shift induced by the paint was only small, being less than 1%. A shift of this magnitude is negligible in many wideband

systems, but may have adverse consequences for narrowband antennas. In such narrowband antennas where the overall bandwidth of the antenna itself may be only a few per cent, a shift of up to 1% of the antenna's impedance bandwidth may disrupt operation of the service in the desired frequency range. The impedance bandwidth of the wideband antenna of Figure 5.2(b) was also altered by the addition of the various types of paint, yet its wideband nature means that possible loss of the desired wireless service by shifting out of band was somewhat less pronounced. This led us to conclude that if an unknown paint were to be used to paint a radiating aperture, it would be wise to use an antenna with greater bandwidth than what was required.

With respect to gain and radiation pattern, a great deal of care was taken to ensure the measurements obtained were as accurate as possible. Steps were taken to ensure the temperature of the anechoic chamber remained reasonably consistent throughout the measurement period. The paint samples were tested in succession, and a sweep of an ETS-Lindgren™ 3115 reference horn antenna was performed and recorded in between each measurement of a paint sample. This enabled an assessment of the fidelity of the measurements at a later stage. Examination of the data produced by the horn antenna over the measurement period revealed that the measured value varied by not more than ± 0.2 dB when the frequency was below 3 GHz, and not more than ± 0.4 dB at higher frequencies throughout the period of testing. Hence, although the absolute value of the gain may have been less certain, the data obtained reveals that relative measurements between different paint samples were repeatable within certain limits.

An examination of the results revealed that the presence of the paints, whether metallic or non-metallic, had only a very small effect on the narrowband antenna gain. It was difficult to be certain of the exact change in gain, given the established tolerance of ± 0.2 dB, but it could be observed to be less than approximately 0.5 dB where no electrostatic primer was used. The two-pack polyurethane paints and water-based paints appeared to have similar electromagnetic performance with little significant difference in the antennas' impedance, radiation or gain performance. Likewise, the presence

of a standard primer or clear topcoat had little measurable effect.

Those paints that are classified as metallic achieved this effect by the inclusion of small aluminium ‘flakes’, as mentioned in Section 5.3. The results demonstrated clearly that, despite small variations in gain for each sample, there was no reason to believe that those paints with metallic inclusions altered the performance of the antenna in any significant way.

Therefore, it was found that the metallic paints behaved as dielectrics despite the included metallic particles. The metallic particles were flakes of aluminium and hence electrically conductive; however, they were precluded from creating a bulk conductive material by the material that surrounded them. The electrons were free to move within each individual flake, but these flakes were small (in the order of 50 µm) and isolated from each other by the dielectric paint binder. The end result was that there were no truly free electrons in the metallic paints, and the material behaved like a dielectric in the microwave region. Given the small size of the particles, a very high frequency in the terahertz region would be required to obtain wavelengths comparable to the particles’ dimension and elicit a different response from the material to an applied electromagnetic wave.

Various metallic paint samples were investigated in the water-based chemistry, as it is the dominant OEM automotive paint type. Only one metallic and non-metallic sample was tested from the polyurethane chemistry. The metallic polyurethane paint (sample D) was the thickest paint in the test, by a factor as high as six, yet it was found to have a smaller value of gain reduction than many of the other metallic paints, which had been applied in thinner layers. This is due to difference in the dielectric constant between water based and urethane (Lower dielectric constant than water-based paints) based paints as discussed by Otoshi et al. (1999) in his extensive study of the dielectric constants for number of paints and primers including water and urethane based systems.

Paint samples M and N, which bore an electrostatic primer, provided a clearly measurable change in the performance of the narrowband antenna. An examination of the plot of $|S_{11}|$ showed a slightly wider bandwidth when samples M and N were present. The electrostatic primer present on these samples was intended to provide a level of DC conductivity to enable electrostatic painting. However, at these microwave frequencies, the electrostatic primer behaved like a lossy dielectric rather than a conductor. This led to a reduction in the antenna's quality factor, and a consequent widening of the antenna's bandwidth. The radiation pattern of the narrowband antenna and corresponding gain plot revealed that samples M and N provided a similar radiation pattern in terms of shape, but at a reduced value of gain. Measured gains were approximately 1.5 dB lower than in non-electrostatic samples. The persistence of the radiation pattern suggested that the directivity of the radiating structure may have been unchanged. Recalling that antenna gain is the product of efficiency and directivity, it may be that the lower gain value was due to a reduced efficiency. This could be because of the additional lossy layer of electrostatic primer. Antenna efficiency measurements are very difficult to perform accurately, and no attempt to measure the efficiency directly was made in this work. However, it would seem that the effect of the addition of the partially conductive electrostatic primer was a widening of the impedance bandwidth and reduction in the gain of the narrowband antenna. The effects of the electrostatic primer were less prominent on the wideband antenna, with no significant gain reduction being visible in the presence of samples M and N.

None of the paint samples provided truly disruptive shielding, as found when the copper-clad superstrate of sample O was applied to the antennas. The highly conductive layer of copper on the surface of this superstrate had extreme effects on the impedance bandwidth, gain and radiation of both antennas. Under the copper-clad superstrate of sample O, the narrowband antenna's impedance never matched to the 50 Ω line, as shown by the curve of $|S_{11}|$ remaining above the 10 dB line as can be seen in Figure 5.6. This resulted in very poor radiation performance, with the co-polarised patterns returning highly negative values of gain.

Interestingly, on the wideband antenna, the copper-clad superstrate did achieve matched impedance at several frequencies at the upper end of the band. An examination of the simulated fields at these frequencies revealed that this was likely a consequence of the energy guided down the CPW coupling into a mode other than the usual radiation mode. This appeared to be a parallel-plate transmission line mode in between the metallic ground plane of the antenna and the copper cladding above, with the wave therefore propagating inside the Rogers RT/duroid® 5880 material of the superstrate and radiating from the superstrate edges.

For many applications, it might be useful to simulate paints in electromagnetic software packages. The paint layer was very thin relative to the wavelength of interest, which posed a challenge for the simulation of such scenarios due to the requirement to increase the mesh density in the plane of the paint to model the thin material accurately. A few investigative simulations were performed using the CST Microwave Studio® Transient solver and the results indicated findings similar to those reported here, but required manual addition of local mesh, which resulted in 30% more mesh cells than with no paint layer present. Note that for those paints that contained metallic flakes, it was not necessary to model the individual conductive particles since the material behaved like a bulk dielectric.

5.7 Conclusion

The addition of superstrates painted with automotive-specific paints caused a shift in the frequency characteristics of both narrowband and wideband antennas. This was due to the change in the effective relative permittivity of the space surrounding the antenna. Hence, the magnitude of the shift was a function of the dielectric constant of the paint and the thickness with which it was applied. The consequences of frequency shifting may be significant for narrowband antennas where a small shift could lead to loss of the desired communications service. If an unknown paint is to be applied to an antenna, it

would be advisable to employ an antenna with greater than required bandwidth.

The automotive metallic paints examined appeared to behave as dielectrics, despite densely packed metallic inclusions. The size of each flake was small relative to the wavelength of interest, and the paint binder prevented electron flow between adjacent flakes under an applied electromagnetic field. The presence of metallic and non-metallic paint on the antenna superstrate led to a very slight gain reduction on the narrowband antenna, less than or equal to 0.5 dB.

Electrostatic primers are used globally in automotive production lines, yet to the authors' knowledge, no previous work in the literature has considered their effect on antennas. This work found that they may cause a reduction in the gain of an antenna, due to the partially conductive nature of this primer. Our test showed a gain reduction of approximately 1.5 dB when applied to the narrowband patch antenna.

5.8 References

- Alexopoulos, N & Jackson, D 1984, 'Fundamental superstrate (cover) effects on printed circuit antennas', *IEEE Transactions on Antennas and Propagation*, vol. 32, no. 8, pp. 807–816.
- Cerretelli, M & Gentili, GB, 2007, 'Progress in compact multifunction automotive antennas', in *International Conference on Electromagnetics in Advanced Applications, ICEAA 2007*, pp. 93–96.
- Chu, T & Semplak, T 1976, 'A note on painted reflecting surfaces', *IEEE Transactions on Antennas and Propagation*, vol. 24, pp. 99–101.
- Gschwendtner, E & Wiesbeck, W 2003, 'Ultra-broadband car antennas for communications and navigation applications', *IEEE Transactions on Antennas and Propagation*, vol. 51, no. 8, pp. 2020–2028.
- Hoare, E & Hill, R 2000, 'System requirements for automotive radar antennas', in *IEE Colloquium on Antennas for Automotives*, pp. 1/1–111.
- Hombach, V & Kuhn, E 1989, 'Complete dual-offset reflector antenna analysis including near-field paint-layer and CFRP-structure effects', *IEEE Transactions on Antennas and Propagation*, vol. 37, no. 9, pp. 1093–1101.
- Huang, C & Lin, D 2006, 'CPW-fed bow-tie slot antenna for ultra-wideband communications', *Electronics Letters*, vol. 42, no. 19, pp. 1073–1074.
- Huang, C & Hsu, P 1991, 'Superstrate effects on slot-coupled microstrip antennas', *Magnetics IEEE Transactions*, vol. 27, no. 5, pp. 3868–3871.
- Jackson, D & Alexopoulos, N 1985, 'Gain enhancement methods for printed circuit antennas', *Antennas and Propagation IEEE Transactions*, vol. 33, no. 9, pp. 976–987.
- Jensen, WK 1971, *Concealed windshield broadband antenna*, US patent 3,576,576.
- Lambourne, R & Strivens, TA (eds.) 1999, *Paint and surface coatings: theory and practice*, Woodhead Publishing Ltd, pp. 450–457.
- Lee, R Zaman, A & Lee, K 1989, 'Effects of dielectric superstrates on a two-layer electromagnetically coupled patch antenna', in *Antennas and Propagation Society International Symposium*, *AP-S. Digest*, vol 2, pp. 620–623.

- Lindenmeier, H, Hopf, J & Reiter, L 1985, 'Active AM-FM windshield antenna with equivalent performance to the whip now as standard equipment in car production', in *Antennas and Propagation Society International Symposium*, pp. 621–624.
- Lindenmeier, H, Hopf, J & Reiter, L 2007, 'Compact multi-antenna system for cars with electrically invisible phone antennas for SDARS frequencies', in *2nd International ITG Conference on Antennas, INICA '07*, pp. 171–175.
- Low, L Langley, R Breden, R & Callaghan, P 2006, 'Hidden automotive antenna performance and simulation'*, IEEE Transactions on Antennas and Propagation*, vol. 54, no. 12, pp. 3707–3712.
- Lyons, C & Taskin, I 2003, 'A low-cost MMIC based radar sensor for frontal, side or rear automotive anticipatory pre-crash sensing applications', in *Proceedings of the IEEE Intelligent Vehicles Symposium*, *IV*, pp. 688–693.
- Otoshi, T, Cirillo, R & Sosnowski, J 1999, 'Measurements of Complex Dielectric Constants of Paints and Primers for DSN Antennas: Part I*, The Telecommunications and Mission Operations* Progress Report 42-138, April - June 1999,Jet Propulsion Laboratory, Pasadena, California, pp. 1-13.
- Otoshi, T, Cirillo, R & Sosnowski, J 1999, 'Measurements of Complex Dielectric Constants of Paints and Primers for DSN Antennas: Part II*, The Telecommunications and Mission Operations* Progress Report 42-139, April - June 1999,Jet Propulsion Laboratory, Pasadena, California, pp. 1-7.
- Otoshi, T, Rahmat-Samil, Y, Cirillo, R & Sosnowski, J 2001, 'Noise temperature and gain loss due to paints and primers: a case study of DSN antennas'*, IEEE Antennas and Propagation Magazine*, vol. 43, no. 3, pp. 11–28.
- Pell, B, Rowe, W, Sulic, E, Ghorbani, K, John, S, Gupta, R, Zhang, KI & Hughes, B 2008, 'Experimental study of the effect of paint on embedded automotive antennas'*,* in *IEEE Vehicular Technology Conference*, *VTC Spring 2008*, pp. 3057–3061.

- Pfanstiehl, J 1998, *Automotive paint handbook: paint technology for auto enthusiasts and body shop professionals*, HP Books, New York, NY.
- Robinson, A & Livesey, A 2006, *The repair of vehicle bodies*, Butterworth-Heinemann, Oxford, UK.
- Sabatier, C 1995, '2 GHz compact antennas on handsets', in *Antennas and Propagation Society International Symposium, AP-S*, vol. 2, pp. 1136–139.
- Shavit, R 1994, 'Dielectric cover effect on rectangular microstrip antenna array'*, IEEE Transactions on Antennas and Propagation*, vol. 42, no. 8, pp. 1180–1184.
- Simons, RN & Lee, RQ 1993, 'Linearly tapered slot antenna with dielectric superstrate', in *Antennas and Propagation Society International Symposium, AP-S. Digest*, vol. 3, pp. 1482–1485.
- Tan, W, Shen, Z & Shao, Z 2008, 'Radiation of high-gain cavity-backed slot antennas through a two-layer superstrate'*, IEEE Antennas and Propagation Magazine*, vol. 50, no. 3, pp. 78–87.
- Yang, H & Alexopoulos, N 1987, 'Gain enhancement methods for printed circuit antennas through multiple superstrates', *IEEE Transactions on Antennas and Propagation*, vol. 35, no. 7, pp. 860–863.

CHAPTER 6: Rheological Characterisation of Sheet Moulding Compound

6.1 Introduction to Rheology

In this chapter rheological properties of SMC material were studied in order to develop detailed understanding of time and temperature dependent viscosity profile.

Rheology is the science that studies material flow and deformation. This approach is primarily used for the study of materials in a liquid state, but also as solids under conditions in which they respond with plastic flow rather than deforming elastically in response to an applied force such as a typical Newtonian fluid. It applies to materials exhibiting a complex molecular structure; some examples of such materials are foodstuff (jams, pastes, spreads, etc.), polymers (thermoset and thermoplastic), body fluids (blood, lipids, etc.) and other organic and non-organic materials (Bird et al. 1980; 1987; 1989; Barnes 2000; Boger et al 1993; Schowalter 1978; Tanner 1988).

In a typical Newtonian fluid, viscosity can be characterised by a single coefficient at a specific temperature. Although this viscosity is temperature dependent, it is not dependent on the flow rate or the strain rate. Fluids that exhibit this type of behaviour are in the minority. There is a significantly larger class of fluids whose viscosity depends on the strain rate. These fluids are termed non-Newtonian fluids (Tanner 1988). Rheology is generally used to characterise the behaviour of non-Newtonian fluids. This is done by characterising the minimum number of functions that are required to relate stresses with the rate of change of strains or strain rates. For example, fluids such as tomato sauce can have their viscosity reduced by mechanical agitation such as shaking. This is achieved by the different layers moving relative to each other and these movements actually cause the reduction in viscosity. The same cannot be done with other fluids such as honey or water. Tomato sauce exhibits behaviour we call ‘shear thinning’, as an increase in

relative velocity causes a reduction in viscosity. However, other non-Newtonian materials exhibit the opposite behaviour (Schowalter 1978), whereby viscosity increases with relative deformation; these fluids are called 'shear-thickening' or 'dilatant' materials. Viscosity curves for Newtonian, shear-thinning and shear-thickening fluids are shown in Figure 6.1.

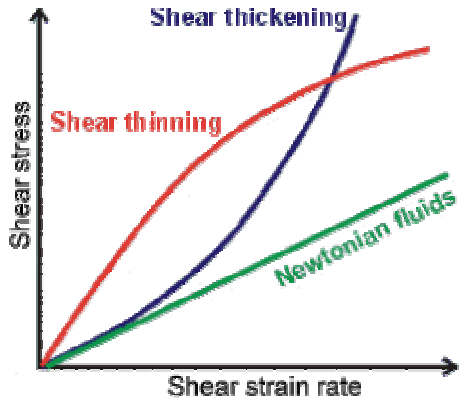

Figure 6.1: Viscosity curves for different fluids © lsbu.ac.uk. with permission

The study of liquids with strain-rate dependent viscosity is commonly known as non-Newtonian fluid mechanics, as it was Sir Isaac Newton who originated the concept of viscosity. Eugene C Bingham, a professor at Lafayette College, was the first person to use the term 'rheology', in the 1920s, after a suggestion by one of his colleagues, Markus Reiner. It is believed that the term was inspired by the aphorism of Simplicius, *panta rei* (everything flows). The term rheometry is often used synonymously with rheometry, particularly by experimentalists. Rheology is used to characterise the relation of the flow/deformation behaviour of materials and their internal structure, such as the orientation and elongation of polymer molecules in polymer melts, and the flow/deformation characterisation of materials that cannot be described by classical fluid mechanics or elasticity.

6.2 Rheometers

The first rheometers were based on an applied stress, which was generated by an arrangement of weights and pulleys, as shown in Figure 6.2. These early designs were quickly superseded by electrically driven motors. These

second-generation rheometers were the first controlled-strain instruments with logarithmic mechanical gearboxes. The most sophisticated rheometers (e.g., the Weissenberg Rheogoniometer) in the 1960s were able to span a shear-rate range typically from 0.001 to 1000 s^{-1} (revolutions per second) (Coussot and Ancey 1996; Barnes et al. 1997; Drew 1983; 1999).

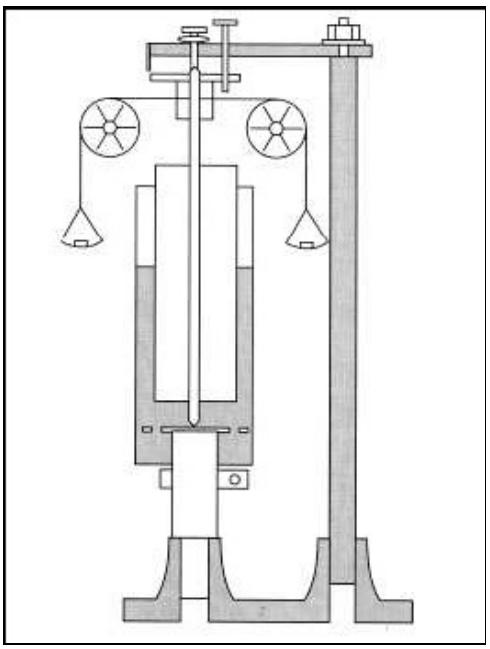

Figure 6.2: Image of early rheometer

Then, in the early 1980s, the first commercial versions of the new generation of electrically driven controlled-stress rheometers appeared. These were based on air bearings that greatly reduced friction, but they also used so-called drag-cup electrical motors. These drag-cup electrical motors allowed the control of stresses to be more easily applied independently of the rotation speed of the test sample. These advancements also brought about new ways of accurately measuring smaller and smaller rotation and rotation rates. With the latest generation of optical-disc technology (see Figure 6.3), rotation rates as low as 0.0000001 s^{-1} (1 revolution in 20 years) can now be measured. This has opened up new avenues, previously unavailable to researchers, to characterise the flow/deformation behaviour of materials.

Figure 6.3: Modern-day rheometer © TA Instruments (with permission)

The anatomy of a modern-day rheometer, as shown in Figure 6.3, is as follows:

1. low-inertia, contact-less, inductive motor assembly without any permanent magnets for accurate torque setting over a wide dynamic range and excellent transient response

2. precision air bearing with thrust and journal surfaces for frictionless support with high axial and radial stiffness
3. inductive, contact-less and multi-layer position sensor assembly for accurate measurement of speed and absolute position
4. precision collett-type chuck for attachment of upper measurement system with minimal axial run-out
5. leads-crew assembly with bespoke pre-tensioned nut and stepper motor for accurate control of measurement sensor position with no backlash
6. linear bearing to support and guide the air bearing and motor assembly
7. integral normal force sensors placed within the instrument mechanics
8. temperature control unit (Peltier plate design shown)
9. universal clamping arrangement designed to accept all available temperature control options
10. push-button acrylic keypad incorporating all key gap setting and control functions with normal force and gap separation display
11. integral electronics and power supply incorporating microprocessor-based control and measurement functions, including torque, speed, position and temperature; data communication is to PC via a high-speed serial link
12. composite outer covers to provide impervious barrier and protect instrument mechanics.

The exact formulation of the SMC used in this project is proprietary information owned by CME; however, generic data can be found in Table 6.1.

Table 6.1: Generic SMC formulation data

Material Data	
Material	*%*
Randomly chopper glass fibers	20-25
Unsaturated polyester	20-30
Calcium carbonate	15-20
Thickener 1	1-4
Thickener 2	1-4
Mold release agent	1-3
Catalyst 1	1-2
Catalyst 2	1-2
Inhibitor	1-2
Water	1-2
Low profile resin	20-30
Pigment	1-3
Styrene	1-3

6.3 The Use of Rheology as a Tool for Understanding SMC Flow in Compression-Moulding Process

Rheology is a part of the fluid dynamics stream and deals with understanding the flow behaviour of complex materials in presence and absence of surfaces (Walters 1975; Truesdell 1974; 1984). Rheological analysis is also used as a tool for understanding the material structure and composition. Chemists use rheology to analyse structures since it is an easier way to characterise molecular structure compared to more complex methods such as scanning electron microscopy, transmission electron microscopy and atomic force microscopy, or other laser-scattering techniques.

Rheological techniques are easy to implement but do not provide conclusive evidence of the structure of the material (Dartevelle 2004). Hence, associated tests such as X-ray diffraction (XRD), differential scanning calorimetry (DSC) and thermo gravimetric analysis (TGA) also need to be performed to validate the results from the rheological tests. There are three basic rheological tools to characterise a material (Huter 2004):

1) shear rheological tests
2) dynamic rheological tests
3) extensional rheological tests.

6.3.1 Shear Rheological Tests

Shear rheological tests are conducted to understand the flow behaviour and structural changes induced in a material in the presence of surfaces. The aim of shear rheological studies is to determine the shear viscosity of the material. The magnitude of shear viscosity helps to estimate the energy losses associated with the transmission through the material. Structural information can also be generated using shear rheological tests (Barnes 2000; Barnes et al. 1997).

The application of a shear field causes the material to deform. The deformation gradient within the material is a function of the structure of the material. Hence, by studying the trend of the shear rheological profile, useful information about the structure of the material can be generated. In addition, the material would have standard recoil against any driving force (Newton's third law), and this recoil behaviour also changes with the structure of the material. For example, in the case of water, the shear viscosity profile has a linear trend (plot of shear stress against shear rate, as shown in the Newtonian fluids trend in Figure 6.1). This structurally indicates that water molecules tend to move together on application of a shear force field; hence, there is no phase lag between the applied shear and the generated shear rate (or velocity profile) within the material.

6.3.2 Dynamic Rheology

Dynamic rheology is a good rheological tool for analysis of material structure (Zdunkowski and Bott 2003). A periodic oscillatory frequency is applied to the material and the rheological response is measured and analysed. The application of a dynamic periodic frequency results in the development of a vibratory field within the material. The vibrations result in the generation of frequencies, which are a function of the inherent molecular structure of the material. The process is very similar to analytic spectroscopic techniques

used to analyse structure. Dynamic rheological tests can be either large amplitude oscillatory shear (LAOS) or small amplitude oscillatory shear (SAOS) tests. These two types of tests can be performed within the linear region or in the nonlinear region. The difference between the two tests is that, in the linear region, the structure of the material does not change permanently. The material eventually recovers its original structure over time. In the nonlinear region, the material experiences a permanent deformation. The application of LAOS results in a response that is a function of the overall structure of the material (macro structure). The use of SAOS specifically focuses on smaller length structures/molecule chains within the material and provides useful information about the microstructure of the material. For example, in the case of a branched polymer (with low branching density), the application of LAOS would not reveal the branching existing within the polymer matrix since LAOS would have an amplitude and frequency that would be larger than the branching chain length. Therefore, use of SAOS would be more appropriate to determine the structure of such a polymer.

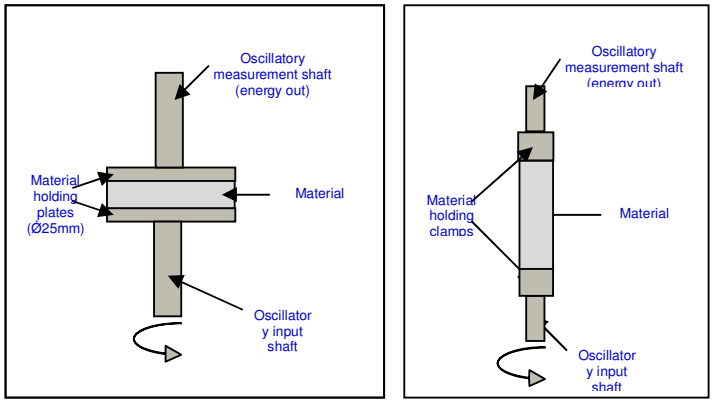

Figure 6.4: LAOS and SAOS test set-up

6.3.3 Extensional Rheology

Extensional rheology is the best rheological technique for analysing the structure of the material (Barnes 2000). The extensional behaviour of the material is noticeable only when there is a complete absence of surfaces. Hence, the rheological response is solely dependent on the inherent structure of the material. In this rheological technique, first, a deformation gradient is

applied, and then, the gradual (speed can vary) relaxation of the deformation gradient provides information about the microstructure of the material. A part of the relaxation response of the material is due to the applied shear in the presence of a surface. In addition, some micro-structural irreversibility is induced in the material during shear rheological tests. In the case of the extensional rheological test, a deformation gradient is generated due to the stretching of the material and the propagation of the gradient across the material is studied. Hence, this test is better and more sensitive to changes in structure of the material. Interestingly, there is a quantitative relation between the extensional viscosity and the shear viscosity of the material. Physically, when the material is experiencing a shear deformation gradient, there is an extension effect at the molecular level and vice versa; hence, the two viscosity behaviours are related. For example, in the case of a linear polymer with a polar group in its form, the shear rheological behaviour would not reflect the effect of the presence of the polar group in the polymer. In the case of extensional rheology, the transferability of the extensional gradient is a function of the mobility of the chain, which in turn would depend on the polarity of the material (meaning the presence of polar groups). Hence, the observed rheological profile can be used to determine the degree of polar groups and the chain mobility (in terms of length) using a suitable extensional viscosity model (Barnes 2000; Barnes et al. 1997).

6.4 Rheology of Polymers and Filled Polymers (Thermosetting Polymers)

The rheological testing of polymers uses the same principles and tools as explained in Section 6.3. The only specific difference in the rheological response is due to the viscoelastic nature of the polymeric materials and the complex architecture at molecular chains. The rheological behaviour of the polymers can be categorised into three basic types:

1) response of a thermoplastic polymer
2) response of a thermosetting polymer
3) response of a filled polymer.

6.4.1 Response of Thermoplastic Polymers

Thermoplastic polymers are characterised by the presence of a shear-thinning behaviour, Newtonian plateaus (regions of constant viscosity) at higher and lower shear rates and frequency, an increasing trend of G' and G'' with occurrence of crossover at a frequency dependent on the structure of the material, a linear extensional viscosity profile, adherence to Trouton's ratio (extensional viscosity/shear viscosity = 3, for Newtonian fluid, and greater than 3 for non-Newtonian polymer melts), and typical slope patterns for the complex viscosity and shear viscosity (log 2 and log 1 slopes). Nonlinearity arises in the rheological response of thermoplastic polymers due to temperature (causing degradation and hence chain scission), branching of polymers, and use of fillers and initiators.

6.4.2 Response of Thermosetting Polymers

The rheological response of the thermosetting polymers is very similar to that of the thermoplastic polymers, with the exception of the curing of thermosetting polymers, which is dependent on time and temperature. The thermosetting polymers are like a combination of two different thermoplastic polymers before and after curing respectively. Before curing, the behaviour is more like a linear thermoplastic polymer. As the curing process is initiated, the polymer chains attain more mobility and the required activation energy to branch or, rather, to recombine among themselves is reduced. At the start of the curing process, viscosity typically reduces, reaching a minimum just before cross-linking starts, and then rapidly increases as the viscoelastic material turns into solid, fully cured material. This process results in an increase in the chain length and causes the formation of a network type of structure, characterised by a decrease in free monomers (see Figure 6.5) (Barnes 2000; Barnes et al. 1997). Hence, the application of a shear, dynamic, extensional field on the material would also provide the activation energy needed for curing (if applied for a sufficient period).

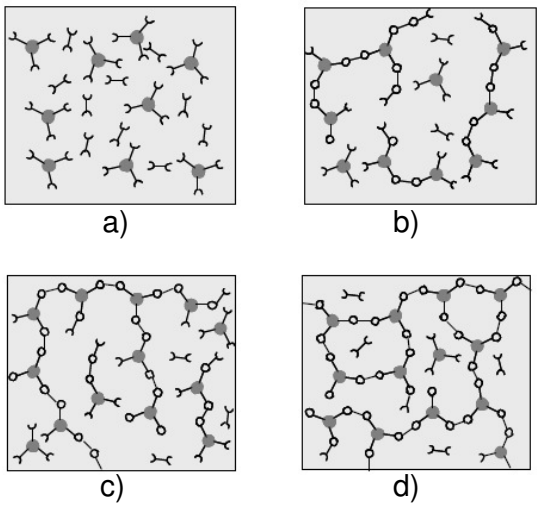

Figure 6.5: Schematical representation of structural development during thermoset curing: a) uncured resin, b) early cure stage of resin, c) gel point and d) fully cured resin with some unreached two-functional and three-functional monomers

6.4.3 Response of a Filled Polymer

The rheological response of the filled polymer as compared to an unfilled polymer changes because of the reduction in free volume of the material due to addition of a filler. The addition of filler improves the solid-like behaviour of the material and hence increases the resistance to flow, as characterised by an increase in shear viscosity and melt strength (Barnes et al. 1997).

The addition of a filler also generates a host of other effects within the material, such as formation of percolation networks (a 3D network of polymer and filler that resists any further addition of filler or polymer to the network), non-idealities at low and high frequencies characterised by the absence of Newtonian plateaus in both cases, generation of a yield stress due to improved elasticity because of the addition of a filler in the matrix, and changes in the relaxation time of the material, characterised by nonlinear areas in the complex viscosity regime (Barnes 2000).

6.5 Rheological Testing of SMC

The characterisation of the SMC material was carried out using the ARES 2000 and the RSI Orchestrator software. The aim of the characterisation studies was to determine the effect of shear stress induced in the material on the embedded antenna. A Maxwell spring-dashpot model was associated with the conducted rheological tests to explain the experimentally observed shear stress, viscosity and relaxation profiles. The SMC charge is a thermosetting material filled with randomly chopped glass fibres with an average length of 25 mm. In addition, $CaCO_3$ was used in powdered form along with the glass fibres. Initially, a time sweep test was conducted on the SMC charge to determine the stability of the material at a set temperature (similar to actual conditions).

6.5.1 Time Sweep Test

The time sweep test is used to perform the stability analysis of the material. If the material is unstable or degrades with time, then a shift to lower values for G' or G' would be observed in the time sweep graph. Physically, the shift to a lower value denotes chain scission and degradation. The material under a degraded condition has very little resistance to flow and has very limited ability to store energy (due to smaller chains); hence, both G' and G' will trend down. The time sweep test is normally conducted in the linear viscoelastic region, which means that the application of a force or a stress only temporarily changes the structure of the material, and once the force is released, the material reverts back to its original state. The idea of performing a rheological test in the linear viscoelastic region has the following benefits:

1) Structural analysis of the material is easier in the linear viscoelastic region.
2) The effect of processing conditions on the material is a function of only the set experimental conditions and does not depend on shear-induced structural changes.
3) Finally, it is easier to detect the presence of yield stress and material degradation.

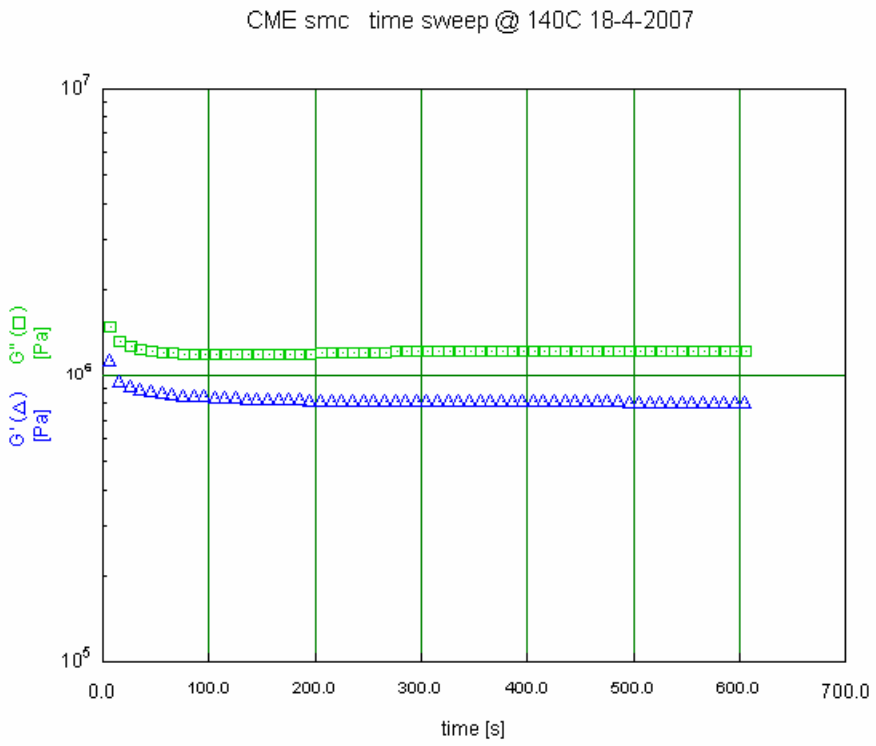

Figure 6.6: Time sweep test at 140 ℃

As shown in Figure 6.6, the values of G' and G' were almost constant with changes in time (from 0 to 600 seconds). The following result shows that the material under consideration did not degrade for at least a period of 600 seconds. There was no chain scission or yield stress generation within the material. Figure 6.7 confirms that the material's gel point was independent of frequency, as confirmed by Barnes et al. (2000) and Bird, Curtis and Armstrong (1989). We observed that the minimum viscosity of about 12 Pa-s was attained at the highest heat-up rate of 40 ºC/minute (see Figure 6.8).

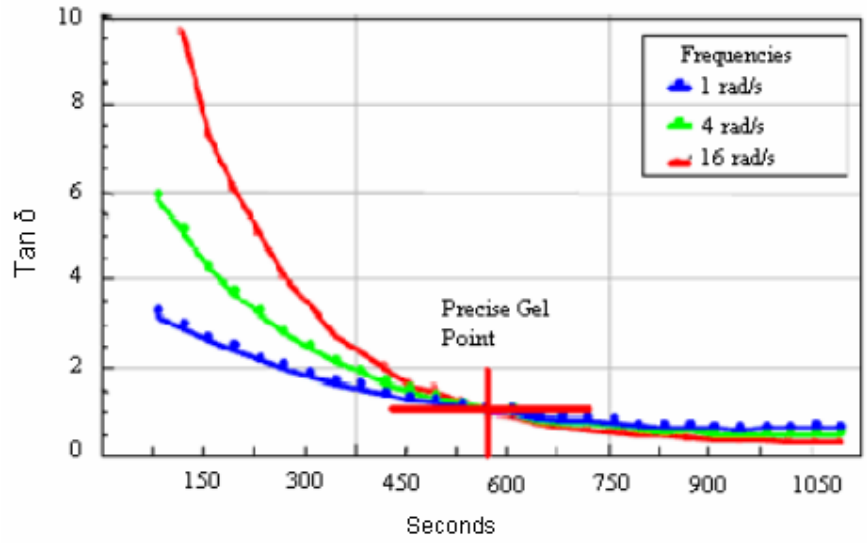

Figure 6.7: Gel point of SMC

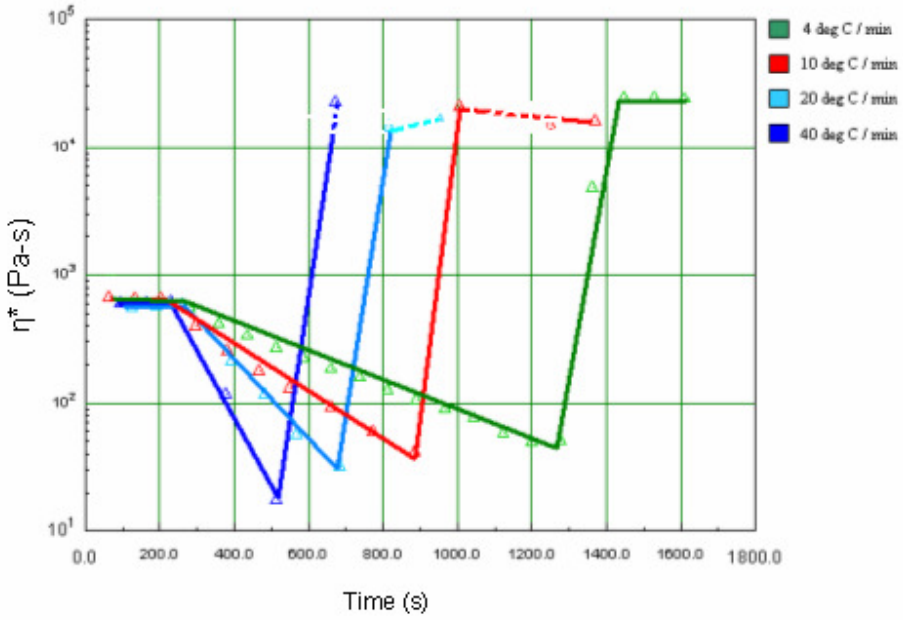

Figure 6.8: Viscosity v. heat-up rate

6.5.2 Shear Rheological Test

Viscosity profiling of the SMC was performed and the results are shown in Figure 6.9. SMC is a non-Newtonian fluid, that is, its viscosity is not a fixed value but is dependent upon the degree of shear to which it is exposed. As expected, shear thinning was observed where the viscosity decreased with an increasing shear rate; hence, a single viscosity value could be meaningless.

Instead, a 'flow curve' of viscosity against shear rate was required, from which the value at a shear rate relevant to the process or product usage conditions could be read.

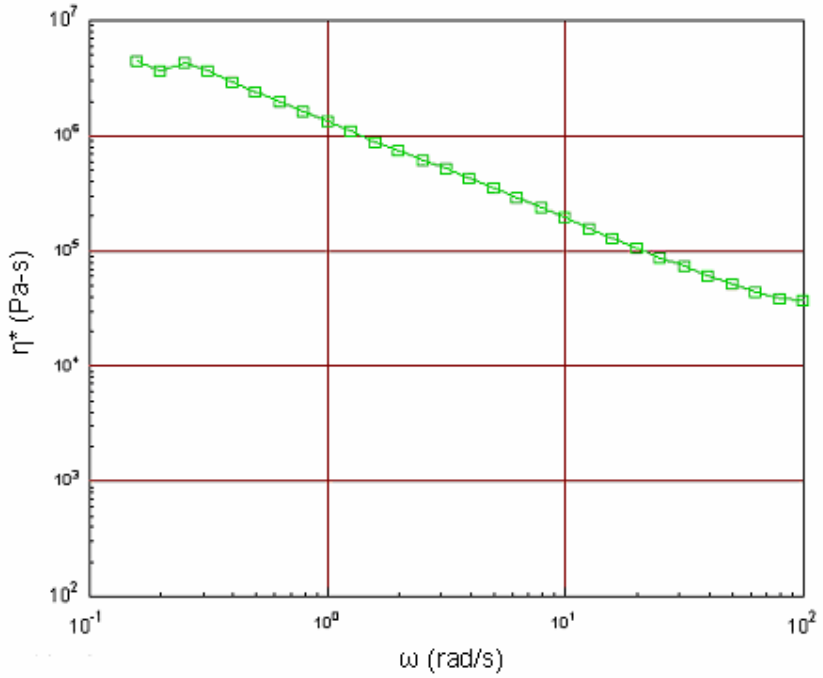

Figure 6.9: Viscosity profile for SMC

The graph in Figure 6.9 can also be used to determine the zero-shear viscosity of SMC, the viscosity of SMC when it is effectively at rest (ω = 0). This parameter is very important as it indicates material stability and it is a sensitive indicator of changes such as aging or changes in the SMC formulation or process used to manufacture it. Therefore, this characteristic is commonly used for SMC quality control purposes in the manufacturing industry.

6.5.3 Dynamic Rheological Test

Dynamic testing was performed using curing profiles, as shown in Figure 6.10:

(a) The test sample was held at 30 ºC for x1 seconds (conditioning stage).

(b) The temperature was increased to the appropriate level in x2 seconds (temperature increase to curing stage).

(c) The temperature was maintained at a set level for x3 seconds (curing stage).

(d) The temperature was reduced to 30 ºC in x4 seconds (cooling down stage).

While the samples were undergoing these set temperature profiles, observations were concurrently recorded for elastic (G') and loss (G'') moduli. The cure profiles used in the study were based on recommendations from the industry partner.

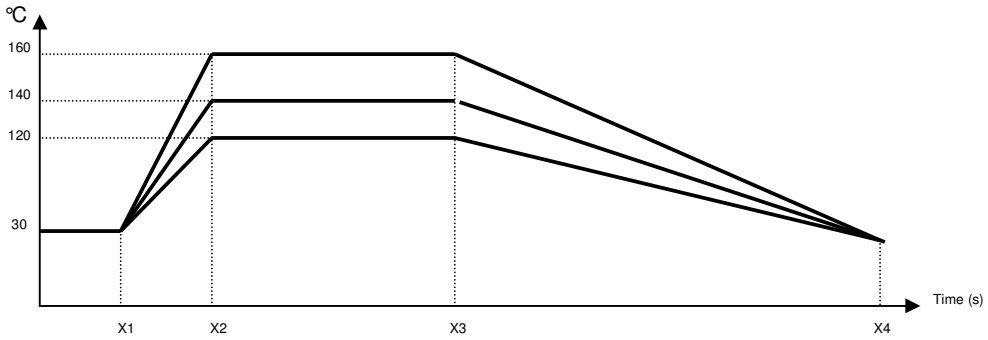

Figure 6.10: Curing profiles used

The viscosity/temperature relationship for SMC exhibited an inverse relationship with temperature, where the viscosity fell as the temperature increased (the heat-up rate is shown as the slope between x1 and x2 in Figure 6.10) as per the results obtained in Figure 6.11. From these results, it was easy to identify the crossover points for G' and G'' for each curing profile. The significance of the crossover point was that it indicated when the cross-linking/gelling of the composite matrix started. These results for viscosity-temperature profiles were obtained using defined imposed shear conditions relevant to the process.

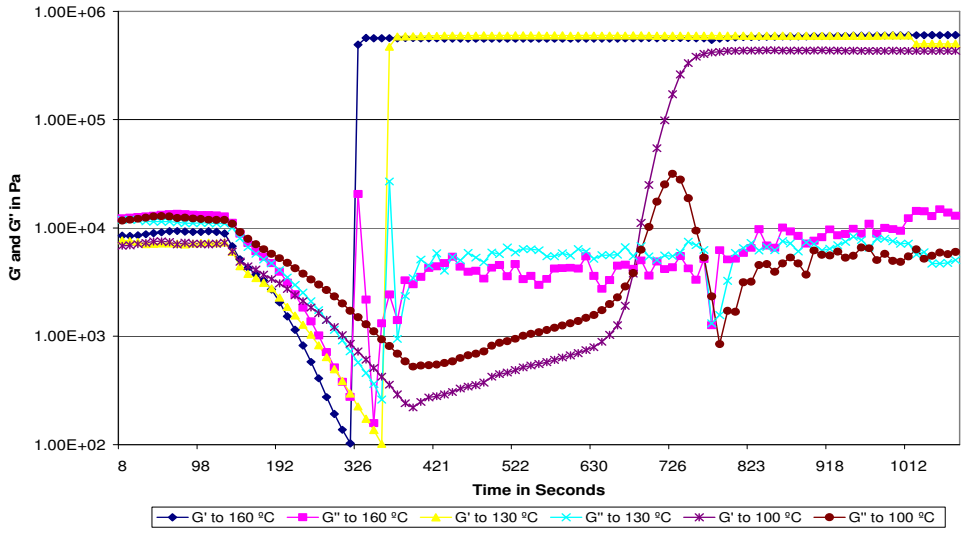

Figure 6.11: G' and G'' for SMC for 3 different curing profiles

6.6 Time–Temperature Superposition

Barnes, Hutton and Walters (1997) and Barnes (2000) have shown experimentally that the elastic modulus (E) of a polymer is influenced by the load and the response time. Time–temperature superposition (TTS) implies that the response time function of the elastic modulus at a certain temperature resembles the shape of the same functions of adjacent temperatures. Curves obtained at one temperature can be shifted to overlap with adjacent curves, as long as the data sets did not suffer from aging effects during the test time.

m = m' + km"

$$\eta = \eta_0 * \exp(m'/T)$$

$$\eta = m"*\exp(2\pi/\omega)$$

$$\eta = \eta_0 \exp(m)$$

where m' is the activation energy to flow (function of temperature)

m" is the slope, which denotes the dependency of shear viscosity on frequency

m is the overall slope parameter taking into effect the temperature and frequency dependency

η is the shear viscosity

η_0 is the zero-shear viscosity

$2\pi/\omega$ is the angular frequency

The above equations can be used for the generation of master curves for shear viscosity. The process is as follows. It is known that the shear viscosity follows an Arrhenius kind of profile mathematically; hence, the slope or the activation energy for flow (represented by m with respect to temperature) remains constant. Once m is calculated by curve-fitting techniques, the data can be shifted with respect to temperature easily. The next point is to shift the data with respect to frequency or a time index. To convert the frequency into time, we divide 2π by frequency ($2\pi/\omega$). Since frequency is in radiant/second and 2*π*r is the circumference covered with this frequency, (2*π*r/ω*r) would give the time required to traverse the circumference at the given frequency, leaving us with 2*π/ω. Once the slope parameters are calculated, the next step is to make a linear function, combining the two slope parameters into one. Once a single slope parameter is calculated, the data can be shifted easily using the single slope parameter.

TTS was used for the generation of master curves. The reason for conducting this process was to extrapolate the observed rheological trend of the material to lower or higher temperatures and/or frequencies. This way, the behaviour of the material could be predicted at different temperatures and frequencies/shear rates without the need for physical testing, which requires the use of significant additional time and cost. In addition, at times, it was not possible to generate data points at very low and high frequencies due to non-responsiveness or nonlinearity of the material, and hence TTS could help to predict the material behaviour in such circumstances.

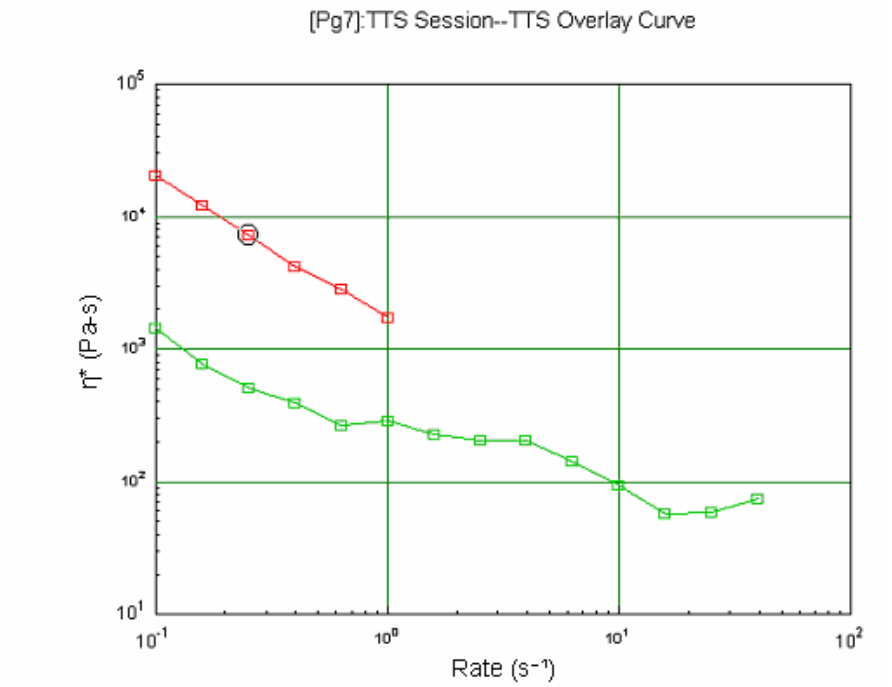

(a)

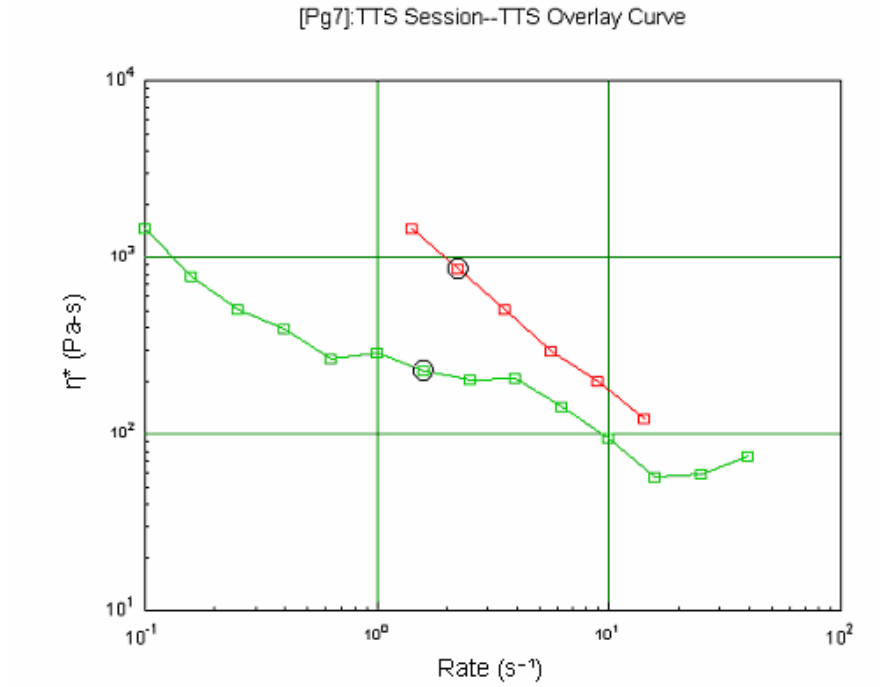

(b)

Figure 6.12: TTS curves for SMC: (a) viscosity profile at 100 ℃ (red curve) and 120 ℃ (green curve) and (b) viscosity profile shifted for 100 ℃ (red curve)

The two curves in Figure 6.12(a) show the shear viscosity profile of the material at two different temperatures: 100 °C and 120 °C. As can be observed in the figure, the shear viscosity of the material reduced with frequency and temperature (indicative of the shear-thinning behaviour). However, the shear viscosity of the material at 100 °C started and finished off very quickly, and hence quantitative comparisons with the viscosity profile at 120 °C were difficult. For example, as shown by the red curve in Figure 6.12(a), it was evident that the viscosity of the material at the two different temperatures would intersect at some point (red curve would cross with green curve), but it was difficult to analyse the exact point of intersection. However, after the TTS shift for the shear viscosity curve at 100 °C, it was found that the intersection of the shear viscosity profile would be around the frequency range of 30–35 rad/sec. In addition, it could be said that the shear viscosity profiles would intersect around the region where curing began to start, as indicated by the abrupt rise in viscosity at higher frequencies (around 20 rad/second) for the 120 °C curve. In addition, the shifted viscosity profile now showed that the zero-shear viscosity of the material was much higher compared to what was observed in the experiment. The shear viscosity shift factors increased linearly with the temperature, indicating that, with the increase in temperature, the material approached the curing stage and hence the flow activation energy increased accordingly.

6.7 Cole–Cole Plots

The Cole–Cole plot is a plot between the complex part and the real part of complex viscosity (G' and G"). These plots could be used to study the changes in structure of the material with changes in temperature and frequency. Specifically in cases where the zero-shear viscosity could not be observed due to presence of nonlinearity, the Cole–Cole plots could be of help. The intersection of the Cole–Cole plot profile with the X axis for complex viscosity was a good estimate of zero-shear viscosity, and the maximum value of the curve for Cole–Cole plots for complex viscosity was a good indication of the longest relaxation time of the SMC material. In addition, the

Cole–Cole plots could be used to understand the effect of the relaxation spectrum on the rheological properties and could therefore be related to the molecular weight distribution in the polymer matrix.

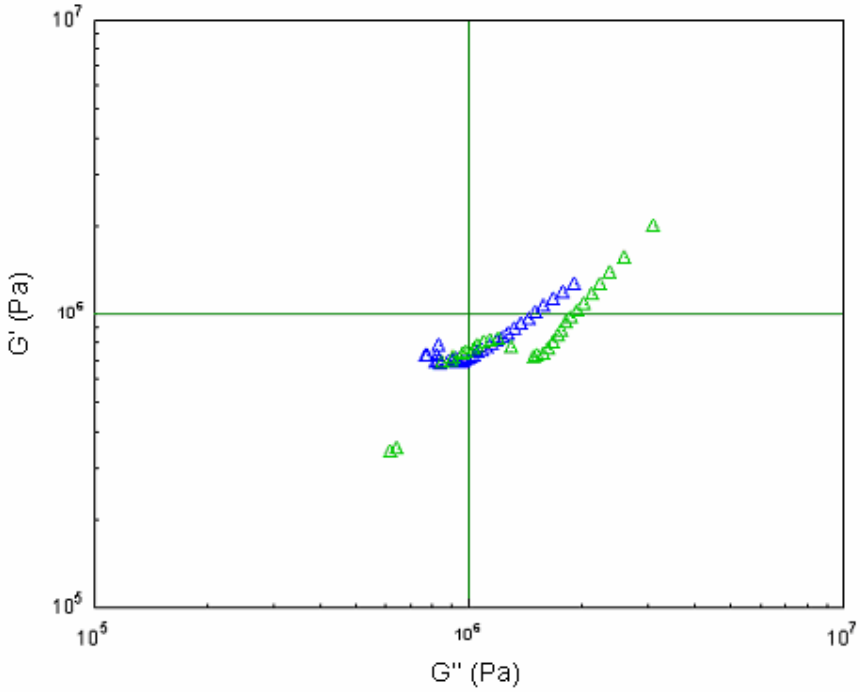

Figure 6.13: Cole–Cole plot at 140 ℃ and 160 ℃

Figure 6.13 shows a Cole–Cole plot at 140 ℃ and 160 ℃. It can be observed from the plot that G' began to fall and attained a minimum at around 2 x 10^6 and then started increasing. At higher temperatures, the point shifted to lower values, as observed in the case of 160 ℃. This indicated that the curing took place over a small range of temperatures and the structural changes induced in the material were not very significant, even after curing commenced. The rise in shear viscosity after curing could have been due to a small chain-induced cross-linking. Interestingly, the curves did not overlay each other completely, indicating that there were small structural changes, because without any changes the curves would have perfectly overlaid each other. The rate of rising reduced with increase in temperature, which was indicative that the curing process tended to level off after a certain period. The levelling-off tendency was more sluggish at higher temperatures since, at higher

temperatures, the initial energy available for curing was high and hence the chains could take sufficient time to cure and cross-link. At lower temperatures, this time was not available and hence cross-linking was more randomised (resulting in shorter average chain length).

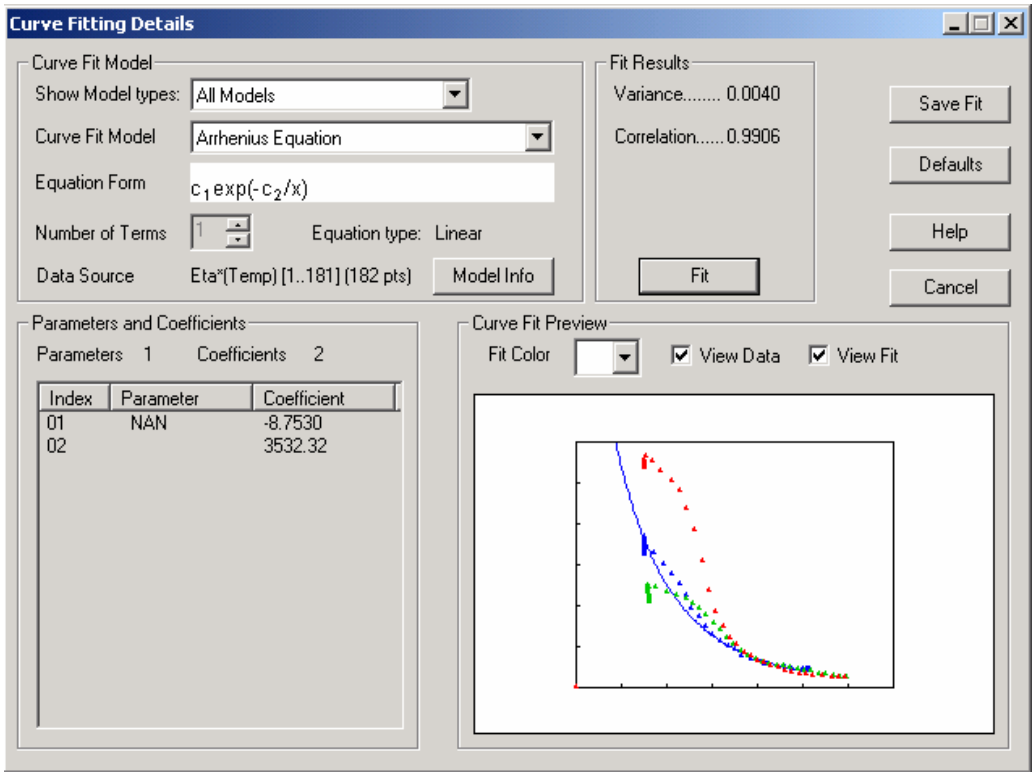

Figure 6.14: Curing activation energy

The activation energy shown in Figure 6.14 was 3532.32 Joule/mol and the zero-shear viscosity or the pre-exponential factor was –8.7530 (dimensionless number). The above model could now be used to simulate the change in viscosity with temperature.

6.8 Discussion (Rheological Testing)

The rheological testing of the SMC material was performed with an aim to analyse the factors that affect the rheological behaviour of the polymer. In addition, it was important to identify the rheologically induced (viscosity-based) structural changes that arise in the SMC material during processing. Hence, the obvious choices for rheological testing were shear and dynamic

rheology tests. Shear rheological tests helped to determine the effect of temperature and time on the viscosity of the material. Further, with different heating rates, it was possible to ascertain the curing mechanism and conditions for the material (SMC). Dynamic rheological tests helped to analyse the structural changes induced in the material under real world processing conditions. In addition, the structural effects of curing on relaxation time were analysed and studied. The dynamic rheological tests, through the use of G' and G", helped in using a structure-based rheological model to predict the shear stress and relaxation profiles.

The shear rheological tests revealed that the material follows the typical shear-thinning behaviour exhibited by thermoplastic polymers, as confirmed by studies performed by Dumont et al. (2003), until the curing temperature is attained. Once the curing temperature is attained, the viscosity rises abruptly as expected for a thermosetting polymer.

Flow activation studies revealed that the flow activation energy remains the same under different structural conditions. Once the curing process is initiated, the activation energy becomes a function of temperature, since at higher temperatures the shear viscosity profile shows a steeper gradient and hence the activation energy would also increase, although there would be a linear relation between the temperature and flow activation energy. In addition, with increase in temperature, as indicated by the heat-up rate, the material's minimum viscosity point is lowered, as can be observed in Figure 6.8. This behaviour can be attributed to the fact that, with increase in heating rate, the chains have a higher energy to dissipate the applied shear force; hence, they can actually shear thin to a point where all the applied shear force is released. However, at lower temperatures, a part of the energy is stored, which is dissipated slowly over time.

The dynamic viscosity tests revealed that the storage and the loss modulus generally decrease with increase in temperature, which is also indicated by the complex viscosity trends. Initially, the loss modulus dominates the process (see Figure 6.8), but once the material starts to cure, the storage

modulus starts increasing rapidly. The storage and the loss modulus, along with the complex viscosity, exhibit nonlinearity at lower as well as higher frequencies. In addition, the crossover point shifts to lower values with increase in temperature, which validates that the curing activation energy is partly provided by temperature and partly by shear energy.

The Cole–Cole plots for the dynamic viscosity tests revealed that there is not much of a structural change induced in the material once the curing mechanism is initiated. The Cole–Cole plot for complex viscosity revealed that the change in relaxation time due to the curing process is in the order of few seconds. That indicates that the curing results in cross-linking are induced by smaller/shorter chains. The overall trend in the Cole–Cole plot indicate that the cross-linking density is not very high during the curing process. If this were not the case, there would be a substantial shift in the plot at different temperatures after the curing point. Hence, it is very much possible that the cross-linking density is a function of the initiator concentration and the propagation additives used in the material formulation.

6.9 Conclusions (Rheological Testing)

The SMC material behaves like a thermosetting polymer and accordingly shows a typical shear-thinning profile. In the initial stages of processing, the material behaviour is dominated by G" (loss modulus) as most of the energy put in to the material is dissipated. Once the curing process starts, there is a crossover point and the G' (storage modulus) dominates, as most of the energy is now stored within the cross-linked structure developed with curing. The process of curing is temperature and time dependent. Initially, the curing rate is not solely dependent on temperature, but also depends on the concentration of the initiator and the amount of propagation additives. The cross-linking induced within the material is due to smaller chains and the cross-linking density is not very high.

Since the material under investigation is a thermosetting polymer, with significant structural changes being dependent on temperature and time, the

best mathematical model to reflect this behaviour would be a model that takes the structural as well as temperature- and time-induced viscosity factors into consideration. The use of such a model would provide details of the changes in the molecular structure that affect the shear stress profile, and hence, such a modelling approach would be able to determine the effect of temperature, time and structural changes within the material on its viscosity and shear stress profile.

The Maxwell model would be used to investigate its suitability to describe this material. The Maxwell model was considered in this case since, unlike other power law models, which only take into account the overall viscosity profile of the material, the Maxwell model uses a spring to model the elasticity of the material and a dashpot to model the viscous behaviour of the material. Thus, it would provide a molecular-based representation of the viscoelastic profile of the SMC.

6.10 References

- Barnes, H 2000, *A handbook of elementary rheology,* University of Wales, Aberystwyth.
- Barnes, H, Hutton, J & Walters, K 1997, *An introduction to rheology,* Elsevier, Amsterdam.
- Baskurt, O & Meiselman H 2003, 'Blood rheology and hemodynamics', *Seminars in Thrombosis and Haemostasis*, vol. 29, no. 5, pp. 435–450.
- Batchelor, G 1967, *An introduction to fluid dynamics,* Cambridge University Press, Cambridge.
- Bird, R, Armstrong, R & Hassager, O 1987, *Dynamics of polymeric liquids,* John Wiley & Sons, New York.
- Bird, R, Curtiss, C & Armstrong, R 1989, *Dynamics of polymeric liquids*, vols. 1 & 2, Wiley Interscience.
- Bird, R, Stewart, W & Lightfoot, E 1960, *Transport phenomena*, John Wiley & Sons, Hoboken, NJ.
- Boger, D & Walters, K 1993, *Rheological phenomena in focus,* Elsevier, Amsterdam.
- Buyevich, Y & Shchelchkova, I 1978, 'Flow of dense suspension', *Progress in Aerospace Science*, vol. 18, pp. 121–150.
- Coleman, B, Markowitz, H & Noll, W 1966, *Viscometric flows of non-Newtonian fluids,* Springer-Verlag, Berlin.
- Coussot, P & Ancey, C 1996, *Rhéophysique des pâtes et des suspensions,* EDP Sciences, Les Ulis.
- Dartevelle, S 2004, 'Numerical modeling of geophysical granular flows: 1. A comprehensive approach to granular rheologies and geophysical multiphase flows, *Geochemistry Geophysics Geosystems*, vol. 5, DOI 10.1029/2003GC000636.
- Drew, D 1983, 'Mathematical modeling of two-phase flows', *Annual Review of Fluid Mechanics*, vol. 15, pp. 261–291.
- Drew, D & Passman, S 1999, *Theory of multicomponent fluids,* Springer, New York.
- Findley, W, Lai, J & Onaran, K 1989, *Creep and relaxation of nonlinear viscoelastic materials*, Dover Publications, New York.

- Gunasekaran, S & Mehmet, M 2003, *Cheese rheology and texture*, CRC Press, Boca Raton, Fla.
- Herczynski, R & Pienkowska, I 1980, 'Toward a statistical theory of suspension', *Annual Review of Fluid Mechanics*, vol. 12, pp. 237–269.
- Hutter, K & Jöhnk, K 2004, *Continuum methods of physical modeling,* Springer, Berlin.
- Kim, S & Karrila, S 1991, *Microhydrodynamics: principles and selected applications,* Butterworth-Heinemann, Stoneham.
- Koch, D & Hill, R 2001, 'Inertial effects in suspension and porous-media flows', *Annual Review of Fluid Mechanics*, vol. 33, pp. 619–647.
- Kumagai, N, Sasajima, S & Ito, H 1978, 'Long-term creep of rocks', *Journal of the Society of Materials Science (Japan)*, vol. 27, p. 157.
- McKenna, B & Lyng, J 2003, *Texture in food: introduction to food rheology and its measurement*, viewed 18 September 2009, <http://books.google.com/?id=wM1asp1LL8EC&pg=PA130&dq=Food+Rheology&q=FoodRheology>.
- Minier, J & Peirano, E 2001, 'The pdf approach to turbulent polydispersed two phase flows', *Physics Reports*, vol. 352, no. 1–3, pp. 1–214.
- Morrison, F 2001, *Understanding rheology,* Oxford University Press, New York.
- Pope, S 2000, *Turbulent flows,* Cambridge University Press, Cambridge.
- Pozrikidis, C 1992, *Boundary integral and singularity methods for linearized viscous flows,* Cambridge University Press, Cambridge.
- Russel, W, Saville, D & Schowalter, W 1995, *Colloidal dispersions,* Cambridge University Press, Cambridge.
- Schowalter, W 1978, *Mechanics of non-Newtonian fluids,* Pergamon Press, Oxford.
- Tanner, R 1988, *Engineering rheology,* Clarendon Press, Oxford.
- Truesdell, C 1974, 'The meaning of viscometry in fluid dynamics', *Annual Review of Fluid Mechanics*, vol. 6, pp. 111–147.
- Truesdell, C 1984, *Rational thermodynamics,* Springer-Verlag, New York.
- Walters K 1975, *Rheometry,* Chapman and Hall, London.

- Zdunkowski, W & Bott, A 2003, *Dynamics of the atmosphere,* Cambridge University Press, Cambridge.

CHAPTER 7: Deformation Modelling

7.1 Introduction

During initial embedding trials of an antenna into SMC (see Figure 7.1), a noticeable antenna deformation was observed, requiring the development of a numerical model capable of predicting this deformation. Antenna deformation in the finished product could have significant deleterious effects on signal quality and overall component performance. The numerical model developed was used to investigate change in parameters, such as mould temperature, initial material temperature and mould closing speed, to minimise antenna deformation during the embedding process.

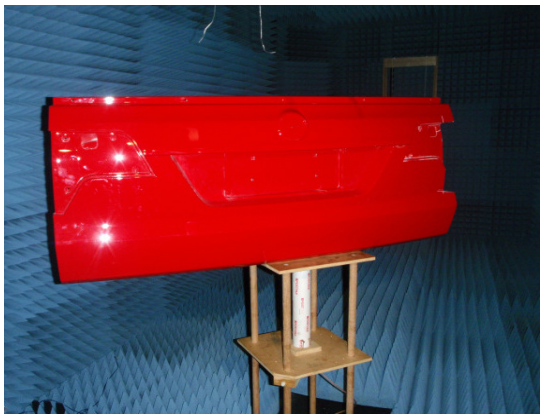

Figure 7.1: Antenna embedded into Holden HSV ute/pickup tailgate

The first research to develop a model for SMC flow based on the experimentally observed kinematics was carried out in the late 1970s and mid-1980s (Barone & Caulk 1979; 1985; 1986; Bird et al. 1987), followed by further work by other researchers in the late 1980s and mid-1990s (Castro & Griffith 1989; Castro & Tomlison 1990; Osswald 1987; Tucker & Tomlison 1995). They explored the early models and developed approximate methods to characterise SMC material based on experimentally measured parameters (Hutter et al. 1999; Werman and Keren 2001; Kohr and Pop 2004; Prosperetti 2004).

7.2 Development of Rheological Model for SMC

The SMC material used in the fabrication process is a shear-thinning, as confirmed in Chapter 6, thermosetting polymer. The curing of the SMC material is time and temperature dependent, and hence, unlike a typical shear-thinning fluid that has exponential decay in viscosity, this material would exhibit an increase in viscosity once cross-linking (curing) starts to occur. The aim of the project was to embed an antenna inside the SMC matrix by compression moulding it into the part. During the process of compression moulding, the SMC material shear thins, where a fluid's viscosity "the measure of a fluid's resistance to flow" decreases with an increasing rate of shear stress, and hence, the first normal stress difference, along with the shear stress originating within the SMC material due to temperature and an applied shear force, resulted in bending of the antenna. The aim of developing a rheological model was to be able to predict the deformation in the antenna due to an applied shear and normal stress within the SMC charge during the process.

The experimental shear rheological studies, conducted at the compression temperature and tool closing speed used in the actual manufacturing process, using the SMC material showed a predominantly shear-thinning behaviour during the initial stage of the process (loading of the charge and closing of the tool). The shear viscosity subsequently rose due to the curing of the SMC material and finally settled at a constant viscosity once material was fully cured. This behaviour can be explained by a simple empirical equation (power law). The power law equation is given by:

$$\tau = K \dot{\gamma}^{n} \qquad (1)$$

where K and n are fluid parameters.

The factor *n* is also known as the power law index and is less than one ($n<1$) for a shear-thinning fluid. Since the material under consideration is viscoelastic, the Maxwell spring-dashpot model is a suitable model to describe the viscoelastic behaviour of the SMC material, rather than other

empirical models, such as power law, Herschel-Buckley and modified power law. The spring in the Maxwell model represents the elasticity of the SMC material and the dashpot represents the viscous part of the material. Hence, the net strain in the material will be only a function of the elasticity and the viscosity of the material. Interestingly, a purely viscous material would actually dissipate all the shear energy and the net strain, with respect to time, would be a constant, whereas a purely elastic part would show a linear increase in net strain with time. The combined effect of both induced strains would result in a curve (as observed experimentally). Thus, the use of the Maxwell model to represent the viscoelasticity of the fluid is justified.

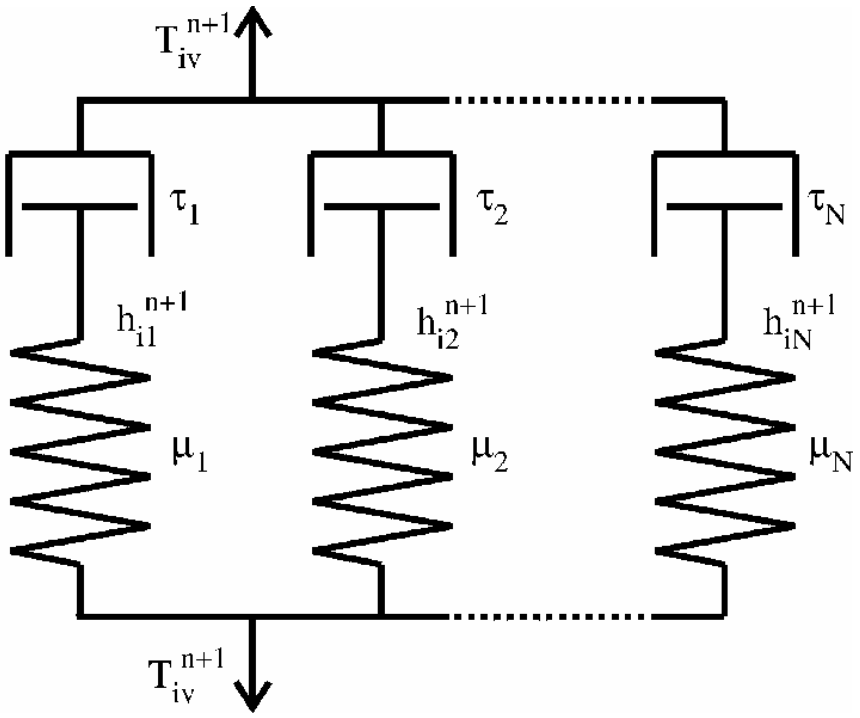

Figure 7.2: Generalised Maxwell model

Figure 7.2 represents a generalised Maxwell model applied to a fluid and Figure 7.7 represents Maxwell model of SMC and antenna substrate. In addition, the Maxwell model takes the relaxation spectrum of the polymer chains into account in its form, thereby incorporating the structural effects of the molecular chains.

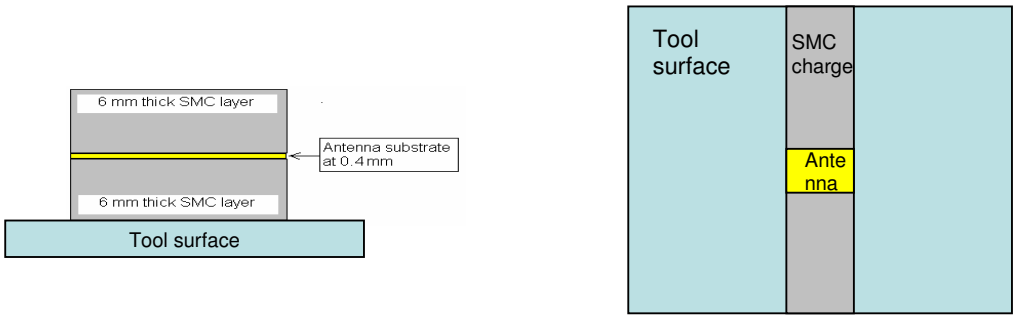

(a) (b)

Figure 7.3: Initial configuration of SMC charge and antenna loaded into tool (not to scale): (a) cross-section view and (b) top view

(a)

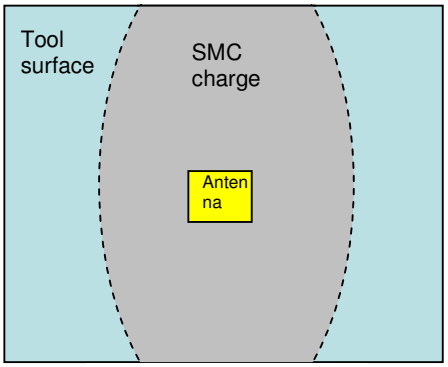

(b)

Figure 7.4: 50% tool filled configuration of SMC charge and antenna substrate loaded into tool (not to scale): (a) cross-section view and (b) top view

(a)

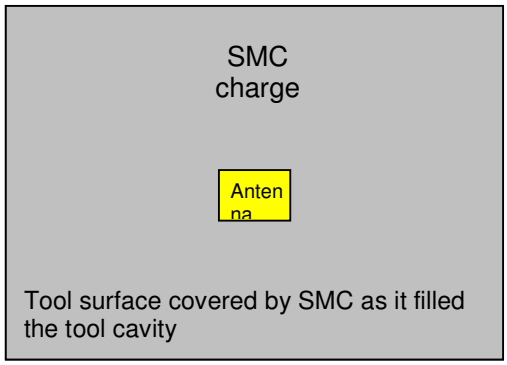

(b)

Figure 7.5: Final configuration of cured component, antenna embedded into SMC (not to scale): (a) cross-section view and (b) top view

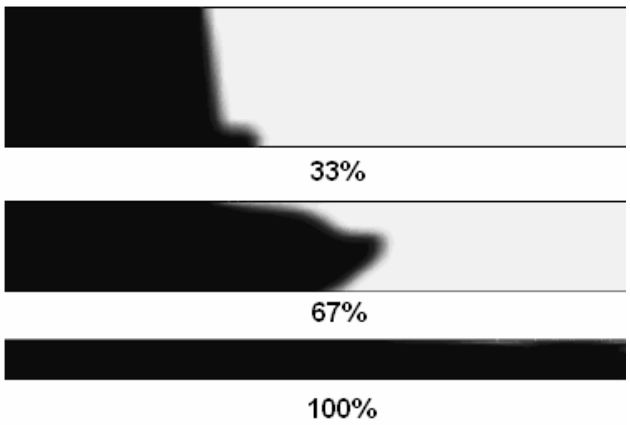

Figure 7.6: SMC flow front at tool positions: 33%, 67% and 100% closed (not to scale)

Figures 7.3, 7.4 and 7.5 show different stages of material flow in the tool, namely initial, intermediate and final stages respectively. Figure 7.6 shows material flow fronts for three fill stages shown in figures 7.3 to 7.5.

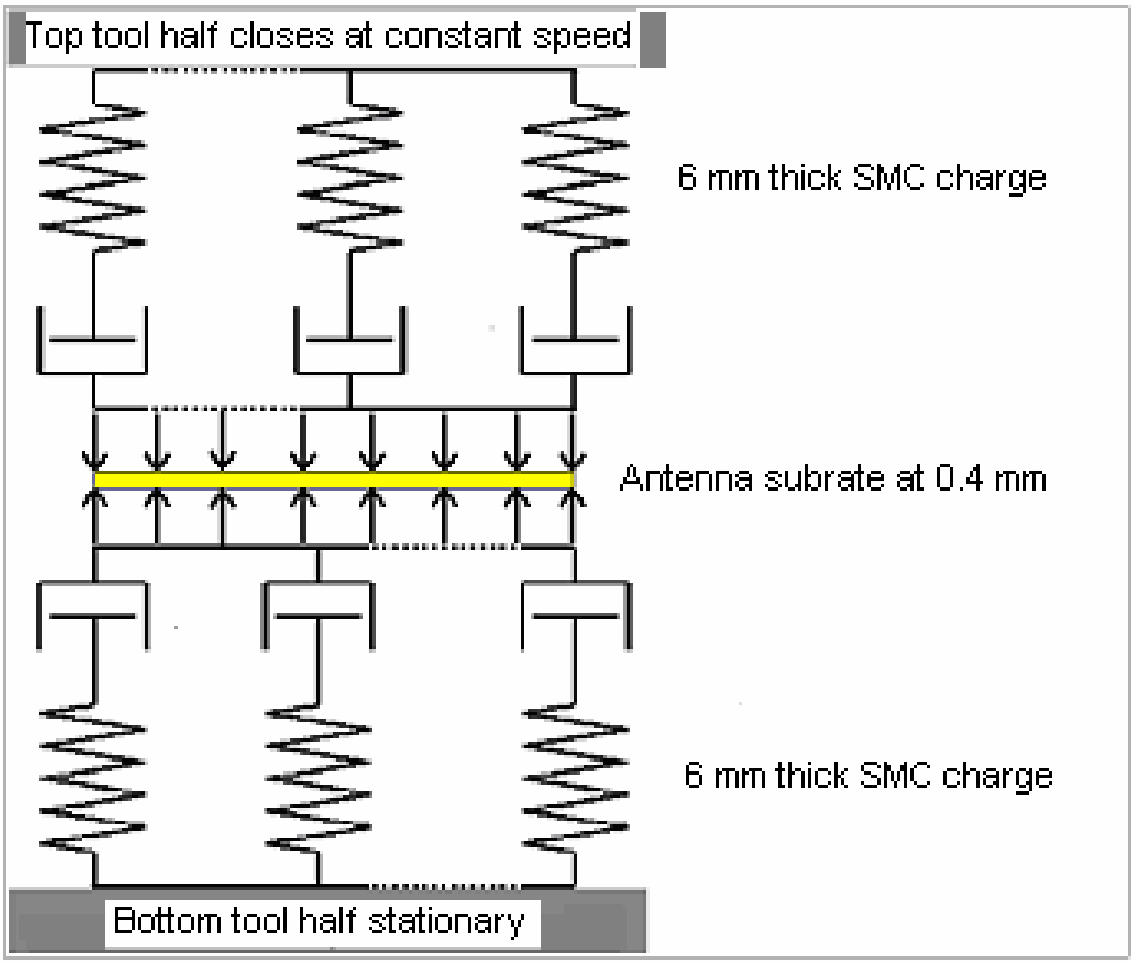

Figure 7.7: Maxwell model representation of SMC and antenna substrate

7.3 Simulation Algorithm

The calculation of the net deformation in the antenna using a rheological model required the use of a scheme that would incorporate the combined effect of temperature, time and viscosity. The simulation or modelling scheme depicted in Figure 7.8 was developed to meet these needs.

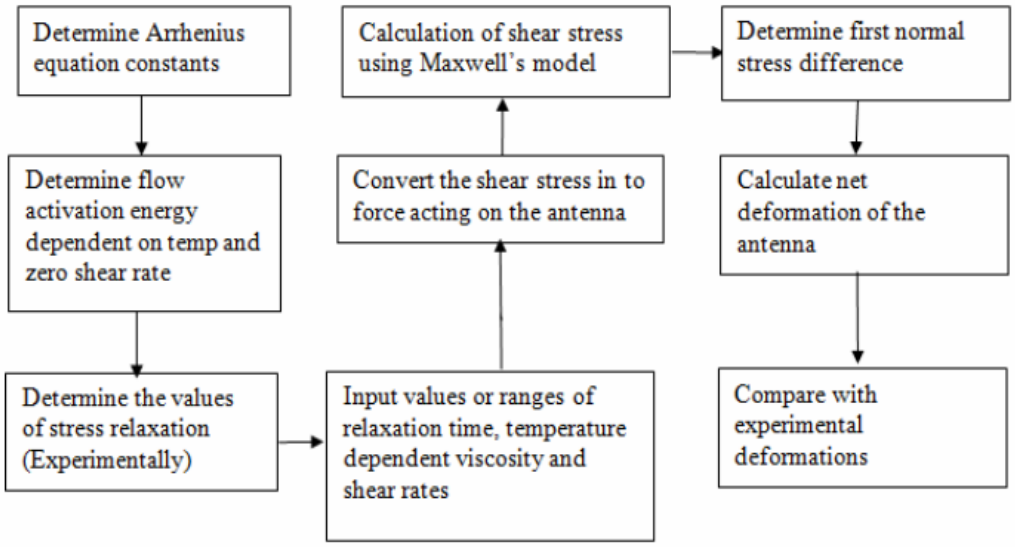

Figure 7.8: Model flow diagram

The scheme first involved the calculation of a temperature-dependent viscosity profile using the Arrhenius equation. Once this was known, the next step was to determine the flow activation energy. The value of the activation energy should be such that the material attains a state of fluidity at the desired operating conditions. The next step was to calculate the relaxation spectrum of the SMC charge from the dynamic rheological tests. The number of elements in the relaxation spectrum was chosen in such a way that the maximum amount of correlation with experimental values was obtained. Once the relaxation spectrum and the temperature-dependent viscosity profile was known, the generalised Maxwell model could be used to calculate the stress acting on the antenna. In addition, the above values could be used to calculate the normal stress difference (elastic recoil of polymer chains). The net deformation in the antenna would be a combined effect of both these stresses. The difference in stress between the two SMC charges, one being above and one being below the antenna substrate, resulted in a deformation of the antenna itself.

7.4 Modelling Approach

In the compression-moulding scenario, before a new part is made, the SMC material is initially in touch with the bottom tool half surface. After the machine

start button is initiated, the top tool half comes down with a constant velocity that equals T_v (tool velocity), and after a time t, contacts the top surface of the SMC charge. Hence, in the initial state when the top tool half is not touching the surface of SMC, the reduction in viscosity is due to the conduction of heat through the bottom tool half surface into the SMC charge. Hence, the overall flow of the material is caused by the temperature dependency of viscosity, as well as by the shear deformation induced in the material as the top tool half is being lowered. The equations to be used to model the spring-dashpot system are as follows. The net velocity gradient in the spring-dashpot system would be a sum of the velocity gradient across the spring and the velocity gradient across the dashpot. The elastic response of the SMC material is given by Hooke's law as follows:

$$\tau_{12} = G\,\gamma_{12} \qquad (2)$$

$$\frac{\tau_{12}}{dt} = G\frac{\gamma_{12}}{dt} = G\,\dot{\gamma}_{12} \qquad (3)$$

where τ_{12} the shear stress is in the elastic material, G is the elasticity modulus of the material and $\dot{\gamma}_{12}$ is the net strain in the material (the above law simply states that the stress is directly proportional to strain within the elastic limits.)

The viscous response of the SMC is given by Newton's law of viscosity:

$$\tau_{12} = \eta_0\,\dot{\gamma}_{12} \qquad (4)$$

where τ_{12} is the shear stress induced in the viscous part of the material and η_0 is the zero-shear viscosity (zero-shear viscosity of the material is the viscosity at a very small or rather at zero-shear rate) and $\dot{\gamma}_{12}$ is the shear rate.

The net shear rate across the entire spring-dashpot system is the sum of the shear rates across each of the individual springs and the dashpots. This can be stated since, at any given time t, the net deformation in the spring-dashpot

system is the sum of the deformation (scalar quantity) in the two types of elements (springs and dashpots). Hence, taking a derivative with respect to time for both the elements would not empirically change the additive nature of shear rates.

$$\dot{\gamma}_{12} = \left(\dot{\gamma}_{12}\right)_d + \left(\frac{d\gamma_{12}}{dt}\right)_s = -\left(\frac{\tau_{12}}{\eta_0}\right) + \left(\frac{1}{G} d\frac{\tau_{12}}{dt}\right) \tag{5}$$

where d and s denote dashpot and spring respectively. Rearranging the above equation by multiplying both sides by η_0 and substituting

$$-\eta_0 \dot{\gamma}_{12} = \tau_{12} + \lambda \frac{d}{dt}\tau_{12} \tag{6}$$

Here, lambda (λ) denotes the relaxation time and is a ratio of the zero-shear viscosity and the elastic modulus. Interestingly, if the elastic modulus is large, then the relaxation time is small, and hence the material behaviour would be similar to that of an elastic solid. The opposite is also true; if the relaxation time is large and the elastic modulus is small, then material behaves like a viscous fluid.

The general solution to the above equation is given by:

$$\tau_{12} = -\int_{-\infty}^{t} \frac{\eta}{\lambda} \exp\left(\frac{-(t-s)}{\lambda}\right) \dot{\gamma}_{12}(s) ds \tag{7}$$

7.5 Arrhenius Equation

$$\eta = \eta_0 e^{-Ea/RT} \tag{8}$$

Taking the log of both sides, we have

$$\log \eta = \log \eta_0 - \frac{Ea}{R}\left(\frac{1}{T}\right) \tag{9}$$

Hence, making a plot of $\log \eta$ with respect to (1/T) will give the slope of the above equation, which is activation energy.

7.5.1 Calculation of Arrhenius Equation Parameters

A temperature ramp-up test (dynamic viscosity parameters) was performed using the ARES 2000. The temperature range investigated was 30℃ ⁻140 ℃ at an applied strain of 1% and a shear rate of 1 s^{-1} with dynamic strain amplitude of 0.5. The Arrhenius equation, which is a one-parameter and two-coefficient based model, was fitted to the experimental data using RSI Orchestrator software. The results of the curve-fitting procedure is as shown in Figure 7.9.

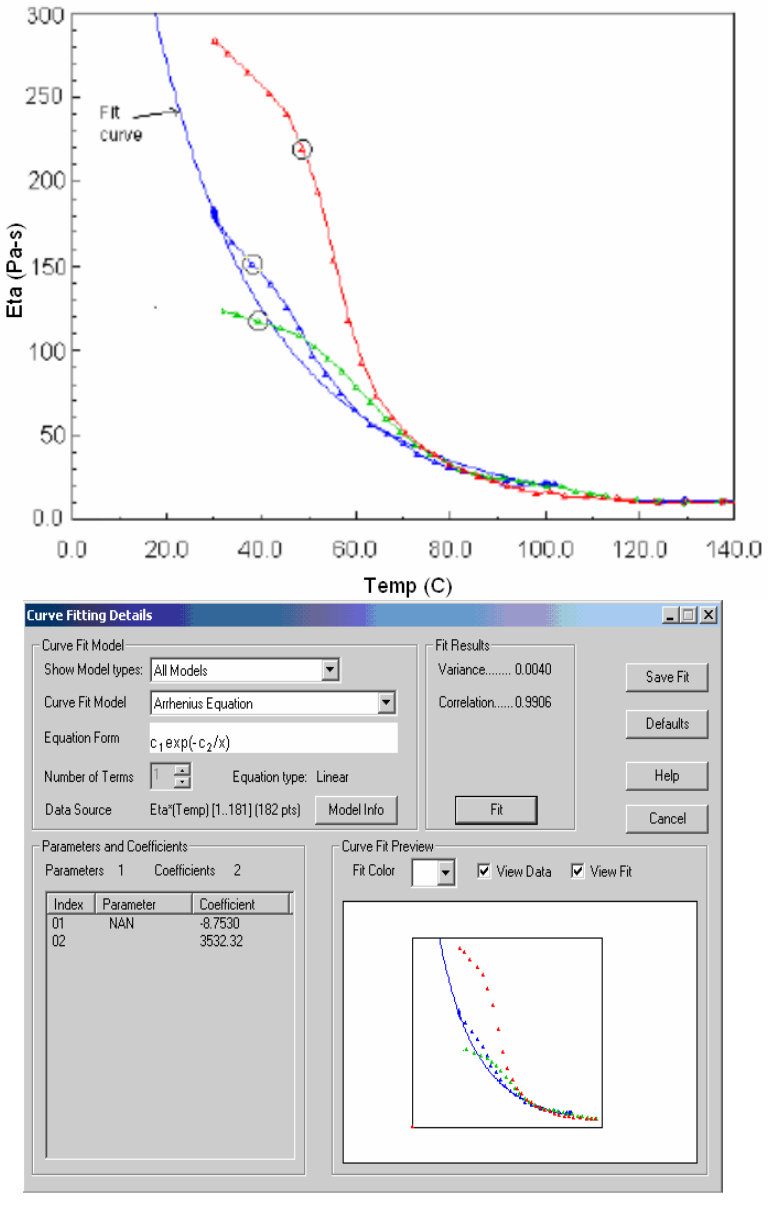

Figure 7.9: Arrhenius equation curve fit to experimental data

The above curves show a plot of dynamic viscosity (y-axis) versus temperature (x axis). The curves can be used with an Arrhenius-type model to develop a relation between temperature and viscosity. The blue line without markers represents the Arrhenius model fit created in Orchestrator 2000. The shear-thinning behaviour of the SMC charge is evident in the model. Overall, the model shows a small amount of discrepancies at lower temperatures but matches well with the data at higher temperatures. The activation energy from the above model was 3532.32 Joule/mol and the zero-shear viscosity or the pre-exponential factor was –8.7530 (dimensionless number). The above model could now be used to simulate the change in viscosity with temperature.

7.6 Determination of Relaxation Time

The next step as per the simulation algorithm was to determine a range of relaxation times for the dynamic frequency in each experimental run. Dynamic frequency tests were conducted at three different temperatures (120 ℃, 140 ℃ and 160 ℃). The above temperatures were selected as they cover the range of commonly used temperatures in the manufacturing of SMC. The dynamic frequency tests were subsequently used to determine G' and G". The values of G' and G" were then used to determine experimental relaxation times. These relaxation times can be used with the Maxwell equation to determine the shear stress acting on the antenna and subsequent antenna deformation.

The relaxation time and modulus is a function of the dynamic rheological parameters (G' storage modulus, G" loss modulus and complex viscosity). The relaxation modulus in terms of the storage modulus (as per Maxwell's model) is given by:

$$\sum G' = \sum \frac{\lambda^2 \omega^2}{1 + \lambda^2 \omega^2} \qquad (10)$$

$$\sum G'' = \sum \frac{\lambda \omega}{1 + \lambda^2 \omega^2} \qquad (11)$$

$$G = G' + iG'' \qquad (12)$$

Thus, the storage modulus of the material, G', as per the Maxwell model, was proportional to the square of the frequency and relaxation time. Physically, for a polymer material, the storage modulus represents the elasticity of the material. Therefore, if the relaxation time is long, it indicates that the molecular chains are long as well.

Equations 10, 11 and 12 can be used to determine the relaxation spectrum of the system, provided an experimental curve for G' versus frequency is available.

Figures 7.10, 7.11 and 7.12 show relaxation model parameters at 120 ℃, 140 ℃ and 160 ℃ respectively. Figure 7.13 shows plot of relaxation curves for models generated in figures 7.10 to 7.12.

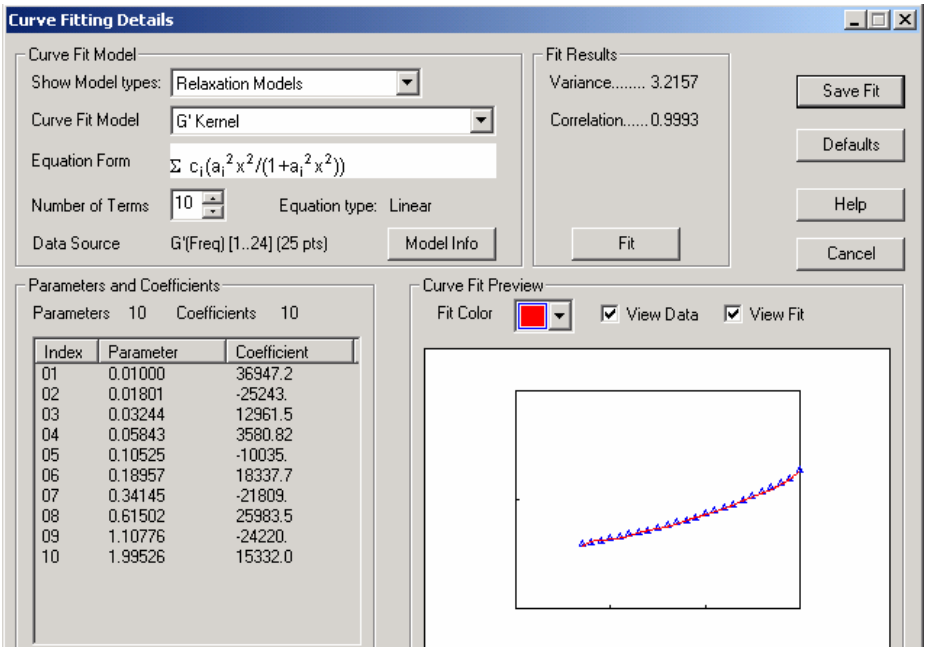

Figure 7.10: 120 ℃ relaxation parameter and coefficient

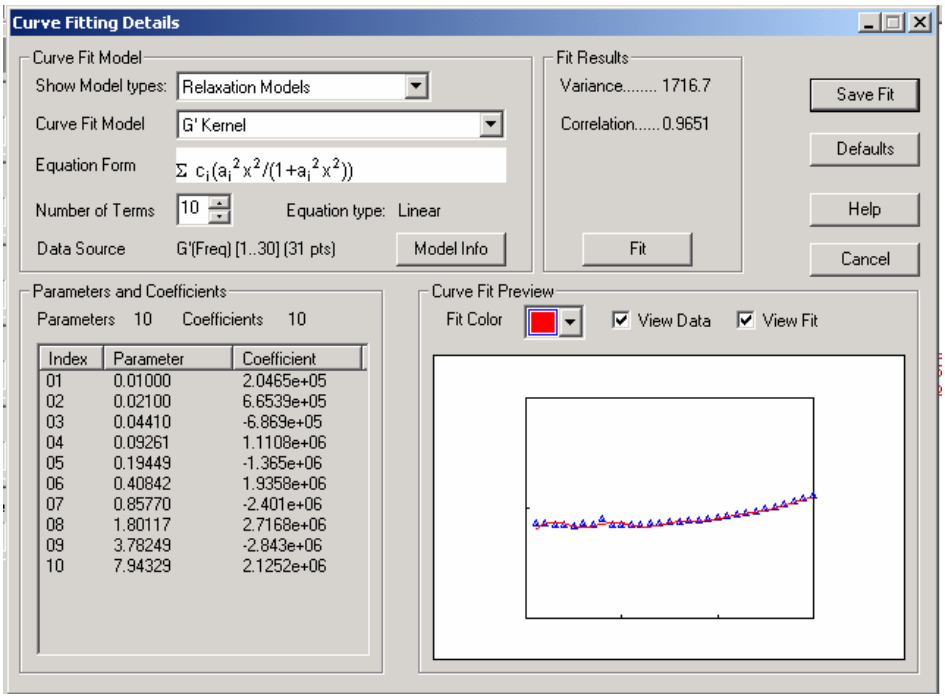

Figure 7.11: 140 ℃ relaxation parameter and coefficient

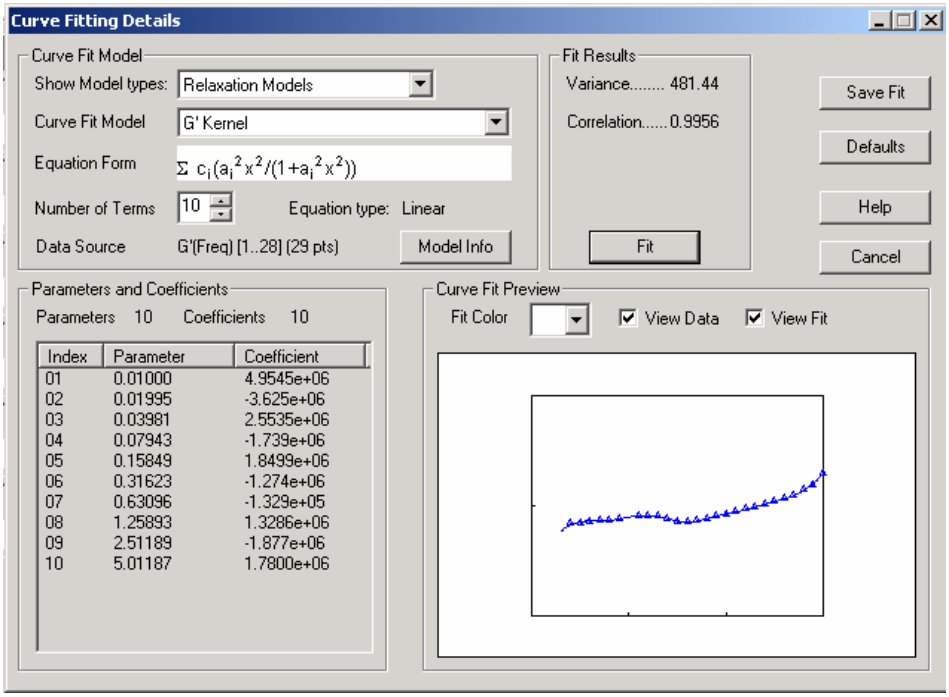

Figure 7.12: 160 ℃ relaxation parameter and coefficient

The model used for fitting the experimental data is empirical in nature. The curing temperature of the SMC charge varied with the age of the material, but

was approximately 100 °C. Hence, at 120 °C the material will cure, but at a lower rate (slower) compared to at 140 °C and 160 °C. At this lower rate of curing, the degree of cross-linking in the polymer chains would be lower, which would result in a longer chain length and longer relaxation time as explained by lower values of the coefficients. At higher temperatures, the chain length fell rapidly due to cross-linking, and hence coefficient values rose. The fact that cross-linking was higher at higher temperatures was evident by the higher value of melt elasticity observed in the experiments at higher temperatures, and hence can be observed in Tables 7.1–7.3. The next step was to generate a relaxation spectrum for the SMC material from the model fit. The curves below validate the above observation by showing a reduction in the relaxation spectrum at higher temperatures due to a higher degree of cross-linking. In addition, the range of relaxation times was much broader at lower temperatures compared to at the higher temperature region. The trend in relaxation was very much similar at 140 °C and 160 °C.

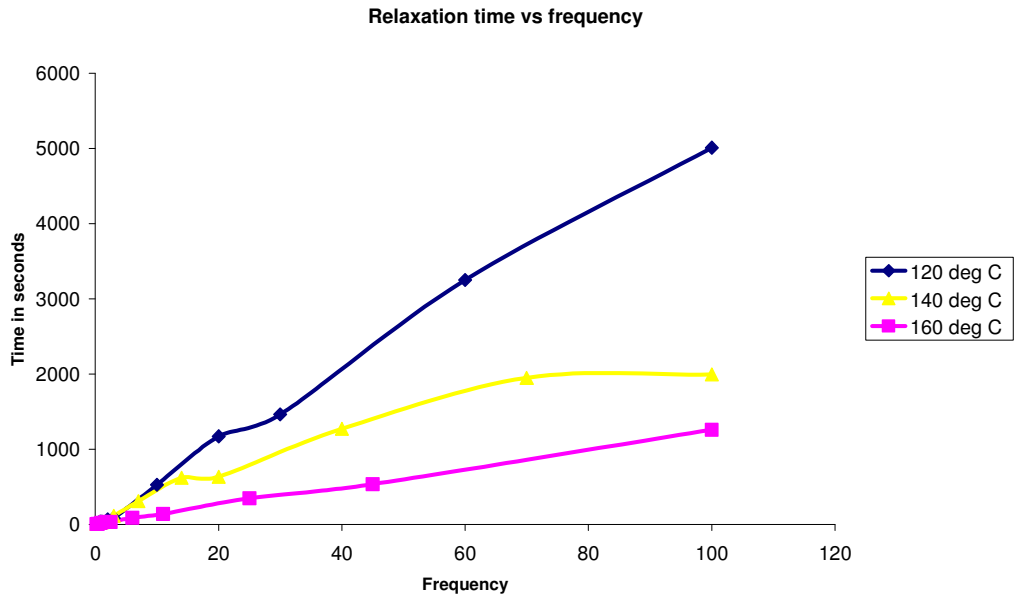

Figure 7.13: Relaxation time curves for 120 °C, 140 °C and 160 °C, frequency in rad/s and time in sec

Table 7.1: Relaxation time for 120 °C

120 °C			
intercept coefficient	parameter	frequency	relaxation time
0.01	36947	0.5	25.00
0.01801	25243	0.8	35.54
0.03244	12962	1.1	37.30
0.05843	3581	2	68.46
0.10525	10035	3	85.51
0.18957	18338	10	527.51
0.34145	21809	20	1171.47
0.615	25984	30	1463.41
1.10776	24220	60	3249.80
1.99526	15332	100	5011.88

Table 7.2: Relaxation time for 140 °C

140 deg C			
intercept coefficient	parameter	frequency	relaxation time
0.01	4954500	0.2	4.00
0.01995	3625000	0.7	24.56
0.03981	2553500	1.1	30.39
0.07943	1739000	3	113.31
0.15849	1849900	7	309.17
0.31623	1274000	14	619.80
0.63096	132900	20	633.95
1.25893	1328600	40	1270.92
2.51189	1887000	70	1950.72
5.01187	1780000	100	1995.26

Table 7.3: Relaxation time for 160 °C

160 deg C			
intercept coefficient	parameter	frequency	relaxation time
0.01	204650	0.2	4.00
0.021	665390	0.4	7.62
0.0441	686900	0.9	18.37
0.09261	1110800	1.7	31.21
0.19449	1365000	2.5	32.14
0.40842	1935800	6	88.14
0.8577	2401000	11	141.07
1.80117	2716800	25	347.00
3.78249	2843000	45	535.36
7.94329	2125200	100	1258.92

7.7 Shear Stress Calculation Using Maxwell's Model

The next step was the calculation of the shear stress acting on the SMC charge. The Maxwell model in conjunction with the relaxation modulus, the

shear-rate regime and the shear viscosity range could be used to determine the shear stress distribution, which could be further used to calculate the net force and the deformation in the antenna. The antenna was embedded in the centre of the SMC charge. At time t=0, the charge was placed in the tool. The lower surface of the charge was then in contact with the face of the heated tool, and hence this lower surface of the charge began heating by conduction. The top tool, however, had a time lag of around 10 seconds before the tool closed and it contacted the top of the charge. This time lag resulted in a transient temperature profile within the SMC charge. The shear stress acting on the antenna was due to the temperature-dependent viscosity and the differential stress between the top and the bottom portion of the charge (below and above the antenna). This stress difference resulted in deformation of the antenna. Generally, three to five Maxwell's elements can be effectively used as a fluid analogue to represent the viscoelastic behaviour of polymers. In this case, 10 different values of viscosity and relaxation times would be used to determine the stress acting on the SMC charge and therefore the antenna. This should aid the accuracy of the modelling involving the viscoelastic properties of the SMC and its effect on the net stress and subsequent strain on the antenna.

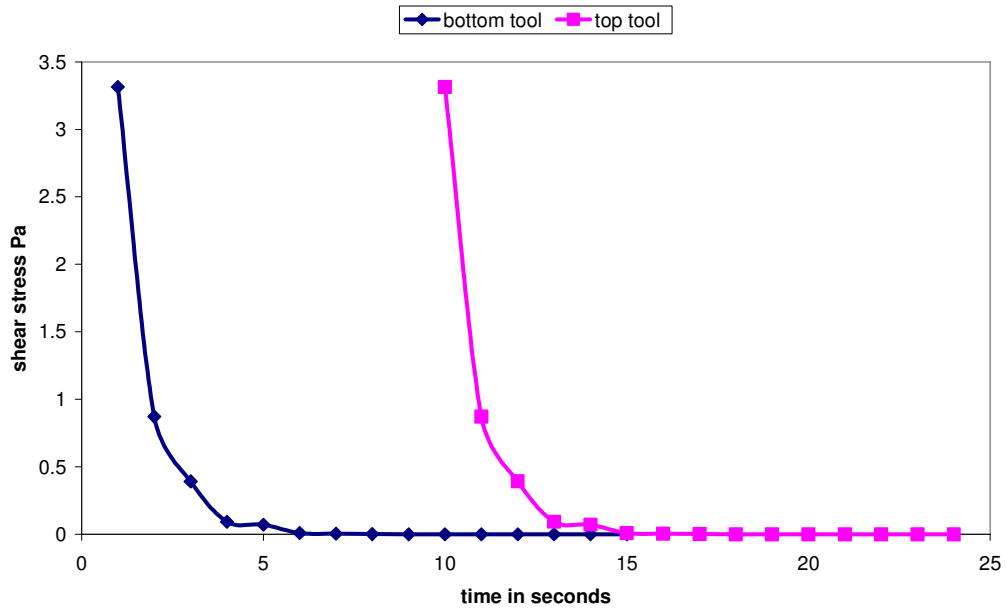

Figure 7.14: Plot of shear stress curves for top and bottom tool halves

The rheological model used to obtain the graphs in Figure 7.14 is as follows and was derived from equation 7:

$$\tau_{12} = -\int_{-\infty}^{t} \frac{\eta}{\lambda} \exp\left(\frac{-(t-s)}{\lambda}\right) \dot{\gamma}_{12}(s)\,ds$$

$$= \frac{\eta}{\lambda} \int_{-\infty}^{t} \exp\left(\frac{-t}{\lambda}\right) \dot{\gamma}_{12}(t)\,dt$$

$$= \frac{\eta}{\lambda^2} \dot{\gamma}_{12}(t) \exp\left(\frac{-t}{\lambda}\right) + \frac{\eta}{\lambda^2} \int_{-\infty}^{t} \exp\left(\frac{-t}{\lambda}\right) . \frac{d\,\dot{\gamma}_{12}}{dt} . dt + C$$

$$= \frac{\eta}{\lambda^2} \dot{\gamma}_{12}(t) \exp\left(\frac{-t}{\lambda}\right) + \frac{\eta}{\lambda^2} \int_{-\infty}^{t} \exp\left(\frac{-t}{\lambda}\right) . m\,.dt + C$$

$$= \frac{\eta}{\lambda^2} \dot{\gamma}_{12}(t) \exp\left(\frac{-t}{\lambda}\right) + \frac{m.\eta}{\lambda^2} \int_{-\infty}^{t} \exp\left(\frac{-t}{\lambda}\right) .. dt + C$$

$$= \frac{\eta}{\lambda^2} \dot{\gamma}_{12} \exp\left(\frac{-t}{\lambda}\right) - \frac{\eta.m}{\lambda^3} \exp\left(\frac{-t}{\lambda}\right) + c \qquad (13)$$

Equation 13 represents shear stress and can be modified to represent the difference in shear stress between SMC below the antenna and SMC material above the antenna, as follows:

$$\tau_{12} = \sum_{t=1}^{i} \frac{\eta}{\lambda^2} \dot{\gamma}_{12} \exp\left(\frac{-t_i}{\lambda}\right) - \frac{\eta.m}{\lambda^3} \exp\left(\frac{-t_i}{\lambda}\right) + c - \sum_{t=1}^{j} \frac{\eta}{\lambda^2} \dot{\gamma}_{12} \exp\left(\frac{-t_j}{\lambda}\right) - \frac{\eta.m}{\lambda^3} \exp\left(\frac{-t_j}{\lambda}\right) + c \quad (14)$$

where η is the viscosity of the material

λ is the relaxation time of the material

$\dot{\gamma}$ is the shear rate

t_i is the time material is in contact with bottom tool surface

t_j is the time material is in contact with top tool surface

c is a constant

m is an adjustable variable (rate of change of shear rate)

For the bottom tool t = 0 to t = 15 and for the top tool t = 10 to t = 25 seconds. The top tool was in contact with the SMC charge and was moving from t = 10 to t = 14 seconds at the constant speed of 3 mm/s second. It was during this time interval that the antenna was deformed. The area under the blue curve from t = 10 to t = 14 seconds was subtracted from the area under the pink curve for the same period. This difference represents the net shear force difference during the moulding cycle of the SMC component.

Equation 14 is the generalised form for calculation of shear stress profile. The equation is summed over the total number of relaxation elements calculated and then equally weighted to determine the average stress. The effect of temperature is taken into consideration by the temperature-dependent viscosity profile.

The first term of the equation (before the minus sign) denotes the viscous part of the net shear stress and the second term is the elastic part of the shear stress, since the second part is independent of shear rate and is only a function of the viscosity and the relaxation modulus, indicating an elastic response tendency. In viscoelastic materials, the elastic response is typically a function of the zero-shear viscosity and the relaxation modulus. The zero-shear viscosity denotes the inherently viscous nature of the material. In conjunction with the exponential decay function and the relaxation time, it demonstrates the tendency of a material to absorb stress as the viscosity decays. The degree of stress absorption is a function of the chain length, which is directly related to relaxation time.

The above equation can be used to calculate the shear stress as a function of time for predetermined values of viscosity, relaxation time and shear-rate range. The parameter *m* in the equation used is an adjustable parameter .It represents the rate of change of shear rate during the experiment. Since this value cannot be calculated theoretically, the best approach is to fit the parameter *m* to experimental values. The selected value of the parameter *m* indicates the effect of shear-rate change on the net shear stress. For the experiment conducted where the net change in shear rate is very rapid, a

good approximation would be to start with a high value for the parameter *m* beyond the experimental shear rate ranges.

Figure 7.14 shows the calculated average stress profile against time for the bottom and the top tool. It can be observed that the stress decayed exponentially and attained a plateau after a time of 5 seconds for the bottom charge (below the antenna). This trend is very logical since, with reduction in shear viscosity as temperature increases, the stress was expected to reduce and finally attain a limiting value. In simple terms, the stress was behaving proportionally to shear viscosity. The other curve shows the stress profile for the top half of the SMC substrate when the top tool touched the SMC and was offset by the time taken for the tool to touch the SMC charge (10 seconds) from the time the charge was loaded. The effective deformation in the embedded antenna is the difference in stress value between the top and the bottom half of the SMC charge from t=10 seconds to t = 14 seconds.

7.8 First Normal Stress Difference

Typically, for thermosetting polymers, the first normal stress difference is larger by a factor of two as compared to the shear stress. Hence, in this case, with a shear stress of 4.7 Pa the normal stress can be assumed to be 9.4 Pa. Hence, the overall stress acting on the antenna would be around 14.1Pa. The first normal stress difference $(\tau_{11} - \tau_{22})$ is generated within the material when the material begins to relax after application of a stress; in simple terms, it is basically a recoil force. In terms of the spring-dashpot model, the first normal stress difference is given by

$$(\tau_{11} - \tau_{22}) = \lambda.(\gamma_{12})^n \qquad (15)$$

The value of lambda is empirically known since it is constant. The functional form of the first normal stress difference can be found by regressing the above equation with experimental values .The regression is performed as follows, taking log of the above equation on both sides we have

$$\ln(\tau_{11} - \tau_{22}) = \ln \lambda + n \ln \gamma_{12} \qquad (16)$$

The above equation is of the form y = mx + c; hence, by running a regression between the experimentally determined values, the value of the constants can be calculated.

7.9 Results—Initial

Since the material under consideration is viscoelastic, a numerical model was developed based on the Maxwell spring-dashpot approach (Bird, Armstrong & Hassager 1987). The benefit of using Maxwell's model as compared to other power law approximations for viscoelasticity is that Maxwell's model incorporates the viscous and elastic behaviour of the SMC resin independently in its form. Hence, the net deformation in the embedded antenna was somewhat predicted. The spring in the Maxwell model represents the elasticity of the SMC material and the dashpot represents the viscous behaviour of the material. Hence, the net strain in the material would only be a function of the elasticity and the viscosity of the material without considering the effects of the spatial position of the antenna and the associated boundary conditions. Interestingly, a purely viscous material would actually dissipate all the shear energy, meaning the net strain with respect to time would be a constant, whereas the elastic part would show a linear increase in net strain with time. In addition, the Maxwell model takes the relaxation spectrum of the polymer chains into account, thereby incorporating the structural effects of the molecular chains.

Figure 7.15 shows schematic representation of forces being exerted by top and bottom tool surfaces on the antenna and antenna substrate that has been embedded into composite panel.

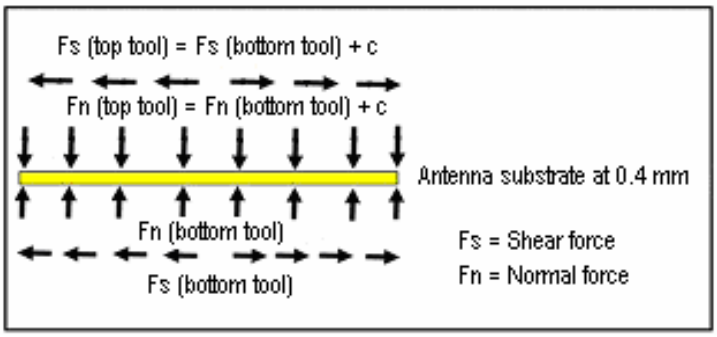

Figure 7.15: Representation of normal and shear forces acting on the antenna

Experimental results for the maximum deformation on a number of samples range from 0.57 to 0.66 mm compared to the calculated value of 0.58 mm.

7.10 Results—After-Process Optimisation

A number of process variables were selected to be investigated to quantify what effect they had on the amount of antenna deformation observed in the process. These variables are:

- initial temperature of the SMC charge in ℃
- closing speed of the tool in mm/sec
- tool/process temperature in ℃.

The approach taken was to evaluate a range of initial charge temperatures with the standard tool closing speed and tool temperature, the result of this is shown in Figure 7.16. The second step was to select the initial SMC charge temperature with the lowest resultant antenna deformation and evaluate it while changing the tool closing speed as per Figure 7.17. Repeating the same procedure, we selected the initial charge and tool closing speed with the lowest resultant antenna deformation and evaluated it against the tool temperature.

The results are summarised in Table 7.4, where calculated deformations were obtained by substituting values from experiments in chapter 7 into equation 14 and experimental deformations were measured by cutting physical samples from each run, measuring distance A as per figure 7.5 (a).

Table 7.4: Test run results

Run	Charge temperature	Closing speed of the tool in mm/s	Tool temperature	Calculated deformation in mm	Average experimental deformation in mm	Comments
1	30 ˚C	3	150 ˚C	0.58	0.6	Good surface finish and material flow.
2	40 ˚C	3	150 ˚C	0.28	0.32	Good surface finish and material flow.
3	50 ˚C	3	150 ˚C	0.17	0.22	Good surface finish and material flow.
4	60 ˚C	3	150 ˚C	0.12	0.17	Surface finish improved.
5	60 ˚C	2	150 ˚C	0.12	0.17	Improvement in material flow, almost perfect circular flow observed.
6	60 ˚C	4	150 ˚C	0.11	0.15	Good surface finish and material flow.
7	60 ˚C	6	150 ˚C	0.1	0.2	Due to high tool speed, poor surface finish and uneven material flow observed.
8	60 ˚C	4	140 ˚C	0.21	0.24	Poor material flow.
9	60 ˚C	4	160 ˚C	0.1	0.13	Improvement in material flow, almost perfect circular flow observed.
10	60 ˚C	4	170 ˚C	0.09	NA	Material starts to cross-link resulting in unacceptable sample finish.

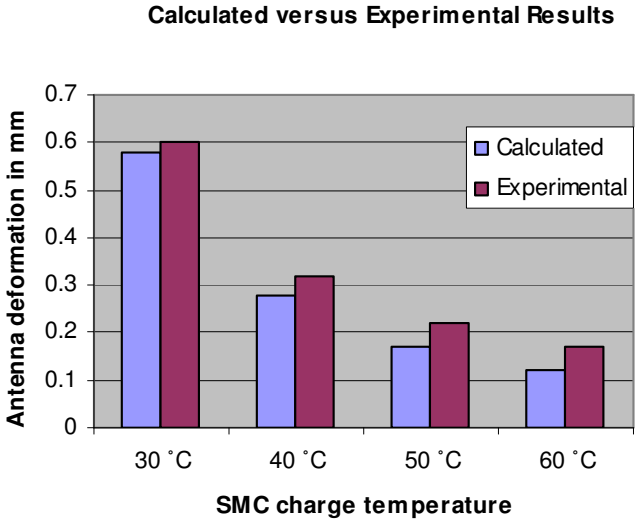

Figure 7.16: Calculated deformation of the antenna v. experimental deformation of the antenna where adjustable parameter is the initial SMC charge temperature

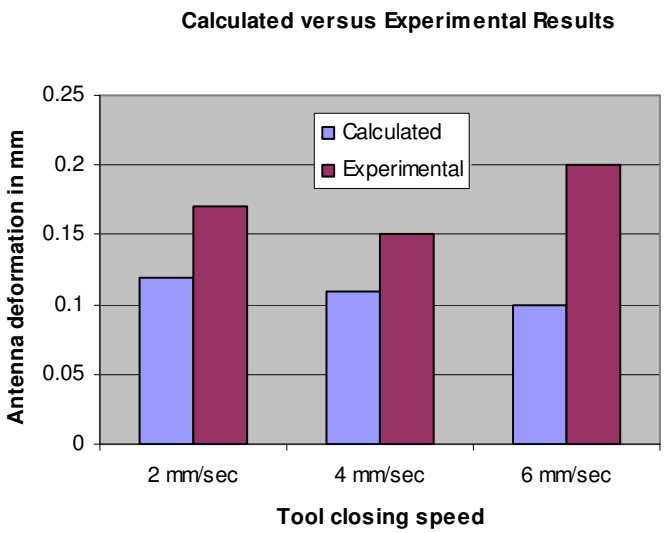

Figure 7.17: Calculated deformation of the antenna v. experimental deformation of the antenna where adjustable parameter is the tool closing speed

7.11 Discussion

As can be observed in Table 7.4, the greatest effect on the antenna deformation was found when the material charge was preheated to 60 ˚C, as in run 4. The influence of other process variables such as tool closing speed and tool temperature did generate some additional reduction in antenna deformation. However, this additional benefit was very small. Further, if the tool closing speed was too high, it could result in unwanted effects, such as poor surface finish and material flow, as occurred in runs 7 and 10. Due to poor material flow, the percentage of reject parts increased significantly, making change to this variable unacceptable to the industry partner in this project.

In Table 7.4, it can be observed that the correlation between calculated values for antenna deformation and experimentally obtained values for antenna deformation was better for the standard values of tool closing speed and tool temperature, as in runs 1 to 4. Once the tool closing speed was increased to 6 mm/sec, as in run 7, or tool temperature was increased to 170

˚C, as in run 10, the correlation between calculated and experimental values reduced. This is possibly due to the fact that, while the material charge was heated up to 60 ˚C and then subsequently placed in the tool at 170 ˚C, some of the molecules started to cross-link very rapidly, resulting in uneven material flow. The behaviour of this uneven material flow was more difficult to predict using the material model developed as it did not take into account the degree of material cure and its effects on material viscosity, on which the shear stress ultimately depended.

7.12 Conclusion

Based on the above results obtained from the material model and experimental runs, it can be concluded that there is some degree of correlation between the two sets of results. However, the correlation decreases when extreme variable settings are used for tool closing speed and tool temperature. This can be corrected by incorporating some degree of material cure into the model to calculate material viscosity correctly and therefore the shear stress induced by the material flow onto the embedded antenna.

Small differences in the deformation observed among the different experimental samples could be explained by changes in the process factors, such as ambient temperature and initial temperature of the charge before it is loaded into the tool (some energy is lost during transfer from preheating oven to tool). In addition, a common manufacturing variation of SMC sheets in terms of fibre/filler/resin distribution per unit area would have a small effect on material flow and therefore on the amount of deformation of the antenna substrate. Further, for more elaborate antenna placements, such as near structural perturbations, the geometric end effects of the mould will need to be factored into the modelling as well as the effects of fibre orientation and fibre clumps formed during the process.

7.13 References

- Barone, R, M & Caulk, DA 1979, 'The effect of deformation and thermoset cure on heat conduction in a chopped-fiber reinforced polyester during compression molding', *International Journal of Heat and Mass Transfer*, vol. 22, no. 7, pp. 1021–1032.
- Barone, MR & Caulk, DA 1985, 'Kinematics of flow in sheet molding compound', *Polymer Composites*, vol. 6, no. 2, pp. 105–109.
- Barone, MR & Caulk, DA 1986, 'A model for the flow of a chopped reinforced polymer compound in compression molding', *Journal of Applied Mechanics,* vol. 53, no. 2. pp. 361–371.
- Bird, RB, Armstrong, RC & Hassager, O 1987, *Dynamics of polymeric liquids*, Wiley.
- Boylan, S, Abrams, LM & Castro, JM 2006, 'Predicting moulding forces during sheet moulding compound (SMC) compression moulding. II: effect of SMC composition', *Polymer Composites*, vol. 24, no. 6, pp.731–747.
- Castro, JM & Griffith, RM 1989, 'Sheet molding compound compression-molding flow', *Polymer Engineering and Science*, vol. 29, no. 10, pp. 632–638.
- Castro, JM & Tomlinson, G 1990, 'Predicting molding forces during sheet molding compound (SMC) compression molding. I: model development', *Polymer Engineering and Science,* vol. 30, no. 24, pp. 1569–1573.
- Hutter, K., Laloui, L. & Vulliet, L. 1999 'Thermodynamically based mixture models of saturated and unsaturated soils'. *Mech. Cohesive-Frict. Mater.* 4, 295–338.
- Jenkins, J. & Hanes, H. 1998 'Collisional sheet flows of sediment driven by a turbulent fluid'. *J. Fluid Mech.* 370, 29–52.
- Kohr, M. & Pop, I. 2004 '*Viscous incompressible flow for low Reynolds numbers*' Southampton: WIT press.
- Prosperetti, A. 2004 The average stress in incompressible disperse flow' *Int. J. Multiphase Flow* 30, 1011–1036.
- Savage, S. 1994 'Marginal ice zone dynamics modelled by computer simulations involving floe collisions' In *Mobile particulate systems* (ed. E. Guazelli & L. Oger), pp. 305–330. Carghese: Kluwer Academic ublishers.

- Werman, M. & Keren, D. 2001 ‘A Bayesian method for fitting parametric and nonparametric models to noisy data’ *IEEE Transactions on Pattern Analysis and Machine Intelligence* 23, 528–534.

CHAPTER 8: Development of Multi-Service Vehicular Antenna

8.1 Introduction

Most of the work presented in this chapter was undertaken with Mr Brendan Pell – Co-researcher on the project. Brendan was involved in antenna design, fabrication and testing.

While searching the antenna literature, it became clear that great advances have been made in wideband antennas throughout the years, particularly in the early part of the 21st century. This was due largely to the interest in the US Federal Communications Commission (FCC) ultra-wideband (UWB) scheme, announced in 2002 (Federal Communications Commission 2002). A survey of the automotive antenna literature and publicly available information on commercial vehicular antennas in production revealed that few people have considered the application of wideband antenna technology to the vehicular antenna domain.

Many present-day automobiles provide dedicated antennas for each of the radio or wireless services used in vehicles. This is necessary, since each antenna element tends to be only narrowband, capable of receiving signals across a fairly narrow frequency range. The antennas may be placed in different locations across the vehicle body, or may be housed together under a 'shark-fin' style radome. This relatively recent approach provides an attractive exterior component, but can lead to excessive mutual coupling between neighbouring antenna elements, distortion of radiation patterns, and high cabling costs due to the duplication of coaxial transmission lines. External antennas of this nature are also prone to damage, accidental or intentional, and add to a vehicle's aerodynamic drag and wind noise.

An alternative approach to vehicular antenna requirements would ideally decrease the component weight, reduce vehicle manufacturing costs, and provide an elegant solution to the challenge of fitting antennas for the

increasing number of wireless services. Rather than affix a specific antenna to vehicles for each narrowband service, a colour-matched radiating aperture could be created, containing a single antenna of wide impedance bandwidth, capable of providing all the necessary wireless capabilities of the vehicle. The concept of a wideband vehicular antenna presents an interesting research topic for antenna designers.

In modern wireless communication system design, antennas with wide impedance bandwidth are desirable for numerous reasons. An antenna with a wide impedance bandwidth may be used for transmission and reception of multiple narrowband services in a multi-purpose platform. Alternatively, a single wideband service may be of interest for various radar and imaging applications, or for impulse-based radio communications in the FCC UWB regime from 3.1 to 10.6 GHz. It is for the first reason mentioned here, in functioning across multiple narrowband services, that this work decided to pursue wideband antennas. Investigations into such a technology would provide an opportunity to break with the automotive antenna trends, and consider the application of UWB and wideband antennas in combination with polymeric composite structures. Such a combination would be attractive for reasons such as the following:

- It would offer the opportunity to investigate new types of antennas in a new configuration and application.
- It would offer the possibility of re-engineering the standard vehicular antenna configuration. In a world where wireless services are rapidly growing, both in number and in popularity, innovative approaches to the integration of antennas are worth investigating.
- It would lead to a reduction in vehicle manufacturing costs. This would be due to a combination of several factors, including:
- A reduction the number of antennas required in a vehicle: is it possible that a single wideband antenna component could meet all the communication needs of a vehicle?
- Reduced complexity: ‘shark-fin’ antennas consist of many complex parts and result in a much more expensive system than a printed

planar antenna. (As an example, four or more individual antennas are typically located inside the housing, which itself is typically composed of at least two parts. The associated rubber seals are required to make the whole assembly watertight. This is a much more expensive system to assemble than a planar printed antenna.)

- Shorter cabling runs inside the vehicle: a single wideband antenna could be connected with a single coaxial cable, replacing the four or more pieces of coax associated with alternative narrowband designs, and reducing costs and total vehicle weight.
- Wideband antennas provide ample bandwidth: they are therefore less likely to be shifted out of the desired band by variances in effective permittivity. Such changes in effective permittivity may be caused by natural variation within the manufacturing process. For example, changes to the effective permittivity of the space surrounding the antenna may be caused by variations in the thickness of the SMC panel, the presence of air gaps between the antenna and the panel, changes to paint chemistry or applied thickness, and changes in the location of the antenna on the panel. The paint investigation in Chapter 5 investigated the frequency shifting effect on an antenna when different paints of a variety of thicknesses are applied to an antenna superstrate. While the frequency shifting effect acts on both narrowband and wideband antennas to equal degrees, a wideband antenna is less likely to be shifted out of band. Hence, by choosing a wideband antenna, the sensitivity of the system to changes in the paint thickness or the permittivity of the polymeric composites can be reduced.

In addition to exploring wideband radiators applied to automotive applications, this chapter examines the additional benefits to the vehicle manufacturer and car purchasing consumer, such as:

- Reducing cost: by taking advantage of low-cost, mass-production printed circuit board (PCB) manufacturing techniques to produce the antenna element, costs will be reduced.

- Sustainability benefits: by integrating the antenna into an existing body panel, aerodynamic drag and therefore fuel consumption will be reduced. All things being equal, a wideband multifunction antenna would also consume fewer materials than would be required to create multiple narrowband antennas. In addition, where recyclable polymers are able to be used, further sustainability benefits may be found.
- Reducing accidental damage and vandalism: antennas that protrude from the vehicle body are likely to be snapped off by accident or by malicious intent. Relocating the radiating element into a dielectric polymeric composite panel reduces both accidental and intentional damage. Indeed, when painted, such a configuration would make it difficult even to identify the exact location of the antenna.
- Shortening the assembly time: if the antenna can be embedded into the body panel, the production time for each vehicle in the factory may be reduced. This is viewed favourably by car makers.
- Designing for single-sided antenna feed access: using a CPW to feed the antenna, or a probe-fed microstrip arrangement, would keep access and connection requirements simple.
- Using low-cost materials such as FR-4: the automotive industry thrives on high-volume, low-cost parts. Although FR-4 has a higher loss tangent than more expensive substrate materials, its use in automotive applications ought to be considered. Most of the automotive services of interest are concentrated at relatively low microwave frequencies below 6 GHz. It may be found that signal attenuation can be mitigated by designing short transmission lines, or that the losses are within acceptable bounds.

8.2 Antenna Considerations

8.2.1 Slot Dipole

The first antenna selected with the aim of obtaining a wideband vehicular antenna was the slot dipole (see Figure 8.1). The slot dipole is not wideband, its bandwidth is only 5%, but it was selected for the several advantages it provides over a traditional conductive dipole. Firstly, slot antennas tend to

have slightly wider bandwidth than their microstrip or conductor-based equivalents. They also tend to be less sensitive to changes in the near-field electromagnetic environment.

This was considered desirable in the automotive environment, where the antenna may be mounted to a non-conducting polymeric aperture. Compared to a traditional antenna, with a slot antenna, the effect of coupling to any nearby metallic conductors would be reduced, as would the effect of frequency shifting caused by tolerances in the permittivity of the polymeric material. A simple slot dipole was created, fed by a CPW. This allowed antenna metallisation to be restricted to a single side of a substrate, reducing manufacturing complexity and cost, and simplifying the edge feeding process. The slot length is the primary factor that influences the wavelength and therefore the frequency of operation. Tuning of the design is possible through adjustment of several basic geometrical factors. The width of the slot has some effect on the tuning, but its width is best left at a fixed value. The tip of the CPW feed terminates in a stub, resulting in a cross-shaped geometry, and this stub provides the most important factor in tuning the antenna. The length of this stub can be adjusted to provide a good impedance match to the 50 ohm transmission line. Additional capacitance can be introduced if desired, by causing the ground plane to encroach on the gap above the stub tip, but for the most part, this gap was left quite large.

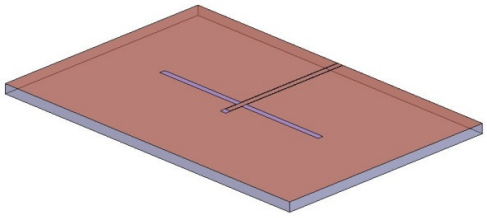

Figure 8.1: Slot dipole antenna

8.2.2 Wideband Bow-tie

The first wideband antenna design considered in this work was a slot bow-tie antenna; its bandwidth is 110%. Bow-tie antennas are well known and have a

long history. The gradual taper and thickening of the element leads to a wide impedance bandwidth antenna. Many symmetrical bow-tie designs exist, and these symmetrical designs most closely represent the case of the 3D biconical antenna, as shown in Figure 8.2. This design was selected, and scaled to a larger size to shift the frequency of operation using the well-understood properties of scaling and frequency shifting.

An examination of the bow-tie's geometry reveals that the antenna is quite similar in design to the CPW-fed dipole considered earlier. However, the slot is triangular, providing a taper, and the impedance matching section is no longer required.

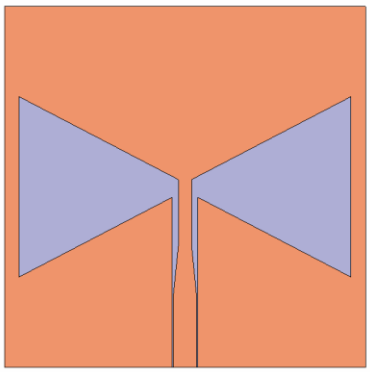

Figure 8.2: Wideband bow-tie antenna

8.2.3 Planar Inverted Conical Antenna

In 2004, Suh, Stutzman and Davis published their design of an antenna with very wideband, bandwidth of 165%, impedance bandwidth (Suh, Stutzman & Davis 2004). The authors termed the antenna the planar inverted cone antenna (PICA). This antenna consisted of a flat sheet of metal mounted vertically above a ground plane (see Figure 8.3(a)), similar to a traditional circular disc antenna, as cited by the authors. In contrast to an ordinary disc, the innovation of the PICA design was the combination of a half disc for the lower part of the antenna, in combination with a triangular upper portion.

Effectively, the upper portion of the circle has been trimmed on either side (see Figure 8.3(a)). The resulting PICA antenna produced a very wideband

impedance match in excess of 10:1, with radiation that approximated that of a monopole antenna over some of that band.

The authors also investigated the effect of slight adjustments to the edges of the PICA by fabricating teardrop-shaped antennas (see Figure 8.3(b)), and found the addition of circular-hole cut-outs in the lower part of the antenna to improve the radiation pattern without degrading impedance bandwidth (Suh, Stutzman & Davis 2004). The publication of this communication on the PICA antenna generated interest among those searching for UWB antennas. This is evidenced by the fact that the paper has received close to 200 citations within several years, at the conclusion of 2011. However, its 3D design, with the PICA element protruding from a ground plane, is not well suited for integration into modern portable communications devices.

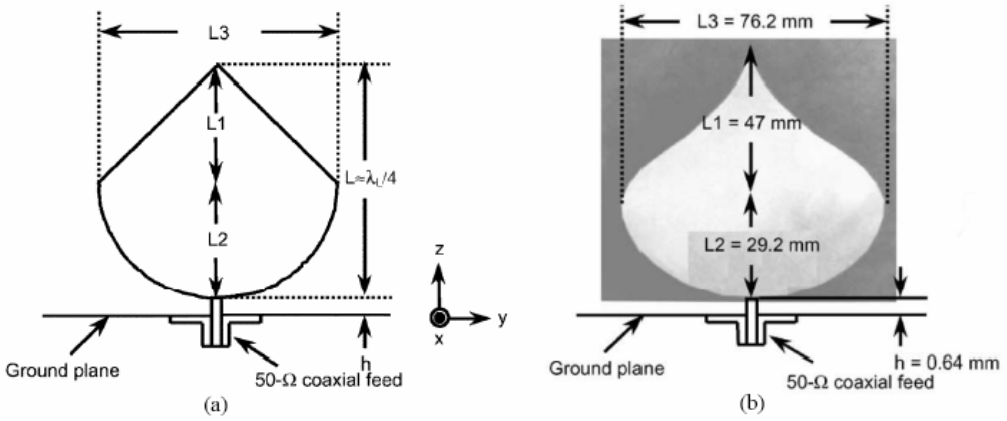

Figure 8.3: Geometry of original PICA antenna proposed by Suh, Stutzman and Davis 2004: (a) basic PICA geometry and (b) hardware test model of the PICA teardrop variation used in measurements

8.2.4 PICA—With Addition of a Slot

In an attempt to overcome the integration issues of the antenna proposed by Suh, Stutzman and Davis (2004), Cheng, Hallbjorner and Rydberg (2008) used the PICA geometry and created a planar PICA slot antenna.

The resulting antenna (see Figure 8.4) preserved the wideband nature of the PICA and was able to be fabricated on a PCB. It provides good radiation

performance and high efficiency over a very wide band. However, the design requires double-sided fabrication of a PCB, and, when used in conjunction with a coaxial cable and connectors such as SMA connectors, access is required to the edge of the substrate. This feature does not well suit integration into a polymeric composite panel.

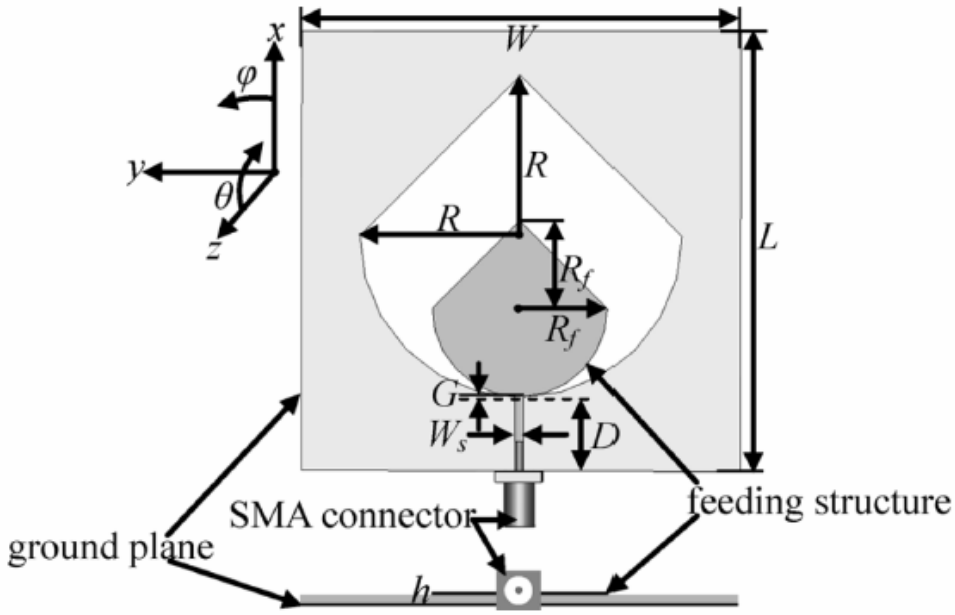

Figure 8.4: Geometry of slot PICA antenna proposed by Cheng, Hallbjorner and Rydberg (2008)—parameters: L = 60 mm, W = 60 mm, R = 22 mm, R = 12 mm, D = 10 mm, G = 0:1 mm, W = 1:22 mm (50 ω characteristic impedance), h = 0:5 mm

8.2.5 Uniplanar CPW-Fed PICA with a Slot

As a consequence of the promising performance of the PICA slot antenna, and despite its integration drawbacks for vehicular applications, it was decided to create a CPW-fed variant of the PICA slot design. This design modification required the whole antenna to be fabricated on only one side of a substrate (hence uniplanar, being confined to a single plane), rather than the double-sided configuration implemented by Cheng, Hallbjorner and Rydberg (2008), which has metallised features on two parallel planes, with one above and one below the substrate.

8.2.5.1 Antenna Configuration

The uniplanar CPW-fed PICA slot antenna is a wideband slot monopole based on the PICA shape proposed by Suh, Stutzman and Davis (2004). The PICA shape is a composition of a semicircle and an isosceles triangle, with the semicircle forming the lower portion of the antenna, and the triangle forming the upper part. In this slot adaptation of the PICA antenna, two PICA shapes may be found. Firstly, the ground plane has the copper removed in the shape of a large PICA to form a slot. This slot is then excited by a smaller PICA shape, which extends part way into the slot. The geometry of the antenna is shown in Figure 8.4. The dimensions presented in Figure 8.4 are optimised for a 0.4 mm thick FR-4 substrate with a relative permittivity ε_r = 4.0 and a loss tangent $\tan\delta$ = 0.013. The antenna is simulated using CST Microwave Studio utilising the transient solver.

The antenna utilises a cheap FR-4 substrate and requires only single-sided fabrication, yet maintains wideband performance.

8.2.5.2 Simulated and Measured Performance

The simulated and measured impedance performance of the CPW-fed PICA slot antenna is presented in Figure 8.6. According to the simulation, the antenna presented a good impedance match to a 50 Ω line from 1.2 GHz up to 15 GHz. The measured impedance response of the fabricated antenna showed a slight impedance mismatch around 13 to 15 GHz, but still obtained an impedance bandwidth of over 10:1 from 1.2 to 13.3 GHz.

The simulated maximum gain of the CPW-fed PICA slot antenna varied from 3.5 to 8.7 dBi with an average of approximately 7 dBi, as shown in Figure 8.7. Note that this gain was in the direction of maximum radiation, which varied depending on the frequency.

The simulated and measured radiation patterns at some common communication bands are depicted in Figure 8.8. These patterns displayed an omnidirectional shape at low frequency (see Figure 8.8(a) and (b)), which

became more directional at higher frequencies (see Figure 8.8(c)). Bidirectionality is evident in the y-z plane of Figure 8.8(c), as two distinct beams encroached upon end fire. There was significant correlation between measured and simulated patterns. High levels of cross polarisation were evident at ± 45° directions in the x-z plane, particularly at higher frequencies. This is typical of PICA slot antennas (Cheng, Hallbjorner & Rydberg 2008).

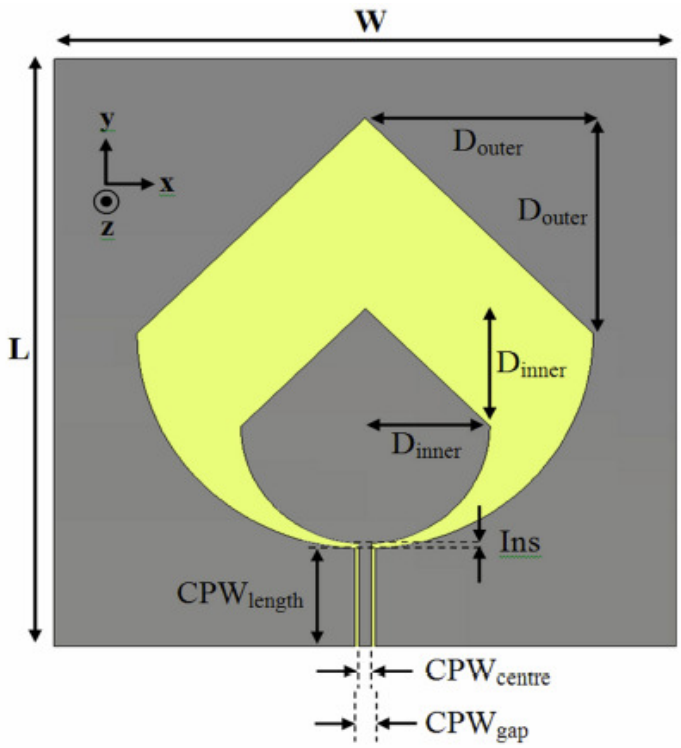

Figure 8.5: Geometry of the proposed CPW-fed PICA with a slot antenna
Parameters: L = 120 mm, W = 120 mm, CPW_{length} = 20 mm,
CPW_{centre} = 2.44 mm, CPW_{gap} = 2.84 mm, D_{outer} = 44 mm, D_{inner} = 24 mm,
Ins = 0.4 mm, h = 0.4 mm

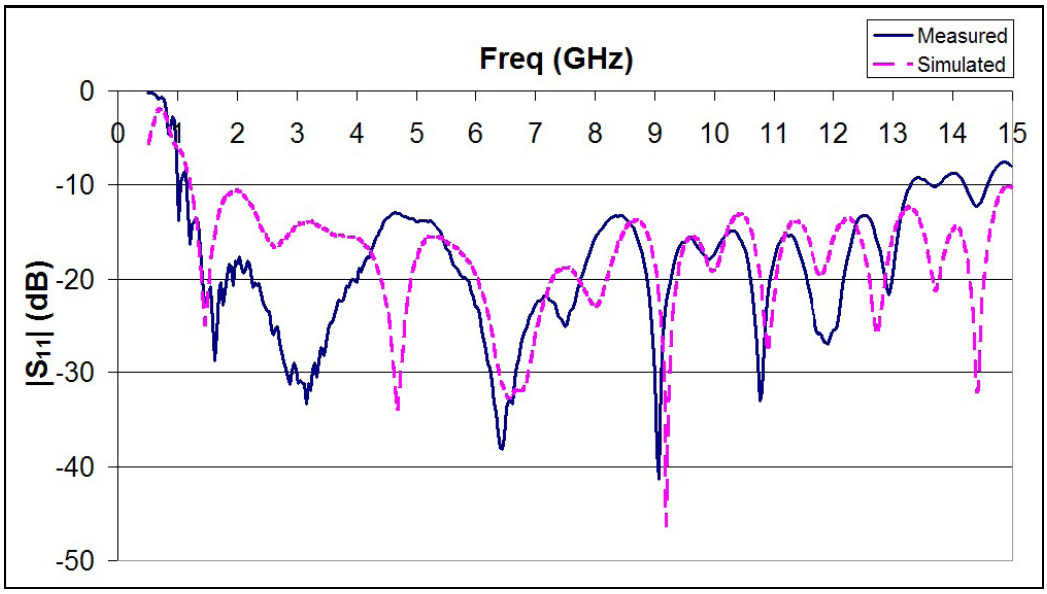

Figure 8.6: Measured and simulated reflection coefficient of the CPW-fed PICA with a slot antenna

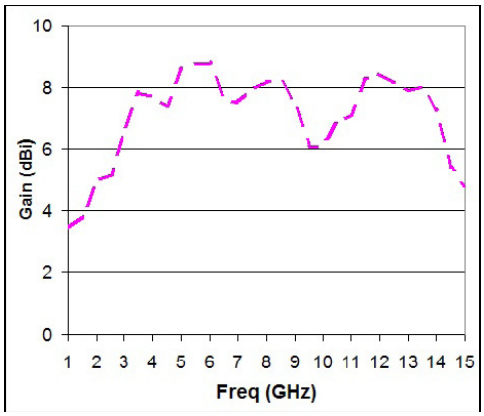

Figure 8.7: Simulated maximum gain v. frequency for the CPW-fed PICA slot antenna

The antenna as presented comfortably provides the necessary bandwidth for UWB of 3.1 to 10.6 GHz. If such an application were desired, substrate space could be conserved by scaling the antenna. Preliminary simulations show that a scaling factor of 0.375 applied to the PICA slot would produce substrate dimensions of 45 by 45 mm, providing impedance matching from 2.5 to 28 GHz.

A search of the literature reveals that a similarly structured CPW-fed PICA slot antenna has been attempted previously (Gupta, Ramesh & Kalghatgi 2006), albeit with several shortcomings. The paper presents two adaptations of the PICA antenna, the second being closest to the geometry presented here. Despite the similarities, the antenna design by Gupta, Ramesh and Kalghatgi (2006) uses a grounded CPW, necessitating double-sided fabrication techniques, and has a teardrop-shaped slot. Although the substrate dimensions and material used are almost identical, their antenna has a narrower bandwidth: the impedance bandwidth starts at around 3 GHz, and the reflection coefficient results reveal a further mismatch near 5 GHz. In contrast to this design, the uniplanar CPW-fed PICA slot antenna provides over an octave of additional bandwidth, with a well-matched response down to approximately 1.2 GHz.

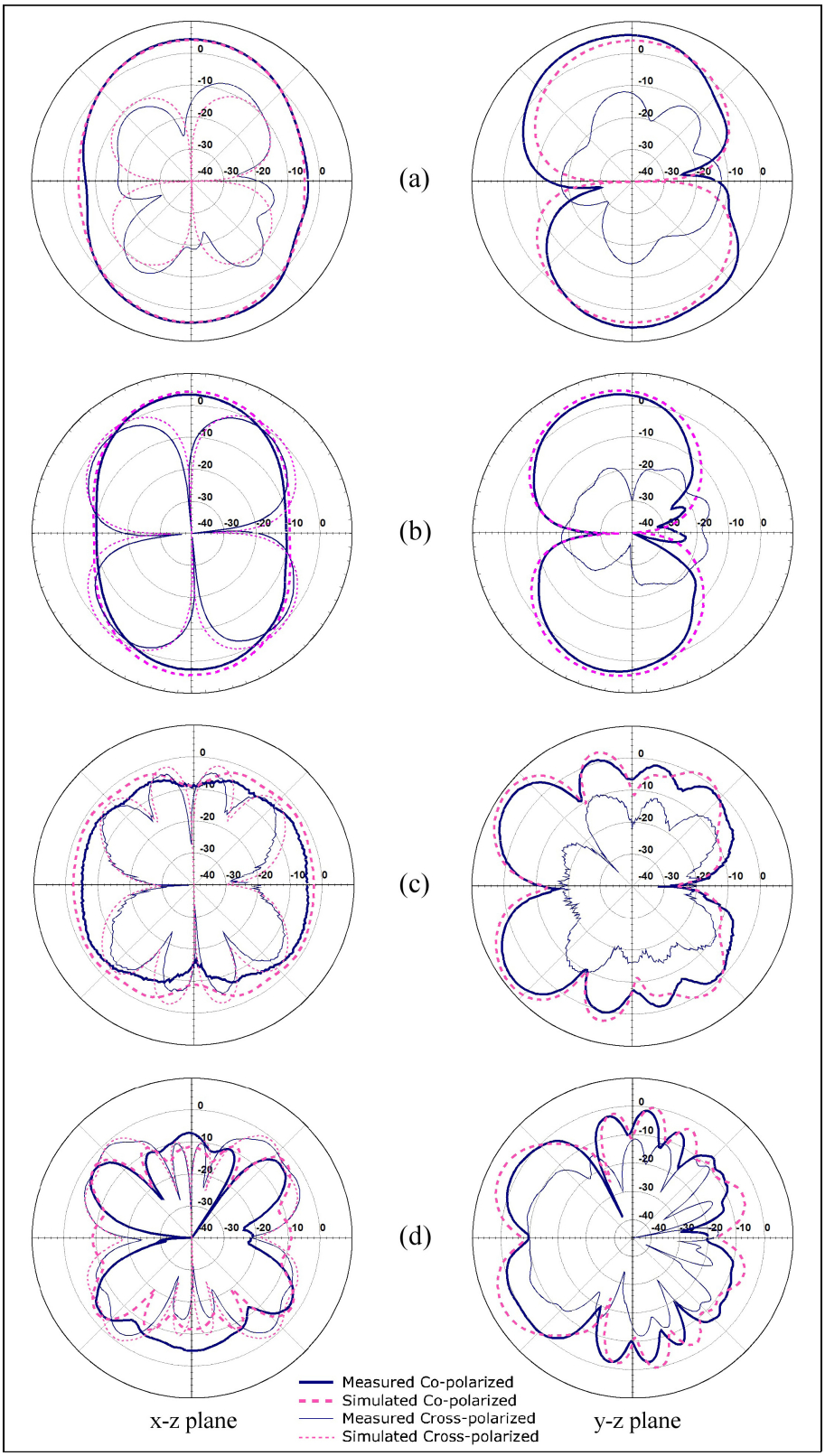

Figure 8.8: Far-field radiation patterns of the CPW-fed PICA with a slot antenna: (a) 1.575 GHz, (b) 2.4,GHz, (c) 5.9 GHz and (d) 9.5 GHz

Therefore, a CPW-fed slot antenna has been presented that is based on the PICA. The PICA's wide impedance bandwidth behaviour has been preserved, demonstrating impedance bandwidth in excess of 10:1. Omnidirectional radiation is exhibited at the lower end of the impedance bandwidth. Notably, the CPW-fed PICA slot antenna presented here is truly uniplanar, requiring only single-sided substrate processing. Uniplanar antennas can be extremely advantageous in certain applications. This antenna underwent trial integration into a vehicular body panel. The findings are presented in Chapter 9.

8.2.6 Scaled Uniplanar CPW-fed PICA

Having created a wideband antenna suitable for automotive use (that is, configured to provide easy integration with polymeric composite body panels, and providing ample impedance bandwidth to cover many services simultaneously), it was necessary to target the design to those frequencies of interest in the automotive environment (see Table 8.1).

It is well known that scaling an antenna's dimensions can produce similar performance at a shifted frequency band. With this aim in mind, we found that an optimal configuration would be achieved if we increased the antennas dimensions to occupy a substrate of 200 by 200 mm. This represents a scaling factor of 5 over 3 (or about 1.67), and results in the geometry shown in Figure 8.9. The scaled antenna has an impedance match down to 730 MHz. This provides a wide range of usable frequencies and covers many of the desired bands in the automotive realm, as listed in Table 8.1. It would likely be possible to scale the antenna up to much larger sizes to accommodate frequencies lower than 730 MHz; however, consideration must be given to the desired radiation patterns at the frequencies of interest, along with the practical concerns regarding the ease of fabrication, handling and integration.

The designer must also evaluate the importance of those services not facilitated by the scaled PICA antenna, and whether or not small existing antennas may suffice for these roles. For example, AM/FM services extend

from approximately 1 to 100 MHz. Using the present PICA design would require an antenna size that would be impractical (many meters in width and length); as such, a separate AM/FM antenna would be required. However, this may be readily provided by an on-glass antenna in the rear windscreen or similar. These antennas are already well developed and commercially available.

The scaled UWB antenna of Figure 8.9 is a good starting point for a wideband vehicular antenna. It clearly has ample provision in its impedance response for many of the vehicular frequency bands in use today, plus an excess for any applications that may arise in the future in the region up to and beyond 10 GHz.

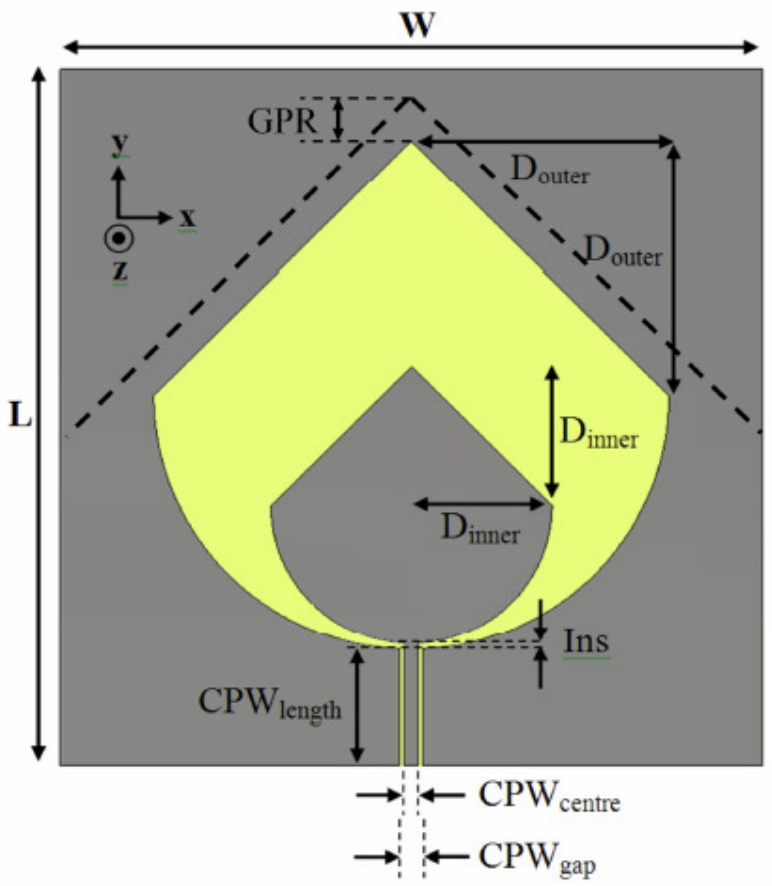

Figure 8.9: Geometry of the baseline enlarged uniplanar CPW-fed PICA

Parameters: L= 200 mm, W = 200 mm, CPWlength = 33.3 mm, CPWcentre = 2.84 mm, CPWgap = 3.24 mm, Douter = 73.3 mm, Dinner = 40 mm, Ins = 0.67 mm, h = 0.4 mm

GPR does not feature in the original design, but is drawn here for clarity.

8.2.6.1 Radiation Mechanism

Simulated radiation patterns of the enlarged PICA vehicular antenna are shown in Figure 8.11. Five key frequency bands of interest have been chosen to characterise the antenna performance. The selected frequencies are spread across the antenna's bandwidth, and where possible, align with those services used in the vehicular environment (see Table 8.1). Taking into account the frequency shifting effect of the scaling of the antenna, these results reveal a similarity with those presented for the smaller original design of Section 8.2.5.2.

Table 8.1: Services in operating range of scaled PICA

Service Name	Frequency	Terrestrial	Satellite
Cellular Phone (and mobile internet over HSPA)	850 MHz	Yes	
Cellular Phone	900 MHz	Yes	
Global Positioning System (GPS)	1.575 GHz		Yes
Cellular Phone (and mobile internet over HSPA)	1.7-2.1 GHz	Yes	
Satellite Digital Audio Radio Service (SDARS)	2.3 GHz	Yes*	Yes
802.11 b/g/n Wi-Fi	2.4 GHz	Yes	
Bluetooth	2.4 GHz	Yes	
WiMAX	3.5 GHz	Yes	
DSRC, V2V, VII, 802.11p	5.9 GHz	Yes	

*Terrestrial transmitters are located in some downtown areas.

An examination of the figures reveals that the radiation behaviour of the PICA changes significantly throughout the operable frequencies. At low frequencies (8.11(a) and (b)), the antenna produces double-sided radiation that is typical of a slot antenna (Brian, Guo & Shi 2008; Yoshimura 1972). At high frequencies (see Figure 8.11(d) and (e)), the radiation appears to be more like that produced by a pair of tapered slots (Kim & Kwon 2005). In the middle of these two bands, the antenna seems to be in a mixed mode of radiation (8.11(c)). It appears that the dimensions of the PICA, and the precise tuning of its parameters, lead to two different modes of operation that may be combined, together producing a single wideband impedance response with alternate radiation patterns. To investigate this mechanism, antennas that we shall call the low-frequency equivalent (LFE) and high-frequency equivalent (HFE) were investigated.

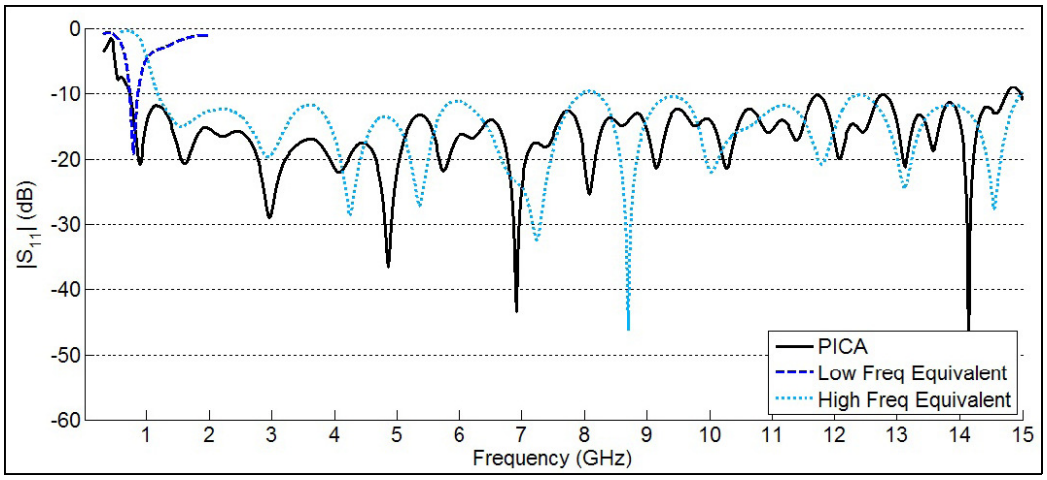

Figure 8.10: Simulated reflection coefficient of the PICA, LFE and HFE antennas

8.2.6.2 Low-Frequency Equivalent

At low frequencies, the PICA creates bidirectional radiation, with two diametrically opposed beams at broadside to the antenna substrate and a minimum in the direction of the y-axis. To explain the low-frequency behaviour of the PICA antenna, the LFE antenna was created, as depicted in 8.12(a). It is a reconfiguration of the PICA antenna, created by using the existing PICA-shaped slot in the ground plane. However, the inner PICA-shaped conductor is replaced with a straight CPW stub line, which excites the slot. The change in geometry results in an LFE antenna similar in design to the one reported by Brian, Guo and Shi (2008), but without the second feed and power divider used to obtain circular polarisation. Simulations using CST Microwave Studio show that the LFE antenna yields the expected low-frequency operation. Figure 8.10 shows the simulated reflection coefficient of both the PICA and the LFE. The antenna begins to match at the same frequency as the PICA, being approximately 730 MHz. The LFE, however, displays only a 16% impedance bandwidth up to 860 MHz. The high-frequency performance has been lost. Radiation performance of the LFE is examined at 850 MHz (see Figure 8.13(a)), and is found to be similar to the PICA's radiation at 850 MHz (8.11(a)). Hence, the LFE antenna has similar radiation performance to the PICA at low frequencies, but is narrowband. The

frequency of operation in this configuration is a function of the slot dimensions and the stub length.

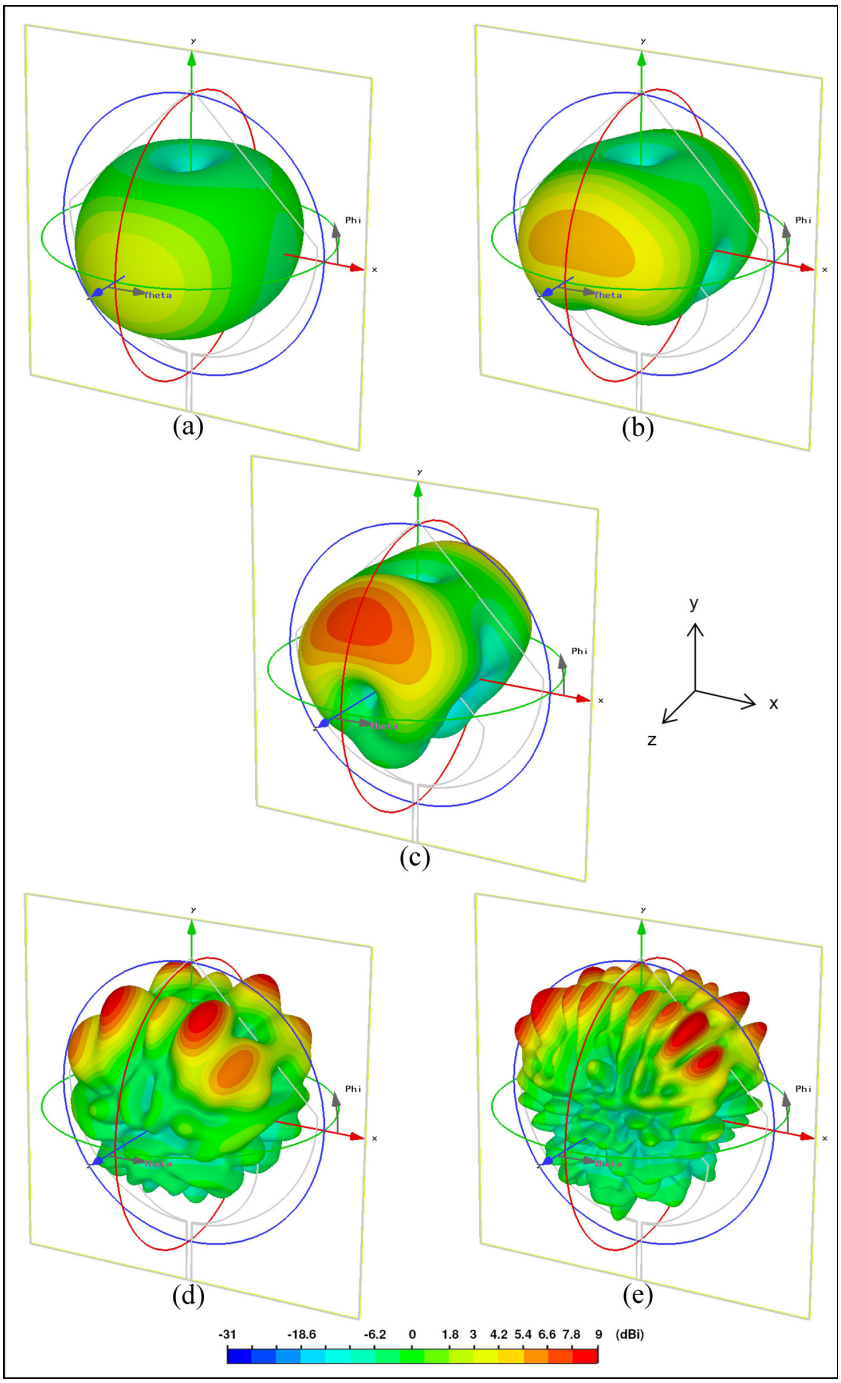

Figure 8.11: Simulated 3D radiation patterns of the enlarged uniplanar CPW-fed PICA: (a) 850 MHz, max gain is 3.9 dBi, (b) 1.575 GHz, max gain is 5.7 dBi, (c) 2.4 GHz, max gain is 8.1 dBi, (d) 5.9 GHz, max gain is 9.6 dBi and (e) 9.5 GHz, max gain is 11 dBi

8.2.6.3 High-Frequency Equivalent

At higher frequencies, the radiation pattern of the uniplanar CPW-fed PICA is substantially different to the low frequencies. Observation of the radiation patterns suggests that the PICA appears to behave in a manner that is similar to a pair of exponentially tapered slot antennas fed from the single CPW feed. The main beams are no longer at broadside, but are encroaching upon end fire. To verify the operation of the PICA at high frequencies, a second generalisation of the PICA antenna was created, shown in Figure 8.12(b). The HFE antenna is similar to the PICA except that the metallic conductors have been removed from the upper portion of the PICA substrate, leaving two open-ended tapered slots fed by a CPW. This modification results in an HFE antenna with the wide bandwidth typical of tapered slot antennas, yet it has lost the extreme low-frequency performance of the PICA (see Figure 8.10). Simulated 3D radiation patterns reveal that, at 9.5 GHz, the radiation of the HFE (see Figure 8.13(b)) is similar to the PICA at the upper end of its band (see Figure 8.11(d) and (e)). It is worth noting that several known antenna designs exist that utilise a CPW to feed two tapered slot antennas in a manner similar to the HFE (Kim & Kwon 2005; Sun, Lee & Lin 2007).

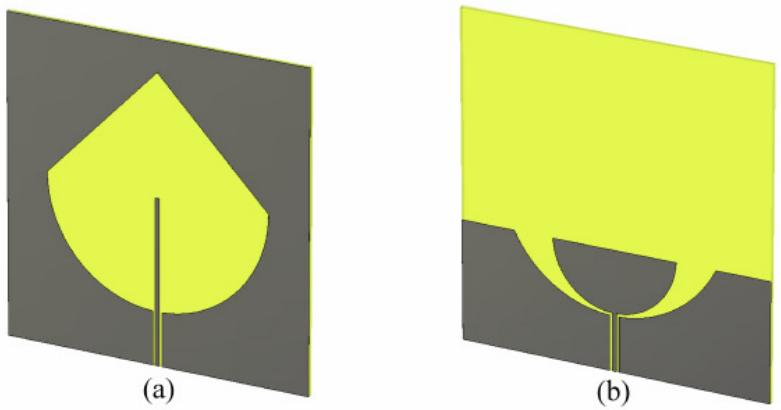

Figure 8.12: Equivalent geometries for: (a) LFE and (b) HFE

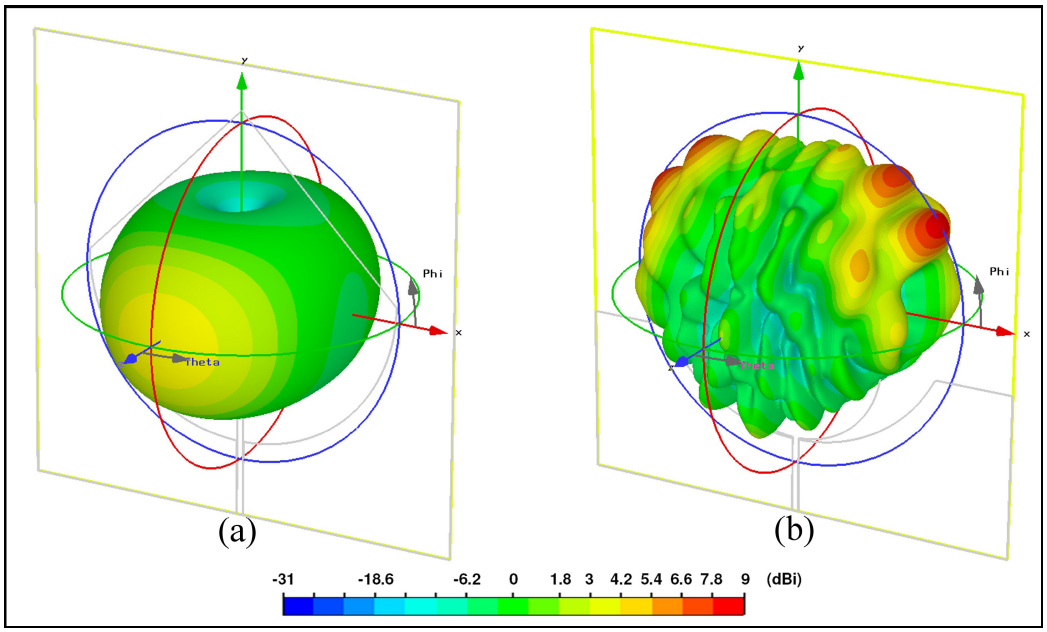

Figure 8.13: Simulated 3D radiation patterns of the equivalent antennas (a) LFE, max gain is 4.7 dBi and (b) HFE, max gain is 9.2 dBi

8.2.6.4 Understanding PICA Operation

An analysis of the behaviour of the uniplanar CPW-fed PICA slot antenna and comparison to LFE and HFE antennas enables an explanation of the behaviour of the PICA. It seems reasonable to infer that the PICA's extremely wide bandwidth is a result of a combination of two primary modes of operation. At low frequencies, when the wavelength is long, the precise shape of the feed is of little importance. Both the PICA and the LFE antenna radiate like a traditional open slot antenna. At high frequencies, the upper portion of the PICA is of lesser importance (although it does have some effect, particularly on radiation behaviour). Instead, the gradual taper between the inner PICA and outer PICA shapes is key for supporting the radiation that originates in what is effectively a tapered slot.

8.2.7 Investigation of Design Parameters Affecting Antenna Performance

This section provides an investigation into the design parameters of the PICA, examining how radiation performance may be controlled through parameter selection.

CST Microwave Studio was used to simulate a variety of antenna configurations, with an aim of tailoring the design to create an optimum configuration for the wideband automotive situation. Figure 8.14 shows the various geometries investigated. Four essential parameters were investigated: the insertion depth (see Figure 8.14(a)), the size of the inner PICA shape (see Figure 8.14(b)), the aspect ratio (AR) (see Figure 8.14(c)), and the thickness of the upper portion of the ground plane (see Figure 8.14(d)) shown by the parameter GPR in Figure 8.9.

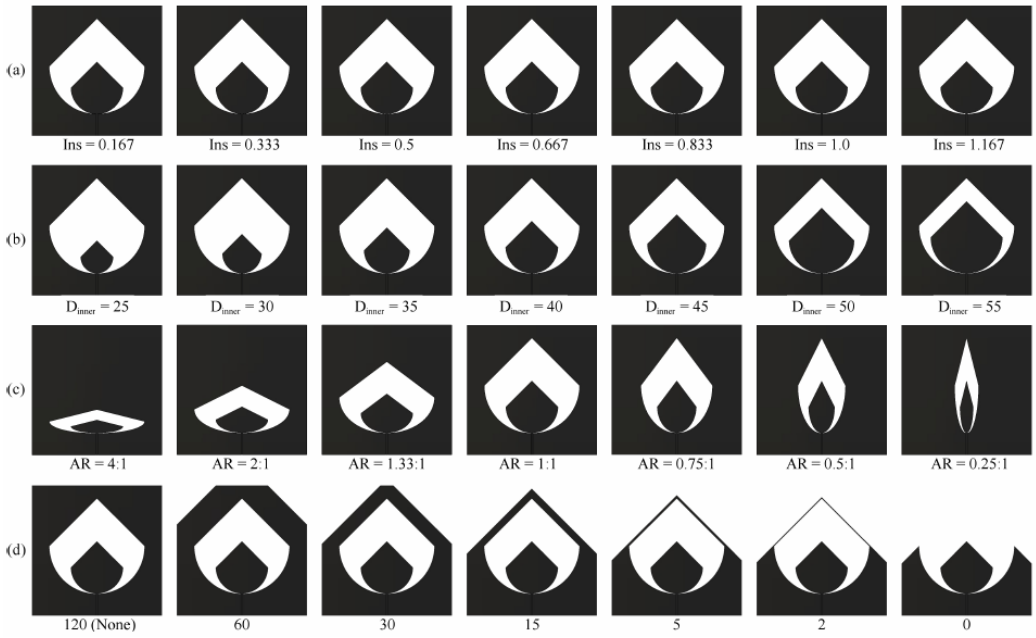

Figure 8.14: Geometry of antenna for parameter sweeps: (a) insertion depth, (b) relative size, (c) AR and (d) ground plane removal

8.2.7.1 Insertion Depth

The parameter 'Ins' labeled in Figure 8.9 symbolises the insertion depth of the smaller inner PICA into the outer PICA. It represents a degree of freedom in the uniplanar CPW-fed PICA slot antenna design. The range of values investigated here is quite small, varying from 0.167 to 1.167 mm, with resulting geometry shown in Figure 8.14(a). Although this range of values represents a total range of only 1 mm from smallest to largest, it produced significant effects on the impedance response of the antenna (see Figure

8.15(a)), revealing that this is a highly sensitive parameter. As the value of 'Ins' approaches zero, the geometry leads to a near overlap at the stem of the two PICA shapes. To continue this action to the extreme would result in a shorting of the centre of the CPW transmission line to ground, thus interfering with proper operation. A large value of 'Ins' is also disruptive to proper operation, particularly the impedance matching, creating a step change in the impedance at the end of the transmission line. Values in the range of 0.333 to 0.667 mm provide a wideband impedance match. Figure 8.15(b) plots the value of gain produced by the antenna in the maximum direction of radiation as the geometry is varied. The parameter 'Ins' can be observed to have very little effect on antenna gain.

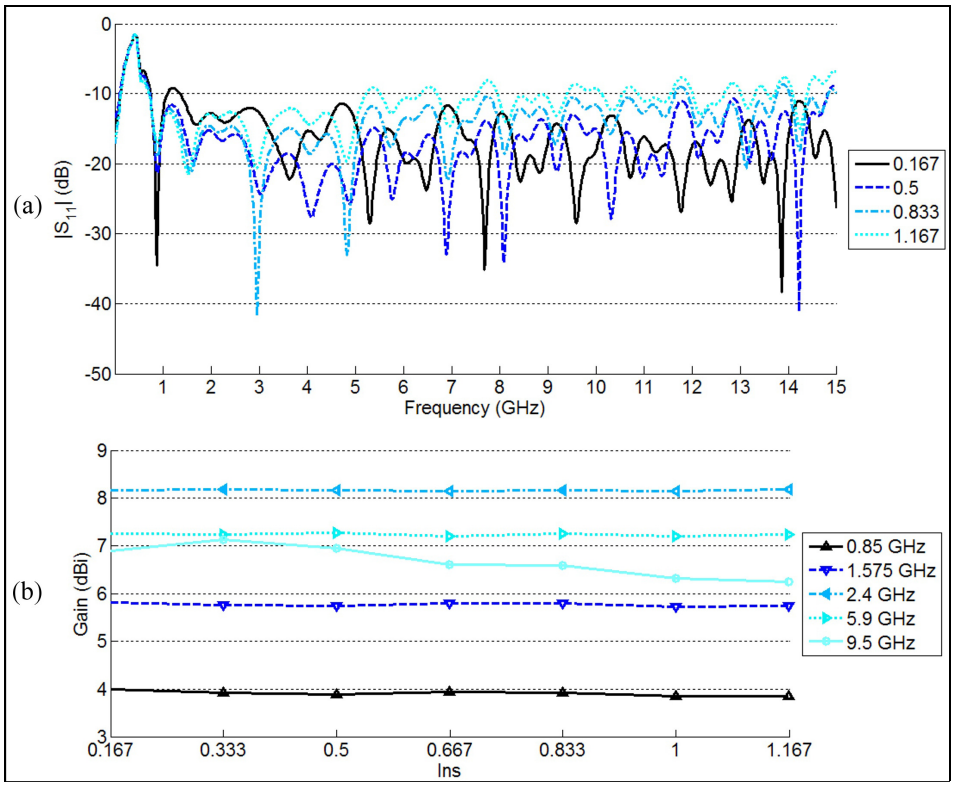

Figure 8.15: (a) Reflection coefficient and (b) max gain for Ins variation

Examining the curves of Figure 8.15(b) reveals that, of the five frequencies of interest, the gain at only one of these frequencies was affected by varying this parameter, and that only moderately, since the effect on the gain was small, being less than 1dB.

8.2.7.2 Relative Size of the Two PICA Shapes

A second degree of freedom in tuning the design of the uniplanar CPW-fed PICA slot antenna is the relative sizes of the two PICA shapes. Rather than varying both of the PICA shapes together, the larger PICA defined by D_{outer} was left unchanged, and D_{inner} was swept through a range from 25 to 55 mm. A sweep of D_{inner} through this range produces significant change in antenna geometry, as shown in Figure 8.14(b). In contrast to the value of Ins, it can be observed that the majority of the configurations of different sizes achieve a wideband impedance match (see Figure 8.16). In fact, all values investigated achieve a good match between 2 and 11 GHz. Decreasing D_{inner} leads to a progressive creep in the low-frequency cut-off (using a –10 dB reflection coefficient), shifting from approximately 520 MHz when D_{inner} is 55 to about 980 MHz when D_{inner} is 25 mm. The requirements for wireless operation at low frequencies, notably the inclusion of the important 850 MHz Universal Mobile Telecommunications System (UMTS) band, may determine which values are acceptable here. In addition, using a value for D_{inner} of 55 mm presents some mismatches at the extreme low end of the band, from 0.9 to 1.2 GHz, and from 1.5 to 1.8 GHz. Nonetheless, a suitable impedance match is obtained from 2 to 11 GHz for most values of D_{inner}.

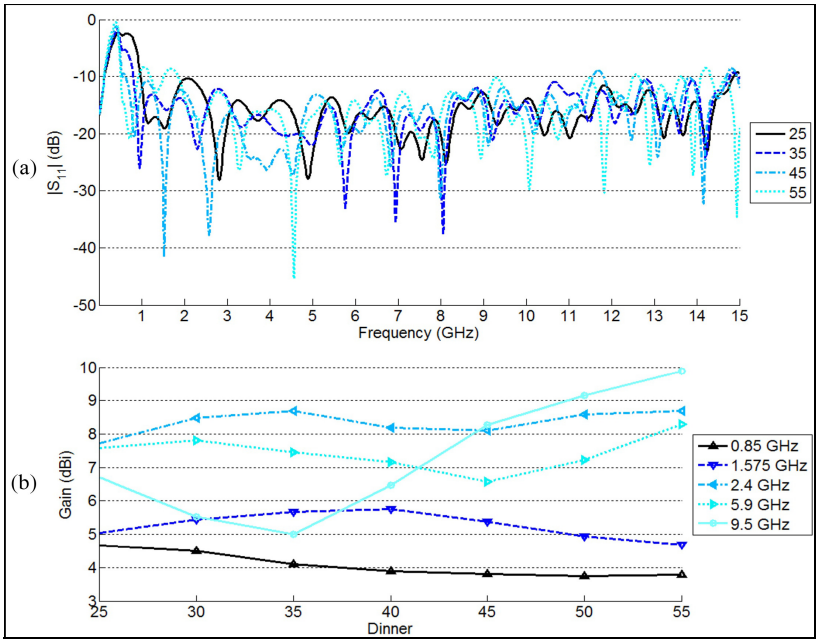

Figure 8.16: (a) Reflection coefficient and (b) max gain for D_{inner} variation

An examination of Figure 8.16(b) reveals significant potential to tailor the gain of the antenna using the relative sizes of the PICA shapes, particularly at 9.5 GHz, where we see a variation in gain from 5 to 9.8 dBi. The reflection coefficient of Figure 8.16(a) shows that, at 9.5 GHz, all values of D_{inner} satisfy the –10 dB |S11| impedance requirement. Therefore, we conclude that the increase in gain is due purely to increased directivity of the antenna at 9.5 GHz. This supports the theory of the modes of operation of the PICA, where increasing D_{inner} results in a lengthening of the tapered slots, and hence a progressive increase in gain and directivity at the upper end of the band.

8.2.7.3 Distortion of the Aspect Ratio of the PICA Shapes

In the original PICA design, the length and width are equal, giving an AR of 1:1. A third parametric investigation performed on the uniplanar CPW-fed PICA slot antenna explored the possibility of alternative ARs (see Figure 8.14(c)). For simplicity, the AR is presented as a decimal number, and has been defined as width divided by height. The resulting geometries are scaled so ARs greater than 1:1 maintain a constant width, and aspect ratios less than 1:1 maintain a constant height. Therefore, in the figures, an AR of 0.25 implies the ratio 0.25:1. In this AR, the PICA's width is one-quarter of its height—the width has been reduced by a factor of four to create a tall, skinny shape. Likewise, an AR denoted 1.33 implies the ratio 1.33:1. Here, the width to height ratio has been altered to create an overall shape width that is 1.33 times wider than the height. To achieve this AR without increasing substrate space, the height of the shape is reduced by a factor of 0.75 in order to obtain the correct proportions.

The performance of the antenna when its AR is distorted produces vastly different results, as shown in Figure 8.17. Of particular note is the loss of wideband matching for both extremely low (0.25:1) and extremely high (4:1) ARs. At 1.2 GHz, for example, only the 1 and 1.33 ARs achieve the required –10 dB reflection coefficient. Close inspection reveals that ARs greater than one display a narrow resonance at 900 MHz. The persistence of the impedance match at this frequency is readily explainable. As the AR is increased, the shape created becomes similar to a folded slot dipole antenna.

The height is reduced, but the width of the slot remains constant and corresponds to approximately half a wavelength at 900 MHz. In general, small variations in AR provide a suitable match throughout the centre of the band. Figure 8.17(b) shows again that the lengthening of the tapered slots that occurs at the lower ARs tends to result in increased gain at the higher frequencies of 5.9 GHz and 9.5 GHz. High-aspect-ratio PICA shapes result in a low gain of about 0 dBi, and low-aspect-ratio shapes result in higher gain exceeding 10 dBi.

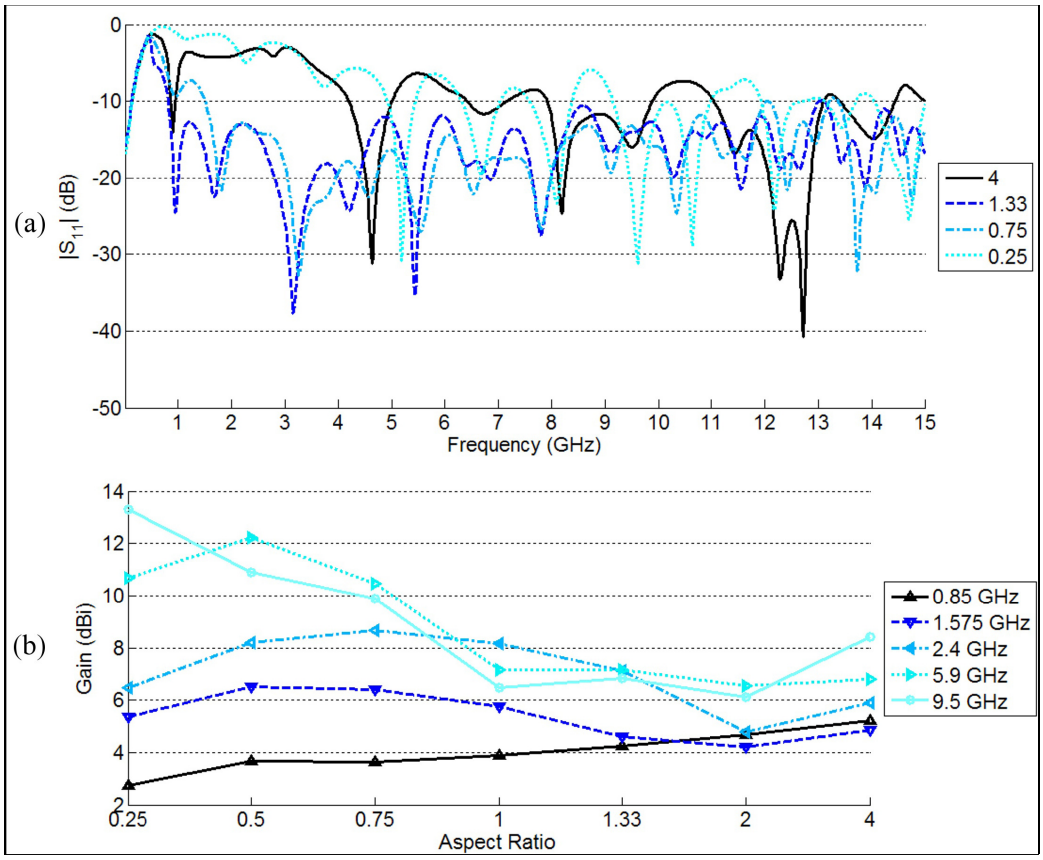

Figure 8.17: (a) Reflection coefficient and (b) max gain for AR variation

8.2.7.4 Ground Plane Removal

The method of operation of the uniplanar CPW-fed PICA slot antenna discussed in Section 8.2.6.1 raised an interesting question: how much ground plane is required on the border of the slot for good operation?

To investigate this question, a simulation model was created that enabled triangular sections of the ground plane to be removed from the upper area of the PICA antenna (see Figure 8.14(d)). The distance between the tip of the vertex of the PICA and the edge of the ground plane was parameterised with the term GPR to enable a number of conductor-free distances to be inspected. Two trends are visible in the reflection coefficient and gain results of Figure 8.18.

Firstly, as the width of the ground border approaches zero, the low-frequency matching begins to deteriorate, particularly at around 1.2 GHz (see Figure 8.18(a)). If the border has a width less than 30 mm, the result is a slight mismatch at the low end of the band. Removal of the border altogether (the 0 mm case) results in a dual-band antenna, matched from 1.5 to 2.1 GHz, and then from 2.5 GHz to almost 15 GHz. A very thin border of 2 mm preserves a moderate impedance match, better than 10 dB above 1.4 GHz, and better than 7.5 dB in the range of from 750 MHz to 1.4 GHz. Although an impedance match resulting in the |S11| being 7.5 dB would normally not be tolerated, some manufacturers may deem this value adequate. A 6 dB match is considered sufficient for mobile phone handset antennas by many in that industry, and this mismatched portion of spectrum falls within the band to be used for that purpose. In fact, the performance at the worst location still exceeds the 6 dB requirement by 1.5 dB.

Secondly, it can be observed that decreasing the width of the upper border tends to reduce the maximum value of gain (see Figure 8.18(b)), while widening the beamwidth. This same behaviour can be observed at 2.4 GHz, and at 1.575 GHz to a lesser extent.

Figure 8.19 shows the 3D radiation patterns at 5.9 GHz for two different cases in the ground plane investigation. In Figure 8.19(a), the radiation pattern corresponds to the case where the ground plane is at full size, unchanged from the baseline PICA shape, while Figure 8.19(b) shows the truncated ground plane case of 0 mm. Both figures also show the corresponding geometries in a faint outline.

The baseline PICA geometry produces the radiation pattern shown in Figure 8.19(a) with nulls in the plane of the antenna substrate. Drawing upon the theory of operation covered in Section 8.2.6.1, we recall that, at high frequencies, the PICA operates in a manner similar to a pair of tapered slots. This would normally produce a beam in the plane of the substrate (see Figure 8.19(b)). In the PICA case, the radiation is split into beams both above and below the substrate by the presence of the ground plane. Decreasing the width of the ground plane, or removing it altogether, tends to soften this bifurcated type of radiation, removing the central null. This is illustrated in Figure 8.19(b), where the upper ground plane is removed, and 8.13(b), where the upper portion of the antenna is truncated to create the HFE.

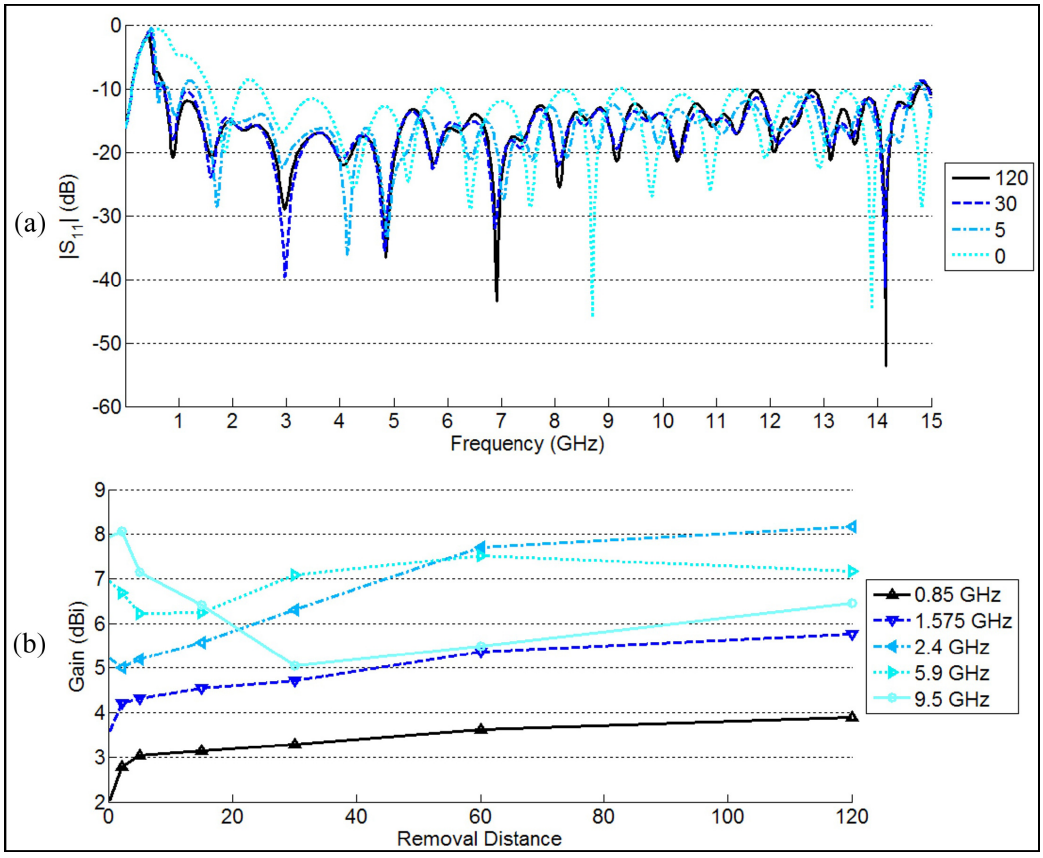

Figure 8.18: (a) Reflection coefficient and (b) max gain for ground plane removal

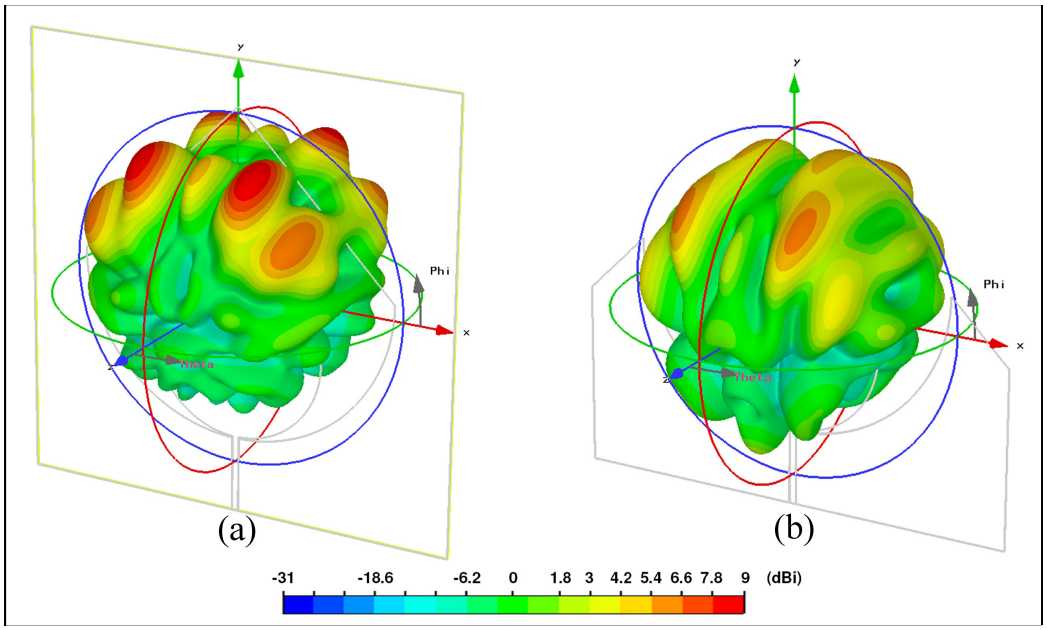

Figure 8.19: 3D radiation patterns at 5.9 GHz for GPR values of (a) 120 mm and (b) 0 mm

8.2.7.5 Summary of Antenna Behaviour and Parameter Effects

The wideband performance achieved in the uniplanar CPW-fed PICA is due to two primary modes of operation. The gradual taper between the inner and outer PICA shapes forms a pair of tapered slots that support high-frequency operation, and produces maximum gain in the direction of the slot openings. At low frequencies, the slot that is formed in the ground plane by the larger PICA shape dominates the antenna behaviour, producing maximum gain at broadside to the substrate. The combination of these two modes extends the bandwidth of the antenna beyond that of either mode alone, and creates distinctly different radiation patterns at the upper and lower ends of the band. These two radiation patterns may provide significant benefit for multi-service operation in the vehicular environment. The PICA could be embedded in a vehicle roof, and employed for GPS operation at 1.575 GHz, providing reception of satellite signals from above, while simultaneously communicating with vehicles or roadside infrastructure in the horizontal direction at 5.9 GHz. Varying 'Ins' in the PICA design created no significant change in gain or radiation performance, but varied impedance matching significantly. Alteration of the relative sizes of the two PICA shapes, achieved by modification of the

parameter $D_{inner,}$ resulted in geometries that, for the most part, achieved acceptable impedance matching, yet allowed for selection of the high-frequency gain between 5 and 10 dBi. Modification of the AR of the shape had an effect on both impedance and radiation performance. Geometries of lower AR are inclined to produce higher gain, particularly at the upper end of the band. Gradual removal of the upper portion of ground plane preserves an acceptable impedance match at the upper end of the band, while introducing a rising mismatch below 1.4 GHz, and tends to reduce the null present in the x-y plane end-fire radiation of the original design.

8.3 The Truncated PICA Antenna

The truncated PICA antenna (see Figure 8.20) represents an intermediate stage in the development of the enlarged uniplanar CPW-fed PICA slot antenna Section 8.2.6.1. The parameter analysis work provided an understanding of the method of radiation of the antenna, describing the antenna performance in terms of a combination of behaviours from two well-known classes of antennas. At the low end of its band, the PICA radiates a low-gain broad beamwidth pattern like a traditional slot antenna, while at the upper end of the band, the PICA behaves like a tapered slot antenna, creating high gain in the direction of the opening of the slots. However, in the original design, the presence of a thick ground plane at the end of the slot opening causes an undesirable split in the radiation pattern in the plane of the substrate. Hence, it was decided to truncate the upper portion of ground plane, as shown in Figure 8.20 (represented by the parameter 'GPR'). Note that the other parameters were left essentially unchanged. The dark grey areas of Figure 8.20 represent the metallised sections of the antenna, while the light green areas show an absence of conductive metal, revealing the FR-4 substrate on which the antenna is constructed. Figure 8.21 shows the radiation pattern of the antenna, both with and without the truncated ground plane. Cartesian coordinates and a thin grey outline of the antenna conductors are drawn to provide orientation. Where the ground plane is kept at the full size, the main beams of radiation can be observed to be split above and below the substrate, with a null in the x-y plane. Removal of a portion of

the ground plane in the manner prescribed increases the gain in the plane of the substrate, and results in a decrease in the value of peak gain by approximately 2 dBi. This corresponds with the reduction in directivity due to the broadening of the beamwidth at this frequency. The modification is advantageous for application in vehicles because, if installed horizontally in a section of bonnet, roof or trunk, the antenna with the truncated ground plane will provide higher gain at 5.9 GHz in the direction of the horizon where roadside beacons or other vehicles are likely to be located. Therefore, the truncation of the ground plane enables the electromagnetic energy to be directed where it is needed at the upper end of the antenna's frequency range. The truncated PICA automotive antenna is flat and low profile, printed on a single side of an industry standard FR-4 PCB material substrate. The fabricated structure is 0.4 mm thick, enabling it to be attached to, or embedded in, polymeric components. It occupies an area of 190 by 200 mm and provides a good impedance match to a 50 Ω transmission line at each of the frequencies mentioned in Table 8.1. This intermediate stage applies some of the knowledge gained in the parametric sweep, but is not the optimal PICA design for vehicular applications.

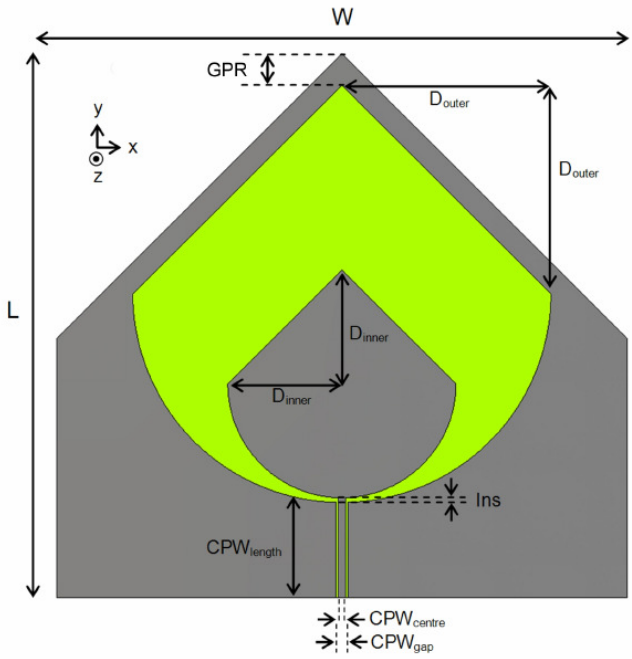

Figure 8.20: Geometry of the truncated PICA

Parameters: L = 190 mm, W = 200 mm, CPW_{length} = 33.3 mm, CPW_{centre} = 2.84 mm, CPW_{gap} = 3.24 mm, D_{outer} = 73.3 mm, D_{inner} = 40 mm, Ins = 0.67 mm, GPR = 10 mm, h = 0.4 mm

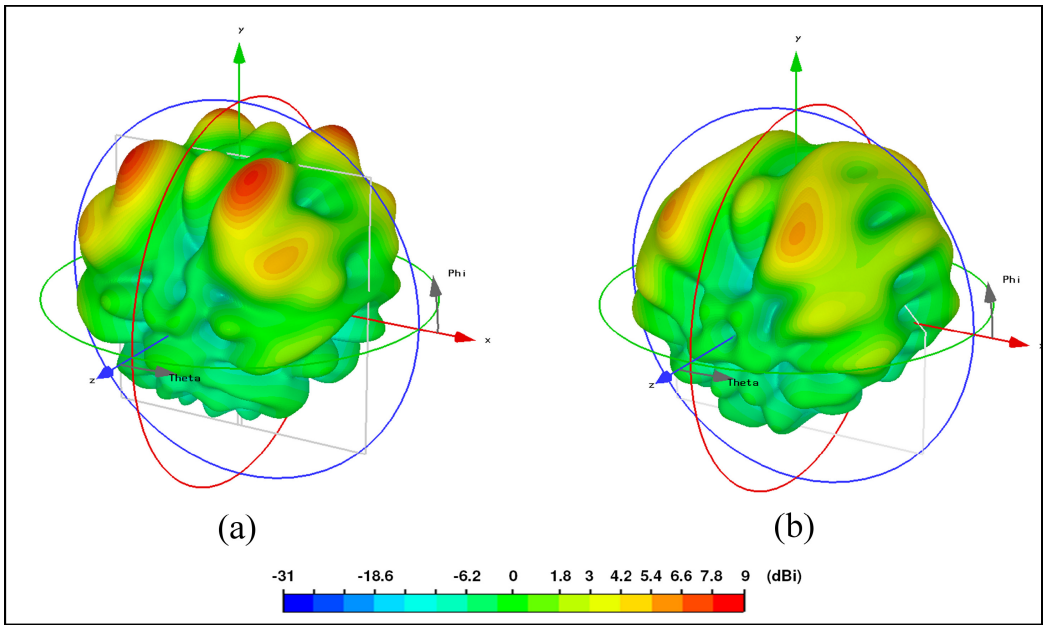

Figure 8.21: Radiation pattern of the PICA antenna at 5.9 GHz: (a) with the original ground plane and (b) with the truncated ground plane (GPR = 10mm)

8.4 Optimised PICA-Based Vehicular Antenna

Equipped with an understanding of the effects of the various S-parameters in the PICA geometry, an optimised PICA (O-PICA) for vehicular applications was produced. There were several competing demands to consider in creating an optimised geometry. The first requirement was to reduce the substrate dimensions occupied by the antenna. Secondly, parameters were selected to improve the antennas radiation performance at 5.9 GHz, while preserving the low-frequency impedance match and radiation. The parametric analysis had demonstrated that careful selection of values ought to enable the x-y plane null in the original design to be reduced. However, the competing requirements at low frequencies placed constraints on acceptable values of AR and GPR. Thirdly, it was desirable to obtain a good impedance match when simulated in both free space and when adjacent to an SMC body panel. This would enable the optimised antenna to be positioned horizontally on a vehicle, behind a polymeric panel, or perform equally well in free space. The resulting antenna is depicted in Figure 8.22. The size of the PICA structure has been significantly reduced, occupying only 45% of the substrate area of the original design. Despite this, the lowest frequency of operation has been maintained at approximately 730 MHz, as shown in Figure 8.23. This was achieved by increasing the size of the inner PICA shape (D_{inner}), as explained in Section 8.2.7. The substrate sides were cropped at 170 mm, and the width further reduced by means of altering the AR. The AR was set to 0.85:1 by applying a transformation that narrows the entire structure, giving an overall substrate width of 144.5 mm. This enhances the forward gain at the upper end of the band.

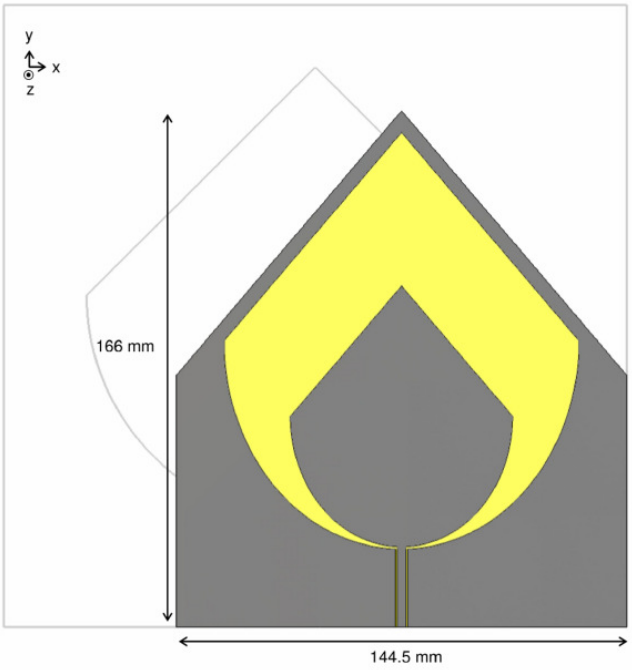

Figure 8.22: Geometry of the O-PICA-based vehicular antenna
A grey outline shows the shape and size of the baseline design (see Figure 8.9 for comparison)
Parameters: L = 200 mm, W = 170 mm, CPW_{length} = 25 mm, CPW_{centre} = 2.84 mm, CPW_{gap} = 3.24 mm, D_{outer} = 67 mm, D_{inner} = 42 mm, Ins = 0.7 mm, h = 0.4 mm, AR = 0.85, GPR = 7 mm

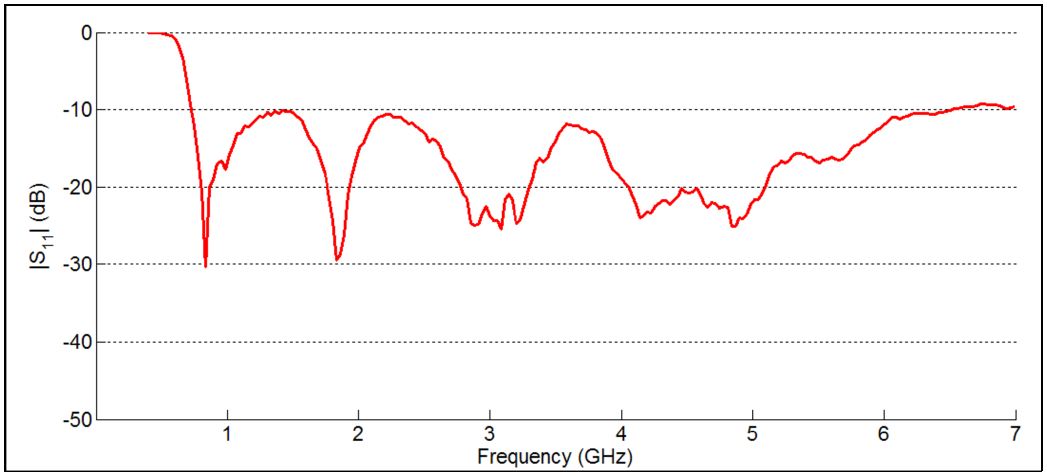

Figure 8.23: Measured reflection coefficient of the O-PICA antenna

To avoid the bifurcation in the radiation pattern at 5.9 GHz caused by the upper portion of ground plane, the ground plane was truncated at a distance

of 7 mm from the antenna structure. The intended result was achieved, with maximums at this frequency occurring in the plane of the substrate (x-y plane), as shown in Figure 8.24. The simulated radiation at other common bands is also presented in Figure 8.24.

Measured radiation patterns of the fabricated O-PICA vehicular antenna agree well with the simulated values in terms of the radiation pattern shape. However, the peak gain obtained at 5.9 GHz is found to be lower than expected at approximately 5 dBi (see Figure 8.25(c)). This may be due to losses in the dielectric substrate (FR-4). A comparison of Figure 8.25(c) and (d) reveals that the radiation emitted in the x-y plane is predominantly horizontally polarised, assuming the antenna was mounted flat on a vehicle roof (i.e., parallel to the surface of the earth). This polarisation should be anticipated, given the origin of the radiation in a horizontally aligned tapered slot.

The O-PICA-based vehicular antenna presented in this section is also the subject of study in Chapter 9. In Chapter 9, the effect of embedding of the antenna to a polymeric vehicle panel is investigated and benchmarked.

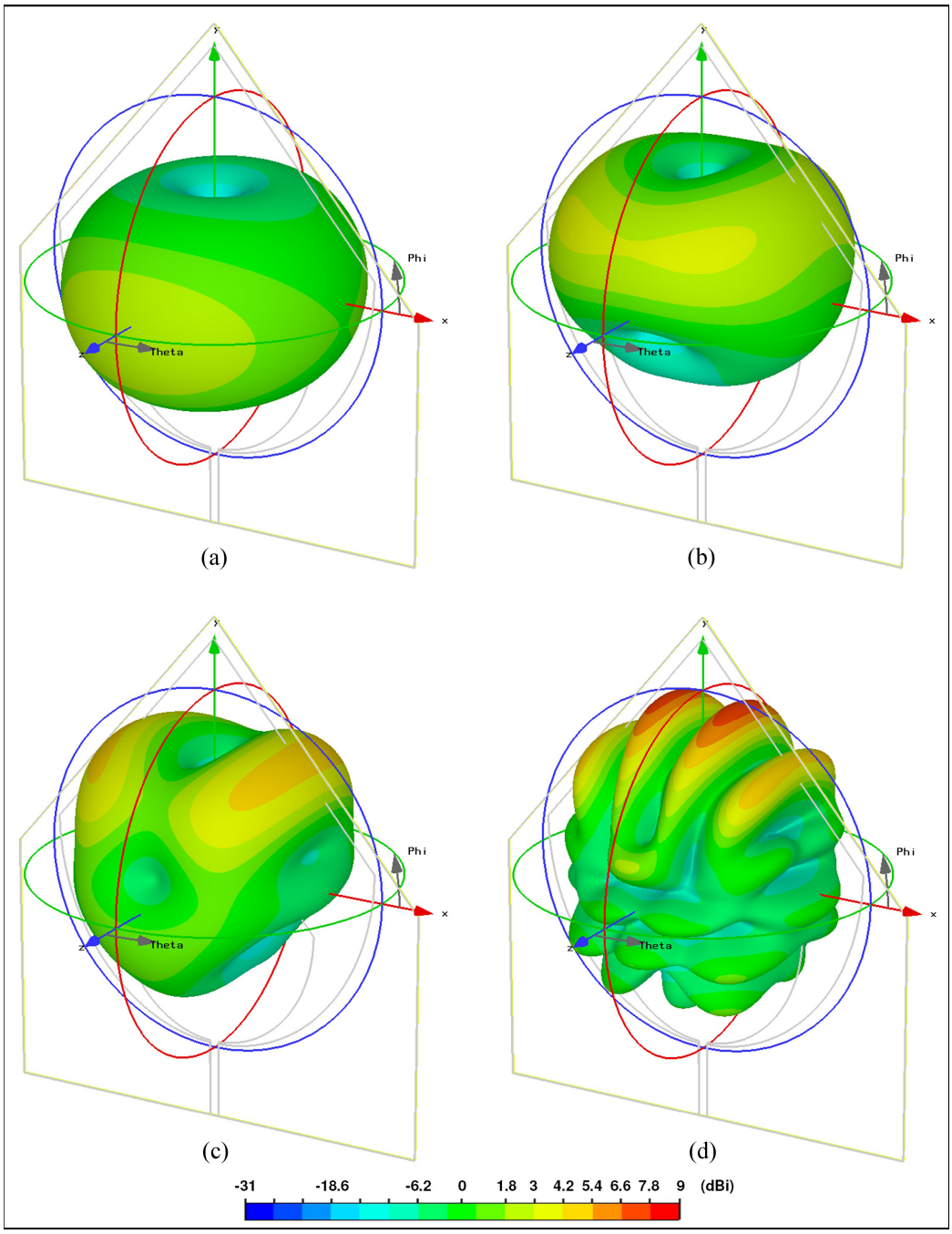

Figure 8.24: Simulated 3D radiation patterns of the O-PICA-based vehicular antenna: (a) 850 MHz, max gain is 3.1 dBi, (b) 1.575 GHz, max gain is 3.5 dBi, (c) 2.4 GHz, max gain is 5.0 dBi and (d) 5.9 GHz, Max gain is 8.0 dBi

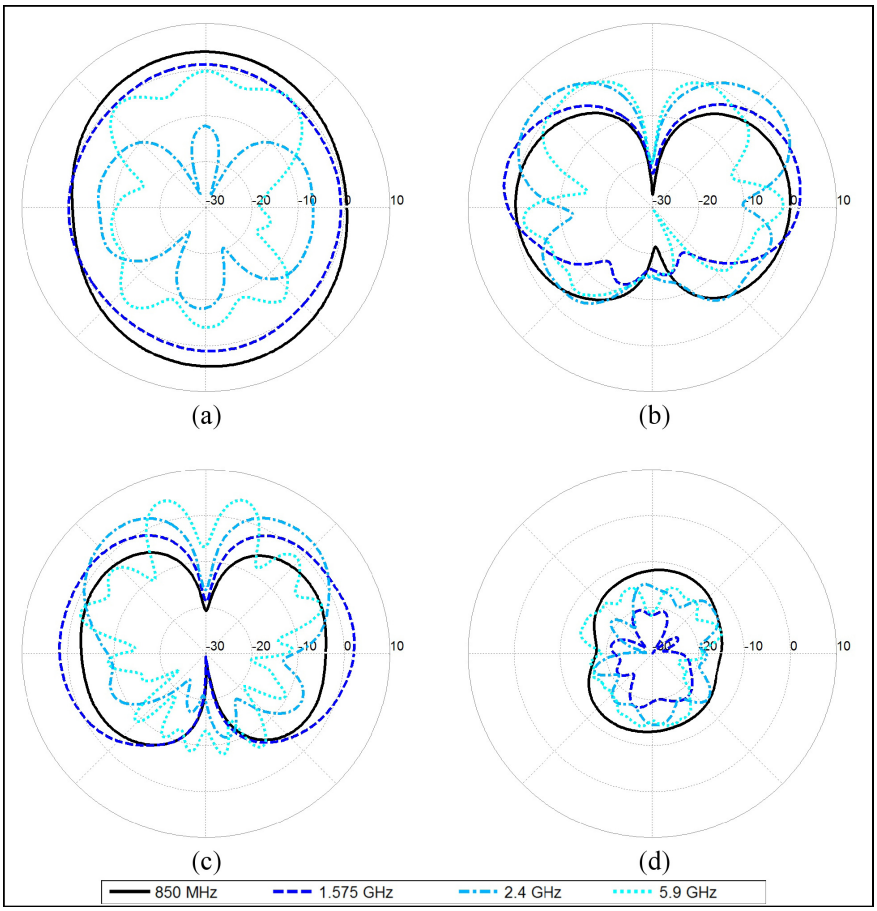

Figure 8.25: Measured radiation patterns of the optimised antenna in free space: (a) x-z plane, (b) y-z plane, (c) x-y plane horizontal polarisation and (d) x-y plane vertical polarisation (cross-pol)

8.5 Conclusion

The wide bandwidth demonstrated by the uniplanar CPW-fed PICA is a combination of two modes of operation. The combination of these two modes extends the bandwidth of the antenna beyond that of either mode alone, and creates distinct radiation patterns at the upper and lower ends of the band. Antennas developed including O-PICA discussed in this chapter seem to exhibit good performance, simulated and measured, at the desired frequency ranges of interest for the end application. Parametric and benchmark studies performed in real word application will be discussed in the next chapter to better understand how they compare to commercially used counterparts. In particular, two frequency ranges will be carefully evaluated: 900 MHz for mobile phone and 1.575 GHz for GPS.

8.6 References

- Bian, L, Guo, Y & Shi, X 2008, 'Broadband slot antenna with circular-polarisation operation', in *IEEE Vehicular Technology Conference, 2008. VTC Spring 2008*, pp. 353–355.
- Cheng, S, Hallbjorner, P & Rydberg, A 2008, 'Printed slot planar inverted cone antenna for ultrawideband applications', *IEEE Antennas and Wireless Propagation Letters*, vol. 7, pp. 18–21.
- Federal Communications Commission 2002, *New public safety applications and broadband internet access among uses envisioned by FCC authorization of ultra-wideband technology*, media release, FCC, Washington, 14 February.
- Gupta, S, Ramesh, M & Kalghatgi, A 2006, 'Ultra wideband embedded planar inverted conical antenna', *Microwave and Optical Technology Letters*, vol. 48, no. 12, pp. 2465–2468.
- Kim, Y & Kwon, D 2005, 'CPW-fed right-angled dual tapered notch antenna for ultrawideband communication', *Electronics Letters*, vol. 41, no. 12, pp. 674–675.
- Pell, B, Sulic, E, Rowe, W, Ghorbani, K, John, S, Gupta, R & Zhang, K 2008, 'The design and realization of uniplanar CPW fed PICA slot antennas', in *2008 Asia-Pacific Microwave Conference*, pp. 1–4.
- Sulic, E, Pell, B, John, S, Rowe, W, Ghorbani, K, Gupta, R & Zhang, K 2008, 'Performance of embedded multi-frequency communication devices in smart composite structures', in *ASME Smart Materials Adaptive Structures and Intelligent Systems (SMASIS2008)*, pp. 1–12.
- Suh, S, Stutzman, W & Davis, W 2004, 'A new ultrawideband printed monopole antenna: the planar inverted cone antenna (PICA)', *IEEE Transactions on Antennas and Propagation*, vol. 52, no. 5, pp. 1361–1364.
- Sun, J, Lee, Y & Lin, S 2007, 'New design of a CPW-fed ultrawideband slot antenna', *Microwave and Optical Technology Letters*, vol. 49, no. 3, pp. 561–564.
- Yoshimura, Y 1972, 'A microstripline slot antenna', *IEEE Transactions on Microwave Theory and Techniques*, vol. 20, no. 11, pp. 760–762.

CHAPTER 9: Antenna Simulation, Measurement and Performance Benchmarking

9.1 Introduction

The work described in this chapter builds upon that in previous chapters by combining the wideband antennas, discussed in Chapter 8, with the polymeric composite body panels. Section 9.2 deals with the radiation behaviour of an antenna that is embedded into an SMC part during production at the factory. Section 9.3 presents an investigation of the effect of bending the substrate of a wideband antenna through both computer simulation and experimental techniques. Section 9.4 describes the use of CST Microwave Studio to assemble an antenna to a full-size vehicle and extract the simulated impedance and radiation results. Section 9.5 deals with the mounting of the O-PICA antenna on an SMC roof panel, which was measured at an outdoor antenna range, before being tested with a Trimble SV6 receiver for GPS use on a vehicle, as described in Section 9.6.

9.2 Embedded Antenna in the Tailgate of an HSV E Series Ute

One of the largest automobile manufacturers in Australia is GM Holden Ltd. As one of the divisions of the worldwide network of General Motors companies, Holden imports and sells a variety of vehicles. Their most popular vehicle over the past few decades has been the locally designed and built model, Holden Commodore, which is a large passenger vehicle available in sedan, wagon and ute (utility) body styles. Holden's designated performance car partner is Holden Special Vehicles (HSV), a private company that is partly owned by Holden.

The embedding trial presented here used a special SMC panel fitted to the HSV Maloo ute in conjunction with the uniplanar CPW-fed PICA slot antenna, described in Chapter 8. This trial was conducted at an early stage of the research project to investigate and validate the embedding concept. At the time of this work, the antenna design had just been completed for the

uniplanar CPW-fed PICA. The panel selected for the embedding test was the tailgate from the E Series Maloo Ute, produced by HSV. HSV's vehicles are fitted with performance upgrades and feature distinctive styling. The Maloo is a performance vehicle based upon the standard Holden ute. As part of the styling changes, the E Series HSV Maloo ute features a revised rear end. This is provided through additional rear light components that are mounted in the tailgate, and an accompanying body kit. While the standard Holden ute comes with a tailgate composed of traditional stamped steel, the HSV Maloo ute has a polymeric composite tailgate, manufactured from SMC by the project research partner Composite Materials Engineering Pty. Ltd. (see Figure 9.1). With this tailgate panel already in production, it provided an excellent opportunity to trial the antenna embedding process, and quickly obtain some results to give an idea of the performance of the device.

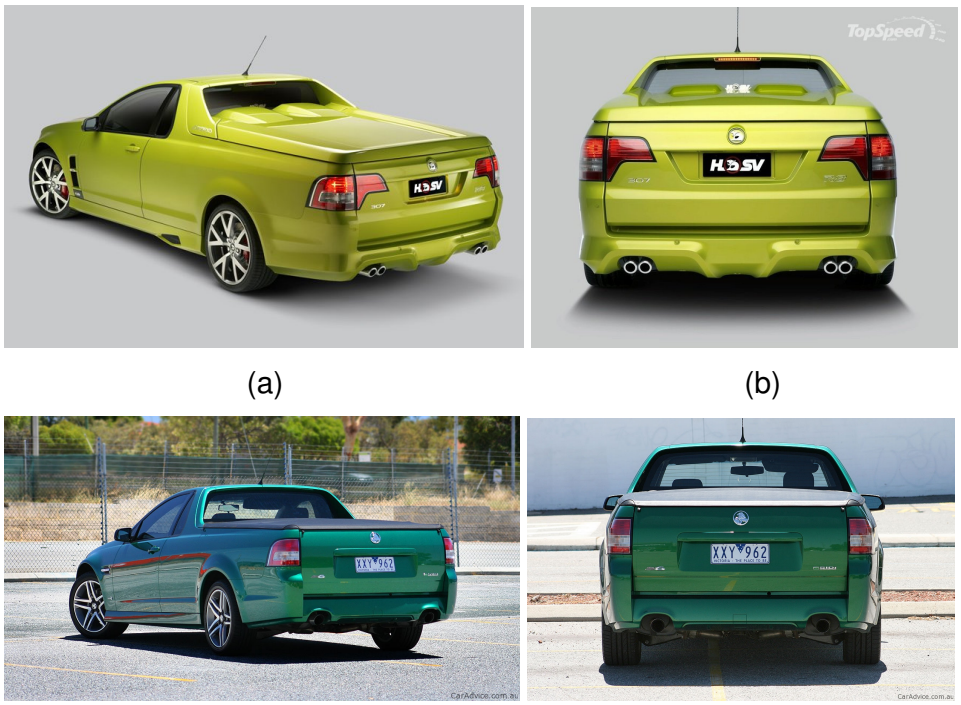

(a) (b)

(c) (d)

Figure 9.1: HSV Maloo ute tailgate (a) and (b) compared with standard Holden ute tailgate (c) and (d) © TopSpeed with permission

Figure 9.2 shows the computer-aided design (CAD) models of the tailgate assembly as used in production. The tailgate is composed of three SMC

panels. The first panel is the outer skin, which forms the visible surface of the tailgate (see Figure 9.2(c)). This panel is a class A quality painted exterior surface. A second panel forms the inner skin (see Figure 9.2(a)). In between these two panels is a high-strength reinforcing panel (see Figure 9.2(b)). The inner skin was selected for embedding in this investigation because it is predominantly flat and has sufficient room to accommodate the smaller uniplanar CPW-fed PICA. Although this smaller version of the PICA antenna does not accommodate all the frequencies of interest in the vehicular environment and does not feature an optimised radiation pattern, its wide bandwidth still incorporates many of the frequency bands of interest, providing an adequate impedance match from 1.2 GHz to beyond 13 GHz. Hence, the smaller design provides for all of the same signals, with the exception of the two lower mobile phone bands (850 and 900 MHz).

9.2.1 Investigation Methodology

The following procedure was followed in this investigation:

- A small uniplanar CPW-fed PICA antenna was manufactured at RMIT University, and transported to the CME factory.
- A compression-moulding operator embedded the antenna along with the usual amount of unprocessed SMC into the tool when manufacturing the 'inner' panel.
- The part was produced with the antenna embedded / encapsulated inside its volume.
- The 'inner' panel with the embedded antenna was assembled with the other two SMC panels to form a complete tailgate component.
- The entire part was painted, but with masking tape covering the antenna feed lines to facilitate the attachment of testing connections.
- A coaxial cable and RF connector were soldered to the embedded antenna (see Figure 9.3).
- An RF anechoic chamber was used to rotate the structure on its axis and measure the radiation performance of the antenna embedded in the tailgate. The system was used in both horizontal and vertical polarisations (see Figure 9.4(a) and (b)).

- For comparison purposes, an identical small uniplanar CPW-fed PICA antenna was measured in the anechoic chamber.
- The results were plotted and compared.

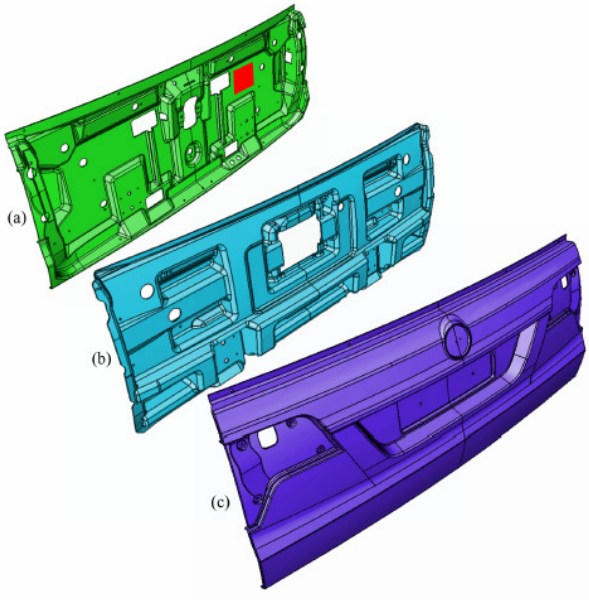

Figure 9.2: HSV tailgate assembly consisting of (a) inner skin, (b) reinforcement panel, (c) outer 'Class A' skin. The antenna was to be embedded into the inner skin at the location marked with red.

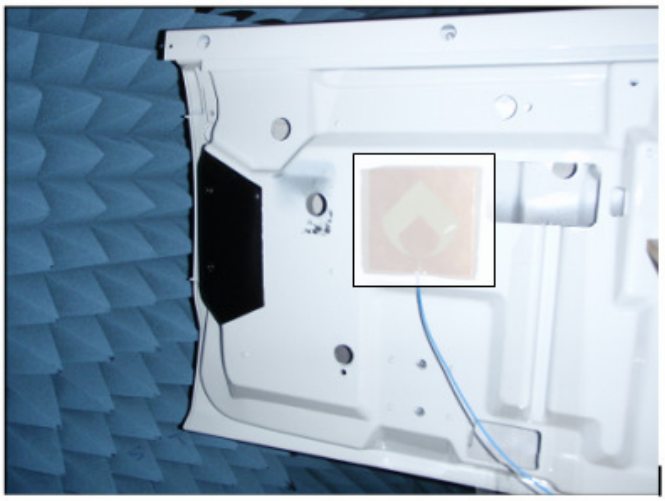

Figure 9.3: Embedded antenna with coaxial cable in HSV Tailgate (image of the antenna overlayed to indicate position and orientation)

While under test in the anechoic chamber, the reference antenna was attached to a piece of polystyrene foam (see Figure 9.5). This allowed for identical antenna placement on the wooden rotator as was used for the embedded antenna in the panel, which allowed accurate investigation of the effects of the embedding process. The polystyrene foam had a dielectric constant close to 1, and therefore had negligible detuning effects on the reference antenna.

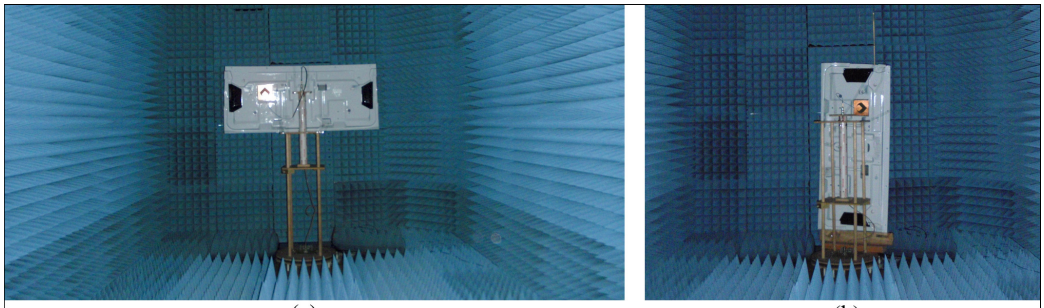

Figure 9.4: Embedded antenna in the anechoic chamber: (a) horizontal orientation and (b) vertical orientation

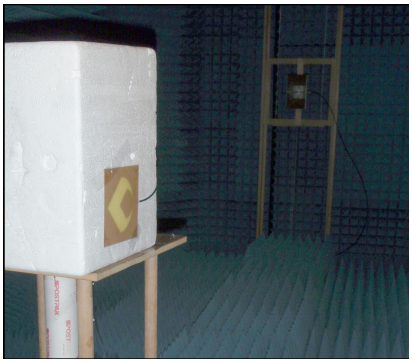

Figure 9.5: Reference antenna

9.2.2 Results Reflection Coefficient

When embedded in the Maloo ute tailgate, the antenna's impedance matching was altered slightly in a way that degraded its performance (see Figure 9.6). The antenna remained reasonably well matched (below a –9.4 dB criterion) over the majority of the band. There were some mismatches beyond this value near 9 GHz. An $|S_{11}|$ of –9.4 dB corresponded with a VSWR

of 2:1. These mismatches occurred because the uniplanar CPW-fed PICA slot antenna was designed to operate in free space without consideration for SMC embedding. The mismatches were due primarily to the addition of the dielectric panels that made up the ute tailgate. The presence of this dielectric material changed the relative permittivity in the space around the antenna, which had the effect of altering the effective electrical length of any antenna or radiating structure in the vicinity. Some additional mismatch may have been due to the conductors that were added into the ute endgate during the assembly process. This included the hinge and lock mechanisms, and a decorative steel strip along the top of the panel (see Figure 9.7). By adjusting some of the antenna geometry, the mismatches that occurred here in the embedded small uniplanar CPW-fed PICA slot antenna might be avoided. The parametric study presented in Chapter 8 indicated the effect of each parameter on the impedance matching of PICA slot antennas.

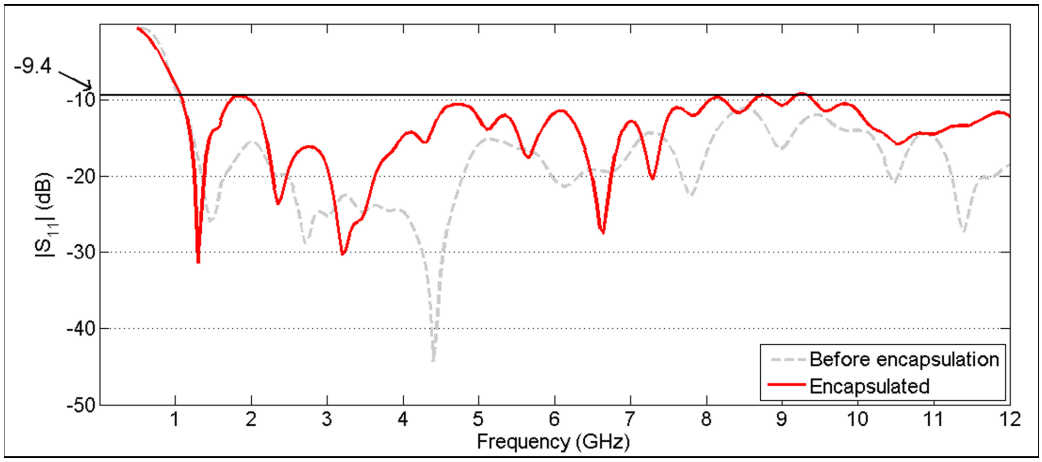

Figure 9.6: Measured reflection coefficient for the antenna in free space v. encapsulated in the ute tailgate

Figure 9.8 shows the radiation patterns of the embedded antenna in the Maloo ute tailgate, along with the reference antenna for comparison. In Figures 9.8(a), (b) and (c), the tailgate assembly is in the orientation shown in Figure 5.4(a), which results in a measurement through the x-z plane of the antenna. In Figure 9.8(d), (e) and (f), the antenna is orientated as shown in Figure 9.4(b), which produces a y-z plane radiation pattern measurement. A

transparent schematic is shown underneath each plot to clarify the aspect angles relative to the part and the antenna.

At the low frequencies (see Figure 9.8(a) and (d)), very little difference was measured between the encapsulated antenna and the antenna in free space. The gain and radiation performance appeared to be approximately equal. As the frequency was increased to 2.4 GHz (see Figure 9.8(b) and (e)), some loss was observed in the upper part of the plots when the device was radiating through three layers of SMC. This loss appeared to be an average of approximately 5–6 dB. Additional ripples were beginning to form, as shown in Figure 9.8(b). This indicates the presence of surface waves propagating along the large dielectric panel's surface.

At 4.8 GHz, the radiation pattern of the antenna was significantly altered by the encapsulation process. Figure 9.8(c) reveals significant loss on some angles, while on other angles, the encapsulated antenna provided higher gain than the reference antenna. Ripples in the radiation pattern became more pronounced. On the whole, radiation through the three layers of the tailgate structure produced some loss in signal strength, while the radiation on the exposed side was approximately equal in average power. Figure 9.8(f) revealed that some of the nulls in the y-z plane were smoothed over while new nulls formed at other angles. The peak gain of the new pattern was approximately 4 dB lower than the reference antenna in this plane, while it was only approximately 1.5 dB lower in the x-z plane (see Figure 9.8(c)).

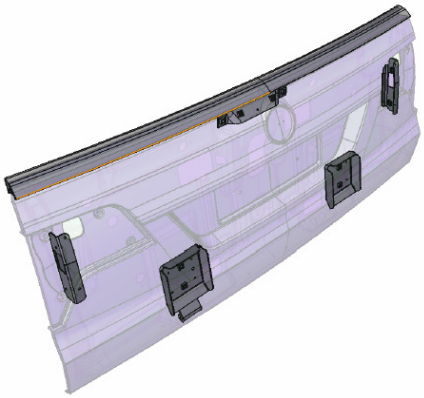

Figure 9.7: Metal inserts highlighted in tailgate

9.2.3 Results Radiation Pattern

The operating bandwidth of the embedded antenna remained very wide, although the matching deteriorated. This was to be expected because the antenna was tuned to operate in free space, rather than embedded in the panel. The majority of the $|S_{11}|$ values measured remained under –9.4 dB, which may be tolerable, given it corresponds with a VSWR of 2:1. A few mismatches near 9 GHz exceeded this value. It was expected that the impedance match of the antenna would be improved with some simple tuning adjustments to the design to optimise the geometry for use in this location. When integrated with the polymeric ute endgate, the radiation patterns of the antenna were predominantly unchanged at the lower end of the band, while ripples became evident at higher frequencies. An average decrease in gain of 3–5 dB seems typical.

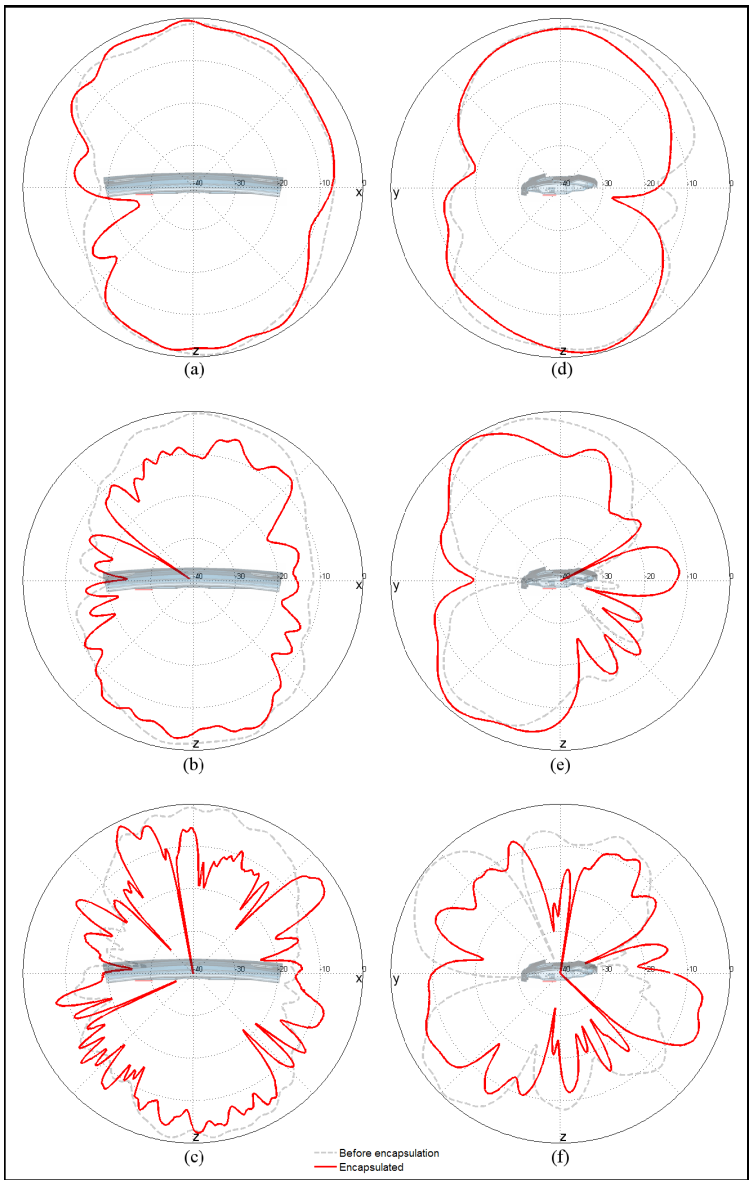

Figure 9.8: Measured radiation patterns for the antenna in free space v. encapsulated in the ute tailgate: (a) 1.2 GHz (x-z plane), (b) 2.4 GHz (x-z plane), (c) 4.8 GHz (x-z plane), (d) 1.2 GHz (y-z plane), (e) 2.4 GHz (y-z plane) and (f) 4.8 GHz (y-z plane—tailgate vertical)

Given that the HSV Maloo ute tailgate is composed of three layers of SMC, a body panel composed of a single layer of SMC, such as a hood or trunk, may provide significantly less loss. The degradation in performance introduced by the encapsulation of the antenna in the SMC body panel was only slight. The resulting system performance is likely to be equivalent to current ‘shark-fin’ or ‘on-glass’ designs. These existing designs also produce imperfect radiation

patterns and suffer from gain loss when compared with the ideal case of a monopole mounted on an infinite ground plane.

9.3 The Effect of Bending on a Truncated PICA Antenna

The truncated PICA antenna introduced in Chapter 8 was an intermediate stage in the development of the CPW-fed PICA slot antenna. This section describes how we applied this antenna as an example of a wideband slot antenna, in an investigation into the effect of curvature on such antennas.

An analysis of the truncated PICA conducted thus far assumed that the antenna substrate was flat in the installed position on the vehicle body. This is unlikely given the styling trends of modern vehicles; in addition, as discussed in Chapter 7, small antenna deformation occurs during the embedding process, when the antenna is embedded using the compression-moulding process. Most vehicles have curved panels, and it is therefore important to investigate the effect this curvature might have on antenna performance. The effect of curvature on other types of antennas has been investigated recently, yet to the author's knowledge no such investigation has been performed on the PICA. It is worth noting that a foldable and stretchable PICA antenna was recently presented, but no indication of performance when folded was able to be provided. Many potential antenna host sites, such as the roof or the hood, typically display curvature that is only slight. However, it may be desirable to locate the truncated PICA or other wideband antennas in panels that have curves of a relatively tight radius. To investigate the effect of such curvature on the antenna, two parallel investigations were conducted using electromagnetic simulation tools and practical measurements in an anechoic chamber. Curvature of the antenna was investigated in four steps of increasing angle: 0°, 22°, 45° and 90° (see Figure 9.9). To achieve these angles for the antenna size given, the centre of the antenna is required to be displaced by 0 mm, 10 mm, 20 mm and 40 mm respectively. Figure 9.10 illustrates the correlation between displacement and angle for the 90° case.

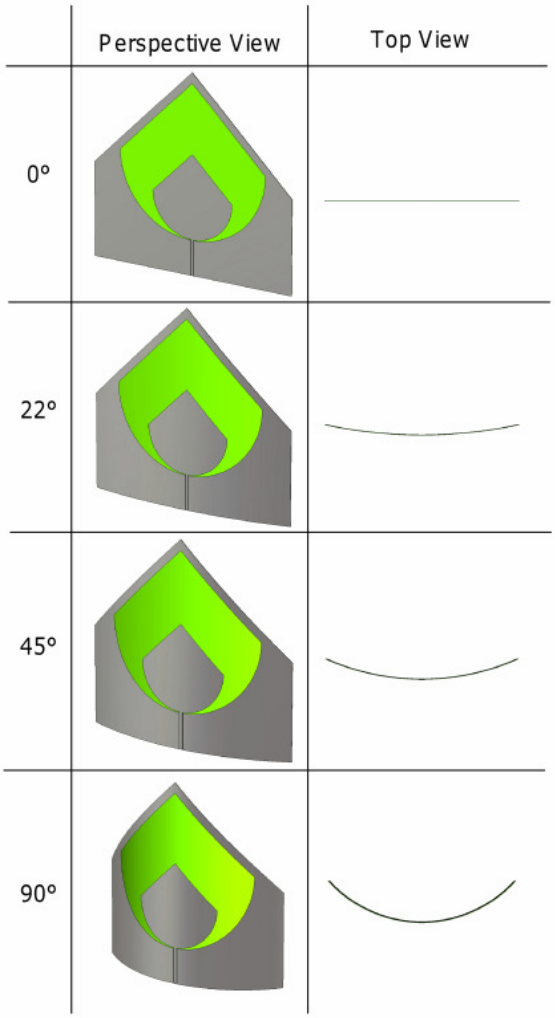

Figure 9.9: Angles of curvature investigated: 0°, 22°, 45° and 90°

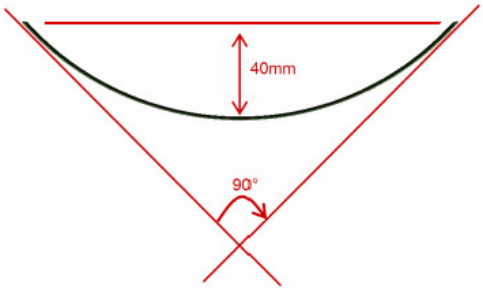

Figure 9.10: Diagram showing relationship between displacement from ground plane and desired angle of curvature

Screws were used in conjunction with the foam and exerted a force on the antenna substrate to induce bending. These screws were intentionally located

in areas of low surface current to further minimise their impact. The finished structure and curved fabricated antenna is shown in the anechoic chamber in Figure 9.11.

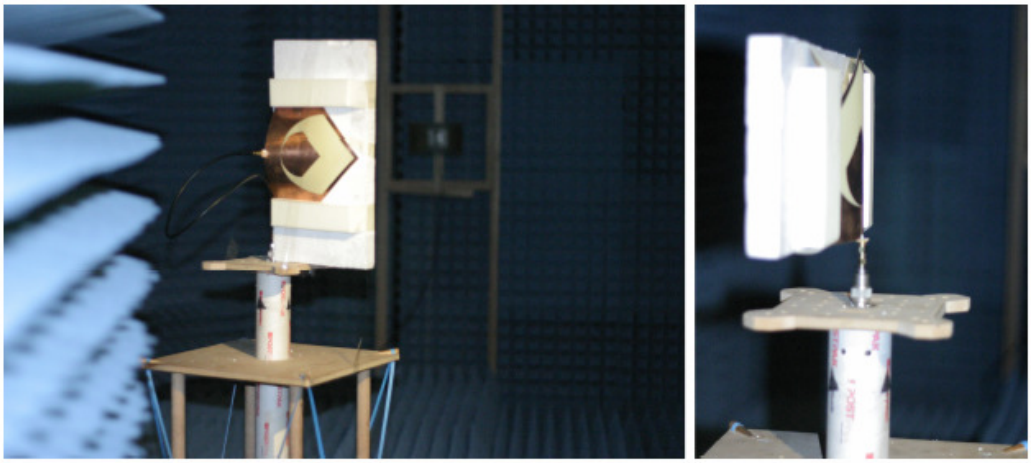

Figure 9.11: Truncated PICA in anechoic chamber

9.3.1 Simulated Results

To operate effectively, the input impedance of an antenna needs to be adequately matched to the impedance of the device to which it is connected. The quality of an impedance match can be measured using the reflection coefficient: a property that describes the relative magnitude of a reflected wave to an incident wave at the antennas input port. Using $|S_{11}|$ in dB to represent the results, an acceptable match is usually deemed to be –10 dB or better. This corresponds to a VSWR of approximately 2:1. The simulated reflection coefficient of the truncated PICA antenna conformed under different degrees of curvature is shown in Figure 9.12. These simulation results from CST Microwave Studio indicate that a wideband impedance match will be preserved even for extreme cases of curvature. A slight mismatch was present for angles of 22° and 45°, affecting the frequencies between 1.2 and 1.4 GHz. This mismatch is of little concern given that the frequencies affected are of little interest for present-day automotive services, and even in the mismatched band, the return loss is predicted to remain below –9 dB.

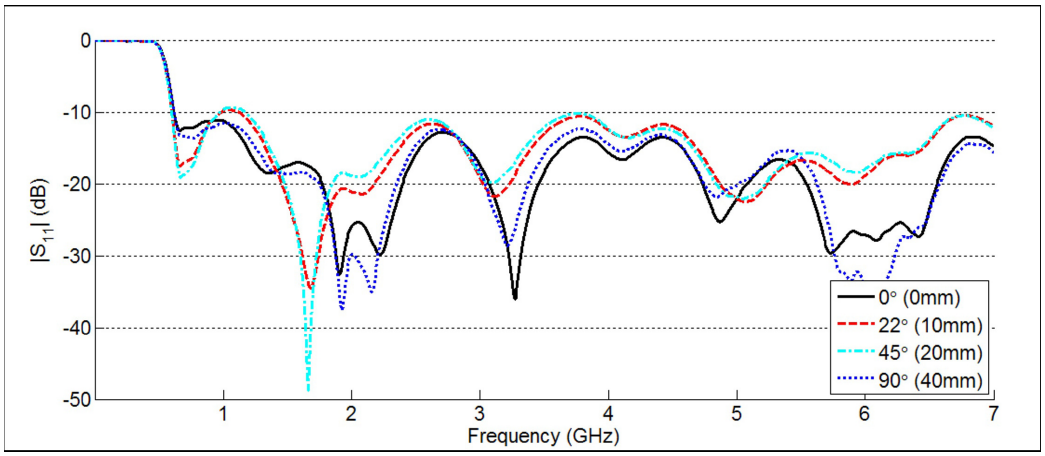

Figure 9.12: Simulated results reflection coefficient

Simulated radiation patterns for different degrees of antenna curvature are shown in Figures 9.13 and 9.14. The omnidirectional behaviour in the x-z plane that is characteristic of the truncated PICA was largely preserved. A slight gain reduction was observed in the negative z direction (see Figure 9.13(a) and (b)). At 2.4 GHz (see Figure 9.13(c)), the radiation pattern widened with increasing degrees of curvature. The simulation results indicate that the effect of bending the antenna substrate may be more substantial in the y-z plane, where the antenna radiates more distinctive lobes. Figure 9.14(c) and (d) indicate a progressive shift downwards towards the negative z direction in the main beams of the antenna radiation at the higher frequencies.

9.3.2 Measured Results Radiation Pattern

The measured reflection coefficient of the fabricated antenna is shown in Figure 9.15. A good match was achieved across the entire band of interest, even where the angle of curvature was increased to a value as high as 90°. The truncated PICA antenna was observed to accept power for any frequencies in the range from approximately 650 MHz to beyond 7 GHz for every value of curvature investigated. Measured radiation patterns of the antenna under test are shown for both the x-z plane and y-z plane in Figures 9.13 and 9.14. The patterns shown in Figure 9.13(a) and (d) very closely resemble the radiation patterns predicted by the simulations, while Figure 9.13(b) and (c) reveal the predicted trends to some degree. The measured

reduction in gain towards the underside of the antenna substrate (see Figure 9.13(b)), and quantifiable increase in gain to the sides of the plot (see Figure 9.13(c)) were present in the equivalent plots shown in Figure 9.13. It is interesting to note that at 1.575 GHz (see Figure 9.13(b)), a 90° bend in the antenna substrate led to a significant narrowing of the edges of the radiated beam in the positive z direction, which was not visible in the simulated results. The measured radiation patterns in the y-z plane (see Figure 9.14) provided very good correlation with the simulated results of Figure 9.14. The beams produced by the antenna in this plane can be observed to curve downward towards the negative z direction as predicted in the simulation.

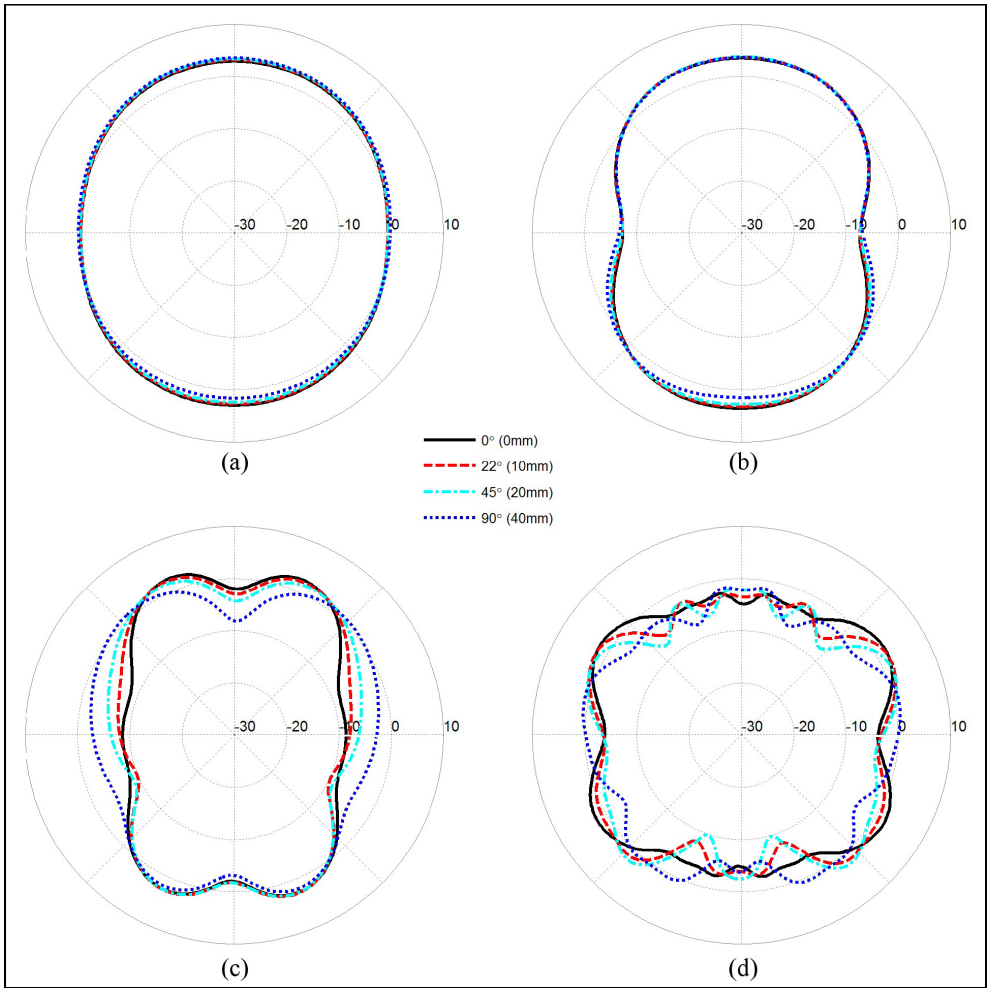

Figure 9.13: Simulated radiation pattern (x-z plane): (a) 850 MHz, (b) 1.575 GHz, (c) 2.4 GHz and (d) 5.9 GHz

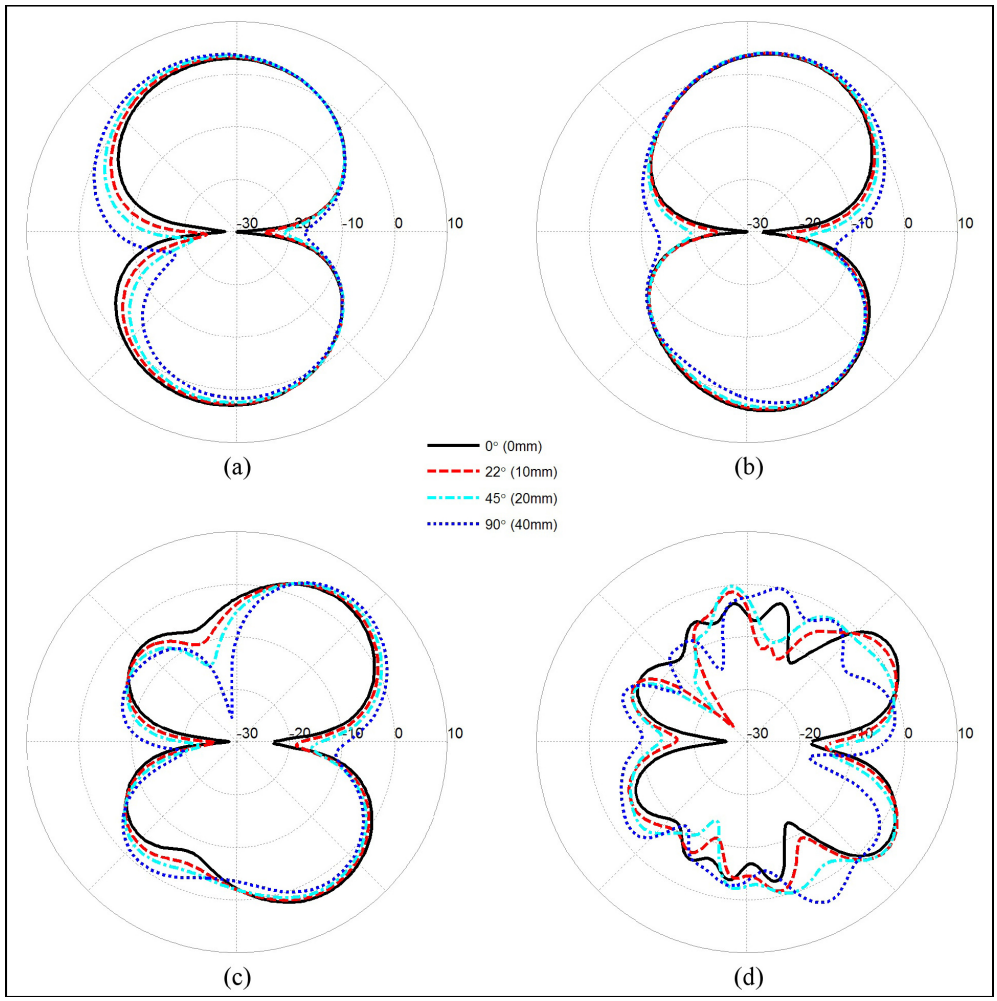

Figure 9.14: Simulated radiation pattern (y-z plane): (a) 850 MHz, (b) 1.575 GHz, (c) 2.4 GHz and (d) 5.9 GHz

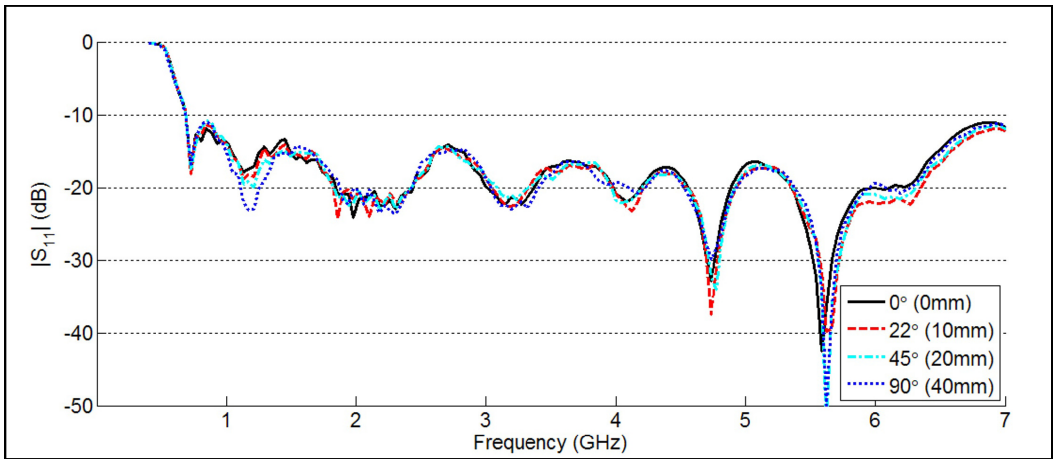

Figure 9.15: Measured reflection coefficient

9.3.3 Curvature Conclusions

The wideband impedance match of the antenna was preserved even when the antenna was curved at an angle of up to 90°, as may be the case when installed in a vehicle. At the low end of the band, when the PICA was acting as a traditional slot antenna, the effect of bending was less significant than at the high end of the band, where the high-gain beams caused by the tapered slots were observed to shift significantly, particularly in the y-z plane. Future applications of the antenna are intended to be confined to the areas of relatively flat roof or boot/trunk, where only the slightest amounts of curvature will be encountered.

Such bends would be significantly closer to 0° than the rather extreme cases investigated here. The results give confidence that such small amounts of curvature would be unlikely to create impedance mismatches, and would cause minimal distortion to radiation patterns.

9.4 Optimised PICA-Based Antenna Embedded into a Vehicle Panel

In the intended application, the O-PICA-based vehicular antenna presented in Chapter 8 was to be attached to the underside of a polymeric vehicular body panel. If painted, this would create a concealed radiating device mounted behind a colour-matched dielectric cover, indistinguishable from an ordinary section of bonnet, roof or trunk. Given the radiation pattern of the antenna, and the services used, the panel would ideally provide a reasonably flat horizontal surface. Therefore, body panels such as the hood, roof and trunk are of interest. An investigation into the effect of curvature in these panels is presented in Section 9.3. Another production vehicle part produced by the research collaborator, Composite Materials Engineering Pty. Ltd., for the Australian automotive industry is the luggage carrier roof panel for the Holden Adventra. The Holden Adventra is an all-wheel-drive crossover vehicle with a 4WD train fitted underneath the body of a modified passenger car station wagon. It features revised styling and several rugged additions, which include

plastic wheel arches and a 'luggage carrier' fitted between the roof racks (see Figure 9.16). This luggage carrier panel is moulded as one large panel out of SMC material by CME. There are some metal parts added to the SMC—notably the large decorative aluminium strips that run longitudinally; however, these would not be required in future designs. It would be possible to make an entire roof panel from SMC with only a basic steel-supporting structure underneath. When mounted in the middle of the Adventra roof panel (see Figure 9.17), a change was induced in the antennas reflection coefficient, as observed in the results shown in Figure 9.18, due to the addition of the SMC dielectric and the decorative aluminium strips on the outer side of the panel. The $|S_{11}|$ curve remained below –10 dB with the exception of a region between 1.7 and 2.0 GHz, where it rose as high as –8 dB. The proposed services in this range are the popular cellular phone frequencies. Cellular handset antennas are required to reach a VSWR of 3:1, which corresponds to a $|S_{11}|$ value of –6 dB, implying that the match achieved is adequate for the application. An outdoor antenna range was used to measure the gain and radiation pattern of the antenna when attached to the fully assembled roof panel. Figure 9.19 shows the measured radiation patterns of the SMC roof panel subassembly with the antenna attached. Comparing Figure 9.19 with Figure 8.31 reveals the distortions introduced by the presence of the roof panel in the antenna's near field. Figure 9.19(a) and (b) show similar features to the radiation pattern present in Figure 8.31(a) and (b). The x-z plane was largely omnidirectional, particularly at the low end of the band. Ripples began to form when the structure was operating at higher frequencies. The y-z plane revealed diametrically opposed nulls and the development of lobes at higher frequencies that encroached upon end fire in the y plane. In the x-y plane, significant distortion of the pattern was visible. This distortion may have been amplified by the nearby aluminium strips, which also lay in the x-y plane. At 5.9 GHz, the radiation was rippled due to operating an electrically large structure at high frequencies, and the addition of the roof panel appeared to scatter the radiation further. Interestingly, at this frequency, the dielectric appeared to fill in the null in the pattern in the y-direction (visible in Figure 9.19(b)) and appeared to scatter the polarisation of the fields in the x-y plane,

increasing the cross-polarised levels. It is important to note that some of the differences in radiation patterns between Figure 8.31 and Figure 9.19 were due to the change in permittivity of the space surrounding the antenna, and the associated frequency shift.

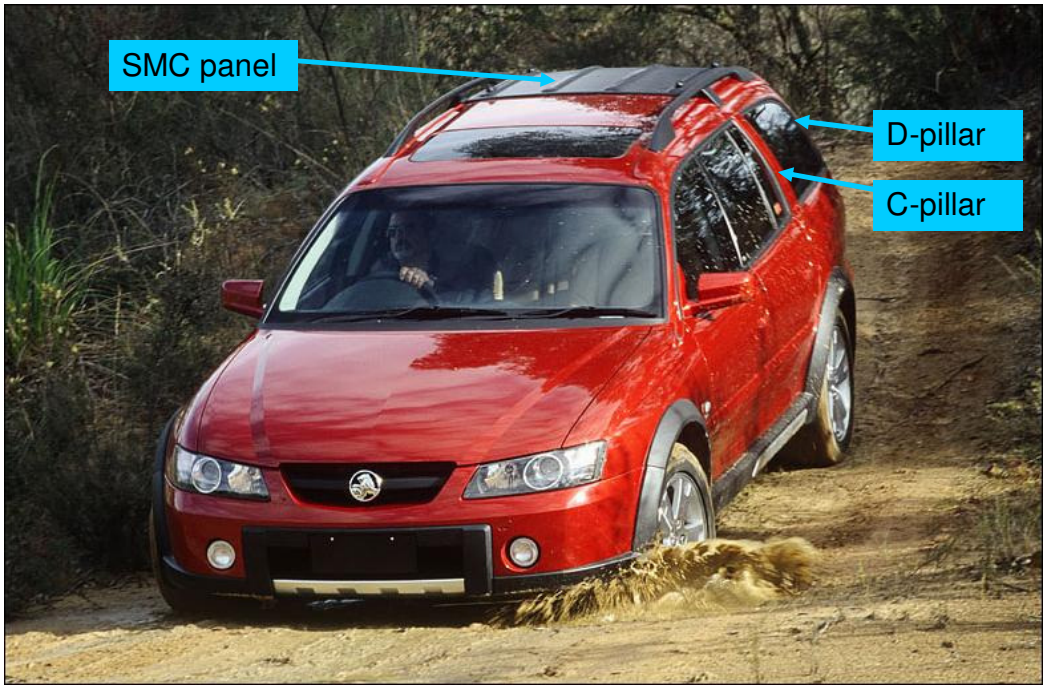

Figure 9.16: SMC roof panel located between the roof racks along C and D pillars on Holden Adventra

Figure 9.17: PICA antenna embedded in Adventra roof panel under test (image of the antenna overlayed to indicate position and orientation)

The O-PICA-based vehicular antenna may provide significant benefit for multi-service operation in the vehicular environment. When used in conjunction with an appropriate system of amplifiers and diplexers, the antenna could be mounted in a vehicle roof, and employed for GPS operation at 1.575 GHz while simultaneously communicating with vehicles or roadside infrastructure in the horizontal direction at 5.9 GHz. At the upper end of the frequency band, the antenna's radiation was dominated by the tapered slots formed between the inner and outer PICA shapes. As a result of this radiation mode, the radiation pattern of the antenna displayed main lobes on either side of the y-axis with a central null, as evidenced at 2.4 GHz (see Figure 9.19(c) and (d)). As the frequency of operation was increased to 5.9 GHz, additional side lobes were formed, as shown in Figure 9.19(c) and (d). This behaviour is typical of UWB antennas, or indeed, any electrically large structure operated at high frequencies. However, this pattern does not

represent the ideal for the V2V communication service, given the accompanying nulls in between the lobes.

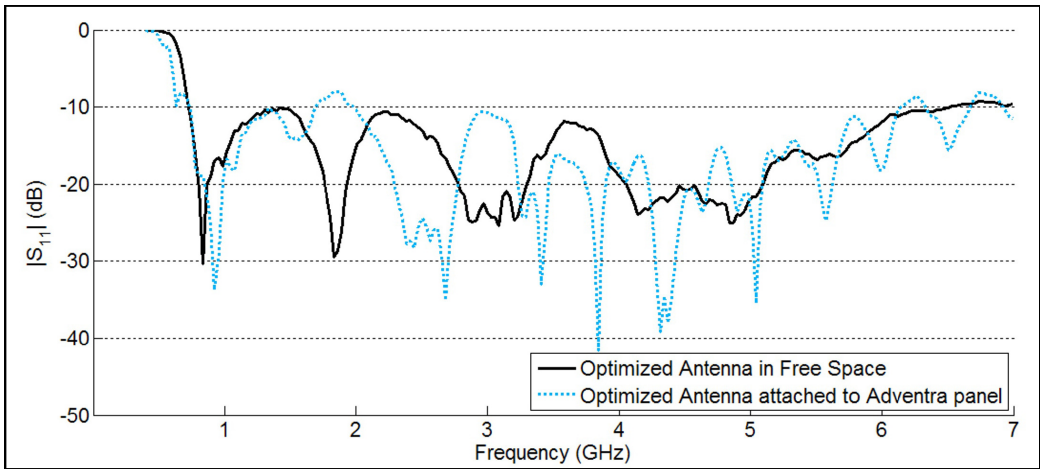

Figure 9.18: Measured reflection coefficient of the O-PICA antenna in free space v. embedded in the Adventra roof panel

While the addition of the SMC roof panel appeared to fill in some nulls, the existence of these nulls may not be problematic for V2V communication, given the likelihood of operating such a service in an urban multipath environment surrounded by vehicles and buildings. In such an environment, reflected signals from the side lobes may permit communication when the direct line of sight path falls in the direction of a null in the antenna pattern. Alternatively, it would be possible to provide multiple O-PICA-based antennas at differing locations and orientations within a single aperture, to create an antenna diversity scheme. In any case, it is clear that the radiation pattern produced at 5.9 GHz is complex. Further testing would be required with actual V2V hardware to detail the performance with certainty. This would be a matter for future work. Preliminary studies of the GPS performance of the O-PICA-based antenna attached to the roof panel have indicated good performance in terms of both signal strength and positioning accuracy.

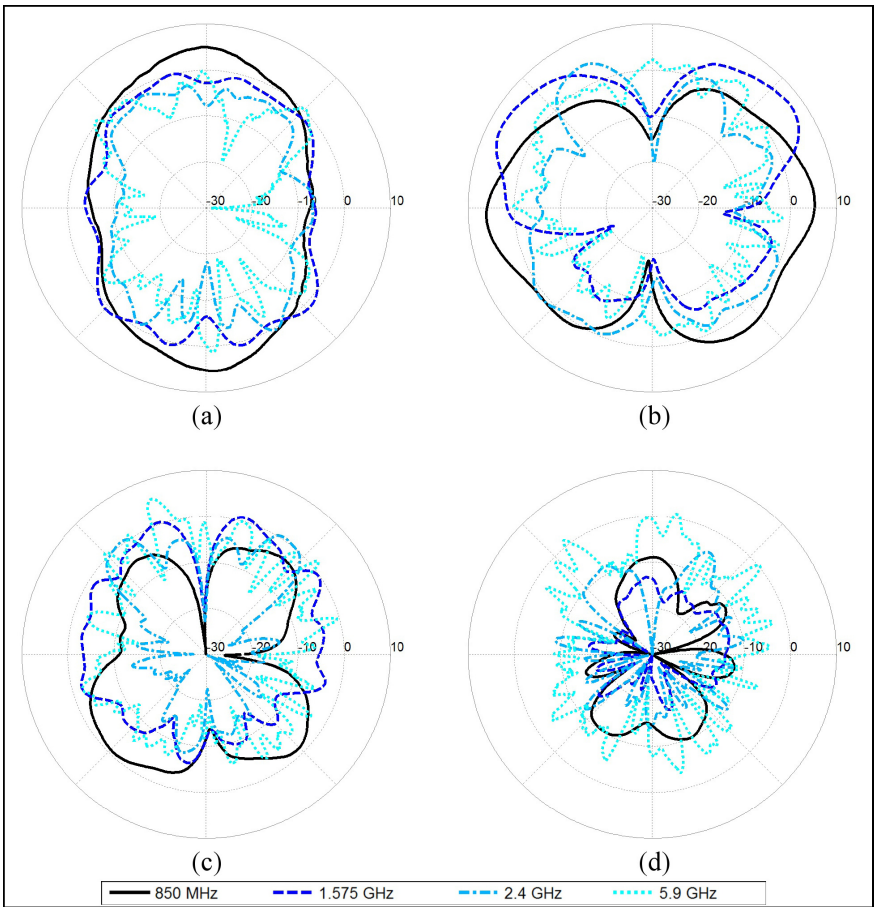

Figure 9.19: Measured radiation patterns of the optimised antenna embedded in the Adventra roof panel: (a) x-z plane, (b) y-z plane, (c) x-y plane horizontal polarisation and (d) x-y plane vertical polarisation (cross-pol)

9.5 GPS Test on Adventra and Jeep Wrangler

GPS antennas come in a variety of shapes and sizes. GPS signals are extremely weak when compared to the terrestrial-based services, and this tends to make the antenna performance an important part of the receiving chain. Certain types of GPS antenna are preferred for different applications. An ideal GPS antenna would provide an impedance match at all the frequencies to be used by the receiver in calculating position. Its radiation pattern would ideally have no variation in gain across the entire hemisphere, providing satellites at any position in the sky with equal signal strength in the receiver input. Ideally, it would then have a very sharp roll-off at the horizon and provide no back radiation (therefore, being insensitive to signals reflected from the ground).

The systems on board global navigation satellite system (GNSS) satellites transmit a circularly polarised signal, specifically a right-hand circular polarisation (RHCP) signal. To receive this signal in the best way, the receiving antennas used in GPS units are typically also RHCP. GPS-receiving antennas should also reject multipath. Such multipath signals are reflected off the ground or buildings, or other obstacles, before arriving at the antenna. Such multipath effects lead to signals arriving at the antenna multiple times with varying time delays. This is undesirable and can lead to errors in position estimation.

An ideal GPS antenna will also have a stable phase centre that does not move with changes in frequency or changes in radiation direction. Use of inherently narrowband antennas, or filters between the antenna and the receiver, can be advantageous to mitigate out-of-band interference. Such interference has potential to saturate amplifiers and interfere with proper operation of the LNA or receiver.

GPS is a type of GNSS. GPS is operated by the US government and is the most widely used of the GNSS systems. The Russian GLONASS system and European Galileo system are competing GNSS systems at various stages of implementation. The frequencies used by each of these services are shown in Table 9.1.

System	L1	L2	L3	L5/E5	E6
GPS	1563–1588	1215–1240	N/A	1164–1189	N/A
GLONASS	1592–1615	1237–1257	1194–1209	N/A	N/A
Galileo	1554–1596	N/A	N/A	1145–1238	1258–1300

Table 9.1: GNSS frequencies in MHz

9.5.1 Typical GPS Antennas

The highest performing GPS antennas in common use are the choke ring antennas. These are used for geodetic work, where maximum positioning

accuracy is desired at the expense of all other parameters. They typically receive at least the L1 and L2 bands. Such choke ring antennas are physically large, bulky and heavy, expensive to fabricate and delicate. Yet they provide excellent rejection of multipath signals. They do not make good candidates for embedding in polymeric vehicular body panels. One of the most common forms of GPS antenna is the patch antenna. These antennas operate at a single band, being the L1 band. They are small and relatively cheap to produce, and produce good hemispherical coverage. GPS patch antennas typically use truncated corners to induce circular polarisation in an otherwise linearly polarised radiator.

Shark-fin antennas commonly incorporate patch antennas underneath their radome. While it is not verifiable anywhere in the scientific literature, it is also known that other cars feature GPS patch antennas that are installed by automakers below the front windscreen under the dash.

Helical antennas are sometimes used in GPS applications. Such devices are inherently circularly polarised. Due to their size and shape, they are not often used for vehicular applications.

Each of these traditional GPS antennas satisfy many of the characteristics of an ideal GPS antenna. They provide narrowband impedance matches combined with uniform coverage of the sky. Their radiation patterns reject signals from below. Circular polarisation ensures the desired signal is received while helping to reject multipath signals. In contrast, the wideband antennas presented in this thesis provide an impedance match at each of the bands used by all of the GNSS systems (see Table 9.1). Yet they do not provide circular polarisation and have low front-to-back ratios, receiving signals equally well from above or below the substrate.

Interestingly, many modern mobile phones are fitted with GPS antennas. The integration challenges associated with integrating so many wireless services within an increasingly small, thin volume mean that compromises must be made in antenna selection and placement. Ceramic chip antennas, such as

the 1575AT47A40 from Johanson Technology, are often used in such devices because of their extremely small volume. These chip antennas are far from the ideal GPS antennas described above. They typically provide linearly polarised radiation, and when mounted on the handset, uneven quasi-omnidirectional radiation patterns result. The gain is also quite low, with the peak gain between –1 and –6 dBi, depending on frequency. These two factors combine to leave the receiver vulnerable to errors due to multipath. Yet, despite all these sources of error, the overall system performance on many mobile devices is satisfactory. Given these considerations, it was decided to evaluate the actual GPS performance of the O-PICA when connected to a vehicle.

9.5.2 PICA Testing Configuration on Vehicle (Jeep Wrangler)

Two identical Trimble SV6 GPS receivers were sourced to enable testing of the O-PICA antenna with actual GPS hardware. The Trimble SV6 GPS receiver was ideal for the task at hand. It has no internal antenna and no built-in display. Instead, it provides an SMB connector for attaching an external antenna, and interfaces to a computer through RS232 to output text-based data.

The two Trimble SV6 receivers were powered by a 12 volt supply and each was connected to a laptop computer via RS232. The receivers were set to an identical configuration and were fitted with identical LNAs. They differed in only one respect, the antenna connected to the input of the LNA. The antennas supplied with the Trimble SV6 receiver were typical of low-cost commercial GPS antennas. They consisted of a probe-fed patch antenna on a high dielectric constant substrate. The antenna unit contained an integrated LNA on the underside of the antenna, and the whole assembly was encased in a black plastic housing (see Figure 9.20(a)). To enable the O-PICA antenna to be connected to an identical LNA with the same length of coaxial cable, the second of the Trimble patch antennas was dismantled and the probe feed pin was soldered to an SMA connector to enable connection of the PICA (see Figure 9.20(b)). To enable the highly realistic practical testing, the Holden Adventra roof panel introduced in Section 9.5 was used to resemble

the eventual scenario in which a wideband antenna would be embedded in a polymeric component moulded from SMC materials.

A Jeep Wrangler was found to be a suitable test vehicle due to its adaptability. The Jeep Wrangler comes with a steel roll cage from the factory, and has a variety of options for weather protection. A folding soft top comes standard, but an SMC hard top (produced in the USA) is available as an option. The Jeep factory hard top is large and bulky, and not readily measurable on the RMIT outdoor range. The O-PICA antenna was measured while embedded in the SMC Adventra roof (see Section 9.6). Given that the radiation performance of this configuration had already been characterised, we implemented it here by mounting the Adventra panel with the O-PICA onto the top of the Jeep's roll cage (see Figure 9.21). The panel was held down on the roll cage using ratchet straps that were positioned away from the radiating structure underneath the panel.

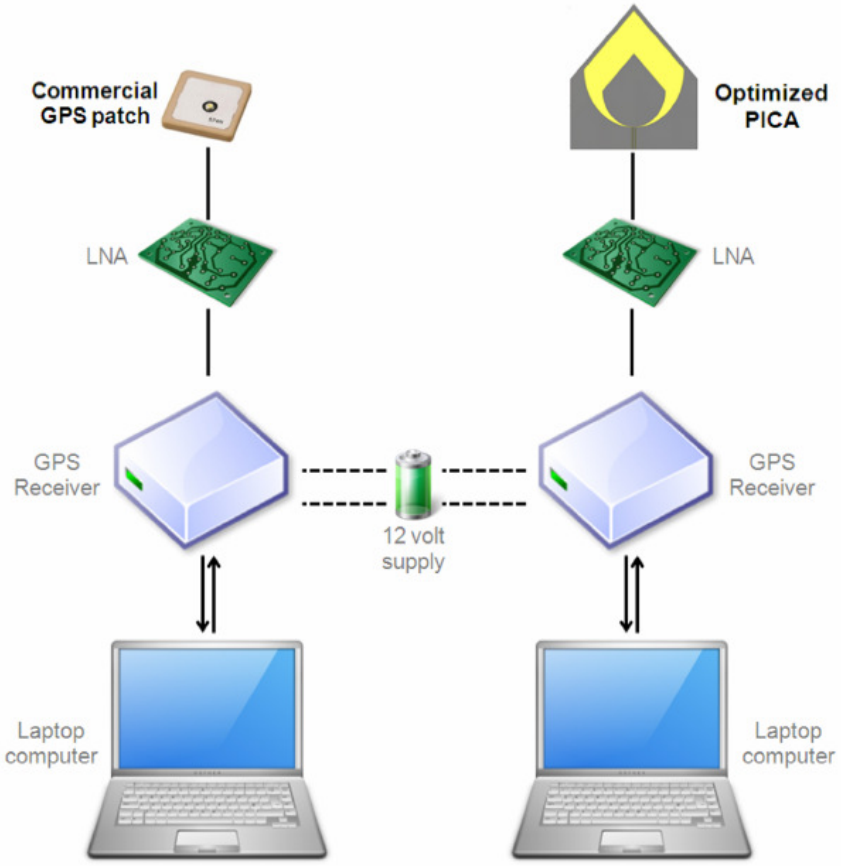

Figure 9.19: Set-up used to compare the GPS performance of the O-PICA with the commercial GPS patch antenna

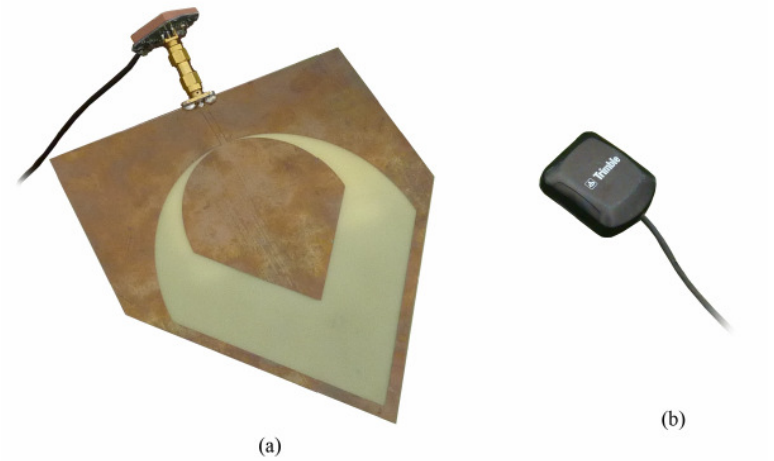

Figure 9.20: (a) O-PICA connected to LAN and (b) Trimble GPS patch antenna with integrated LNA

With the O-PICA antenna attached to the underside of the panel on the Jeep roof, the remaining Trimble GPS antenna was placed in an upright position on the rear seat with a clear view of the sky.

9.5.3 Results of PICA on Jeep

The GPS receiver systems were switched on, and the vehicle was left stationary for several minutes while the receivers downloaded the ephemeris and achieved a position fix.

Figure 9.21: The test vehicle at the start/finish point of the test route

The Jeep was then repeatedly driven along a preplanned route over a period spanning several hours. The route was planned to provide a variety of propagation environments to test the performance of the antennas over its length of 4.1 km. Relatively open areas with few obstructions were paths along the route, as well as busy city streets at the eastern end of Collins Street in Melbourne, which is surrounded by high-rise buildings that ought to create many multipath propagation channels. To verify that the receivers were providing an equivalent level of performance, the input cables to each receiver were exchanged several times throughout the driving tests. This resulted in both receivers operating with the O-PICA as its antenna. The vehicle was then driven around along the preplanned route several times while measurements were taken. The route is shown in Figure 9.22. Two of the recordings from the GPS units are shown in Figure 9.23 and Figure 9.24. Figure 9.26 shows the view looking south from above Faraday Street, looking south towards the central business district (CBD) of Melbourne, and reveals

the harsh propagation environment that would be experienced due to the density of tall buildings.

Trip A (see Figure 9.23) shows the position outputs from both GPS receivers throughout the journey. Both the Trimble patch antenna (shown in blue) and O-PICA antenna (red) provided good signal to the receivers. The receiver connected to the Trimble patch antenna appeared to drift while travelling south on Exhibition Street, and then to rapidly correct itself between Lonsdale and Bourke Streets, producing a zigzag in the output. The receiver connected to the O-PICA produced some slight errors in the turn from Exhibition Street to Collins Street, effectively cutting the corner. Given the tall buildings that surround the roads in these areas, both receivers performed very well at maintaining their position, and clearly received good signals from both the PICA and commercial antennas.

The particular GPS satellites and signals that can be received by a GPS receiver change over time. This is due to changes in satellite position, as they move across the sky in the course of their orbit around the earth. This created some variation in the results obtained throughout the driving testing. On each journey along the test route, a different propagation environment was encountered by the receiver, with the satellites in new locations in the sky.

Trip B (see Figure 9.24) represents one trip along the test route in which both receivers produced a higher level of errors than in any other trip, including Trip A. As Trip B was conducted several hours after Trip A, this is likely due to the changes in position of the satellites, but may also have been a result of other factors, such as a higher level of interference. Both receivers performed well at the beginning of the journey in the open environment where multipath was low. Erroneous positions were calculated by both receivers when approaching Lonsdale Street from the north. Interestingly, at this time the receiver connected to the Trimble patch antenna provided more highly inaccurate positions than did its counterpart with the O-PICA. Both receivers outputted slightly westward-shifted positions in the approach to Bourke Street. For the next 1.5 km of the journey through the high-density urban

environment, the receiver with the Trimble patch antenna provided much more accurate position than the receiver with the O-PICA.

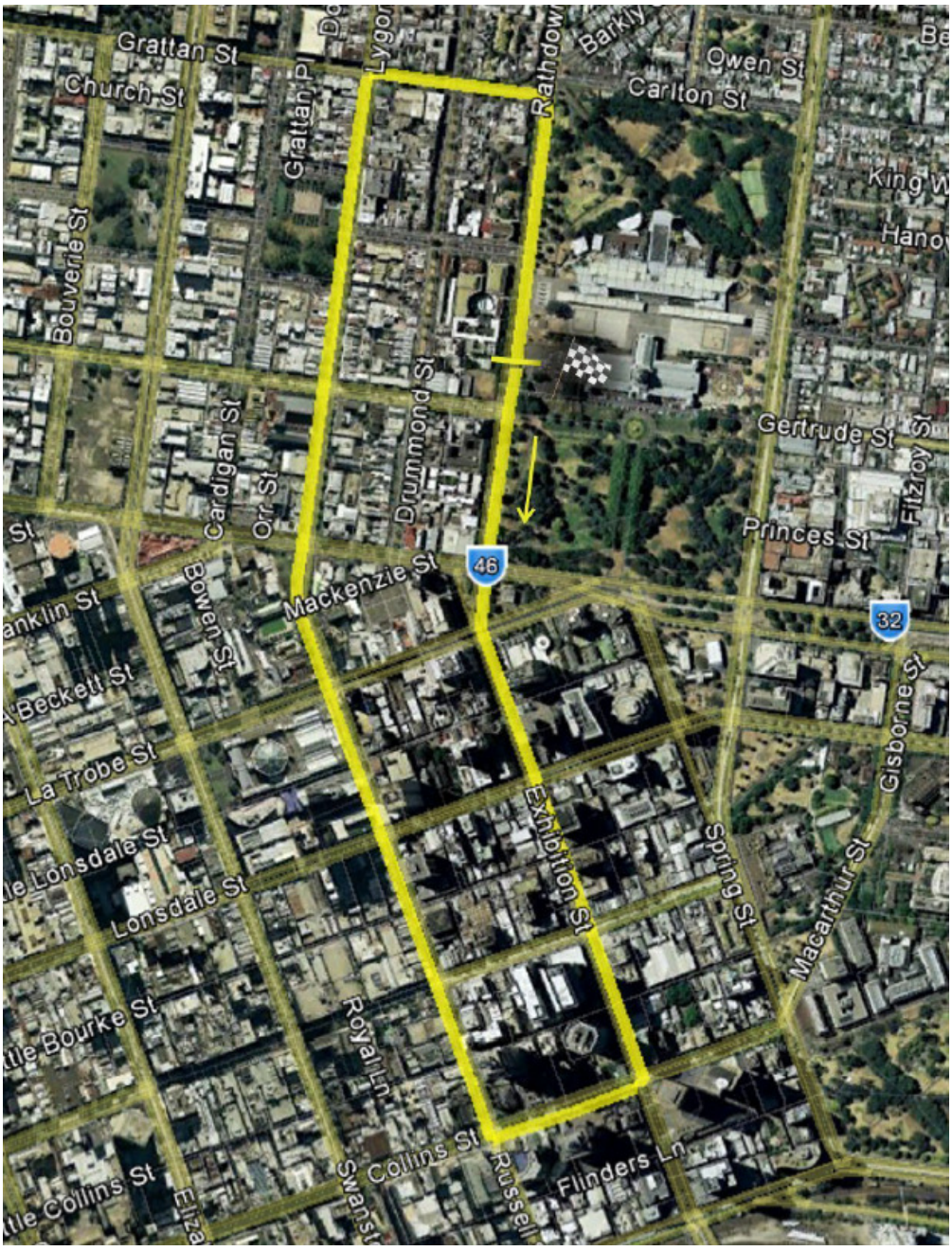

Figure 9.22: GPS testing route

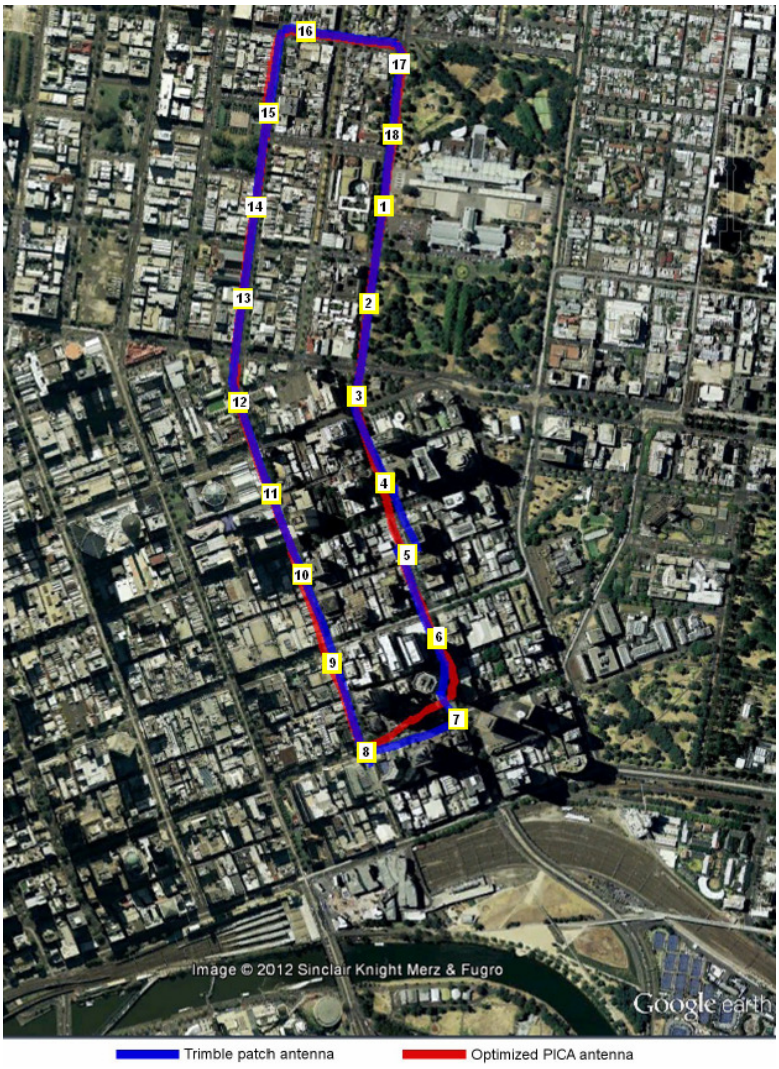

Figure 9.23: GPS testing Trip A

Table 9.2: Positional error in meters for 2 antennas for Trip A

Position	Optimised PICA antenna	Trimble patch antenna
1	2	3
2	4	3
3	3	3
4	2	18
5	4	30
6	3	4
7	35	8
8	2	4
9	6	2
10	3	3
11	2	2
12	2	2
13	3	2
14	2	4
15	3	4
16	3	3
17	3	2
18	2	2
Average	**4.7**	**5.5**

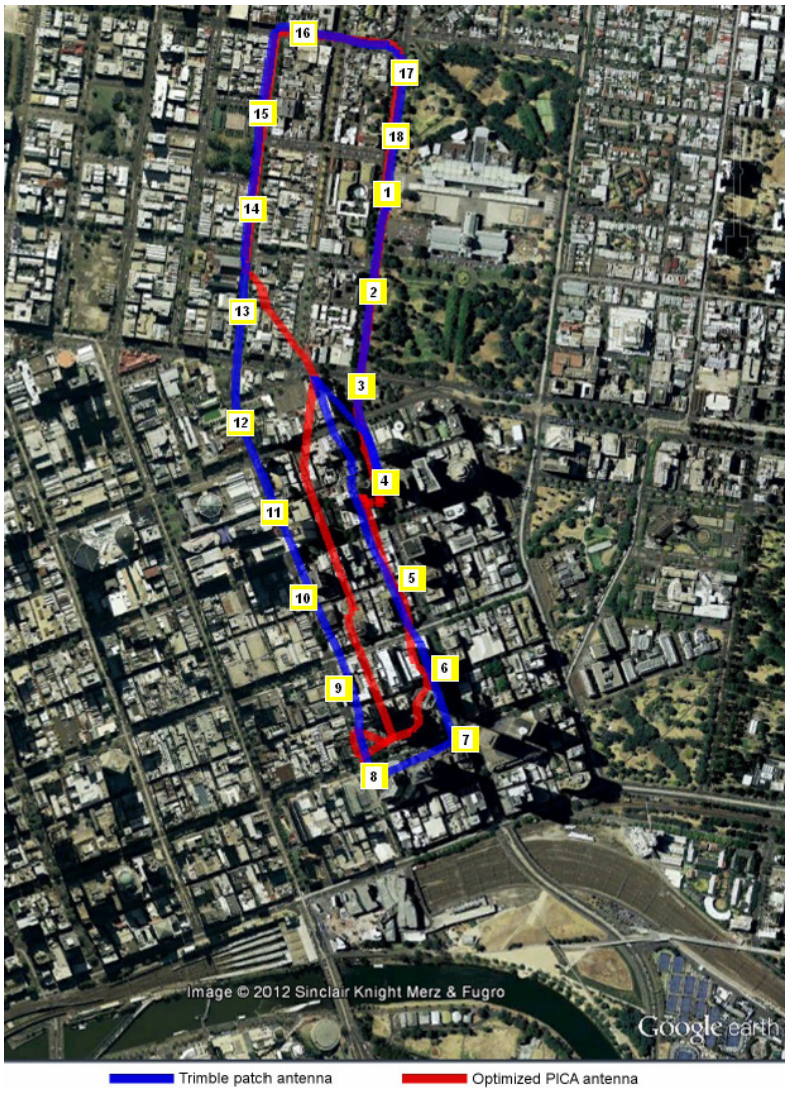

Figure 9.24: GPS testing Trip B

Table 9.3: Positional error in meters for 2 antennas for Trip B

Position	Optimised PICA antenna	Trimble patch antenna
1	1	3
2	2	2
3	5	80
4	10	7
5	23	25
6	24	28
7	85	12
8	68	9
9	54	18
10	72	16
11	79	7
12	126	4
13	35	4
14	1	3
15	2	7
16	2	5
17	1	3
18	2	4
Average	**32.9**	**13.2**

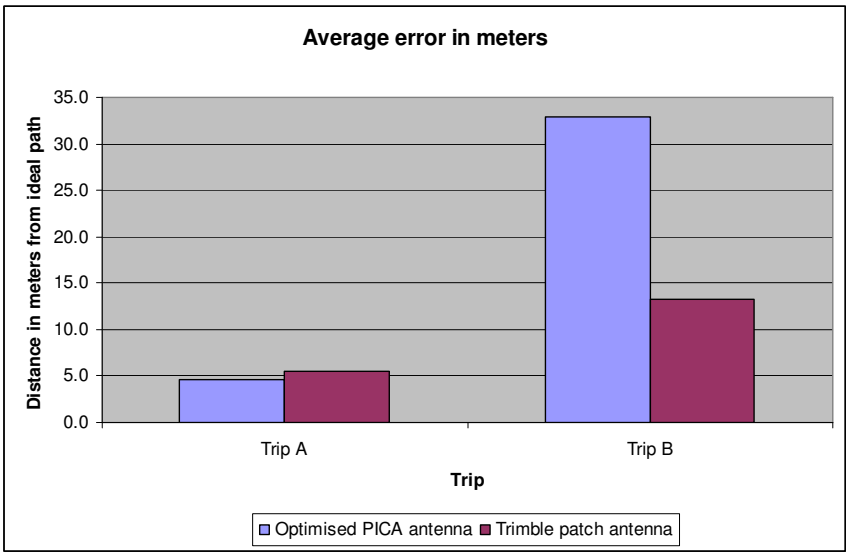

Figure 9.25: Performance of O-PICA v. Trimble GPS antenna

Figure 9.26: View to the south from above Faraday Street. The tall buildings of the CBD are shown in the distance.

This may have been due to the lack of circular polarisation and the back lobe of the O-PICA, which limited its multipath rejection capability. Once in the low-density, open urban environment, both receivers produced accurate position outputs for the remaining 1 km of the test route along Lygon, Grattan and Rathdowne Streets.

9.6 GSM Mobile Phone Test

Simple testing was also performed for the mobile phone band at 900 MHz. A second-hand GSM car kit from the late 1990s was obtained. This car kit was selected because it lacked an internal antenna and provided an external antenna connector instead. A short coaxial cable was created to enable connection of the car kit with the SMA connector fitted to the antenna. After inserting a SIM card, and turning the power on, test calls were made in various locations. In each location, the calls were clear and without dropouts. If, midway through a call, the antenna was disconnected, the calls were terminated immediately due to a loss of service. This basic testing confirms the operation of the antenna at 900 MHz in conjunction with GSM equipment.

9.7 Conclusion

Initial testing of the antenna embedded into the tailgate of the HSV Maloo ute indicated that the performance of the antenna was degraded slightly. The resulting system performance is likely to be equivalent to current ‘shark-fin’ or ‘on-glass’ designs. These existing designs also produce imperfect radiation patterns and suffer from gain loss when compared with the ideal case of a monopole mounted on an infinite ground plane. As noted, the antenna design was not optimised to work inside dielectric material such as SMC; however, this optimisation could be easily achieved through CAE tools.

The wideband impedance match of the antenna was preserved even when the antenna was curved at an angle of up to 90°, as may be the case when installed in a vehicle. At the low end of the band, when the PICA was acting as a traditional slot antenna, the effect of bending was less significant than at the high end of the band, where the high-gain beams caused by the tapered

slots were observed to shift significantly, particularly in the y-z plane. Preliminary studies of the GPS performance of the O-PICA-based antenna attached to the roof panel of the Adventra vehicle indicated good performance in terms of both signal strength and positioning accuracy when tested in an environment where the effects of the signal deflections were minimised.

In the real world testing, as evidenced in Tables 9.2 and 9.3, the performance of the antenna was significantly affected by the deflected signals. The GPS paths plotted in Figures 9.23 and 9.24 demonstrate that the O-PICA can be used in conjunction with an SMC roof panel to provide GPS signals to a GPS receiver in a vehicle. The O-PICA provided GPS performance that almost matched that of a commercial GPS patch antenna marketed by Trimble, or even outperformed it, as shown in Table 9.2. The O-PICA performed very well in low-density urban environments, but may have been susceptible to multipath in very dense high-rise areas, as shown in Table 9.3. This issue could be addressed by integrating filters—one possible design is shown in Figure 9.27 and is based on a design proposed by Bonache et al. (2005)—in the antenna design that would help reject multipath signals that typically occur in the urban environment. While the lack of ground plane on the underside of the O-PICA and the corresponding double-sided radiation pattern led to sensitivity from reflected signals, the Trimble SV6 receiver was able to determine accurate position information from the received signals. It is possible that the mounting of the antenna and the polymeric Adventra roof on the Jeep body minimised planar reflections from the ground and mitigated the reflection problem, due to the complex interior shape of the vehicle

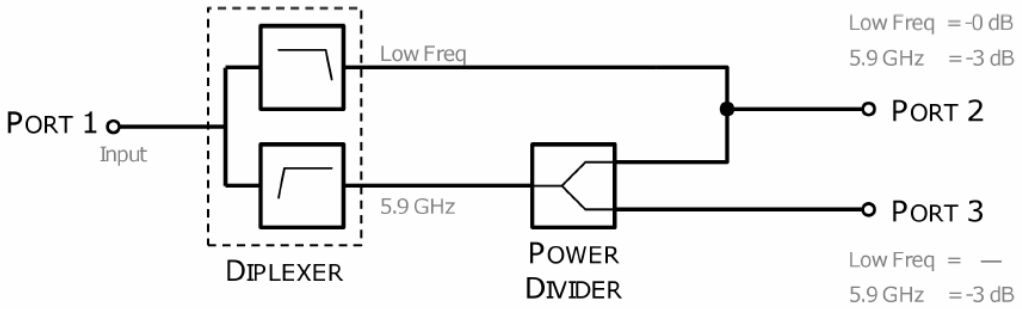

Figure 9.27: Schematic of the required device

CHAPTER 10: Conclusion

10.1 Introduction

The main aim of the research study was to develop the technology of a smart composite vehicle panel, as a proof of the concept that an antenna could be embedded into a painted composite panel that would provide the signals required by a number of devices in the vehicle. This panel needed to resemble an ordinary vehicle panel.

10.2 Dielectric Test Findings

Two test techniques were used to determine the dielectric properties of SMC at 1.5 GHz. The techniques, free-space measurement and rectangular waveguide, were used rather than other techniques, such as two parallel metallic plate or cavity resonator techniques, both of which unfortunately have a restricted frequency range and require rigorous sample preparation.

Both sets of the results obtained, with free-space measurement and rectangular waveguide, showed good correlation, where the dielectric constant was about 4.5. This indicates that the SMC material selected is suitable as a host material in which an antenna can be embedded and still retain good performance and signal quality. This result correlates well with results found in the literature for similar glass fibre reinforced polyester resins and their range is from 4 to 5.2. In addition, understanding what the dielectric constant for SMC is enables small modifications to be done to the antenna design to correct for the presence of the SMC material.

10.3 Paint Effect Findings

As the literature review revealed, references in the literature involving paint and antennas are sparse. The most complete are three investigations that involve paint applied to the surface of reflector antennas. These papers pertain to testing at frequencies in excess of 10 GHz, and report observed effects in cross-polar performance, noise temperature and gain loss.

Both antennas used in this research were planar, and were appropriately dimensioned to allow either the radiating patch or slot to be covered by the paint sample during testing. The L1-band GPS frequency of 1.575 GHz was chosen as the target frequency for the narrowband investigation because of the ubiquitous satellite navigation facilities in modern vehicles. The required bandwidth of 20 MHz at 1.575 GHz led to a narrow percentage bandwidth of 1.3%. RT/duroid® 5880 material with 0.062" thickness was chosen for the substrate and superstrate. The antenna was fabricated and tested on a VNA and was found to have a centre frequency of 1.583 GHz in the presence of the reference superstrate. The slight variation from the centre frequency in the design is attributable to magnification inaccuracies in the photographic stage of fabrication. For the wideband investigation, an asymmetrical bow-tie slot antenna was designed and fabricated on FR-4 material. It operated from 1.4 to 9.7 GHz, providing a bandwidth of 150% or approximately 7:1. The study results were confirmed by integrating an actual wideband antenna into a composite vehicle panel and comparing return loss results before and after embedding.

Application of paint to a part that has an antenna embedded in it, be it the narrowband or wideband type, will have some effect on the antenna performance. This addition of paint caused a shift in the frequency characteristics of both narrowband and wideband antennas. This was due to the change in the effective relative permittivity of the space surrounding the antenna, and it was a function of the dielectric constant of the paint and the thickness with which it was applied. The consequences of frequency shifting may be significant for narrowband antennas, where a small shift could lead to loss of the desired communications service, while the effect on the wideband antenna is very minimal. As the intended antenna to be used in this application is a wideband antenna, the effects of the paint to be applied to the finished panel can be disregarded.

10.4 Rheological Testing Findings

Rheological testing confirmed that the SMC material behaved as a typical thermoset polymer, that is, it exhibited shear-thinning behaviour until it reached gel point and started to cure. In the initial stages of processing, the material behaviour was dominated by G" (loss modulus) as most of the energy put into the material was dissipated by movement of the molecular chains in respect to each other. Once the curing process started, there was a crossover point and the G' (storage modulus) dominated as most of the energy was now stored within the cross-linked structure developed with curing.

There was no chain scission or yield stress generation within the material. The test also confirmed that the material's gel point was independent of frequency and we observed that the minimum viscosity of about 12 Pa-s was attained at the highest heat-up rate of 40 deg ˚C/minute.

10.5 Antenna Deformation Model Findings

A viscoelastic model of the SMC was developed that showed good correlation with experiments in predicting antenna deformation during embedding. The results obtained were used to optimise the manufacturing process in order to minimise antenna deformation. The optimal process parameters were found to be:

- tool closing speed of 4 mm/sec
- SMC charge to be preheated to 60 ˚C
- tool temperature to be set to 160 ˚C

10.6 Wideband Antenna Development Finding

A number of wideband antenna types were developed, including PICA, truncated PICA and O-PICA. All three antenna types had desirable properties, such as geometry that lends itself to embedding, as they were all printed on a common FR4 substrate with good physical properties and a thickness of 0.4 mm. The O-PICA was developed with specific services in mind and its size and shape were validated via simulation and experimentally

before it was embedded in a vehicle panel and then tested in real world environments at mobile phone frequency of 900 MHZ and GPS frequency at 1.575 GHz.

10.7 Antenna Testing Findings

These tests confirmed that the performance of the O-PICA was comparable to other commercially available antennas developed specifically for each service, the Trimble antenna for GPS and common mobile phone antenna. The test showed acceptable performance at mobile phone frequency; however, as shown in the results for GPS, the performance varied from very good, as in Trip A, where it outperformed the commercially used GPS antenna, to borderline acceptable, as in Trip B. However, this marginal performance can be improved by adding a filter that would reject some of the deflected signals and only accept the strongest signal.

Future Work

Future work needs to focus on several areas, such as:

1. Converting the compression-moulding process from a prototype to a production one by developing automatic placement of the antenna in the SMC charge, loading the charge into the tool (the tool would require a specific access point to be created in the SMC for feed lines of the antenna to be connected to a connector such as the one proposed in Figure 10.1)
2. Wireless transmission of signals between antenna and devices requiring the signal to simplify the process and reduce cost
3. Effects of water droplets (rain on the vehicle roof) on the antenna performance and signal quality
4. Effects of snow/ice (on the vehicle roof) on the antenna performance and signal quality
5. Optimisation of the rheological model to include effects of near structural perturbations on the material flow
6. Development of suitable filters to correct for multipath signals that have a large effect on GPS performance
7. Evaluation of RFID tag performance, as they could be used to embed into various components such as pallets to enable automated material tracking; as the pallets move in and out of the warehouse, RFID tags could be automatically read by RFID readers installed at the access points.

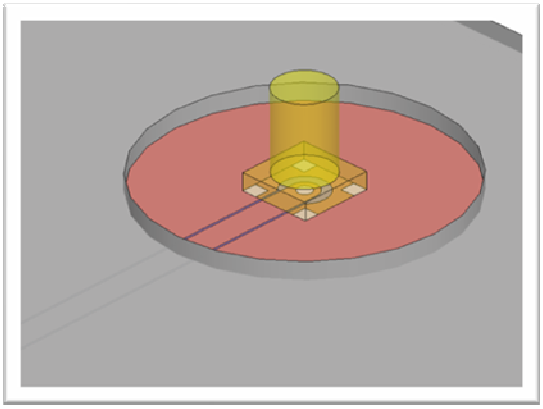

Figure 10.1: Gray is SMC, brown is antenna, blue are feed lines and yellow is the connector

References:

Afsar, M, Birch, JB, Clarke, RN & Chantry, EW 1986, 'Measurement of the properties of materials', *Proceedings of the IEEE*, vol. 74, no. 1, pp. 183–199.

Agilent 2000a, *Application note 1287-1, Understanding the fundamental principles of vector network analysis,* Agilent literature number 5965-7707E.

Agilent 2000b, *Application note 1287-2, Exploring the architectures of network analyzers,* Agilent literature number 5965-7708E.

Agilent 2002, *Application note 1287-3, Applying error correction to network analyzer measurements,* Agilent literature number 5965-7709E.

Agilent 2003, *Application note 1369-1, Solutions for measuring permittivity and permeability with LCR meters and impedance analyzers*, Agilent literature number 5980-2862EN.

Agilent application note 380-1, 1998, *Dielectric constant measurement of solid materials using the 16451B dielectric test fixture*, Agilent literature number 5950-2390.

Alexopoulos, N & Jackson, D 1984, 'Fundamental superstrate (cover) effects on printed circuit antennas', *IEEE Transactions on Antennas and Propagation*, vol. 32, no. 8, pp. 807–816.

Altschuler, HM 1963, 'Dielectric constant', in *Handbook of microwave measurements*, Wiley.

American Society for Testing and Materials , *Standard test methods for complex permittivity (dielectric constant) of solid electrical insulating materials at microwave frequencies and temperatures to 1650°C,* ASTM Standard D2520.

Amiet, A & Jewsbury, P 2000, 'Free space microwave permittivity and permeability measurements', in *Asia-Pacific Microwave Conference 2000*, pp. 445–448.

Baker-Jarvis, J, Janezic, MD, Grosvenor, JS & Geyer, RG 1993, *Transmission/reflection and short-circuit methods for measuring permittivity and permeability*, NIST technical note 1355-R.

Balanis, A.C, 2005, 'Antenna theory: Analysis and Design', Third Edition, John Wileys and Sons Inc., ISBN 0-471-66782-7

Barnes, H, Hutton, J & Walters, K 1997, *An introduction to rheology,* Elsevier, Amsterdam.

Barnes, H 2000, *A handbook of elementary rheology,* University of Wales, Aberystwyth.

Barone, R, M & Caulk, DA 1979, 'The effect of deformation and thermoset cure on heat conduction in a chopped-fiber reinforced polyester during compression molding', *International Journal of Heat and Mass Transfer*, vol. 22, no. 7, pp. 1021–1032.

Barone, MR & Caulk, DA 1985, 'Kinematics of flow in sheet molding compound', *Polymer Composites*, vol. 6, no. 2, pp. 105–109.

Barone, MR & Caulk, DA 1986, 'A model for the flow of a chopped reinforced polymer compound in compression moulding', *Journal of Applied Mechanics*, vol. 53, no. 2, pp. 361–371.

Baskurt, O & Meiselman H 2003, 'Blood rheology and hemodynamics', *Seminars in Thrombosis and Haemostasis*, vol. 29, no. 5, pp. 435–450.

Batchelor, G 1967, *An introduction to fluid dynamics,* Cambridge University Press, Cambridge.

Batchelor, GK 1970, 'The stress system in a suspension of force-free particles'*, Journal of Fluid Mechanics*, vol. 41, no. 3, pp. 545–570.

Beer, S, Adamiuk, G & Zwick, T 2009, 'Novel antenna concept for compact millimeter-wave automotive radar sensors', *Antennas and Wireless Propagation Letters, IEEE*, vol. 8, pp. 771–774.

Betten, J 1988, 'Applications of tensor functions to the formulation of yield criteria for anisotropic materials'*, International Journal of Plasticity*, vol. 4, no. 1, pp. 29–46.

Bian, L, Guo, Y & Shi, X 2008, 'Broadband slot antenna with circular-polarisation operation', in *IEEE Vehicular Technology Conference, 2008. VTC Spring 2008*, pp. 353–355.

Bird, R, Stewart, W & Lightfoot, E 1960, *Transport phenomena*, John Wiley & Sons, Hoboken, NJ.

Bird, R, Armstrong, R & Hassager, O 1987, *Dynamics of polymeric liquids,* John Wiley & Sons, New York.

Bird, R, Curtiss, C & Armstrong, R 1989, *Dynamics of polymeric liquids*, vols. 1 & 2, Wiley Interscience.

Blackham, DV & Pollard, D 1997, 'An improved technique for permittivity measurements using a coaxial probe', *IEEE Transactions on Instrumentation and Measurements*, vol. 46, no. 5, pp. 1093–1099.

Boehler, J-P 1987, 'Applications of tensor functions in solid mechanics', vol. 292, *Courses and lectures—International Centre for Mechanical Sciences*, Springer-Verlag, Wien, NY.

Bogdanov, F, Karkashadze, D, Jobava, R, Gheonjian, A, Yavolovskaya, E, Bondarenko, N & Ullrich, C 2010, 'Validation of hybrid MoM scheme with included equivalent glass antenna model for handling automotive EMC problems', *IEEE Transactions on Electromagnetic Compatibility*, vol. 52, no. 1, pp. 164–172.

Boger, D & Walters, K 1993, *Rheological phenomena in focus,* Elsevier, Amsterdam.

Boylan, S, Abrams, LM & Castro, JM 2006, 'Predicting moulding forces during sheet moulding compound (SMC) compression moulding. II: effect of SMC composition', *Polymer Composites*, vol. 24, no. 6, pp.731–747.

Bussey, HE 1967, 'Measurement of RF properties of materials: a survey', *Proceedings of the IEEE*, vol. 55, No. 6, pp. 1046–1053.

Buyevich, Y & Shchelchkova, I 1978, 'Flow of dense suspension', *Progress in Aerospace Science*, vol. 18, pp. 121–150.

Castro, JM & Griffith, RM 1989, 'Sheet molding compound compression-molding flow'*, Polymer Engineering and Science*, vol. 29, no. 10, pp. 632–637.

Castro, JM & Tomlinson, G 1990, 'Predicting molding forces during sheet molding compound (SMC) compression molding. I: model development', *Polymer Engineering and Science,* vol. 30, no. 24, pp. 1569–1573.

Cerretelli, M & Biffi Gentili, G 2007, 'Progress in compact multifunction automotive antennas', in *International Conference on Electromagnetics in Advanced Applications*, pp. 93–96.

Cheng, S, Hallbjorner, P & Rydberg, A 2008, 'Printed slot planar inverted cone antenna for ultrawideband applications', *IEEE Antennas and Wireless Propagation Letters*, vol. 7, pp. 18–21.

Chu, T & Semplak, T 1976, 'A note on painted reflecting surfaces', *IEEE Transactions on Antennas and Propagation*, vol. 24, pp. 99–101.

Coleman, B, Markowitz, H & Noll, W 1966, *Viscometric flows of non-Newtonian fluids,* Springer-Verlag, Berlin.

Costigan, PJ et al. 1985, 'The rheology of SMC during compression molding, and resultant material properties', in *40th Annual Conference, Reinforced Plastics/Composites Institute, The Society of the Plastics Industry, Inc. Jan. 28–Feb. 1, 1985.*

Coussot, P & Ancey, C 1996, *Rhéophysique des pâtes et des suspensions,* EDP Sciences, Les Ulis.

Dartevelle, S 2004, 'Numerical modeling of geophysical granular flows: 1. A comprehensive approach to granular rheologies and geophysical multiphase flows, *Geochemistry Geophysics Geosystems*, vol. 5, DOI 10.1029/2003GC000636.

Davis, B, Theriault, A & Osswald, T 1997, 'Optimization of the compression (injection/compression) molding process using numerical simulation', *ASME Conference*.

Drew, D 1983, 'Mathematical modeling of two-phase flows', *Annual Review of Fluid Mechanics*, vol. 15, pp. 261–291.

Drew, D & Passman, S 1999, *Theory of multicomponent fluids,* Springer, New York.

Dumont, P et al. 2003, 'Anisotropic viscous behaviour of sheet moulding compounds (SMC) during compression moulding'*, International Journal of Plasticity*, vol. 19, no. 5, pp. 625–646.

Economou, L & Langley, J 1998, 'Circular microstrip patch antennas on glass for vehicle applications', *IEEE Proceedings Microwaves, Antennas and Propagation*, vol. 145, no. 5, pp. 416–420.

Eom, SY, Son, SH, Jung, YB, Jeon, SI, Ganin, S, Shubov, A, Tobolev, A & Shishlov, A 2007, 'Design and test of a mobile antenna system with tri-band operation for broadband satellite communications and reception', *IEEE Transactions on Antennas and Propagation*, vol. 55, no. 11, pp. 3123–3133.

Federal Communications Commission 2002, *New public safety applications and broadband internet access among uses envisioned by FCC authorization of ultra-wideband technology*, media release, FCC, Washington, 14 February.

Findley, W, Lai, J & Onaran, K 1989, *Creep and relaxation of nonlinear viscoelastic materials*, Dover Publications, New York.

Folgar, F & Tucker, CL 1984, 'Orientation behavior of fibers in concentrated suspensions', *Journal of Reinforced Plastic Composites*, vol. 3, no. 2, pp. 98–119.

Ghodgaonkar, D & Varadan, V 1989, 'A free-space method for measurement of dielectric constants and loss tangents at microwave frequencies', *IEEE Transactions on Instrumentation and Measurement*, vol. 38, no. 3, pp. 789–793.

Ghodgaonkar DK, Varadan, VV & Varadan, VK 1990, 'Free-space measurement of complex permittivity and complex permeability of magnetic materials at microwave frequencies', *IEEE Transactions on Instrumentation and Measurement*, vol. 39, no. 2, pp. 387–394.

Gottwald, G 1998, 'Numerical analysis of integrated glass antenna systems', *SAE Technical Paper Series*, Paper ID 982386, Society of Automotive Engineers.

Gschwendtner, E & Wiesbeck, W 2003, 'Ultra-broadband car antennas for communications and navigation applications', *IEEE Transactions on Antennas and Propagation*, vol. 51, no. 8, pp. 2020–2027.

Gunasekaran, S & Mehmet, M 2003, *Cheese rheology and texture*, CRC Press, Boca Raton, Fla.

Gupta, S, Ramesh, M & Kalghatgi, A 2006, 'Ultra wideband embedded planar inverted conical antenna', *Microwave and Optical Technology Letters*, vol. 48, no. 12, pp. 2465–2468.

Herczynski, R & Pienkowska, I 1980, 'Toward a statistical theory of suspension', *Annual Review of Fluid Mechanics*, vol. 12, pp. 237–269.

Hill, R 1950, *Mathematical theory of plasticity*, Oxford University Press, Oxford, UK.

Hoare, E & Hill, R 2000, 'System requirements for automotive radar antennas', in *IEE Colloquium on Antennas for Automotives*, pp. 1/1–111.

Hombach, V & Kuhn, E 1989, 'Complete dual-offset reflector antenna analysis including near-field paint-layer and CFRP-structure effects', *IEEE Transactions on Antennas and Propagation*, vol. 37, no. 9, pp. 1093–1101.

Hopf, J, Reiter, L & Lindenmeier, S 2007, 'Compact multi-antenna system for cars with electrically invisible phone antennas for SDARS frequencies', in *2nd International ITG Conference on Antennas, INICA '07,* pp.171–175.

Huang, C & Hsu, P 1991, 'Superstrate effects on slot-coupled microstrip antennas', *Magnetics IEEE Transactions*, vol. 27, no. 5, pp. 3868–3871.

Huang, C & Lin, D 2006, 'CPW-fed bow-tie slot antenna for ultra-wideband communications'*, Electronics Letters*, vol. 42, no. 19, pp. 1073–1074.

Hull, D 1996, *Introduction to Composite Materials*, Cambridge University Press, New York.

Hutter, K & Jöhnk, K 2004, *Continuum methods of physical modeling,* Springer, Berlin.

IEEE, *IEEE standard definitions of terms for antennas*, IEEE Std 145-1993.

Iizuka, H, Watanabe, T, Sato, K & Nishikawa, K 2005, 'Modified H-shaped antenna for automotive digital terrestrial reception', *IEEE Transactions on Antennas and Propagation*, vol. 53, no. 8, pp. 2542–2548.

Jackson, D & Alexopoulos, N 1985, 'Gain enhancement methods for printed circuit antennas', *Antennas and Propagation IEEE Transactions*, vol. 33, no. 9, pp. 976–987.

Jensen, WK 1971, *Concealed windshield broadband antenna*, US patent 3,576,576.

Khan, A & Haoyue, Z 2001, 'Finite deformation of a polymer: experiments and modeling'*, International Journal of Plasticity*, vol. 17, no. 9, pp. 1167–1188.

Kim, J, Shiau, YC, Lee, LJ & Im, YT 1992, 'Compression molding simulation of chopped fiber reinforced polymeric composites in plate-rib type geometry'*, Polymer Composites*, vol. 13, no. 2, pp. 97–107.

Kim, K-T, Jeong, J-H & Im, Y-T, 1997, 'Effect of molding parameters on compression molded sheet molding compounds parts', *Journal of Materials Processing Technology*, vol. 67, no. 1–3, pp. 105–111.

Kim, S & Karrila, S 1991, *Microhydrodynamics: principles and selected applications,* Butterworth-Heinemann, Stoneham.

Kim, Y & Kwon, D 2005, 'CPW-fed right-angled dual tapered notch antenna for ultrawideband communication', *Electronics Letters*, vol. 41, no. 12, pp. 674–675.

Koch, D & Hill, R 2001, 'Inertial effects in suspension and porous-media flows', *Annual Review of Fluid Mechanics*, vol. 33, pp. 619–647.

Koike, T, Hase, N, Koide, E, Murakami, Y, Izawa, S, Ohira, T, Nagasaka, O, Tanaka, Y & Suzuki, T 1999, 'Development of a rear spoiler with built-in antenna', *SAE Technical Paper Series*, Paper ID 1999-01-0807, Society of Automotive Engineers.

Kumagai, N, Sasajima, S & Ito, H 1978, 'Long-term creep of rocks', *Journal of the Society of Materials Science (Japan)*, vol. 27, p. 157.

Lambourne, R & Strivens, TA (eds.) 1999, *Paint and surface coatings: theory and practice*, Woodhead Publishing Ltd, pp. 450–457.

Le Corre, S, Orgéas, L, Favier, D, Tourabi, A, Maazouz, A & Venet, C, n.d. Shear and compression behavior of sheet molding compounds, *Composite Science and Technology*, in press.

Lee, CC, Folgar, F & Tucker, C 1984, 'Simulation of compression molding for fiber-reinforced thermosetting polymers', *Polymer Composites*, 106, pp. 114–125.

Lee, HS, Kim, J, Hong, S & Yoon, J 2005, 'Micromachined CPW-fed suspended patch antenna for 77 GHz automotive radar applications', in *The New Trends and Developments in Automotive System Engineering 538*

European Conference on Wireless Technology, 2005, pp. 249–252, DOI 10.1109/ECWT.2005.1617704.

Lee, LJ, Marker, LF & Griffith, RM 1981, 'The rheology and mold flow of polyester sheet molding compound', *Polymer Composites*, vol. 2, no. 4, pp. 209–218.

Lee, R Zaman, A & Lee, K 1989, 'Effects of dielectric superstrates on a two-layer electromagnetically coupled patch antenna', in *Antennas and Propagation Society International Symposium*, *AP-S. Digest*, vol 2, pp. 620–623.

Lin, CM, Weng, CI & Ho, CT 1997, 'Anisotropy in sheet molding compounds during compression molding'*, Polymer Composites*, vol. 18, no. 5, pp. 613–622.

Lin, CM & Weng, CI 1999, 'Simulation of compression molding for sheet molding compound considering the anisotropic effect'*, Polymer Composites*, vol. 20, no. 1, pp. 98–113.

Lindenmeier, H, Hopf, J & Reiter, L 1985, 'Active AM-FM windshield antenna with equivalent performance to the whip now as standard equipment in car production', in *Antennas and Propagation Society International Symposium*, pp. 621–624.

Lindenmeier, H, Reiter, L, Ramadan, A, Hopf, J & Lindenmeier, S 2006, 'A new design principle of active receiving antennas applied with a high impedance amplifier-diversity-module in a compact multi-band-antenna-system on a plastic trunk lid', *SAE Technical Paper Series*, Paper ID 2006-01-0480, Society of Automotive Engineers.

Lindenmeier, H, Hopf, J & Reiter, L 2007, 'Compact multi-antenna system for cars with electrically invisible phone antennas for SDARS frequencies', in *2nd International ITG Conference on Antennas, INICA '07*, pp. 171–175.

Low, L Langley, R Breden, R & Callaghan, P 2006, 'Hidden automotive antenna performance and simulation'*, IEEE Transactions on Antennas and Propagation*, vol. 54, no. 12, pp. 3707–3712.

Lynch, AC 1974, 'Precise measurements on dielectric and magnetic materials', *IEEE Transactions on Instrumentation and Measurement*, vol. 23, no. 4, pp. 425–443.

Lyons, C & Taskin, I 2003, 'A low-cost MMIC based radar sensor for frontal, side or rear automotive anticipatory pre-crash sensing applications', in *Proceedings of the IEEE Intelligent Vehicles Symposium*, *IV*, pp. 688–693.

Marker, LF & Ford, B 1977, 'Flow and curing behavior of SMC during molding'*, Modern Plastics*, vol. 54, pp. 64–70.

Martin, CL, Favier, D & Suery, M 1997, 'Viscoplastic behaviour of porous metallic materials saturated with liquid. Part I: constitutive equations', *International Journal of Plasticity*, vol. 13, no. 3, pp. 215–235.

Martin, CL, Favier, D & Suery, M 1999, 'Fracture behaviour in tension of viscoplastic porous metallic materials saturated with liquid', *International Journal of Plasticity*, vol. 15, no. 10, pp. 981–1008.

McKenna, B & Lyng, J 2003, *Texture in food: introduction to food rheology and its measurement*, viewed 18 September 2009, <http://books.google.com/?id=wM1asp1LL8EC&pg=PA130&dq=Food+Rheology&q=FoodRheology>.

Meyssonnier, J, Duval, P, Gagliardini, O & Philip, A 2001, 'Constitutive modelling and flow simulation of anisotropic polar ice', in Straughan, B, Greve, R, Ehrentraut, H & Wang, Y (eds.), *Continuum mechanics and applications in geophysics and the environment*. Springer, Berlin, pp. 250–275.

Michaeli, W, Mahlke & M, Osswald, TA 1990, 'Analyse und messung des fliessens von SMC mit einem pressrheometer', *Kunstoffe*, vol. 80, pp. 70–74.

Minier, J & Peirano, E 2001, 'The pdf approach to turbulent polydispersed two phase flows', *Physics Reports*, vol. 352, no. 1–3, pp. 1–214.

Morrison, F 2001, *Understanding rheology,* Oxford University Press, New York.

Mousavi, P, Fakharzadeh, M, Jamali, S, Narimani, K, Hossu, M, Bolandhemmat, H, Rafi, G & Safavi-Naeini, S 2008, 'A low-cost ultra low profile phased array system for mobile satellite reception using zero-knowledge beamforming algorithm', *IEEE Transactions on Antennas and Propagation*, vol. 56, no. 12, pp. 3667–3679.

Nguyen, TG, Favier, D & Suery, M, 1994, 'Theoretical and experimental study of the isothermal mechanical behavior of alloys in the semi-solid state', *International Journal of Plasticity*, vol. 10, no. 6, pp. 663–693.

Nicolson, AM & Ross, G 1970, 'Measurement of the intrinsic properties of materials by time-domain techniques', *IEEE Transactions on Instrumentation and Measurement*, vol. 19, no. 4, pp. 377–382.

Odenberger, PT, Andersson, HM & Lundström, TS 2004, 'Experimental flow-front visualisation in compression moulding of SMC', *Composites Part A: Applied Science and Manufacturing*, vol. *35*, no. 10, pp. 1125–1134.

Okada, Y, Tanaka, H & Yamane, K 2007, 'Electromagnetic field analysis for smart key antenna', *SAE Technical Paper Series*, Paper ID 2007-01-0943, Society of Automotive Engineers.

Olsson, NEJ et al. 2008, 'Process study on compression moulding of SMC using factorial design', in *Proceedings of the 19th International Symposium on Transport Phenomena (ISTP-19): Reykjavik, Iceland, August 17–21, 2008*.

Osswald, TA 1980, 'Numerical methods for compression mold filling simulation', PhD Thesis, University of Illinois at Urbana-Champaign.

Osswald, TA & Tucker, TL 1989, 'Compression mold filling simulation for non-planar parts using the finite element/control volume approach', *International Polymer Processing*, vol. 5, no. 2, p. 79.

Osswald, TA, Sun, EM & Tseng, S 1996, 'Orientation and warpage prediction in polymer processing', in Stevenson, J (ed.), *Innovation in polymer processing: molding*.

Osswald, T, Sun, M & Tseng, S 2004, 'Experimental verification on simulating shrinkage and warpage of thin compression moulded SMC parts', *Polymers & Polymer Composites*, vol. 2, no. 3, p. 187.

Otoshi, T, Cirillo, R & Sosnowski, J 1999, 'Measurements of Complex Dielectric Constants of Paints and Primers for DSN Antennas: Part I*, The Telecommunications and Mission Operations* Progress Report 42-138, April - June 1999,Jet Propulsion Laboratory, Pasadena, California, pp. 1-13.

Otoshi, T, Cirillo, R & Sosnowski, J 1999, 'Measurements of Complex Dielectric Constants of Paints and Primers for DSN Antennas: Part II*, The Telecommunications and Mission Operations* Progress Report 42-139, April - June 1999,Jet Propulsion Laboratory, Pasadena, California, pp. 1-7.

Otoshi, T, Rahmat-Samil, Y, Cirillo, R & Sosnowski, J 2001, 'Noise temperature and gain loss due to paints and primers: a case study of DSN antennas'*, IEEE Antennas and Propagation Magazine*, vol. 43, no. 3, pp. 11–28.

Pell, B, Rowe, W, Sulic, E, Ghorbani, K, John, S, Gupta, R, Zhang, KI & Hughes, B 2008, 'Experimental study of the effect of paint on embedded automotive antennas'*,* in *IEEE Vehicular Technology Conference*, *VTC Spring 2008*, pp. 3057–3061.

Pell, B, Sulic, E, Rowe, W, Ghorbani, K, John, S, Gupta, R & Zhang, K 2008, 'The design and realization of uniplanar CPW fed PICA slot antennas', in *2008 Asia-Pacific Microwave Conference*, pp. 1–4.

Pell, BD, Sulic, E, Rowe, WST & Ghorbani, K 2009, 'Custom-directional wideband PICA for multi-service vehicular applications', in *APMC 2009. Asia Pacific Microwave Conference, 2009,* pp. 1863–1866.

Pell, BD, Sulic, E, Rowe, WST, Ghorbani, K & John, S n.d. Experimental study of the effect of modern automotive paints on vehicular antennas, *IEEE Transactions on Antennas and Propagation*, in press.

Pfanstiehl, J 1998, *Automotive paint handbook: paint technology for auto enthusiasts and body shop professionals*, HP Books, New York, NY.

Pope, S 2000, *Turbulent flows,* Cambridge University Press, Cambridge.

Pozrikidis, C 1992, *Boundary integral and singularity methods for linearized viscous flows,* Cambridge University Press, Cambridge.

Robinson, A & Livesey, A 2006, *The repair of vehicle bodies*, Butterworth-Heinemann, Oxford, UK.

Rowan, CW & Altgelt, CA 1985, 'When car radios were illegal: a history of early American and European car radios', *SAE Technical Paper Series*, Paper ID 850019, Society of Automotive Engineers.

Russel, W, Saville, D & Schowalter, W 1995, *Colloidal dispersions,* Cambridge University Press, Cambridge.

Sabatier, C 1995, '2 GHz compact antennas on handsets', in *Antennas and Propagation Society International Symposium, AP-S*, vol. 2, pp. 1136–139.

Sabatier, C 1995, '2 GHz compact antennas on handsets', in *Antennas and Propagation Society International Symposium, 1995. AP-S. Digest, June 1995, Volume 2*, pp. 1136–1139.

Schowalter, W 1978, *Mechanics of non-Newtonian fluids,* Pergamon Press, Oxford.

Scott, JR 1931, 'Theory and application of the parallel-plate plastimeter', *Trans. Inst. Rubber Ind*, vol. 7, pp. 169–186.

Shavit, R 1994, 'Dielectric cover effect on rectangular microstrip antenna array'*, IEEE Transactions on Antennas and Propagation*, vol. 42, no. 8, pp. 1180–1184.

Silva-Nieto, RJ, Fisher, BC & Birley, AW 1980, 'Predicting mold flow for unsaturated polyester resin sheet molding compounds'*, Polymer Composites*, vol. 1, no. 1, pp. 14–23.

Silva-Nieto, RJ, Fisher, BC & Birley, AW 1981, 'Rheological characterization of unsaturated polyester resin sheet molding compounds', *Polymer Engineering and Science*, vol. 21, no. 8, pp. 499–506.

Simons, RN & Lee, RQ 1993, 'Linearly tapered slot antenna with dielectric superstrate', in *Antennas and Propagation Society International Symposium, AP-S. Digest*, vol. 3, pp. 1482–1485.

Stutzman, W, and Thiele, G 1997, 'Antenna Theory and Design', Second Edition, John Wileys and Sons Inc., ISBN 0-471-02590-9

Suh, S, Stutzman, W & Davis, W 2004, 'A new ultrawideband printed monopole antenna: the planar inverted cone antenna (PICA)', *IEEE Transactions on Antennas and Propagation*, vol. 52, no. 5, pp. 1361–1364.

Sulic, E, Pell, B, John, S, Gupta, R, Rowe, W, Ghorbani, K & Zhang, K 2010, 'Deformation evaluation of embedded antennas in vehicular components', in *Proceedings of the World Congress of Engineering*, London, UK, pp. 2389–2394.

Sulic, E, Pell, B, John, S, Gupta, R, Rowe, W, Ghorbani, K, Zhang, K & Lewis, M 2007, 'Parametric evaluation of communication devices in smart composite structures', in *Proceedings of the 5th Australasian Congress on Applied Mechanics (ACAM)*, Engineers Australia, Brisbane, Australia, pp. 477–482.

Sulic, E, Pell, B, John, S, Rowe, W, Ghorbani, K, Gupta, R & Zhang, K 2008, 'Performance of embedded multi-frequency communication devices in smart composite structures', in *ASME Smart Materials Adaptive Structures and Intelligent Systems (SMASIS2008)*, pp. 1–12.

Sun, J, Lee, Y & Lin, S 2007, 'New design of a CPW-fed ultrawideband slot antenna', *Microwave and Optical Technology Letters*, vol. 49, no. 3, pp. 561–564.

Schwartz, M.M. 1996, 'Composite Materials: Processing, Fabrication and Applications', Prentice Hall PTR, New Jersey.

Tan, W, Shen, Z & Shao, Z 2008, 'Radiation of high-gain cavity-backed slot antennas through a two-layer superstrate'*, IEEE Antennas and Propagation Magazine*, vol. 50, no. 3, pp. 78–87.

Tanner, R 1988, *Engineering rheology,* Clarendon Press, Oxford.

Toriyama, H, Ohe, J, Kondo, H & Yotsuya, H 1987, 'Development of printed-on glass TV antenna system for car', in *37th IEEE Vehicular Technology Conference, 1987*, pp. 334–342.

Truesdell, C 1974, 'The meaning of viscometry in fluid dynamics', *Annual Review of Fluid Mechanics*, vol. 6, pp. 111–147.

Truesdell, C 1984, *Rational thermodynamics,* Springer-Verlag, New York.

Tucker, CL & Liang, EW 1995, 'A finite element method for flow in compression molding of thin and thick parts', *Polymer Composites,* vol. 16, no. 1, pp.70–80.

Von Hippel, A 1961, *Dielectric materials and applications,* MIT Press, Cambridge, MA.

Walbeoff, A & Langley, RJ 2005, 'Multiband PCB antenna', *IEE Proceedings Microwaves, Antennas and Propagation*, pp. 471–475.

Walters K 1975, *Rheometry,* Chapman and Hall, London.

Ward, IM 1979, *Mechanical properties of solid polymers*, John Wiley & Sons, New York.

Waterhouse, R 2008, *Printed antennas for wireless communications,* Wiley, Chichester, UK.

Weir, WB 1974, 'Automatic measurement of complex dielectric constant and permeability at microwave frequencies'*, Proceedings of the IEEE*, vol. 62, no. 1, pp. 33–36.

Wenger, J 2005, 'Automotive radar—status and perspectives', in *IEEE Compound Semiconductor Integrated Circuit Symposium, 2005. CSIC '05*, p. 4, DOI 10.1109/CSICS.2005.1531741.

Xu, J, Kim, J, Ho, T & Lee, JL 1993, 'Compression molding of sheet molding compounds in plate-rib type geometry'*, Polymer Composites*, vol. 14, no. 1, pp. 51–58.

Yang, H & Alexopoulos, N 1987, 'Gain enhancement methods for printed circuit antennas through multiple superstrates', *IEEE Transactions on Antennas and Propagation*, vol. 35, no. 7, pp. 860–863.

Yoshimura, Y 1972, 'A microstripline slot antenna', *IEEE Transactions on Microwave Theory and Techniques*, vol. 20, no. 11, pp. 760–762.

Zdunkowski, W & Bott, A 2003, *Dynamics of the atmosphere,* Cambridge University Press, Cambridge.

Appendix A - Additional Rheology test results – related to chapters 6 and 7

Table 1: Temp rump up to 100 ºC

time	Temp	Torque	G'	G''	tan_delta
s	℃	g-cm	Pa	Pa	
8	30.1078	12.1498	1.86E+07	7.97E+06	0.42871
18	30.0385	12.051	1.84E+07	7.91E+06	0.42912
28	30.0289	12.0282	1.84E+07	7.89E+06	0.42872
38	30.0523	12.0327	1.84E+07	7.88E+06	0.42813
48	30.0698	12.0489	1.84E+07	7.88E+06	0.42738
57	30.0733	12.0685	1.85E+07	7.88E+06	0.42678
66	30.068	12.0947	1.85E+07	7.89E+06	0.42633
75	30.0578	12.1102	1.85E+07	7.90E+06	0.4261
85	30.0632	12.129	1.86E+07	7.90E+06	0.42539
94	30.0853	12.1554	1.86E+07	7.91E+06	0.42511
104	30.0905	12.1888	1.87E+07	7.93E+06	0.42453
113	30.0808	12.2122	1.87E+07	7.93E+06	0.42389
122	30.0762	12.2343	1.87E+07	7.94E+06	0.42345
133	30.0957	10.6089	1.62E+07	7.10E+06	0.4397
142	36.9952	6.3031	9.04E+06	5.23E+06	0.57824
152	66.7478	3.59166	4.75E+06	3.56E+06	0.7498
161	99.8317	3.17527	4.24E+06	3.10E+06	0.72973
170	118.897	3.40967	4.70E+06	3.16E+06	0.67266
179	120.867	3.71661	5.21E+06	3.31E+06	0.63581
189	112.363	3.82141	5.40E+06	3.35E+06	0.62098
198	103.085	3.72233	5.25E+06	3.27E+06	0.62371
207	97.345	3.54591	4.98E+06	3.15E+06	0.63265
216	95.9112	3.46986	4.87E+06	3.08E+06	0.63275
225	96.3378	3.51706	4.96E+06	3.09E+06	0.62337
234	96.4378	3.59335	5.08E+06	3.12E+06	0.61432
244	95.7503	3.65283	5.19E+06	3.14E+06	0.60566
253	94.8481	3.69012	5.25E+06	3.16E+06	0.60138
262	94.268	3.72535	5.31E+06	3.18E+06	0.59792
271	94.0409	3.76215	5.37E+06	3.20E+06	0.59466
280	93.9937	3.82698	5.48E+06	3.24E+06	0.59111
289	93.9343	3.87567	5.55E+06	3.26E+06	0.58768
298	93.8138	3.94277	5.66E+06	3.31E+06	0.58497
307	93.6789	4.0098	5.76E+06	3.35E+06	0.58257
316	93.5869	4.07064	5.86E+06	3.39E+06	0.57868
325	93.5383	4.13064	5.95E+06	3.43E+06	0.57623
334	93.5291	4.19687	6.05E+06	3.47E+06	0.57418
343	93.5326	4.26442	6.15E+06	3.52E+06	0.5729
353	93.524	4.33507	6.26E+06	3.57E+06	0.56981
362	93.5003	4.40762	6.37E+06	3.62E+06	0.56752
371	93.4992	4.48035	6.48E+06	3.67E+06	0.56597
380	93.514	4.55748	6.60E+06	3.72E+06	0.56437
389	93.5092	4.64418	6.73E+06	3.79E+06	0.56292
398	93.4927	4.73306	6.86E+06	3.85E+06	0.5613
407	93.4671	4.82772	7.00E+06	3.92E+06	0.55959
416	93.4627	4.92419	7.15E+06	3.99E+06	0.55778

425	93.4752	5.03945	7.32E+06	4.07E+06	0.55579
434	93.4826	5.15475	7.50E+06	4.15E+06	0.55413
443	93.4897	5.29315	7.71E+06	4.25E+06	0.55183
452	93.4983	5.45249	7.94E+06	4.37E+06	0.5498
461	93.5073	5.64242	8.24E+06	4.50E+06	0.546
471	93.503	5.86049	8.57E+06	4.64E+06	0.5419
480	93.4955	6.1376	9.00E+06	4.82E+06	0.53581
489	93.4994	6.42692	9.44E+06	5.01E+06	0.53074
498	93.503	6.81042	1.00E+07	5.26E+06	0.5236
507	93.5122	7.24419	1.07E+07	5.53E+06	0.51598
516	93.5231	7.81759	1.16E+07	5.89E+06	0.50804
527	93.8124	8.47077	1.26E+07	6.32E+06	0.50136
536	93.7211	9.1869	1.37E+07	6.79E+06	0.49571
545	93.4442	9.91114	1.48E+07	7.28E+06	0.49137
554	93.2853	10.673	1.60E+07	7.81E+06	0.48898
563	93.3254	11.4979	1.72E+07	8.39E+06	0.48713
572	93.4511	12.7396	1.91E+07	9.29E+06	0.4869
584	93.5335	13.6724	2.05E+07	9.98E+06	0.48709
593	93.5364	14.605	2.19E+07	1.07E+07	0.48836
603	93.5173	15.5944	2.33E+07	1.14E+07	0.48994
612	93.5047	16.6203	2.49E+07	1.22E+07	0.49197
621	93.5084	17.6812	2.64E+07	1.30E+07	0.4931
630	93.5258	18.7868	2.81E+07	1.39E+07	0.4941
639	93.5395	19.9709	2.99E+07	1.47E+07	0.49317
648	93.5327	21.2181	3.18E+07	1.56E+07	0.49144
657	93.5251	22.5055	3.37E+07	1.65E+07	0.49013
666	93.5246	23.8573	3.58E+07	1.75E+07	0.48772
675	93.5273	25.8439	3.89E+07	1.88E+07	0.48215
686	93.5308	27.4854	4.15E+07	1.97E+07	0.47555
695	93.5362	29.3687	4.45E+07	2.08E+07	0.46715
705	93.5368	31.5312	4.80E+07	2.19E+07	0.45599
714	93.5301	33.9411	5.19E+07	2.31E+07	0.44506
723	93.5222	36.6418	5.63E+07	2.44E+07	0.43268
732	93.5219	39.3667	6.09E+07	2.55E+07	0.41938
741	93.5346	42.5894	6.62E+07	2.68E+07	0.40515
750	93.5426	46.1168	7.21E+07	2.82E+07	0.39162
759	93.5391	50.8298	8.00E+07	3.00E+07	0.37498
769	93.3132	54.9941	8.70E+07	3.14E+07	0.361
778	92.5689	59.4881	9.47E+07	3.29E+07	0.34739
787	91.5143	64.1902	1.03E+08	3.43E+07	0.33356
797	90.4523	69.0061	1.11E+08	3.55E+07	0.31949

Table 2: Temp rump up to 130 ºC

time	Temp	Torque	G'	G''	tan_delta
s	℃	g-cm	Pa	Pa	
8	36.7792	8.9485	1.32E+07	6.86E+06	0.51911
17	35.4348	9.00404	1.33E+07	6.86E+06	0.51507
26	34.1108	9.12203	1.35E+07	6.90E+06	0.51076
36	32.9525	9.26867	1.37E+07	6.95E+06	0.50577

45	32.0117	9.41382	1.40E+07	7.00E+06	0.50088
54	31.2782	9.55378	1.42E+07	7.05E+06	0.49582
63	30.7157	9.69241	1.45E+07	7.10E+06	0.49148
72	30.2843	9.82279	1.47E+07	7.14E+06	0.48681
81	29.9441	9.95345	1.49E+07	7.19E+06	0.48287
90	29.68	10.0747	1.51E+07	7.23E+06	0.47913
99	29.4566	10.1939	1.53E+07	7.27E+06	0.47534
108	29.2689	10.3077	1.55E+07	7.31E+06	0.47203
117	29.1104	10.4097	1.57E+07	7.35E+06	0.46905
126	29.0397	10.4554	1.57E+07	7.35E+06	0.46654
136	29.2396	9.54693	1.43E+07	6.84E+06	0.47834
145	33.8771	6.97896	1.01E+07	5.66E+06	0.56085
154	48.4873	4.88778	6.69E+06	4.56E+06	0.68185
163	68.6296	3.65466	4.79E+06	3.70E+06	0.77091
172	88.7894	2.85804	3.65E+06	3.01E+06	0.82336
181	106.214	2.25503	2.85E+06	2.42E+06	0.85071
190	121.487	1.87038	2.37E+06	2.00E+06	0.84129
199	132.773	1.87782	2.44E+06	1.93E+06	0.79127
208	134.652	1.98335	2.63E+06	1.98E+06	0.75457
217	129.08	1.99446	2.66E+06	1.97E+06	0.74004
226	122.352	1.87997	2.50E+06	1.86E+06	0.74518
236	119.443	1.79768	2.39E+06	1.79E+06	0.74699
245	120.336	1.95848	2.64E+06	1.90E+06	0.72244
254	122.112	2.72383	3.78E+06	2.48E+06	0.6562
263	122.82	4.04908	5.66E+06	3.62E+06	0.63983
272	122.458	5.50572	7.52E+06	5.20E+06	0.69236
282	121.883	6.71961	9.04E+06	6.55E+06	0.72489
291	121.76	8.09646	1.09E+07	7.92E+06	0.72798
300	121.915	10.3934	1.40E+07	1.01E+07	0.72286
309	122.042	14.8449	2.00E+07	1.45E+07	0.72856
319	122.024	18.7418	2.50E+07	1.86E+07	0.74265
328	121.958	24.2111	3.41E+07	2.16E+07	0.63389
341	121.865	29.4862	4.44E+07	2.12E+07	0.47725
350	121.809	34.0534	5.34E+07	1.95E+07	0.36424
359	121.78	37.4622	5.99E+07	1.84E+07	0.30704
368	121.782	39.5813	6.39E+07	1.77E+07	0.27712
377	121.788	40.978	6.64E+07	1.74E+07	0.26254
386	121.803	42.696	6.94E+07	1.75E+07	0.25228
396	121.781	41.1653	6.70E+07	1.62E+07	0.24206
405	121.796	40.0167	6.52E+07	1.57E+07	0.2406
414	121.807	39.3108	6.40E+07	1.54E+07	0.24005
423	121.796	39.152	6.37E+07	1.56E+07	0.2445
432	121.819	38.9063	6.33E+07	1.54E+07	0.24398
441	121.833	38.7383	6.30E+07	1.54E+07	0.24483
450	121.845	38.6554	6.29E+07	1.54E+07	0.24501
459	121.827	38.7002	6.30E+07	1.53E+07	0.24231
469	121.806	38.8644	6.33E+07	1.52E+07	0.24046
477	121.819	39.2875	6.40E+07	1.53E+07	0.23987
486	121.832	39.5905	6.45E+07	1.53E+07	0.23774
495	121.839	39.8948	6.50E+07	1.54E+07	0.23616
504	121.852	40.2659	6.57E+07	1.55E+07	0.23549
513	121.867	40.3113	6.58E+07	1.52E+07	0.23116

522	121.863	40.5217	6.61E+07	1.53E+07	0.23094
531	121.862	40.6258	6.63E+07	1.52E+07	0.2298
541	121.828	40.7111	6.65E+07	1.52E+07	0.2284
550	121.808	40.7336	6.65E+07	1.53E+07	0.22968
559	121.823	40.8504	6.67E+07	1.53E+07	0.22964
567	121.845	40.8296	6.67E+07	1.52E+07	0.22819
576	121.856	40.849	6.67E+07	1.53E+07	0.22931
585	121.862	40.8573	6.67E+07	1.53E+07	0.22949
594	121.865	40.7886	6.66E+07	1.52E+07	0.2274
603	121.857	40.7398	6.66E+07	1.51E+07	0.22763
613	121.845	40.6891	6.65E+07	1.51E+07	0.22778
622	121.856	40.4	6.60E+07	1.50E+07	0.22679
631	121.854	40.3453	6.59E+07	1.49E+07	0.22594
640	121.837	40.1959	6.57E+07	1.47E+07	0.22362
649	121.838	40.0229	6.54E+07	1.46E+07	0.22349
657	121.84	39.9193	6.52E+07	1.46E+07	0.22455
666	121.859	39.7963	6.50E+07	1.47E+07	0.2254
675	121.88	39.5541	6.46E+07	1.45E+07	0.22511
685	121.88	39.3568	6.43E+07	1.45E+07	0.22567
694	121.886	39.2443	6.41E+07	1.45E+07	0.22668
703	121.884	39.229	6.41E+07	1.46E+07	0.22721
712	121.896	38.9649	6.36E+07	1.44E+07	0.22641
721	121.897	38.8755	6.35E+07	1.44E+07	0.22659
730	121.87	38.5133	6.29E+07	1.41E+07	0.22458
739	121.844	38.408	6.27E+07	1.41E+07	0.22453
747	121.842	29.9223	6.13E+07	1.47E+07	0.25659
759	121.925	38.626	6.30E+07	1.45E+07	0.23036
768	122.188	38.2639	6.25E+07	1.41E+07	0.22641
777	122.06	37.8154	6.18E+07	1.38E+07	0.223
787	121.763	36.2975	5.95E+07	1.32E+07	0.20514
796	121.625	38.6593	6.30E+07	1.39E+07	0.23911

Table 3: Temp rump up to 160 ºC

time	Temp	Torque	G'	G''	tan_delta
s	℃	g-cm	Pa	Pa	
9	30.0819	11.7479	1.77E+07	8.31E+06	0.46996
18	31.6345	11.7328	1.77E+07	8.29E+06	0.46925
26	32.0543	11.844	1.78E+07	8.33E+06	0.46702
35	31.7883	12.0031	1.81E+07	8.40E+06	0.46397
44	31.178	12.169	1.84E+07	8.47E+06	0.46067
52	30.5822	12.3229	1.86E+07	8.53E+06	0.45767
61	29.9823	12.4809	1.89E+07	8.59E+06	0.45454
71	29.4891	12.6179	1.91E+07	8.64E+06	0.452
80	29.1096	12.7365	1.93E+07	8.68E+06	0.44942
89	28.8488	12.7912	1.94E+07	8.69E+06	0.44761
97	28.8721	12.7697	1.94E+07	8.66E+06	0.44677
106	29.2304	12.7337	1.93E+07	8.63E+06	0.44649
115	29.7213	12.7386	1.93E+07	8.63E+06	0.44608
123	30.0356	12.8021	1.94E+07	8.66E+06	0.44529
132	30.1163	9.10423	1.35E+07	6.79E+06	0.50248
141	47.1897	2.88964	3.56E+06	3.19E+06	0.89365

149	96.184	1.37779	1.69E+06	1.52E+06	0.90296
159	155.472	8.21507	1.11E+07	7.87E+06	0.70991
172	191.123	10.4465	1.37E+07	1.06E+07	0.77293
181	186.466	11.1872	1.46E+07	1.16E+07	0.79703
190	173.377	12.2257	1.60E+07	1.26E+07	0.78639
201	160.333	14.4649	1.89E+07	1.49E+07	0.79132
210	158.214	19.7987	2.59E+07	2.04E+07	0.79024
219	160.737	31.3331	4.42E+07	2.78E+07	0.62929
227	162.645	55.0515	8.50E+07	3.58E+07	0.42162
236	162.49	73.2034	1.18E+08	3.50E+07	0.29656
246	160.941	83.34	1.35E+08	3.95E+07	0.29286
255	159.781	88.1606	1.42E+08	4.41E+07	0.31009
264	159.72	88.8473	1.43E+08	4.63E+07	0.32475
272	160.158	94.6546	1.52E+08	4.96E+07	0.32632
282	160.555	100.55	1.62E+08	5.18E+07	0.31991
290	160.503	106.535	1.72E+08	5.39E+07	0.31303
299	160.245	112.689	1.83E+08	5.61E+07	0.30723
308	160.022	117.984	1.92E+08	5.86E+07	0.30569
318	159.996	122.692	1.99E+08	6.07E+07	0.30451
327	160.064	126.859	2.06E+08	6.26E+07	0.30318
336	160.143	130.346	2.12E+08	6.42E+07	0.30208
345	160.167	133.672	2.18E+08	6.56E+07	0.30095
357	160.109	136.394	2.23E+08	6.69E+07	0.30073
366	160.071	138.359	2.26E+08	6.76E+07	0.29909
375	160.085	140.218	2.29E+08	6.86E+07	0.29921
384	160.12	141.978	2.32E+08	6.93E+07	0.29835
393	160.124	143.587	2.35E+08	6.98E+07	0.29733
401	160.123	144.958	2.37E+08	7.05E+07	0.29709
410	160.113	146.221	2.39E+08	7.10E+07	0.29662
419	160.093	147.303	2.41E+08	7.14E+07	0.29576
427	160.091	148.205	2.43E+08	7.16E+07	0.29472
436	160.08	149.289	2.45E+08	7.19E+07	0.29364
445	160.081	150.306	2.46E+08	7.25E+07	0.29427
453	160.091	151.028	2.48E+08	7.23E+07	0.29194
463	160.122	151.63	2.49E+08	7.23E+07	0.29057
472	160.123	152.219	2.50E+08	7.23E+07	0.28922
481	160.104	152.758	2.51E+08	7.25E+07	0.28874
489	160.089	153.363	2.52E+08	7.25E+07	0.28765
498	160.122	153.916	2.53E+08	7.26E+07	0.28671
507	160.124	154.415	2.54E+08	7.26E+07	0.28596
515	160.113	154.861	2.55E+08	7.27E+07	0.2855
524	160.08	155.138	2.55E+08	7.26E+07	0.28439
533	160.062	155.538	2.56E+08	7.25E+07	0.28321
542	160.069	155.914	2.57E+08	7.25E+07	0.28248
551	160.101	156.222	2.57E+08	7.27E+07	0.28264
560	160.13	156.416	2.58E+08	7.25E+07	0.28151
568	160.13	156.737	2.58E+08	7.26E+07	0.28127
577	160.105	156.877	2.59E+08	7.26E+07	0.28078
586	160.1	157.326	2.59E+08	7.27E+07	0.28024
595	160.11	157.693	2.60E+08	7.26E+07	0.27921
603	160.125	157.825	2.60E+08	7.26E+07	0.27913
612	160.135	157.95	2.60E+08	7.27E+07	0.27926

621	160.133	158.291	2.61E+08	7.26E+07	0.27796
630	160.103	158.466	2.61E+08	7.28E+07	0.27857
639	160.084	158.573	2.62E+08	7.26E+07	0.27735
648	160.087	158.697	2.62E+08	7.25E+07	0.27685
656	160.09	158.638	2.62E+08	7.27E+07	0.27792
665	160.118	158.733	2.62E+08	7.22E+07	0.27565
674	160.134	158.66	2.62E+08	7.24E+07	0.27645
682	160.122	158.795	2.62E+08	7.26E+07	0.27711
691	160.114	159.053	2.62E+08	7.26E+07	0.27669
700	160.123	159.321	2.63E+08	7.26E+07	0.27624
709	160.131	159.668	2.64E+08	7.26E+07	0.27532
718	160.123	160.046	2.64E+08	7.26E+07	0.27455
727	160.115	160.138	2.64E+08	7.27E+07	0.27492
736	160.105	160.279	2.65E+08	7.28E+07	0.27493
744	160.119	160.356	2.65E+08	7.28E+07	0.27508
753	160.111	160.393	2.65E+08	7.26E+07	0.27383
762	159.978	160.246	2.65E+08	7.19E+07	0.27126
770	159.484	159.746	2.64E+08	7.08E+07	0.26791
779	158.527	159.146	2.64E+08	6.95E+07	0.26362
788	157.418	158.536	2.63E+08	6.85E+07	0.26086
797	156.537	157.601	2.61E+08	6.74E+07	0.25789

Figure 1: Graph of the G’ for the rump up temperatures 100 C, 130 C and 160 C

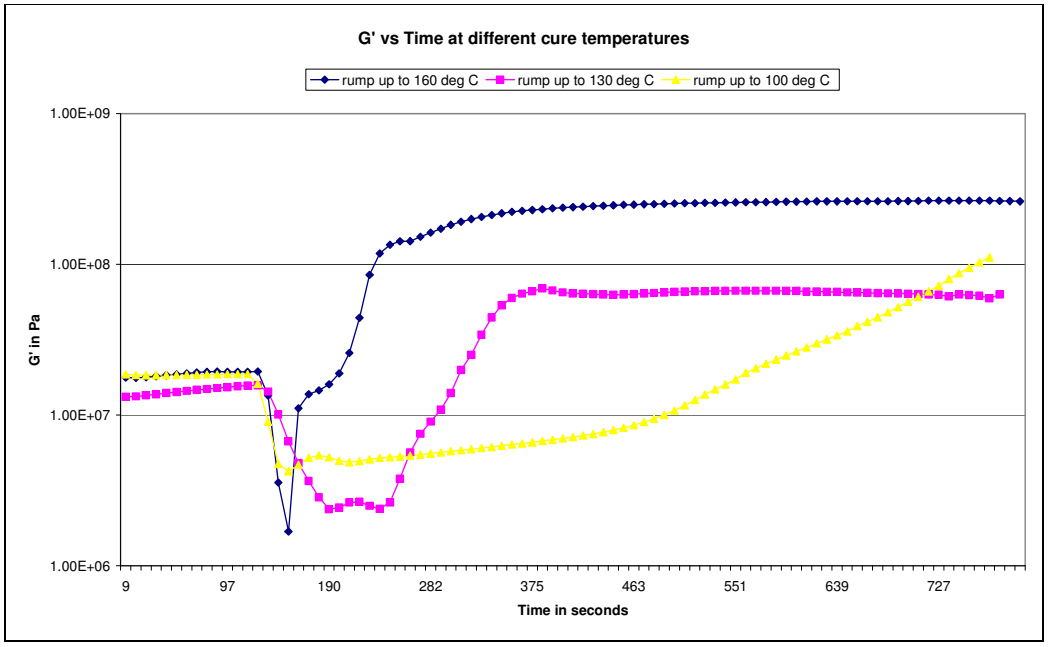

Figure 2: Graph of the G’’ for the rump up temperatures 100 C, 130 C and 160 C

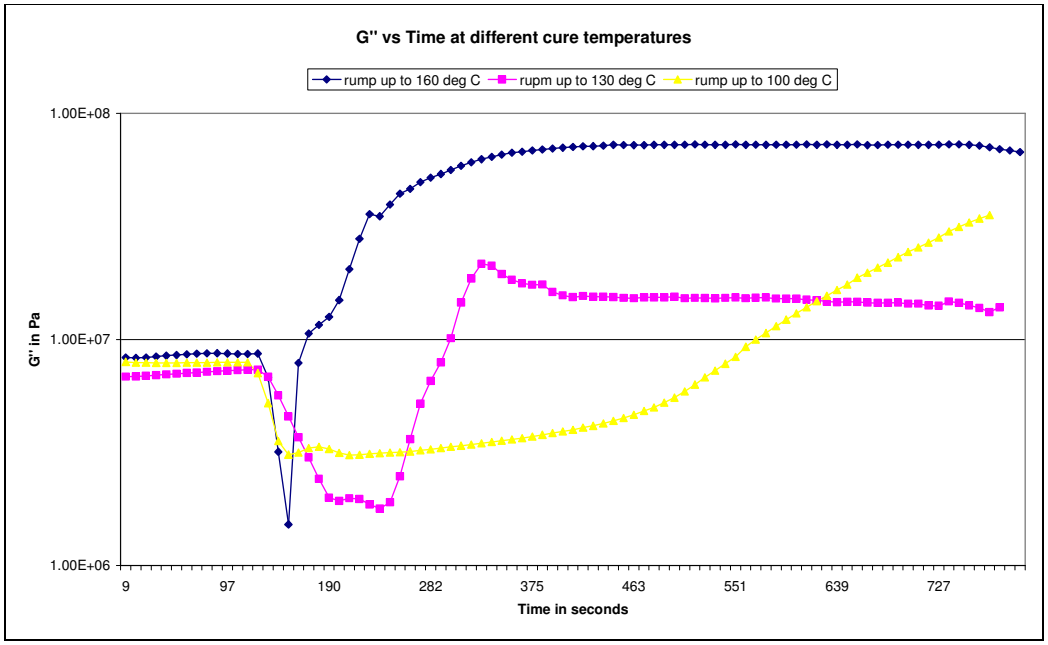

Figure 3: Cure profile for G’ and G’’ at different rump up temperatures

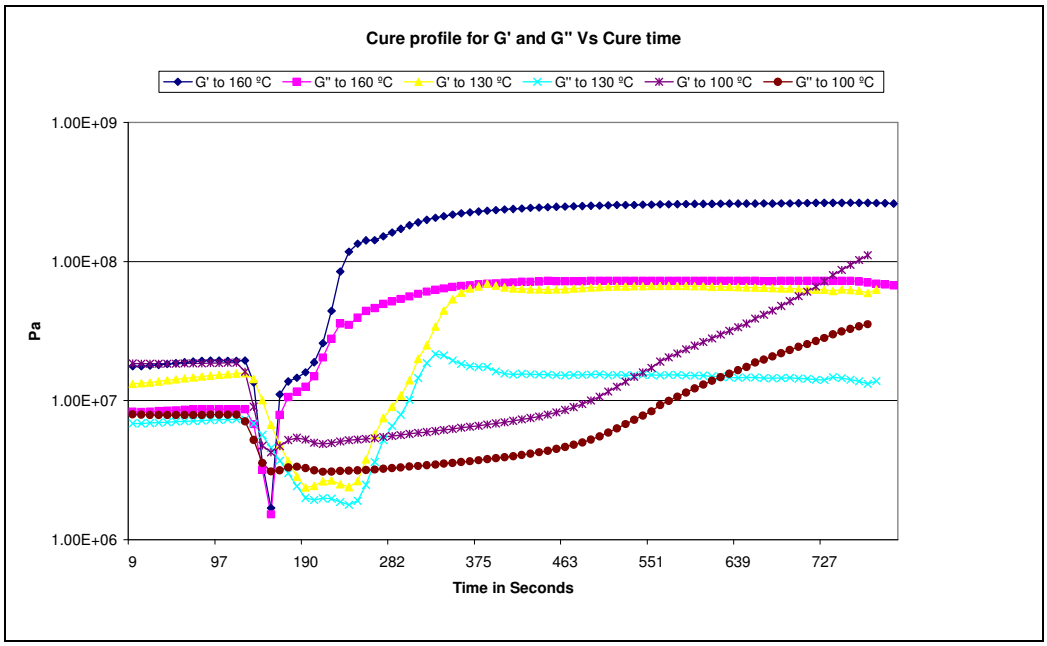

Table 4: Frequency sweep data for 100 ºC cure temperature

Freq	G'	G''	tan_delta	PhaseAngle	Eta*	Strain	CMD Strain	Torque	Temp
rad/s	Pa	Pa		rad	Pa-s	%	%	g-cm	℃
100	18313	39622	2.16	1.14	436	1.01	1	13.8	100.0
79	15414	32353	2.10	1.13	451	1.01	1	11.4	100.0
63	13856	27979	2.02	1.11	495	1.01	1	9.9	100.0
50	12630	24391	1.93	1.09	548	1.01	1	8.7	100.0
40	11519	21430	1.86	1.08	611	1.01	1	7.7	100.0
32	10581	18861	1.78	1.06	684	1.00	1	6.8	100.0
25	9752	16616	1.70	1.04	767	1.00	1	6.0	100.0
20	8992	14651	1.63	1.02	862	1.00	1	5.4	100.0
16	8348	12967	1.55	1.00	973	1.00	1	4.8	100.0
13	7789	11493	1.48	0.98	1103	1.00	1	4.3	100.0
10	7257	10211	1.41	0.95	1253	1.00	1	3.9	100.0
8	6804	9068	1.33	0.93	1427	1.00	1	3.5	100.0
6	6402	8084	1.26	0.90	1634	0.99	1	3.2	100.0
5	6041	7243	1.20	0.88	1882	0.99	1	2.9	100.0
4	5716	6490	1.14	0.85	2172	0.99	1	2.7	100.0
3	5431	5850	1.08	0.82	2524	0.99	1	2.5	100.0
3	5148	5278	1.03	0.80	2935	0.99	1	2.3	100.0
2	4928	4811	0.98	0.77	3452	0.99	1	2.1	100.0
2	4713	4405	0.93	0.75	4070	0.99	1	2.0	100.0
1	4522	4025	0.89	0.73	4808	0.99	1	1.9	100.0
1	4335	3681	0.85	0.70	5687	0.99	1	1.8	100.0
1	4151	3360	0.81	0.68	6723	0.99	1	1.7	100.0
1	4016	3130	0.78	0.66	8069	0.99	1	1.6	100.0
1	3858	2874	0.75	0.64	9599	0.99	1	1.5	100.0

Table 5: Frequency sweep data for 130 ºC cure temperature

Freq	G'	G''	tan delta	Phase Angle	Eta*	Strain	CMD Strain	Torque	Temp
rad/s	Pa	Pa		rad	Pa-s	%	%	g-cm	℃
100.00	1269400	1929100	1.52	0.99	23092.8	0.82	1	591.6	130.0
79.43	1187500	1790100	1.51	0.99	27043.6	0.83	1	559.8	130.0
63.10	1120500	1686700	1.51	0.98	32093.6	0.84	1	533.8	130.0
50.12	1064100	1599400	1.50	0.98	38330.3	0.85	1	510.6	130.0
39.81	1010700	1519900	1.50	0.98	45848.1	0.86	1	488.6	130.0
31.62	965130	1452700	1.51	0.98	55153.6	0.86	1	469.5	130.0
25.12	924310	1391600	1.51	0.98	66506.8	0.86	1	451.9	130.0
19.95	887960	1334400	1.50	0.98	80334.4	0.87	1	435.5	130.0
15.85	860960	1283900	1.49	0.98	97535.3	0.87	1	421.4	130.0
12.59	834170	1238400	1.48	0.98	1.19E+05	0.87	1	408.4	130.0
10.00	809840	1197500	1.48	0.98	1.45E+05	0.88	1	396.6	130.0
7.94	789890	1158800	1.47	0.97	1.77E+05	0.88	1	385.8	130.0
6.31	771220	1124800	1.46	0.97	2.16E+05	0.88	1	376.1	130.0
5.01	754800	1093600	1.45	0.97	2.65E+05	0.88	1	367.3	130.0
3.98	740490	1066000	1.44	0.96	3.26E+05	0.89	1	359.5	130.0
3.16	726280	1038700	1.43	0.96	4.01E+05	0.89	1	351.8	130.0

2.51	714770	1015500	1.42	0.96	4.94E+05	0.89	1	345.3	130.0
2.00	703600	997630	1.42	0.96	6.12E+05	0.89	1	339.9	130.0
1.58	696010	980570	1.41	0.95	7.59E+05	0.89	1	335.2	130.0
1.26	689630	967910	1.40	0.95	9.44E+05	0.89	1	331.6	130.0
1.00	700370	931940	1.33	0.93	1.17E+06	0.89	1	325.0	130.0
0.79	700180	913940	1.31	0.92	1.45E+06	0.89	1	321.1	130.0
0.63	779440	836250	1.07	0.82	1.81E+06	0.88	1	315.8	130.0
0.50	688670	884820	1.28	0.91	2.24E+06	0.89	1	313.3	130.0
0.40	719650	831200	1.16	0.86	2.76E+06	0.89	1	306.2	130.0
0.32	681810	846650	1.24	0.89	3.44E+06	0.89	1	304.2	130.0
0.25	691730	840280	1.21	0.88	4.33E+06	0.89	1	304.2	130.0
0.20	683450	824100	1.21	0.88	5.37E+06	0.89	1	299.6	130.0
0.16	720700	780770	1.08	0.83	6.70E+06	0.89	1	296.0	130.0
0.13	723790	773400	1.07	0.82	8.41E+06	0.89	1	295.1	130.0

Table 6: Frequency sweep data for 160 ºC cure temperature

Freq	G'	G''	tan delta	Phase Angle	Eta*	Strain	CMD Strain	Torque	Temp
rad/s	Pa	Pa		rad	Pa-s	%	%	g-cm	℃
100.00	1982200	3123700	1.58	1.01	36995	0.70	1	806.57	160.0
79.43	1555600	2624100	1.69	1.04	38404	0.75	1	717.03	160.0
63.10	1386700	2404100	1.73	1.05	43986	0.77	1	672.68	160.0
50.12	1259000	2265200	1.80	1.06	51709	0.79	1	639.13	160.0
39.81	1164900	2144700	1.84	1.07	61305	0.80	1	611.29	160.0
31.62	1089700	2045200	1.88	1.08	73283	0.81	1	587.40	160.0
25.12	1024400	1964100	1.92	1.09	88190	0.82	1	567.20	160.0
19.95	972330	1891300	1.95	1.10	106580	0.83	1	548.95	160.0
15.85	935310	1823000	1.95	1.10	129280	0.83	1	532.11	160.0
12.59	884390	1781300	2.01	1.11	157970	0.84	1	520.37	160.0
10.00	844130	1736700	2.06	1.12	193100	0.84	1	508.39	160.0
7.94	799520	1688900	2.11	1.13	235240	0.85	1	495.59	160.0
6.31	765630	1639200	2.14	1.13	286740	0.85	1	482.69	160.0
5.01	733130	1592800	2.17	1.14	349860	0.86	1	470.57	160.0
3.98	723520	1539000	2.13	1.13	427180	0.86	1	457.61	160.0
3.16	709640	1498300	2.11	1.13	524250	0.86	1	447.56	160.0
2.51	769060	1308700	1.70	1.04	604320	0.86	1	408.55	160.0
2.00	819320	1208100	1.47	0.98	731590	0.86	1	391.47	160.0
1.58	811510	1149700	1.42	0.96	887920	0.86	1	378.42	160.0
1.26	796840	1108600	1.39	0.95	1084500	0.86	1	368.25	160.0
1.00	784690	1057100	1.35	0.93	1316500	0.86	1	356.11	160.0
0.79	766310	1036000	1.35	0.93	1622300	0.87	1	349.73	160.0
0.63	745420	987440	1.32	0.92	1960800	0.87	1	337.16	160.0
0.50	737150	968530	1.31	0.92	2428500	0.87	1	332.18	160.0
0.40	717510	914840	1.28	0.91	2920400	0.88	1	318.58	160.0
0.32	699890	903300	1.29	0.91	3613600	0.88	1	314.14	160.0
0.25	684830	849980	1.24	0.89	4345500	0.88	1	301.05	160.0
0.20	350460	644240	1.84	1.07	3675700	0.93	1	213.85	160.0
0.16	342120	618400	1.81	1.07	4459100	0.93	1	206.44	160.0

Figure 4: Frequency sweep data for G’ and G”

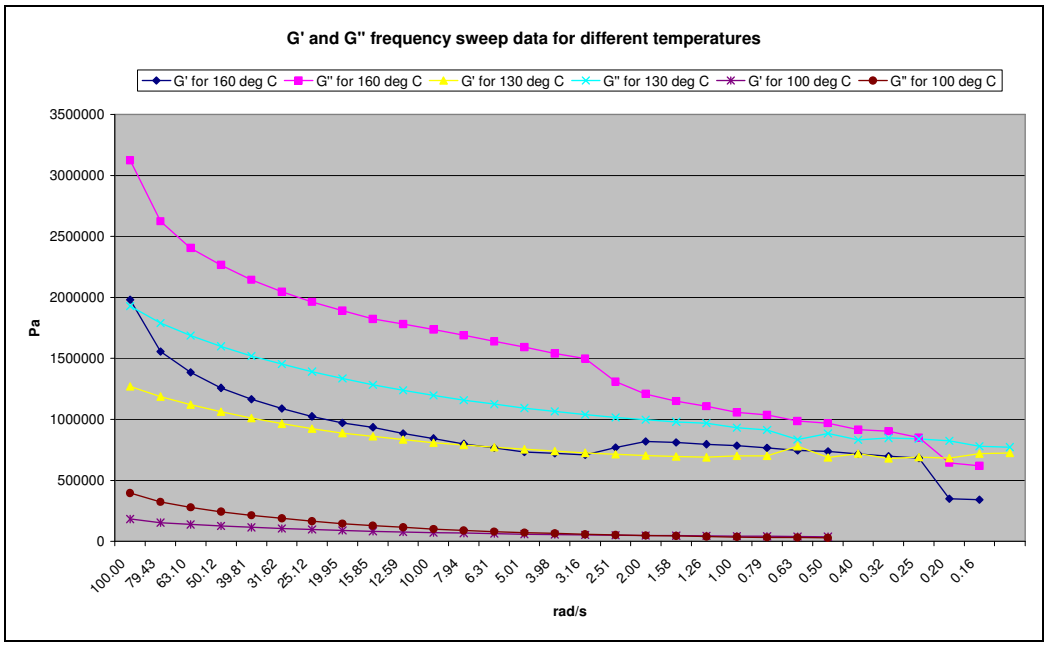

Appendix B – Matlab code

This Matlab code was used to calculate mean on large data sets generated in antenna radiation plots in chapters 8 and 9.

```
function Y = runmean(X, m, dim, modestr) ;
%  RUNMEAN - Very fast running mean (aka moving average) filter
%  For vectors, Y = RUNMEAN(X,M) computes a running mean (also known as
%  moving average) on the elements of the vector X. It uses a window of
%  2*M+1 datapoints. M an positive integer defining (half) the size of the
%  window. In pseudo code:
%  Y(i) = sum(X(j)) / (2*M+1), for j = (i-M):(i+M), and i=1:length(X)
%  For matrices, Y = RUNMEAN(X,M) or RUNMEAN(X,M,[]) operates on the first
%  non-singleton dimension of X. RUNMEAN(X,M,DIM) computes the running
%  mean along the dimension DIM.
%  If the total window size (2*M+1) is larger than the size in dimension
%  DIM, the overall average along dimension DIM is computed.
%  As always with filtering, the values of Y can be inaccurate at the
%  edges. RUNMEAN(..., MODESTR) determines how the edges are treated. MODESTR can be
%  one of the following strings:
%  'edge'    : X is padded with first and last values along dimension
%  DIM (default)
%  'zero'    : X is padded with zeros
%  'mean'    : X is padded with the mean along dimension DIM
%  X should not contains NaNs, yielding an all NaN result. NaNs can be
%  replaced by using, e.g., "inpaint_nans" created by John D'Errico.
%  Examples
%  runmean([1:5],1) ->  1.33  2  3  4 4.67
%  runmean([1:5],1,'mean')  ->  2 2 3 4 4
%  runmean([2:2:10],1,1) % dimension 1 is larger than 2*(M=1)+1 ...-> 2 4 6 8 10
%  runmean(ones(10,7),3,2,'zero') ; % along columns, using mode 'zero'
%  runmean(repmat([1 2 4 8 NaN 5 6],5,1),2,2) ; -> all NaN result
%  A = rand(10,10) ; A(2,7) = NaN ;
%  runmean(A,3,2) ; -> column 7 is all NaN
%  runmean(1:2:10,100) % mean -> 5 5 5 5 5
%  This is an incredibly fast implementation of a running mean, since
%  execution time does not depend on the size of the window.
%  for Matlab R13
%  Acknowledgements: (sep 2008) Thanks to Markus Hahn for the idea of
%  working in multi-dimensions and the way to treat edges.
```

```
error(nargchk(2,4,nargin)) ;
if ~isnumeric(m) || (numel(m) ~= 1) || (m < 0) || fix(m) ~= m,
   error('The window size (M) should be a positive integer') ;
end
if nargin == 2,
   dim = [] ;
   modestr = 'edge' ;
elseif nargin==3,
   if ischar(dim),
      % no dimension given
      modestr = dim ;
      dim = [] ;
   else
      modestr = 'edge' ;
   end
end
modestr = lower(modestr) ;
% check mode specifier
if ~ismember(modestr,{'edge','zero','mean'}),
   error('Unknown mode') ;
end
szX = size(X) ;
if isempty(dim),
   dim = min(find(szX>1)) ;
end
if m == 0 || dim > ndims(X),
   % easy
   Y = X ;
else
   mm = 2*m+1 ;
   if mm >= szX(dim),
      % if the window is larger than X, average all
      sz2 = ones(size(szX)) ;
      sz2(dim) = szX(dim) ;
      Y = repmat(mean(X,dim),sz2) ;
   else
      % here starts the real stuff
      % shift dimensions so that the desired dimensions comes first
      [X, nshifts] = shiftdim(X, dim-1);
```

```
    szX = size(X) ;
    % make the rest of the dimensions columns, so we have a 2D matrix
    % (suggested of Markus Hahn)
    X = reshape(X,szX(1),[]) ;
    % select how to pad the matrix
    switch (modestr),
      case 'edge'
        % pad with first and last elements
        Xfirst = repmat(X(1,:),m,1) ;
        Xlast = repmat(X(end,:),m,1) ;
      case 'zero'
        % pad with zeros
        Xfirst = zeros(m,1) ;
        Xlast= zeros(m,1) ;
      case 'mean',
        % pad with the average
        Xfirst = repmat(mean(X,1),m,1) ;
        Xlast = Xfirst ;
    end
    % pad the array
    Y = [zeros(1,size(X,2)) ; Xfirst ; X ; Xlast] ;
    % the cumsum trick (by Peter Acklam ?)
    Y = cumsum(Y,1) ;
    Y = (Y(mm+1:end,:)-Y(1:end-mm,:)) ./ mm ;
    % reshape into original size
    Y = reshape(Y,szX)   ;
    % and re-shift the dimensions
    Y = shiftdim(Y,ndims(Y)-nshifts) ;
  end
end
```

This Matlab code was used to plot and manipulate polar plots.

```
function [] = pp(varargin)
%PP  Plots and manipulates polar plots
%
%   PP(THETA,R) plots the polar representation of THEATA and R with the
%   centre and max values being the minimum and maximum values of R.
%
%   PP(THETA,R,S) plots as above, where S is a character string made from
%   standard plotting formatting in the PLOT function. See HELP PLOT.
%
%   PP(THETA,R,A) plots as above, but within the axis limits of A. A is
%   a 1x2 or 2x1 array containing the centre value and maximum value of
%   the polar plot ring axes.
%
%   PP(THETA,R,'Property 1',...) plots as above with the selected
%   properties. See below for propterties.
%
%   PP('Property 1',...) edits the current figure (if it is a polar plot
%   figure) to the assigned properties.
%
%   PP('Trace', 3, 'Property 1', ... , 'Trace', 1, 'Property 10', ... )
%   changes properties of trace 3 and trace one. Any properties defined
%   after the trace belong to that trace until a new trace number is
%   defined.
%
%           PROPERTIES:            DEFAULT         POSSIBLE
%          ---------------        -----------      ----------
%
%   GENERAL PLOTTING:
%         'ThetaDirection'           'ccw'          'cw','ccw'
%         'LineStyle'                '-'            see PLOT
%         'LineWidth'                 1              1,2,...
%         'LineColor'                'b'             see PLOT or RGB vector
%         'Marker'                   'none'          see PLOT
%         'ThetaStartAngle'           0              0-360
%         'ppStyle'                  0              0,1,2
%
%   AXES RANGE:
%         'MaxValue'                 'max'          numeric value (greater than CetreValue)
%         'CentreValue'              'min'          numeric value (less than MaxValue)
%
%   ANGLE AXIS:
%         'AngleAxis'                'on'           'on','off','none'
%         'AngleStep'                30             numeric value
%         'AngleAxisStyle'           ':'            see PLOT
%         'AngleAxisColor'           black          see PLOT or RGB vector
%         'AngleLineWidth'           1              1,2,...
%         'AngleLabel'               'on'           'on','off','none'
%         'AngleLabelStep'           same as axis   numeric value
%         'AngleFontSize'            10             numeric value
%         'AngleFontColor'           black          see PLOT or RGB vector
%         'AngleFontWeight'          'normal'       'normal','bold','light','demi'
%         'AngleDegreeMark'          'off'          'off',0, 'on',1
%
%   RING AXIS:
%         'NumRings'                  4             integer value >= 0
%         'RingAxis'                 'on'           'on','off','none'
%         'RingAxisStyle'            ':'            see PLOT
```

```
%       'RingAxisColor'             black          see PLOT or RGB vector
%       'RingStep'          cal. from No. rings   integer value > 0
%       'RingLineWidth'             0.1            1,2,...
%       'RingLabel'               'on'           'on','off','none'
%       'RingFontSize'              10             numeric value
%       'RingFontWeight'          'normal'       'normal','bold','light','demi'
%       'RingFontColor'             black          see PLOT or RGB vector
%       'AxisOuterRingStyle'       '-'             see PLOT
%       'RingUnits'                 ''             Some String Value
%       'MagMarkAngle'              45             0-360
%
%   FIGURE PROPERTIES:
%       'FigurePosition'
%       'FigureBackgroundColor'
%       'PlotBackgroundColor'
%       'PlotBorderColor'
%       'PlotBorderLineColor'
%
%   TRACE:
%       'Trace'                     1              any trace number
%       'LineStyle'                 '-'            see PLOT
%       'LineWidth'                  1             1,2,...
%       'LineColor'                 'b'            see PLOT or RGB vector
%       'Marker'                   'none'          see PLOT
%       'RhoData'
%       'ThetaData'
%
%   OTHER:
%       'SetupVariables'
%       'Axes'
%

 %Setup global variables that will be used within function blocks
global DB args oc NewTrace Traces CreateNewFigure r theta tc axis_limits HoldWasOn ErrorFlag
ppStyle;

%default settings
tc = struct( 'line_color',    [0 0 1]           ,...   RGB or PLOT value of line color
   'line_style',             '-'               ,...   line style string same as PLOT function
   'line_width',              1                ,...   line width of trace
   'line_marker',            'none'            ,...   line marker style
   'trace_index',             1                ,...   trace number identifier
   'trace_string',           ''                );%    trace string identifier
oc = struct( 'theta_start',            0                ,...   theta start angle in degrees
   'angle_step',             30               ,...   number of theta markers
   'angle_label_step',       0                ,...   number of theta labels
   'number_of_rings',        4                ,...   number of magnitude rings
   'max_mag',                'max'            ,...   maximum ring magnitude ('max' makes data's max value it)
   'centre_value',           'min'            ,...   minimum ring value (centre value)
   'background_color',       [0.8 0.8 0.8]    ,...   background color
   'theta_direction',        'ccw'            ,...   direction of theta increment
   'ring_step',              0                ,...   step size of rings
   'mag_mark_angle',         45               ,...   angle of magnitude labels
   'axes_hold',              'off'            ,...   flag to tell whether axis hold is on or off
   'ring_color',             'k'              ,...   ring axis color
   'ring_style',             ':'              ,...   ring axis style
   'ring_line_width',        0.1              ,...   ring axis line width
   'ring_border_line_width',0.5               ,...   ring border line width
   'angle_axis',             ''               ,...   angle axis is ON or OFF
   'angle_color',            'k'              ,...   angle axis color
```

```
    'angle_style',          ':'             ,...   angle axis style
    'angle_label',          ''              ,...   angle axis labels are ON or OFF
    'angle_line_width',     0.1             ,...   angle axis line width
    'angle_font_size',      10              ,...   angle axis font size
    'angle_font_color',     'k'             ,...   angle axis font color
    'angle_font_weight',    'normal'        ,...   angle axis font weight
    'angle_degree_mark',    'off'           ,...   degree symbol placed with angle text
    'ring_axis',            ''              ,...   ring axis is ON or OFF
    'ring_label',           ''              ,...   ring axis labels are ON or OFF
    'ring_font_size',       10              ,...   ring axis font size
    'ring_font_color',      'k'             ,...   ring axis font color
    'ring_font_weight',     'normal'        ,...   ring axis font weight
    'figure_position',      [300 150 583 500]  ,...   figure position and size
    'outer_ring_style',     '-'             ,...   ring axis border style
    'ring_units',           ''              ,...   ring axis units string
    'plot_area_color',      [1 1 1]         ,...   color inside ring axes (the plot area)
    'circ_border_color',    ''              ,...   color of circular border
    'circ_border_line_color', ''            );%    color of line defining circular border

%First Argument defines what is expected as the user input to say which option is wanted
%First Flag is: 1 if there is data expected after the argurment
%               0 if no data expected but contents of third column gets copied into 4th column variable
%Second Flag is : s if string data only is expected
%                 v if numerical data only is expected (values)
%                 vs if numerical or string data can be accepted
%                 st if structure data expected
%Final string variable points to which variable which the corresponding data is to be assigned to

%           Argument        flag flag  variable to alter
args = {'SetupVariables'          1 'st'  'oc'                        %initial setup variables
    'ThetaDirection'      1 's'   'oc.theta_direction'        %theta direction (CW/CCW)
    'CentreValue'           1 'vs'  'oc.centre_value'          %centre value of graph
    'MaxValue'              1 'vs'  'oc.max_mag'               %max value of graph
    'LineStyle'             1 's'   'Traces{TraceIndex*2}.line_style'            %trace style
    'LineWidth'             1 'v'   'Traces{TraceIndex*2}.line_width'            %trace width
    'LineColor'             1 'vs'  'Traces{TraceIndex*2}.line_color'            %trace color
    'Marker'                1 's'   'Traces{TraceIndex*2}.line_marker'           %trace marker style
    'ThetaStartAngle'       1 'v'   'oc.theta_start'            %theta start angle (refer note below)
    'AngleAxis'             1 's'   'oc.angle_axis'             %angle axis is ON or OFF
    'AngleStep'             1 'v'   'oc.angle_step'             %angle axis step size (between axes)
    'AngleAxisStyle'        1 's'   'oc.angle_style'            %angle axis style
    'AngleAxisColor'        1 'vs'  'oc.angle_color'            %angle axis color
    'AngleLineWidth'        1 'vs'  'oc.angle_line_width'       %angle axis line width
    'AngleLabel'            1 's'   'oc.angle_label'            %angle axis label is ON or OFF
    'AngleLabelStep'        1 'v'   'oc.angle_label_step'       %angle axis label step size
    'AngleFontSize'         1 'v'   'oc.angle_font_size'        %angle axis label font size
    'AngleFontColor'        1 'vs'  'oc.angle_font_color'       %angle axis font color
    'AngleFontWeight'       1 's'   'oc.angle_font_weight'      %angle axis label font weight
    'AngleDegreeMark',      1 'vs'    'oc.angle_degree_mark'        %marks the degrees character with
angle text
    'NumRings'              1 'v'   'oc.number_of_rings'        %ring axes number
    'RingAxis'              1 's'   'oc.ring_axis'              %ring axis is on or off
    'RingAxisStyle'         1 's'   'oc.ring_style'             %ring axis style
    'RingAxisColor'         1 'vs'  'oc.ring_color'             %ring axis color
    'RingStep'              1 'v'   'oc.ring_step'              %ring axis step size
    'RingBorderLineWidth'   1 'v'   'oc_ring_border_line_width'   %ring border line width
    'RingLineWidth'         1 'vs'  'oc.ring_line_width'        %ring axis line width
    'RingLabel'             1 's'   'oc.ring_label'             %ring axis labeling is ON or OFF
    'RingFontSize'          1 'v'   'oc.ring_font_size'         %ring axis label font size
    'RingFontWeight'        1 's'   'oc.ring_font_weight'       %ring axis label font size
```

```
   'RingFontColor'            1 'vs'  'oc.ring_font_color'          %ring axis font color
   'AxisOuterRingStyle'       1 's'   'oc.outer_ring_style'        %ring axis border (circumference) style
   'RingUnits'              1 's'   'oc.ring_units'              %ring axis label units
   'MagMarkAngle'             1 'v'   'oc.mag_mark_angle'          %ring axis label angle
   'FigurePosition'           1 'vs'  'oc.figure_position'         %position and size of figure on screen
   'FigureBackgroundColor'    1 'vs'  'oc.background_color'           %figure background color (outside
plot area)
   'PlotBackgroundColor'      1 'vs'  'oc.plot_area_color'         %plot area background color
   'PlotBorderLineColor'      1 'vs'  'oc.circ_border_line_color'  %circular border line color
   'PlotBorderColor'          1 'vs'  'oc.circ_border_color'       %circular border color
   'Axis'                   1 'vs'  'axis_limits'               %limits of axis
   'Axes'                     1 'vs'  'axis_limits'                %limits of axes (as in plural spelling but same
result)
   'Trace'                    1 'v'    'TraceIndex'                %current trace number - used to edit plot
parameters of the trace
   'ThetaData',               1 'v'   'Traces{TraceIndex*2-1}(:,2)'    %Theta data
   'RhoData',                 1 'v'   'Traces{TraceIndex*2-1}(:,1)'    %Rho Data
   'ppStyle',                 1 'v'   'ppStyle'                %A style of axes presentation
};
%NOTES:
%ThetaStartAngle is relative to the direction of theta. ie, a start angle of 90 will be 180 differnt
between clock wise and counter clock wise direction of theta.

%Setup a space for Traces
Traces = '';

%set up the variable axis limits. It is a 1x2 array whose first element contains the centre value and
second element contains the max magnitude.
axis_limits = [0 0];

%If ErrorFlag ever goes to 1 then will be quitting out
ErrorFlag = 0;

%Set default value of ppStyle
%Style Types:
%           0: No Changes
%           1: Default
%           2: Grey solid axes with 'dB' as ring units and degree marks present
%
ppStyle = 0;


%%%%%%%%%%%%%%%%%%%%%%%%%%%%%%%%%%%%%%%%%%%%%%%%%%%%%%%%%%%%%%%%%%%%%%%%%%%%%%%%%%%%%%%%%%%%%%%%
%                                                                                                   %
%                                       MAIN                                                        %
%                                                                                                   %
%%%%%%%%%%%%%%%%%%%%%%%%%%%%%%%%%%%%%%%%%%%%%%%%%%%%%%%%%%%%%%%%%%%%%%%%%%%%%%%%%%%%%%%%%%%%%%%%

%First check all input arguments and ensure they are valid. Also get back a flag to say whether the
new data  %is being added or not (if not, then simple figure/axes/current_trace properties are being
changed
CheckInput(varargin);
if ErrorFlag, return; end

%if NewTrace == 0 or hold is on, then load the user_data from the current figure and fill 'oc' and
'Traces'
LoadExistingData;
if ErrorFlag, return; end

%Assign input arguments to their corresponding variables
```

```
AssignInput(varargin); %this will overwrite any varibales in oc etc that have been updated
if ErrorFlag, return; end

AssignStyle(ppStyle);
if ErrorFlag, return; end

CheckAxisLimits;
if ErrorFlag, return; end

CheckPlotLimits;
if ErrorFlag, return; end

SetupFigure;

%Save Userdata to figure
UserData{1} = 'Bobs Polar Plot';
UserData{2} = oc;
UserData = [UserData Traces];
set(gcf,'UserData', UserData);      %save updated trace data into figure

PlotAxes;
for i=1:2:length(Traces)
   ThetaPlot = SetupTheta(  Traces{i}(:,2)  );
   DB = 0;
   if(i>1)
      DB = 1;
%       keyboard
   end

   [RPlot ThetaPlot PlotProperties] = SetupR(  Traces{i}(:,1)  ,  ThetaPlot  );
   PlotTrace(ThetaPlot, RPlot, PlotProperties, Traces{i+1});
end

if HoldWasOn == 0
   hold off
end


%%%%%%%%%%%%%%%%%%%%%%%%%%%%%%%%%%%%%%%%%%%%%%%%%%%%%%%%%%%%%%%%%%%%%%%%%%%%
%                                                                               %
%                              CHECK INPUT                                      %
%                                                                               %
%%%%%%%%%%%%%%%%%%%%%%%%%%%%%%%%%%%%%%%%%%%%%%%%%%%%%%%%%%%%%%%%%%%%%%%%%%%%

%This function will go through the input string entered into pp(). It will simply ensure
%valid ordering of commands and will assign NewTrace a value depending on if Trace Data
%is present or not in the input arguments

function CheckInput(VariableArgIn)

global args NewTrace ErrorFlag;

%find the number or inputs and the number of possible arguments
num_inputs = length(VariableArgIn);

m = 0;
NewTrace = 0;   %This is set if there is data (in the form of a trace) to be added to the plot

%now, step through all the arguments and compare them to valid arguments
```

```
while m < num_inputs    %number of inputs into function (ie number of variables separated by commas)
   m = m + 1;
   n = 0;

   %if the first element is numeric check the second element to ensure it is also numberic and the same length
   %as theta and r must be the same sizes
   if m == 1 & isnumeric(VariableArgIn{m})
      %check to make sure there is a second input argument
      if num_inputs < 2
         DispError('No Rho values Present');
         return
      end
      if isnumeric(VariableArgIn{m+1}) & max(length(VariableArgIn{m+1})) == max(length(VariableArgIn{m}))
         m = 2;   %move to after the RHO element which was just analysed
         %now check to see if the next input is the axes limits (it will be if its a numeric value)
         %this is the only case the third input can be numeric (without a property identifier)
         if num_inputs > 2
            if isnumeric(VariableArgIn{m+1})     %m = 3 now
               m = 3;  %move to after the AXIS LIMITS variable which was just analysed
            end
         end
      else
         DispError('THETA and R must be an equal length 1xm or mx1 array or variables');
         return
      end

      %if we have got here without error then there is a valid new trace being added or created
      NewTrace = 1;
      continue; %skip through to start of while loop again
   end

   %search for the string in the args array and return the args index
   index = FindArgsIndex(VariableArgIn{m});

   %if an index was found and another agument is expected to complete it, then ensure that
   %the input after it is valid (string, value of struct)
   if index > 0 & args{index,2} == 1            %if another argument is expected to complete this one
         if m + 1 > num_inputs      %if there is no more completeing argument
            DispError(['No input argument for "' VariableArgIn{m} '"'])  %exit
            return
         end
         %check 2nd flag of args to see if string or number is expected
         switch args{index,3}
         case 'v'                                 %assign variable with number
            if ischar(VariableArgIn{m+1})
               DispError(['The input argument for "' VariableArgIn{m} '" must be numerical']);
               return
            end       %note the lack of break sends the case through to string check
         case 's'                                 %assign variable with string
            if ischar(VariableArgIn{m+1}) == 0
               DispError(['The input argument for "' VariableArgIn{m} '" must be a string']);
               return
            end
         case 'vs'
            if (ischar(VariableArgIn{m+1}) == 0 & isnumeric(VariableArgIn{m+1}) == 0)
               DispError(['The input argument for "' VariableArgIn{m} '" must be either numerical, or a string (not a cell, struct etc.)']);
```

```
            return
          end
        case 'st'  %the only structure  is the 'SetupVariables' cell
          if isstruct(VariableArgIn{m+1}) == 0
            DispError(['The input argument for "' VariableArgIn{m} '" must be a structure']);
            return
          end
        end
        m = m+1;  %increment the m counter so that input of the argument is not checked as an
argument

   %in the case that the string wasn't found in args, it might be a standard plotting string. This will only
   %happen if m = 3 and a trace is being added. If thats the case then ensure then ensure the string is
valid
   elseif index == 0 & m == 3 & NewTrace & length(VariableArgIn{m}) <= 4
      CheckStandardPlot(VariableArgIn{m});      %this will quit out if there is a syntax error in the
string
      if ErrorFlag, return; end

      %Otherwise the string is not valid
   else
      DispError(['The argument "' VariableArgIn{m} '" is not valid. See help']);
      return
   end
end


%%%%%%%%%%%%%%%%%%%%%%%%%%%%%%%%%%%%%%%%%%%%%%%%%%%%%%%%%%%%%%%%%%%%%%%%%%%%%%%
%                                                                                 %
%                  LoadExistingData - LOAD EXISTING DATA                          %
%                                                                                 %
%%%%%%%%%%%%%%%%%%%%%%%%%%%%%%%%%%%%%%%%%%%%%%%%%%%%%%%%%%%%%%%%%%%%%%%%%%%%%%%

%If hold is on or existing figure properties are being modified, then load the existing figures user_data
function LoadExistingData

global Traces oc NewTrace CreateNewFigure HoldWasOn;

%Default is to Create a new figure
CreateNewFigure = 1;

%Default HoldWasOn flag is 0 (ie hold was not on)
HoldWasOn = 0;

if max(findobj) ~= 0
   %if hold is on then set the HoldWasOn flag so it can be turned on after all plotting complete

   if ishold
      HoldWasOn = 1;
   end

   %if the current figure has hold on or we are editing an existing figure then we need to check to make
sure its valid
   if ishold | NewTrace==0
      user_data = get(gcf, 'UserData');
      if ~strcmp(user_data{1}, 'Bobs Polar Plot')
         DispError('Current figure is not a valid polar plot figure - it must be created using the pp
function');
         return
      end
```

```
      %If the figure is valid, then load the oc structure from it
      oc = user_data{2};

      %Load the existing Traces
      if(length(user_data)>2)
         Traces = cell(1,length(user_data)-2);
         for i=1:length(user_data)-2
            Traces{i} = user_data{i+2};
         end
      end

      %if hold is on, or just properties are being added then we don't want to be creating a new figure
later on
      CreateNewFigure = 0;
   end
   %Otherwise if no figure is present but no new trace data exists then there is an error
elseif NewTrace == 0
   DispError('No figure to modify properties of');
   return
end


%%%%%%%%%%%%%%%%%%%%%%%%%%%%%%%%%%%%%%%%%%%%%%%%%%%%%%%%%%%%%%%%%%%%%%%%%%%%
%                                                                               %
%                              ASIGN INPUT                                      %
%                                                                               %
%%%%%%%%%%%%%%%%%%%%%%%%%%%%%%%%%%%%%%%%%%%%%%%%%%%%%%%%%%%%%%%%%%%%%%%%%%%%

function AssignInput(VariableArgIn)

global theta r args axis_limits NewTrace Traces tc oc ppStyle;

num_inputs = length(VariableArgIn);

%set default trace
TraceIndex = 1;

m = 0; %needs to be zero for the while loop 35 lines below

%First assign theta, r and axis_limits if a new trace is being entered
if NewTrace

   %If a trace is being added append two cells on the end of Traces (one for the r/theta values
   %and the other for tc)
   Traces = [Traces cell(1,2)];

   %set the trace number an unassigned number
   TraceIndex = length(Traces)/2;

   %setup the default trace properties structure;
   tc.trace_index = TraceIndex;
   Traces{TraceIndex*2} = tc;

   m = 1;    %Look at the first element of VariableArgIn (which should be the theta data)

   theta = VariableArgIn{m};  %Get the Theta Data

   r = VariableArgIn{m+1};   %Get the Rho Data
```

```
    %set theta, rho and original theta to be column vectors if they aren't already
    [rows cols] = size(theta);
    if rows == 1
        theta = theta';
    end
    [rows cols] = size(r);
    if rows == 1
        r = r';
    end

    %assign the theta and r values to the appropriate trace
    Traces{TraceIndex*2-1} = [r theta];

    m = 2;   %move to the RHO element which was just analysed

    %now check to see if the next input is the axes limits (it will be if its a numeric value) or
    %the standard plot string (it will be if its a string that can't be found)
    if num_inputs > 2
        %if numeric, then must be axis limits
        if isnumeric(VariableArgIn{m+1})     %m = 2 now (3 lines up)
            axis_limits = VariableArgIn{m+1};
            m = 3;  %move to the axis limits variable which was just analysed

        %if string and non existant in args, then must be standard plotting values
        elseif FindArgsIndex(VariableArgIn{m+1}) == 0
            [Color, Marker, Style] = CheckStandardPlot(VariableArgIn{m+1});
            %Assign the color, marker and style if they were defined

            if ~isempty(Color)
                Traces{TraceIndex*2}.line_color = Color;
            end
            if ~isempty(Marker)
                Traces{TraceIndex*2}.line_marker = Marker;
            end
            if ~isempty(Style)
                Traces{TraceIndex*2}.line_style = Style;
            end
            m = 3;
        end
    end
end

%now, step through all the remaining string arguments and compare them to valid arguments (in args)
while m < num_inputs     %number of inputs into function (ie number of variables separated by
commas)
    m = m + 1;

    %find the index in args of the current input argument - we know the index exists as error checking
    %has been done previously
    index = FindArgsIndex(VariableArgIn{m});

    %if another argument is expected to complete this one then assign it (error checking has already
    %been performed)
    if args{index,2} == 1
        eval([args{index,4} '= VariableArgIn{m+1};'])
        m = m+1;  %increment the m counter so that input of the argument is not checked as an argument
    else   %if no other arugument is needed assign third colum of args to variable in 4th column
        eval([args{index,4} '= args{index,3}']);
    end
end
```

```
%NOTES:
%
% TaceIndex:   The user must enter the argument "..., 'Trace', 3, ..." for trace parameters
%              of trace 3 to be altered. In doing so, the while loop above will set TraceIndex
%              to 3. Afterwards, when line style/color etc are altered the evaluation
%              'Traces{TraceIndex*2}.line_style' (see args) will be used so trace 3 will have
%              its properties successfully altered.

%%%%%%%%%%%%%%%%%%%%%%%%%%%%%%%%%%%%%%%%%%%%%%%%
%                                                                                              %
%                          FIND ARGS INDEX                                                    %
%                                                                                              %
%%%%%%%%%%%%%%%%%%%%%%%%%%%%%%%%%%%%%%%%%%%%%%%%

function [index] = FindArgsIndex(StringToFind)
global args;
index = 1;    %start at the first row

%search through the args struct till find index varibale in StringToFind
while ~strcmp(args{index,1},StringToFind)
   index = index + 1;

   %if searched through entire args rows and couldn't find a match then break and return 0
   if index > length(args(:,1))
      index = 0;
      break;
   end
end


%%%%%%%%%%%%%%%%%%%%%%%%%%%%%%%%%%%%%%%%%%%%%%%%
%                                                                                              %
%                        CHECK AXIS LIMITS                                                    %
%                                                                                              %
%%%%%%%%%%%%%%%%%%%%%%%%%%%%%%%%%%%%%%%%%%%%%%%%

function CheckAxisLimits
global oc axis_limits args

%check to see if the axis_limits array elments are empty. If they are not, then it means they have been
%filled by the user in the arguments of the function call. Therefore, change the appropriate centre
value
%and/or maximum magnitude. Because this happens after the assigning of arguments and their
variables (above),
%then if the 'CentreValue' or 'MaxMag' arguments were used, then they will be overwritten by the
axis_limits
if isnumeric(axis_limits) & (size(axis_limits) == [1 2] | size(axis_limits) == [2 1])
   %if both are zero then user hasn't changed axis (or if they have entered [0 0], then its invalid
   %because you can't have centre value and max mag equal and therefore this pretends that they
haven't
   %been this stupid on purpose)
   if axis_limits(1) ~= 0 | axis_limits(2) ~= 0
      %but sometimes, you just have to protect the users from themselves
      if axis_limits(1) == axis_limits(2)
         disp(' ');disp('Cannot make centre value and maximum mag value the same');disp(' ');
      else
         %if valid then assign the centre and max variables to their vew values
         oc.centre_value = axis_limits(1);                  %set the center value to the first element
         oc.max_mag = axis_limits(2);                       %set the max value to the second element
```

```
      end
   end
elseif ischar(axis_limits) & (strcmpi(axis_limits,'off') | strcmpi(axis_limits,'none'))
   oc.ring_axis = 'off';
   oc.angle_axis = 'off';
elseif ischar(axis_limits) & strcmpi(axis_limits,'on')
   oc.ring_axis = 'on';
   oc.angle_axis = 'on';
else
   DispError('"Axis" must be followed by 1x2 or 2x1 numerical vector, or by "on", "off" or "none"
strings');
   return
end

%%%%%%%%%%%%%%%%%%%%%%%%%%%%%%%%%%%%%%%%%%%%%%%%%%%%%%%%%%%%%%%%%%%%%%%%%%%%%%%
%                                                                                 %
%                            SETUP FIGURE                                         %
%                                                                                 %
%%%%%%%%%%%%%%%%%%%%%%%%%%%%%%%%%%%%%%%%%%%%%%%%%%%%%%%%%%%%%%%%%%%%%%%%%%%%%%%

function SetupFigure

global CreateNewFigure oc

%If creating a new figure (flag set in LoadExistingData) then create one
%if CreateNewFigure
%    figure;
%else
   clf reset;   %Otherwise if hold is on, or property modification only, then reset
   %end             %the current figure for full redraw

%Set the figure properties
set(gcf,'Color',oc.background_color,'Position',oc.figure_position)

%Turn hold on for drawing of axes and traces
hold on


%%%%%%%%%%%%%%%%%%%%%%%%%%%%%%%%%%%%%%%%%%%%%%%%%%%%%%%%%%%%%%%%%%%%%%%%%%%%%%%
%                                                                                 %
%                              PLOT AXES                                          %
%                                                                                 %
%%%%%%%%%%%%%%%%%%%%%%%%%%%%%%%%%%%%%%%%%%%%%%%%%%%%%%%%%%%%%%%%%%%%%%%%%%%%%%%

function PlotAxes

global oc r

%check to see if the degrees character is supposed to be plotted or not
degrees_string = '';
if(min(oc.angle_degree_mark == 1) == 1 | strcmp(oc.angle_degree_mark, 'on'))
   degrees_string = '^{\o}';
end

%angle system for all corresponding axis
phi = 0:0.01:2*pi;

%make a circle for the plot's circular border
if ~isempty(oc.circ_border_line_color) | ~isempty(oc.circ_border_color)
   border_line = 1.3;
```

```
    x = border_line*cos(phi);
    y = border_line*sin(phi);
    if ~isempty(oc.circ_border_color)
        fill(x,y,oc.circ_border_color,'LineStyle','none','HandleVisibility','off');
    end
    if ~isempty(oc.circ_border_line_color)
        plot(x,y,'Color',oc.circ_border_line_color,'LineWidth',2,'HandleVisibility','off');
    end
    axis([-1.55 1.55 -1.55 1.55])
else
    axis([-1.2 1.2 -1.2 1.2])
end

%Make up maximum magnitudes and minimum magnitudes
if strcmp(oc.max_mag,'max')
    oc.max_mag = max(r);
end

if strcmp(oc.centre_value, 'min')
    oc.centre_value = min(r);
end
plot_range = oc.max_mag - oc.centre_value;

%Draw the concentric circles (rings)
rings = 1;          %outer ring
if oc.ring_step == 0       %if number of rings defined (default) and not ring step then...
    for i = 1:1:oc.number_of_rings
        rings = [rings (oc.number_of_rings-i)/oc.number_of_rings];
    end
else
    if oc.ring_step > plot_range
        disp('Warning: Ring step is larger than plotting range (max_mag - centre_value)');
    end
    for i = 1-oc.ring_step/plot_range:-oc.ring_step/plot_range:0  %If user define ring step then...
        rings = [rings i];
    end

end

%draw the plot fill circle only if one of the axes are on
if (~strcmpi(oc.ring_axis,'off') & ~strcmpi(oc.ring_axis,'none')) |...
        (~strcmpi(oc.angle_axis, 'none') & ~strcmpi(oc.angle_axis, 'off'))
    fill(cos(phi),sin(phi),oc.plot_area_color,'HandleVisibility','off')
end

%only draw the ring axis and its labels if axis is not set of 'OFF'
if ~strcmpi(oc.ring_axis, 'off') & ~strcmpi(oc.ring_axis, 'none')
    for i = 1:1:length(rings)     %plot the rings
        x = rings(i)*cos(phi);
        y = rings(i)*sin(phi);
        if(rings(i) == 1)      %if on the outer ring, then make a solid line unless user specifies otherwise

plot(x,y,'Color',oc.ring_color,'LineStyle',oc.outer_ring_style,'LineWidth',oc.ring_border_line_width,...
                'HandleVisibility','off');
        else
            plot(x,y,'Color',oc.ring_color,'LineStyle',oc.ring_style,'LineWidth',oc.ring_line_width,...
                'HandleVisibility','off');
        end
    end
```

```
   %Draw on the text labeling the magnitude
   angle_of_mark = oc.mag_mark_angle*pi/180;
   if ~strcmpi(oc.ring_label,'off') & ~strcmpi(oc.ring_label,'none')  %the strcmpi is case insensitive
      for i = 1:1:length(rings)
         x = (rings(i)+0.0*oc.max_mag)*cos(angle_of_mark);
         y = (rings(i)+0.0*oc.max_mag)*sin(angle_of_mark);
         if(rings(i) == 1)   %if on the outer ring's value, then insert units if user has defined them

text(x,y,[num2str(round(rings(i)*plot_range*1000)/1000+round(oc.centre_value*1000)/1000)
oc.ring_units],...
               'FontSize',oc.ring_font_size,  'FontWeight',oc.ring_font_weight,...
               'HorizontalAlignment','left',  'VerticalAlignment','bottom','Color',oc.ring_font_color,...
               'HandleVisibility','off')
         else

text(x,y,num2str(round(rings(i)*plot_range*1000)/1000+round(oc.centre_value*1000)/1000),...
               'FontSize',oc.ring_font_size,  'FontWeight',oc.ring_font_weight,...
               'HorizontalAlignment','left','VerticalAlignment','bottom','Color',oc.ring_font_color,...
               'HandleVisibility','off')
         end
      end
   end
end

%Draw the angle markers
if strcmp(oc.angle_step,'')   %if angle step not defined
   phi = (oc.theta_start:360/no_angle_marks:oc.theta_start+359)*pi/180;   %angle of marks
   phit = oc.theta_start:360/no_angle_marks:oc.theta_start+359;           %angle of labels
else                    %if angle step defined
   phi = (oc.theta_start:oc.angle_step:oc.theta_start+359)*pi/180;
   phit = oc.theta_start:oc.angle_step:oc.theta_start+359;
end

%only draw the angle axis and its labels if axis is not set of 'OFF'
if ~strcmpi(oc.angle_axis, 'off') & ~strcmpi(oc.angle_axis, 'none')
   for i = 1:1:length(phi)
      x = 1*cos(phi(i));
      y = 1*sin(phi(i));
      plot([0x],[0y],'Color',oc.angle_color,'LineStyle',oc.angle_style,'LineWidth',oc.angle_line_width,...
         'HandleVisibility','off')
   end

   %if labels should not be put on every anlge mark then change the text anlges accordingly
   if oc.angle_label_step ~= 0
      phit = oc.theta_start:oc.angle_label_step:oc.theta_start+359;
   end

   if strcmp(oc.theta_direction,'cw')
      phit = -phit;
   end

   %Draw on text labeling the angles
   if ~strcmpi(oc.angle_label,'off') & ~strcmpi(oc.angle_label,'none')
      for i = 1:1:length(phit)
         x = 1*1.15*cos(phit(i)*pi/180);
         y = 1*1.15*sin(phit(i)*pi/180);
         text(x,y,[num2str(abs(phit(i))-oc.theta_start) degrees_string],...
            'FontSize',oc.angle_font_size,'FontWeight',oc.angle_font_weight,...
            'HorizontalAlignment','center','VerticalAlignment','middle',...
            'Color',oc.angle_font_color,'HandleVisibility','off')
```

```
      end
   end
end
axis off


%%%%%%%%%%%%%%%%%%%%%%%%%%%%%%%%%%%%%%%%%%%%%%%%%%%%%%%%%%%%%%%%%%%%%%%%
%                                                                         %
%                          SETUP THETA                                    %
%                                                                         %
%%%%%%%%%%%%%%%%%%%%%%%%%%%%%%%%%%%%%%%%%%%%%%%%%%%%%%%%%%%%%%%%%%%%%%%%

%transform the input to plot out correctly in cartesian coordinates
function theta = SetupTheta(theta)
global oc
theta = theta + oc.theta_start/180*pi;
if strcmp(oc.theta_direction,'cw')
   theta = -theta;
end

%%%%%%%%%%%%%%%%%%%%%%%%%%%%%%%%%%%%%%%%%%%%%%%%%%%%%%%%%%%%%%%%%%%%%%%%
%                                                                         %
%                          SETUP R                                        %
%                                                                         %
%%%%%%%%%%%%%%%%%%%%%%%%%%%%%%%%%%%%%%%%%%%%%%%%%%%%%%%%%%%%%%%%%%%%%%%%

function [norm_r, theta, PlotProperties] = SetupR(r, theta)
global oc DB

%make a note of the original maximum and minimum values of r
max_r = max(r);
min_r = min(r);

plot_range = oc.max_mag - oc.centre_value;

%shift r values so minimum is at 0 + centre value difference
norm_r = r - oc.centre_value;
norm_r = norm_r/plot_range;     %normalise r values between 0 and 1 where 0 is centre
%value and 1 is max distance from centre (plot_range)
%check all values and any that are negative (and therefore less than the centre value) are made
%equal to the centre value
for i = 1:1:length(norm_r)
   if norm_r(i) < 0
      norm_r(i) = 0;
   end
end

%These normalised r values now need to be examined and any values outiside of the
%the maximum magnitude need to be discarded. However, if there is interpolation between
%2 points (one inside the max and one outside) then a new point on this interpolation needs
%to be added in so the line from the point inside the axis still extends out to the outer
%ring. Therefore, a new array of r values which only contain plottable values and additional
%points that are needed is made.

PlotNumCounter = 0;          %Number of plots (ie number of sections within the unity circle)
InPlotFlag = 0;           %if 1, this flag means that current points are in a plotting section
PlotStartFlag = [];       %This will be an array containing the start points for the plot sections
PlotBreakFlag = [];       %This will be an array containing the break points for the plot sections

for i = 1:1:length(norm_r)
```

```
   %the first point that is on or in the unity circle is allocated as the first section's start point
   if isempty(PlotStartFlag) & norm_r(i)<=1
      PlotStartFlag = i;
      InPlotFlag = 1;
      PlotNumCounter = 1;
   else
      %If a point is outside the unity circle and not in the void between a break point
      %and start point then allocate the break point to the point previous to this one
      if(norm_r(i) > 1 & InPlotFlag == 1)
         PlotBreakFlag = [PlotBreakFlag i-1];
         InPlotFlag = 0;
      end

      %If a point is on or in the unity circle and currently is in the void between a break
      %point and start point then allocate this point as the start point of a new section
      if(norm_r(i) <= 1 & InPlotFlag == 0)
         PlotStartFlag = [PlotStartFlag i];
         InPlotFlag = 1;
         PlotNumCounter = PlotNumCounter + 1;
      end
   end
end

%finally, if the last point was in a plotting section then have to define it as the break point
%Bugfixed as per Dr. Thomas Patzelts suggestion from 2/12-08.
if(InPlotFlag == 1)
   if isempty(PlotBreakFlag)
      PlotBreakFlag = length(norm_r);
   else
      PlotBreakFlag = [PlotBreakFlag length(norm_r)];
   end
end

%go through each of the start and end points and for each go to the point next to it that is in
%the void (between start and break points) and calculate the gradient and then add in a point between
%the void point and the valid point that lies on this gradient AND the unity circle. This procedure is
%therefore only needed it a plot exists and it exceeds the unity boundary (ie the only break flag doesn't
%index the last point in the set of data)
if(PlotNumCounter > 0)
   for i = 1:1:PlotNumCounter
      if PlotStartFlag(i) ~= 1   %only look at section starts if its not the first point
         x = norm_r.*cos(theta);   %need to recalculate x and y every time incase norm_r and
         y = norm_r.*sin(theta);   %theta were changed in the previous loop

         %if the gradient between the void and valid points is infinity (ie x1=x2) then the line equation
         %simple becomes x=b, where b is the x coordinate of both points. We also know that for our
wanted
         %point to be on the unity circle we need 1=sqrt(x^2+y^2) => 1=x^2+y^2. Therefore, as x=b,
we can
         %find y as:
         %           y = 1-x^2 = 1-b^2
         %
         %Now, if the void point is in the y>0 quadrants, then the crossing point must occur in the y>0
part
         %of the unity circle. Conversely, if the void point has y<0, then the cross point must occur in
the
         %y<0 semicircle of the unty circle
         if x(PlotStartFlag(i))==x(PlotStartFlag(i)-1)
            Voidx = x(PlotStartFlag(i));
            Voidy = 1-Voidx^2;
```

```
            if(y(PlotStartFlag(i)-1)<0)
               Voidy = -Voidy;
            end
            %however, if the gradient is defined, then we need to calc the gradient to find the point on
the
            %unity circle
         else
            if x(PlotStartFlag(i)-1)<x(PlotStartFlag(i))
               gradient = (y(PlotStartFlag(i)) - y(PlotStartFlag(i)-1))/(x(PlotStartFlag(i)) -
x(PlotStartFlag(i)-1));
            elseif x(PlotStartFlag(i)-1)>x(PlotStartFlag(i))
       %        x(PlotStartFlag(i))
       %        y(PlotStartFlag(i))
       %        keyboard
       %        r(PlotStartFlag(i))
               gradient = (y(PlotStartFlag(i)-1) - y(PlotStartFlag(i)))/(x(PlotStartFlag(i)-1) -
x(PlotStartFlag(i)));
            end
            %C is y intercept of y=mx+c eqation for a straign line
            C = y(PlotStartFlag(i)) - gradient*x(PlotStartFlag(i));
            m = gradient;

            %at the crossing point between line bewteen void and valid and unity circle we know the x,y
            %coordinates must satisfy the straight line eqn y=mx+c and 1=sqrt(x^2+y^2) =>
1=x^2+y+2.
            %Rearranging this yeilds
            %                  0 = (m^2+1)x^2 + (2mc)x + (c^2-1)
            %
            %the roots of this can be solved and x found. Note that there will always be one or two
            %real roots as this procedure is only being implemented when the line DOES cross the unity
            %circle (there will only be one root when the line is a tangent to the unit circle).
            Voidx = roots([m^2+1 2*m*C C^2-1]);
            Voidy = m*Voidx+C;
            %if there are two roots, check which x coordinate is between the void point and valid point
            %and then use that as the true coordinate
            x_limits = [x(PlotStartFlag(i)-1) x(PlotStartFlag(i))];
            y_limits = [y(PlotStartFlag(i)-1) y(PlotStartFlag(i))];
            if length(Voidx) == 2
               if Voidx(1)>min(x_limits) & Voidx(1)<max(x_limits) & Voidy(1)>min(y_limits) &
Voidy(1)<max(y_limits)
                  Voidx = Voidx(1);
                  Voidy = Voidy(1);
               else
                  Voidx = Voidx(2);
                  Voidy = Voidy(2);
               end
            end
         end

         %insert new point into array or points
         norm_r = [norm_r(1:PlotStartFlag(i)-1); sqrt(Voidx^2+Voidy^2);
norm_r(PlotStartFlag(i):length(norm_r))];

         %insert new angle into array of angles
         if(Voidx == 0)
            new_theta = pi/2*sign(Voidy);   %this puts the point in the correct quadrant (CA or ST)
         else
            new_theta = atan(Voidy/Voidx);
            %if x is negative then the definition of atan needs to be added to 180 degrees
            if(Voidx < 0)
```

```
            new_theta = pi+new_theta;
          end
        end
        theta = [theta(1:PlotStartFlag(i)-1); new_theta; theta(PlotStartFlag(i):length(theta))];

        %increment appropiate indecies in PlotStart and PlotBreak flags to take into accout the new
points
        %(remembering you want the new points to be within the plotting segement)
        if(i < PlotNumCounter)  %if not at the last PlotStartFlag
          PlotStartFlag(i+1:PlotNumCounter) = PlotStartFlag(i+1:PlotNumCounter) + 1;
        end
        PlotBreakFlag(i:PlotNumCounter) = PlotBreakFlag(i:PlotNumCounter) + 1;
      end

      %now do the same thing for the break flags, ie going from valid point to void
      %But only consider if the break is NOT the first element, or the break is NOT the last element
      if  (PlotBreakFlag(i) ~= length(norm_r))
        x = norm_r.*cos(theta);  %need to recalc x and y incase norm_r and theta were changed in
previous
        y = norm_r.*sin(theta);  %if statement (for PlotStartFlag) or previous loop

        %refer to previous IF statement (for PlotStartFlag) for full explanation
        if x(PlotBreakFlag(i))==x(PlotBreakFlag(i)+1)
          Voidx = x(PlotBreakFlag(i));
          Voidy = 1-Voidx^2;
          if(y(PlotBreakFlag(i)+1)<0)
            Voidy = -Voidy;
          end
        else
          if x(PlotBreakFlag(i)+1)<x(PlotBreakFlag(i))
            gradient = (y(PlotBreakFlag(i)) - y(PlotBreakFlag(i)+1))/(x(PlotBreakFlag(i)) -
x(PlotBreakFlag(i)+1));
          elseif x(PlotBreakFlag(i)+1)>x(PlotBreakFlag(i))
            gradient = (y(PlotBreakFlag(i)+1) - y(PlotBreakFlag(i)))/(x(PlotBreakFlag(i)+1) -
x(PlotBreakFlag(i)));
          end
          %C is y intercept of y=mx+c eqation for a straign line
          C = y(PlotBreakFlag(i)) - gradient*x(PlotBreakFlag(i));
          m = gradient;

          Voidx = roots([m^2+1 2*m*C C^2-1]);
          Voidy = m*Voidx+C;
          %if there are two roots, check which x coordinate is between the void point and valid point
          %and then use that as the true coordinate
          x_limits = [x(PlotBreakFlag(i)+1) x(PlotBreakFlag(i))];
          y_limits = [y(PlotBreakFlag(i)+1) y(PlotBreakFlag(i))];
          if length(Voidx) == 2
            if Voidx(1)>min(x_limits) &  Voidx(1)<max(x_limits) &  Voidy(1)>min(y_limits) &
Voidy(1)<max(y_limits)
              Voidx = Voidx(1);
              Voidy = Voidy(1);
            else
              Voidx = Voidx(2);
              Voidy = Voidy(2);
            end
          end
        end
        %insert new point into array or points
```

```
        norm_r = [norm_r(1:PlotBreakFlag(i)); sqrt(Voidx^2+Voidy^2);
norm_r(PlotBreakFlag(i)+1:length(norm_r))];

        %calculate and insert new angle into array of angles
        if(Voidx == 0)
           new_theta = pi/2*sign(Voidy);
        else
           new_theta = atan(Voidy/Voidx);
           %if x is negative then the definition of atan needs to be added to 180 degrees
           if(Voidx < 0)
              new_theta = pi+new_theta;
           end
        end
        theta = [theta(1:PlotBreakFlag(i)); new_theta; theta(PlotBreakFlag(i)+1:length(theta))];

        %increment appropiate indecies in PlotBreak and PlotBreak flags to take into accout the new
points
        %(remembering you want the new points to be within the plotting segement)
        if(i < PlotNumCounter)  %if not at the last PlotBreakFlag
           PlotStartFlag(i+1:PlotNumCounter) = PlotStartFlag(i+1:PlotNumCounter) + 1;
        end
        PlotBreakFlag(i:PlotNumCounter) = PlotBreakFlag(i:PlotNumCounter) + 1;
     end
  end
end

PlotProperties{1} = PlotNumCounter;
PlotProperties{2} = PlotStartFlag;
PlotProperties{3} = PlotBreakFlag;

%%%%%%%%%%%%%%%%%%%%%%%%%%%%%%%%%%%%%%%%%%%%%%%%%%%%%%%%%%%%%%%%%%%%%%%%%%%%%%%
%                                                                                 %
%                              PLOT TRACE                                         %
%                                                                                 %
%%%%%%%%%%%%%%%%%%%%%%%%%%%%%%%%%%%%%%%%%%%%%%%%%%%%%%%%%%%%%%%%%%%%%%%%%%%%%%%

function PlotTrace(theta, norm_r, PlotProperties, TraceProps)

PlotNumCounter = PlotProperties{1};
PlotStartFlag = PlotProperties{2};
PlotBreakFlag = PlotProperties{3};

x = norm_r.*cos(theta);
y = norm_r.*sin(theta);

handle_visibility = 'on';  %first segment trace is to have a handle that can be access by prompt

%(eg - to use to make the legend)
%if there are any plot sections to plot then go ahead and plot
if(PlotNumCounter > 0)
   for i = 1:1:PlotNumCounter      %for each plot section redefine x and y between the start and break
flags
      x = norm_r(PlotStartFlag(i):PlotBreakFlag(i)).*cos(theta(PlotStartFlag(i):PlotBreakFlag(i)));
      y = norm_r(PlotStartFlag(i):PlotBreakFlag(i)).*sin(theta(PlotStartFlag(i):PlotBreakFlag(i)));
      %plot the thing - FINALLY

      plot(x,y,'LineWidth', TraceProps.line_width,
'LineStyle',TraceProps.line_style,'Color',TraceProps.line_color,...
         'Marker',TraceProps.line_marker, 'HandleVisibility',handle_visibility);
```

```
      handle_visibility = 'off';  %once the first trace segment is plotted, want the remaining handles hidden so
   end                        %the legend doesn't display them, but moves straight onto the next trace
end

%%%%%%%%%%%%%%%%%%%%%%%%%%%%%%%%%%%%%%%%%%%%%%%%%%%%%%%%%%%%%%%%%%%%%%%%%%%%%%%
%                                                                              %
%                          CHECK PLOT LIMITS                                   %
%                                                                              %
%%%%%%%%%%%%%%%%%%%%%%%%%%%%%%%%%%%%%%%%%%%%%%%%%%%%%%%%%%%%%%%%%%%%%%%%%%%%%%%

function CheckPlotLimits

global oc Traces

%Make up maximum magnitudes and minimum magnitudes
if ~isnumeric(oc.max_mag)
   if strcmp(lower(oc.max_mag),'max')
      TraceMax = '';
      for i = 1:2:length(Traces)
         TraceMax = [TraceMax max(Traces{i}(:,1))];
      end
      oc.max_mag = max(TraceMax);
   else
      DispError('"MaxValue" must be a value or "max"');
      return
   end
end

if ~isnumeric(oc.centre_value)
   if strcmp(lower(oc.centre_value), 'min')
      TraceMin = '';
      for i = 1:2:length(Traces)
         TraceMin = [TraceMin min(Traces{i}(:,1))];
      end
      oc.centre_value = min(TraceMin);
   else
      DispError('"CentreValue" must be a value or "min"');
      return
   end
end

%make sure input is not bogus
if oc.max_mag < oc.centre_value
   DispError('Centre value is larger than maximum input value');
   return
end

if oc.max_mag == oc.centre_value
   DispError('Centre value is same as maximum input value - define CentreValue if all r values are same - see help');
   return
end

%%%%%%%%%%%%%%%%%%%%%%%%%%%%%%%%%%%%%%%%%%%%%%%%%%%%%%%%%%%%%%%%%%%%%%%%%%%%%%%
%                                                                              %
%                       CHECK STANDARD PLOT                                    %
%                                                                              %
%%%%%%%%%%%%%%%%%%%%%%%%%%%%%%%%%%%%%%%%%%%%%%%%%%%%%%%%%%%%%%%%%%%%%%%%%%%%%%%
```

```
%This function will check a string that is a shortcut plotting string incorperating the marker, style and
color.
%It will return seperate color, marker and style strings if they are found in the combined string. If the
%combined string has a syntax error then the function will exit the m file and return an error referring
the
%user to the HELP PLOT help command.
function [Color, Marker, Style] = CheckStandardPlot(PlotString)

LineColorFlag = 0;
LineMarkerFlag = 0;
LineStyleFlag = 0;

Color = '';
Marker = '';
Style = '';

%check the standard_plot variable. If it is not emplty, that means the user has selected the PLOT
%functions shortcut arguments to make a plot. Therefore, convert these arguments to the appropriate
%line color and style. Note, that this will overwrite future uses of LineColor and LineStyle in the
%arguments

if length(PlotString) > 4 | isempty(PlotString)            %color, marker, style
   DispError(['Incorrect plot parameters: ''' PlotString '''. Type HELP PLOT to see correct usage']);
   return
end
i = 1;
while i <= length(PlotString)
   c = PlotString(i);         %temp character variable
   %check the color
   if (c == 'y' | c == 'm' | c == 'c' | c == 'r' | c == 'g' | c == 'b' | c == 'w' | c == 'k') & LineColorFlag == 0
      LineColorFlag = 1;
      Color = c;

   %check the marker style
   elseif (c == '.' | c == 'o' | c == 'x' | c == '+' | c == '*' | c == 's' | c == 'd' | ...
         c == 'v' | c == '^' | c == '<' | c == '>' | c == 'p' | c == 'h') & LineMarkerFlag == 0
      LineMarkerFlag = 1;
      Marker = c;

   %check the line style
   elseif (c == '-' | c == ':') & LineStyleFlag == 0 %| c == '-.' | c == '--'  %THIS NEEDS FIXING
      LineStyleFlag = 1;
      Style = c;
      if(c == '-' & i < length(PlotString) )
         if PlotString(i+1) == '.' | PlotString(i+1) == '-'
            Style = [Style PlotString(i+1)];
            i = i + 1;
         end
      end
      %if neither color nor marker nor style then error
   else
      DispError(['Incorrect plot parameters: ''' PlotString '''. Type HELP PLOT to see correct usage']);
      return
   end
   i = i+1;
end
```